LA-7474-PR
Progress Report

C.3

REPRODUCTION
COPY
IS-4 REPORT SECTION

LASL

Controlled Thermonuclear Research Program

January—December 1977

LOS ALAMOS SCIENTIFIC LABORATORY
Post Office Box 1663 Los Alamos, New Mexico 87545

The four most recent reports in this series, unclassified, are LA-5656-PR, LA-6044-PR, LA-6582-PR, and LA-7082-PR.

This work was supported by the US Department of Energy, Office of Fusion Energy.

UNITED STATES
DEPARTMENT OF ENERGY
CONTRACT W-7405-ENG. 36

LA-7474-PR
Progress Report
UC-20
Issued: February 1979

LASL

Controlled Thermonuclear Research Program

January—December 1977

Compiled by

K. S. Thomas
G. A. Sawyer

ABSTRACT

This report presents the status of the Controlled Thermonuclear Research program at the Los Alamos Scientific Laboratory for calendar year 1977.

CONTENTS

I. INTRODUCTION

H. Dreicer, G. A. Sawyer, K. S. Thomas

In the Reversed-Field Pinch Program, experiments continued on the 15-cm-bore ZT-S experiment. Efforts concentrated on the measurement of the radiation loss from impurities and on raising the electron temperature by operating at a lower filling pressure and by the use of low-temperature discharge cleaning. Construction of the 40-cm-bore ZT-40 experiment was begun. ZT-40 has been designed to have great versatility and can operate over a wide range of risetimes (2.5 μs-1 ms). It will allow the study of the high-beta programmed reversed-field profiles as well as the generally lower beta configurations obtained by self-reversal. Once the desirable properties of the high-beta equilibrium can be demonstrated, efforts will be made to determine the optimum method for setting up and maintaining the configurations from the reactor technology point of view.

The final experiments on the Scyllac feedback stabilization project have been completed, and the experiments have been terminated. The last experiments differed from previous efforts in several important aspects. First, the equilibrium configuration was changed from the $\ell=0,1$ combination of stellarator fields to $\ell=1,2$ stellarator fields. Secondly, the helical plasma perturbation was much larger on these final experiments than on the previous Scyllac experiments giving a plasma helical radius of about 3 cm vs the value of 1.4 cm used in the earlier experiments. Also the wavelength of the fields was increased from 0.62 m to 1.0 m. The feedback system in the final series of experiments was also different from the previous cases in that the output of the position detectors was processed in such a manner as to drive the power amplifiers in response to the model structure of the plasma instability rather than the displacements as seen by the individual detectors.

Experiments continued in the 5-m-long Scylla IV-P linear theta pinch. The main experiments were an investigation of the characteristic end-loss times, study of the plasma flow processes near the theta-pinch coil ends, and material end-plug end-stoppering experiments designed to eliminate axial particle flow.

Activities in the Staged Theta Pinch concentrated on constructing, checking out, and collecting data with a Thomson scattering apparatus. Data were collected at two axial positions, one near the center of the main compression coil and one near the end. At the center of the coil, data were taken at three radial positions; at the end, data were taken at four radial positions. Measurements were made as a function of time with initial D_2 fills from 3 to 15 mtorr.

Two small experiments were used to study the stability and confinement properties of the reversed-field configuration formed in a theta pinch when a reversed bias field is used. This configuration shows unexpectedly favorable stability characteristics which are of interest for increasing energy confinement in open-ended systems such as mirrors, theta pinches, and liners.

Experiments on the Implosion Heating Experiment were ended in November 1977, and the personnel involved transferred to the Fast Liner Program. The first part of the year was spent finishing a detailed measurement of the magnetic field as a function of time and radius using magnetic probes and Faraday rotation. The major part of the year was spent taking temperature and density data using Thomson scattering at four radial positions.

In the fall of 1977, approval was given to begin a Fast Liner experimental program. Initial experiments on the imploding liner will use three capacitor racks of the Scyllac bank. Plasma preparation studies will be conducted on the Gun Injection Experiment.

The Gun Injection Experiment operated throughout the year. The initial measurements were of the properties of the gun plasma itself. These were followed by an investigation of plasma injection into a short (50-cm-long) solenoidal guide field having a typical strength of about 10 kG.

The primary efforts of the Experimental Plasma Physics Group are directed toward the study of high-frequency plasma resistivity, plasma

heating, and heat flow in the presence of plasma turbulence, electron drifts, and other effects likely to be present in plasmas of current fusion interest. Experimental studies, which were being done on a Q-machine, were temporarily suspended on May 25, 1977, to allow dismantling of the equipment to make room for the construction of the ZT-40 experiment. Relocation of the experiment into a new area was begun in late December, and it is planned to be in operation by June 1978.

An experimental program was set up in May 1977, to investigate a very high density Z-pinch initiated by a small-diameter laser beam. During 1977, a prototype of one module of the power supply was built and brought into operation. Studies of plasma initiation using a ruby laser will begin in early 1978.

The Plasma Diagnostic group continued work on the spatially resolved Thomson scattering apparatus and the scanning infrared heterodyne interferometer. Work on several new diagnostics was begun. Some general-purpose computer codes were developed and a major effort continued on the use of minicomputers for data acquisition and device control.

The work of the theory group is closely associated with and motivated by the experimental CTR program at LASL. For several years the problems and requirements of the Scyllac experiment provided the major motivation for research in the theory group. However, now that the Scyllac program has ended and the CTR effort at LASL has become directed toward alternate concepts, the variety of theoretical research has increased. Areas of activity included MHD calculations, numerical simulations, and studies of kinetic effects and magnetoacoustic heating.

The shortage of computer resources at LASL, coupled with the increased utility of the PDP-10 and MFE network, has made the USC facility a vital link in the LASL MFE effort. The PDP-10 has been used for scientific problems, administrative accounting, and inventory control. Many of the large-particle simulation and MHD stability codes have been shifted to the network from the LASL computers. Preliminary design of the ZT-40 control and data acquisition system was completed and the Scylla IV-P operating system was upgraded.

During the year the goal of the Magnetic Energy Transfer and Storage program changed from development of the superconducting magnetic transfer and storage system for use in future theta-pinch experiments to development of superconducting tokamak poloidal field systems. The emphasis in this program is directed toward future large tokamak experiments.

The focus of all systems and design studies of magnetically confined fusion concepts was on alternative or exploratory concepts. A major design effort on the Reversed-Field Pinch Reactor concept was completed, based upon a moderately pulsed mode of operation. On the basis of this design, a second design study was begun that investigated both the physics and technology associated with a larger, extended-burn operating mode. Studies of both the Fast Liner Reactor and Liner Magnetic Fusion concepts emphasized physics and energy-balance constraints for fusion power, although crucial technological issues for both the concepts were addressed. A study of toroidal bicusp confinement (Tormac) was begun which focused on elucidating viable physics operating points with total power, energy balance, and first-wall loading being enforced as major constraints. Scoping studies of generalized hybrid (fusion/fission) and synfuel (thermochemical hydrogen) applications of fusion power were also begun. Work on neutronics studies and insulator research continued.

The main activity of the engineering groups was the development, design, and testing of components for the new ZT-40 experiment. Other areas of activity included the design of the high-density Z-pinch, capacitor and ignition switch life testing, and design and testing of advanced components which may be needed in future experiments.

The Tritium Systems Test Assembly, which was initiated in February 1977, is dedicated to the development, demonstration, and interfacing of technologies related to the deuterium-tritium fuel cycle for fusion reactor systems.

II. REVERSED-FIELD PINCH PROGRAM

D. A. Baker, G. P. Boicourt, C. J. Buchenauer, R. T. Buck, A. Buffa (Visiting Scientist, Universita di Padova, Padova, Italy), L. C. Burkhardt, G. I. Chandler, J. N. Di Marco, R. S. Dike, J. N. Downing, Jr., P. R. Forman, A. Haberstich, C. F. Hammer, K. W. Hanks, L. D. Hansborough, R. B. Howell, A. R. Jacobson, F. C. Jahoda, R. W. Kewish, Jr., R. Kristal, K. J. Kutac, J. W. Lillberg, E. M. Little, M. D. Machalek, J. G. Melton, W. C. Nunnally, A. E. Schofield, K. S. Thomas, L. C. Wilkerson, R. W. Wilkins, and P. C. T. Van der Laan

A. INTRODUCTION

The toroidal reversed-field pinch program continues to be motivated by its promise of high-beta stable equilibrium configuration with the possibility of ohmic heating to ignition with moderate magnetic fields. Further advantages stem from the freedom of choice of aspect ratio that gives an escape from possible adverse trapped-particle effects and can lead to a simpler modular construction with easier access as compared to a compact torus.

The LASL program is currently centered on the 15-cm-bore ZT-S experiment and the 40-cm-bore ZT-40 experiment presently under construction. In 1977, efforts on the ZT-S experiment have been concentrated on the measurement of the radiation loss from impurities and in the study of possible raising of electron temperature by operating a lower filling pressure and by the use of low-temperature discharge cleaning.

The ZT-40 experiment is presently about at midpoint in its construction schedule. The experiment has been designed to have great versatility and can operate over a wide range of risetimes (2.5 μs-1 ms). It will allow the study of the high-beta programmed reversed-field profiles as well as the generally lower beta configurations obtained by self-reversal. Once the desirable properties of the high-beta equilibrium can be demonstrated, efforts will be to determine the optimum method for setting up and maintaining the configurations from the reactor technology point of view. The scheduled date for beginning physics on ZT-40 is July 1979.

B. ZT-S

1. General. A chief factor limiting the confinement time in the ZT-S reversed-field experiment after favorable plasma-field profiles are produced is the degeneration of the stability of the configuration with time due to resistive effects. The measured electron temperatures are low and field diffusion rates are high. One candidate for keeping the temperature down is the energy loss from impurity line radiation. The general objectives this past year have been to (1) determine the nature and magnitude of the radiation loss, (2) operate at lower filling pressures in an attempt to raise electron temperatures, (3) design and test a discharge cleaning scheme, (4) design, build, and test a power crowbar circuit to lengthen useful time of the field. Starting in February 1978, the plan is to then upgrade the ZT-S experiment in cleanliness, ease of changing programming modes, and to incorporate improved diagnostics. The experiment is to be used to give as much information as possible in the areas of cleaner systems, impurities, discharge cleaning of alumina tori, and, if possible, programming at elevated electron temperatures. This information is to give guidance for the LASL ZT-40 experiment currently under construction.

2. Radiation Loss Measurements.

a. Nature and Level of Impurities. Spectroscopic and mass analyzer measurements of the ZT-S discharge have shown that the main impurity is oxygen with smaller amounts of carbon and nitrogen. The impurity number density is in the range from ~ 0.3% to ~ 1% of the deuterium fill. Theoretical calculations[1] predict serious energy losses that can cause limitations on the electron temperatures for the current densities being studied (J_{Total} = 1-3 kA cm^2).

b. Absolute Measurements of the Radiation Loss.

(1) Method. A survey of the impurity lines was made spectroscopically to determine the spectral range of the line radiation emitted from the ZT-S plasma. The wavelength region containing the substantial portion of radiation is between 200-1000 Å. A fast system that was sensitive to vacuum ultraviolet radiation was assembled,

tested, and arranged to view the ZT-S pinch through a pump port. A schematic of the detector arrangement is shown in Fig. II-1. Basically the detecting system consists of a fast, linear photodiode of wide dynamic range (ITT FW 128). This detector is sensitive to visible wavelengths and is used with a sodium salicylate phosphor wavelength shifter that intercepts the photons emerging from the plasma. The fluorescence emission spectrum of the phosphor varies by a factor of 1.45 from 2500 Å to 1200 Å and then is flat down to 200 Å. The fluorescence spectrum centers at ~ 4200 Å, well within the high-sensitivity range of the photodiode. This was the primary detection system used for results reported below.

The radiation from the plasma in the ZT-S discharge passes through the aperture in the alumina plug inserted into the pump port and then through two successive 1-cm-diam apertures to the detector. The last two apertures are covered with a wire mesh grid to improve the detector shielding against electrical noise. The signal from the detector is amplified and then transmitted to an oscilloscope display.

(2) Results. The analysis and interpretation of the results of the measurements involve several factors (a) the calibration of the detector, (b) the source and detailed solid angle corrections, (c) the determination of mean photon energy. Since the measurement was made through a single port, assumptions about the source distribution are needed to make determinations of the absolute value of the radiative energy loss. Comparisons with different assumed source distributions show that this introduces the largest uncertainty, about a factor of two, into this determination.

The results indicate that, for sharp boundary plasma with a flat emission profile, a radiative loss of 5 to 8 MW per meter length is obtained during the ~ 30-μs stable time of the discharge. The total energy balance for a sample discharge is shown in Fig. II-2. The two curves show the energy input and energy content per meter of length (plasma + field energy) of the discharge as a function of time as deduced from current, voltage, and magnetic probe data. For comparison, the difference between the two curves, which represents the energy loss, is shown in Fig. II-3 along with the radiation loss as deduced from the above detector measurements. The same radiation loss curve is compared with the calculated ohmic heating for T_e = 15 eV in Fig. II-4. These curves indicate that essentially all of the loss is due to the radiation. In view of the factor of ~ 2 in uncertainty in the absolute radiation measurement mentioned earlier, this agreement may be fortuitous. The measurement does indicate however that the radiation contributes in a significant way to the energy loss.

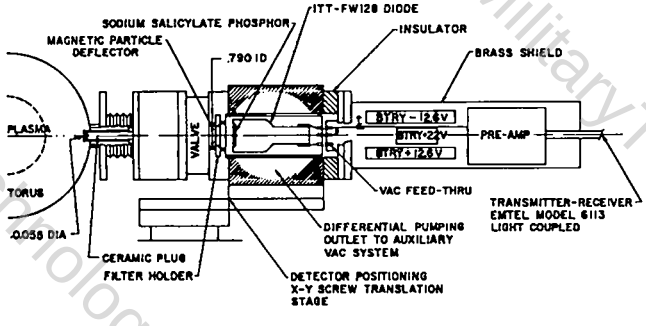

Fig. II-1.
Schematic of radiation detector.

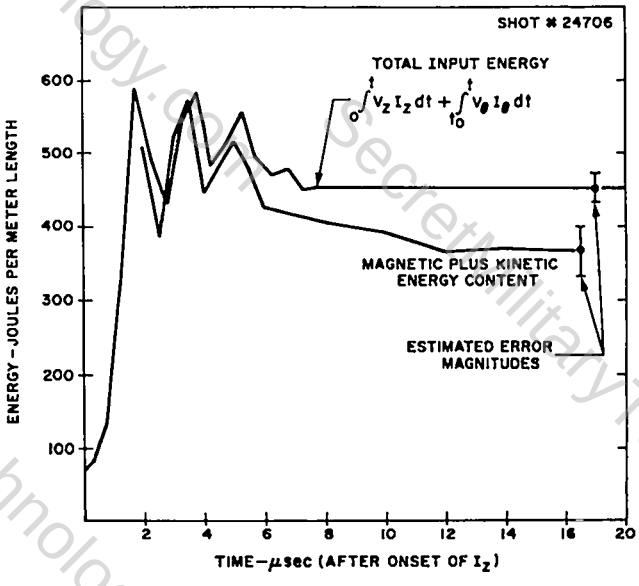

Fig. II-2.
Curves of energy input and content vs time in ZT-S.

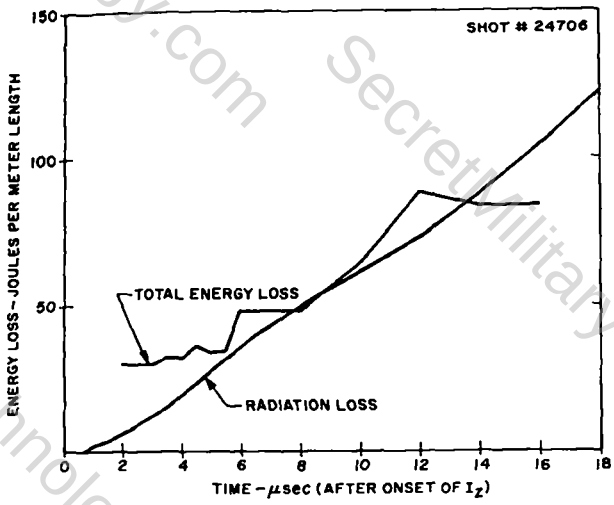

Fig. II-3.
Curves comparing measured radiation loss with that deduced from energy balance shown in Fig. II-2.

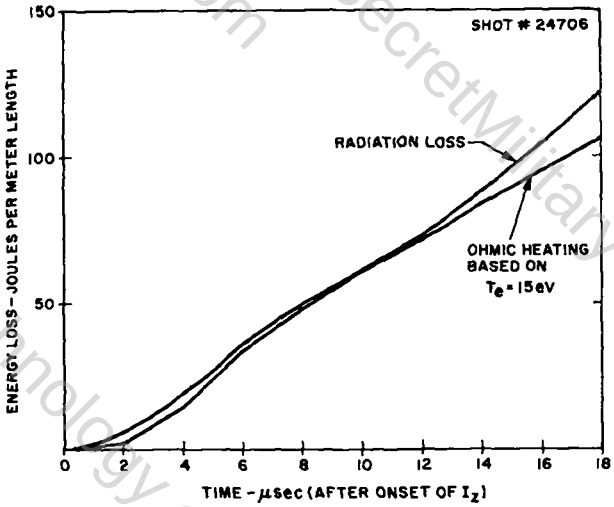

Fig. II-4.
Curves comparing the measured radiation loss with the calculated ohmic input.

For plasma temperatures of 15-20 eV, as estimated for ZT-S from Thomson scattering and spectral impurity ionization state measurements, a calculation of the theoretical radiation loss rate gives values of 8-10 MW per meter. The radiation loss rates were computed for assumed values of T_e using Ortolani's POWRAD code[2] based on McWhirter's radiation loss equation[3] with a multiplying factor of 5 as suggested by the Maryland Group results.[4] This agreement is better than expected in view of the uncertainties in the measurements and the approximations made in the functions used in determining the ionization, excitation, and emission processes.

The conclusions of these studies are as follows. For ZT-S operating at I = 60 kA and a filling pressure of 20 mtorr, (a) the radiation loss is $\gtrsim$ 50% of the energy loss in ZT-S, (b) the radiation is primarily in the vacuum uv with a mean energy of ~ 30 eV ($\lambda \sim 400$ Å), (c) the chief impurities are oxygen and carbon, (d) these results are comparable to those predicted by theory.

3. Electron Temperature Measurement. Thomson scattering measurements of electron temperature at filling pressures of 18 and 34 mtorr have been described in the previous LASL Controlled Thermonuclear Research annual report.[1] Measurements at lower densities were then hampered by instrumental scattering. This problem has now been resolved by the addition of two 6943-Å notch filters to the scattered spectrum detector. The width at half maximum of each filter is 10.2 Å. The overall sensitivity of the detector is reduced by a factor of 2, whereas the instrumental scattering signal is down by a factor of 15. Good data have been obtained at filling pressures of 10 mtorr. Data acquisition at 5 mtorr is limited by the stability of the pinch rather than by the sensitivity of the diagnostic.

The temperature measurements shown in Fig. II-5 have been obtained with a filling pressure of D_2 of 10 mtorr, and a peak toroidal current of 60 kA with an initial rise of 35 kA/μs. The initial bias field was set at 0.064 T and the toroidal field at the wall reversed to -0.079 T in about 15 μs. The postimplosion plasma radius as estimated from pressure profiles was of the order of 4 cm.

The square data points have been obtained with a polychromator dispersion of 33 Å/mm and the circles with a dispersion of 66 Å/mm. The solid circles are the result of a least squares fit to 7 polychromator channels. The open circles are based on the same data, but using the two closest channels only on each side of the 6943-Å channel. The difference between the two analyses is relatively minor at late time in the discharges (> 10 μs). At early times, however, the analysis based on 4 data points gives a much lower

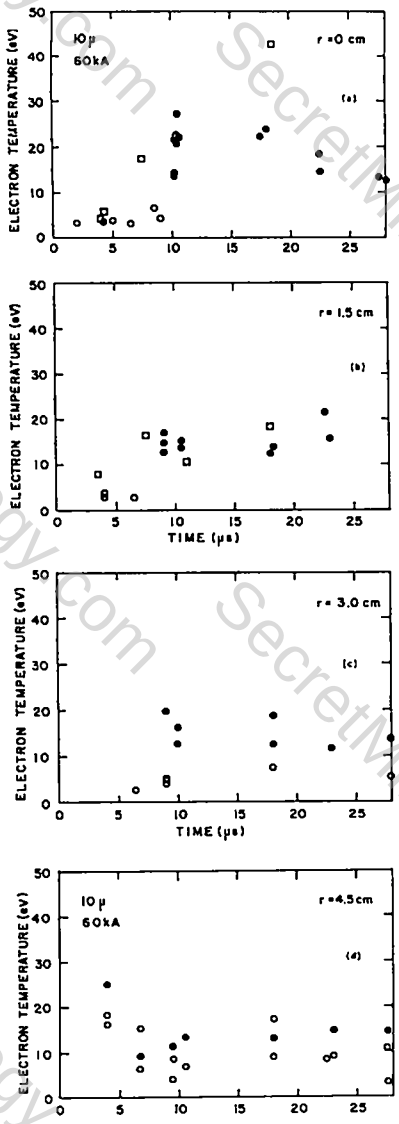

Fig. II-5.
Thomson scattering measurement of electron temperature at (a) 0-, (b) 1.5-, (c) 3.0-, and (d) 4.5-cm radius. Peak toroidal current 60 kA, filling pressure 10 mtorr of D_2.

temperature and, perhaps, a better representation of the main body of the electron distribution than the 7-point analysis.

Figure II-5(a) shows a peak central value of T_e of 25 eV, which then decays gradually to 15 eV at 25 μs. The electron temperature at 1.5- and 3-cm radii levels off at about 15 eV. Assuming full preionization, conservation of particles, and a poloidal β of 0.6, one would expect a value of $T_i + T_e$ of approximately 60 eV at peak current and of 27 eV at 25 μs.

Comparison of this result with the previous T_e measurements indicates an increase of the electron temperature at lower filling pressures. The peak values of T_e reported earlier[1] were 12 eV at 34 mtorr and 15 eV at 18 mtorr.

4. Discharge Cleaning Studies.

a. Motivation. The radiation loss studies indicate the need for determining if suitable discharge cleaning methods can be developed in order to reduce the impurity level to acceptable limits. A preliminary investigation was made to determine the usefulness of the low-temperature discharge technique[5] for oxygen removal from an alumina discharge vessel. Previous work in this area has been limited to metal-walled systems. It is known, however, from the results of the Petula group at Grenoble that the replacement of a tungsten limiter with an alumina one can reduce the oxygen in the discharge a factor of three to four.

If the simple low-temperature discharge cleaning proves successful, it is planned to use discharge cleaning pulses on ZT-40 prior to the main discharge, thus minimizing the amount of baking required.

b. Discharge Cleaning Circuit. The discharge cleaning circuit consists of capacitor and switching circuit capable of delivering ~ 110 J per pulse to a series connection of the toroidal and poloidal field circuits. This arrangement forms a 2-kA screw pinch and is capable of producing one to five pulses per second. The circuit can be quickly removed from the experiment by the use of a pair of pneumatically operated switches thus minimizing the time between the cleanup discharges and the normal firing of ZT-S.

c. Discharge Characteristics. The wave forms for the discharge cleaning circuit are shown in Fig. II-6 for the low-pressure case. The voltage shown in the figure is the voltage across the feedplates for one quadrant of the torus. The current I_p is the toroidal plasma current. The current I_θ is the current in the toroidal field windings, in this case breakdown is delayed for the first 150 μs.

Plasma was generated over a range of 0.7 to 40 mtorr, 0.7 mtorr being a limit below which breakdown would not occur. At these lowest

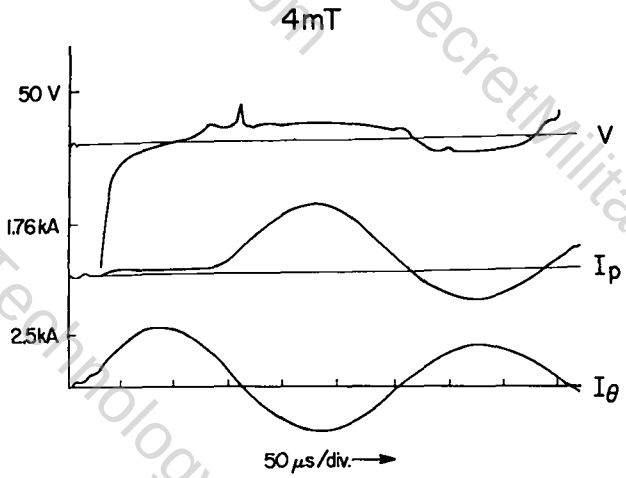

Fig. II-6.
Voltage, plasma current, and input toroidal field current wave forms during a discharge cleaning pulse in ZT-S.

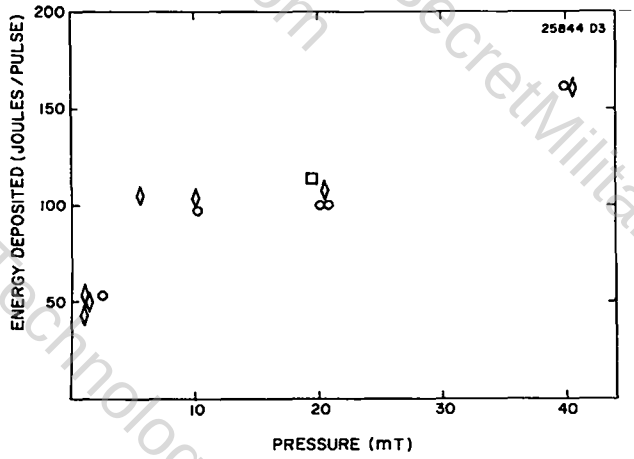

Fig. II-7.
Plasma energy deposition per pulse with probes in (○), out (◊), and an independent check (□) of the probe-out case.

pressures uv radiation was required to initiate breakdown, and then substantial plasma currents failed to flow during the first half-cycle.

Also from Fig. II-6 a dc offset can be seen in the plasma current I_p. This is due to trapping of the poloidal flux in the plasma, and leads thereby to a time variation of q. When B_ϕ goes through zero, q is zero. When this happens there is probably an instability and/or a rapid expansion of the plasma radius which causes the plasma to contact the wall. The result of q's going through zero shows up as a voltage spike across the current feed terminals.

The energy input for different pressures is shown in Fig. II-7.

The electron temperature of the plasma during discharge cleaning was measured by two methods. First the resistivity of the plasma was calculated from the voltage and current traces. Using the Spitzer equation and obtaining the plasma radius from the streak pictures we find ~ 2-3 eV for the filling pressures of 1, 10, and 20 mtorr. The second method was a line to continuum measurement using D_ξ 4861 Å. From this we found 3.0 eV at 10 mtorr and 2.0 eV at 1 mtorr.

d. Vacuum System. The torus is pumped by a turbomolecular pump and an ion pump through a long pipe and five 1.4-cm-diam tubulations. The conductance for this system is ~ 17 ℓ/s at the torus and the background pressure is normally about 4×10^{-6} torr in the torus. A mass analyzer is attached to the pumping system just above the pumps so that it samples the gases pumped out during the discharge cleaning.

e. Results. The mass analyzer has been used to observe the gases that are pumped from the torus before and during discharge cleaning. The principal mass numbers observed are 14, 16, 18, 19, 20, and 28. These correspond to N, O or CH_4, H_2O, HDO, D_2O, and CO or N_2. The ambiguity between D_2O and CD_4 was resolved by comparing results between hydrogen and deuterium discharges.

The mass analyzer was used to monitor the D_2O line during the discharge cleaning. The behavior of D_2O during and after discharge cleaning is shown in Fig. II-8 for 1, 10, and 20 mtorr. With the turn-on of discharge cleaning there is an increase in D_2O. The amplitude of this signal decreases rapidly in the first few minutes and then levels off. When the discharge cleaning is terminated, the D_2O decreases immediately. When the gas flow is terminated the D_2O further decreases usually below the initial level present.

These data indicate that, as previously observed by R. J. Taylor in metal-wall systems, oxygen is being converted to water by the low-temperature discharge and is then pumped out.

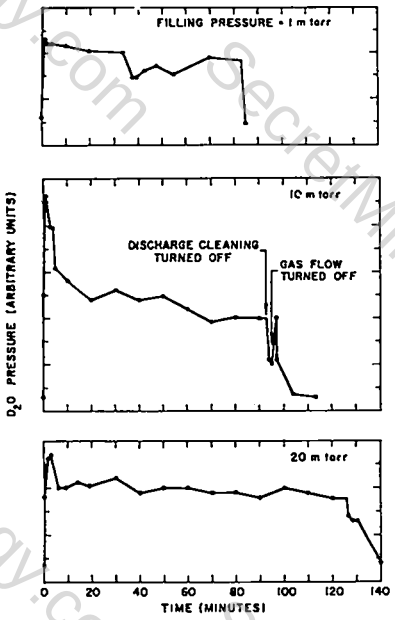

Fig. II-8.
The time history of D_2O during a discharge cleaning process as measured by a mass spectrometer for 3 different gas fill pressures.

f. Conclusions.

(1) Water is generated by the 2- to 5-eV plasma and is pumped from the system as has been observed in metal tori. This was done without overheating the polyethylene electrical insulation of ZT-S.

(2) Five hours of discharge cleaning reduced the outgassing rate a factor of two or more.

(3) In addition to water the main impurity observed on the mass spectrograph was found to be mass 28 (CO or N_2).

(4) A simple capacitive discharge circuit allowing immediate switching between discharge cleaning and normal high-voltage operation has been demonstrated to be practical for this application.

5. ZT-S Upgrade.

a. Torus and Vacuum System. The ZT-S experiment is scheduled to undergo major modifications starting in February 1978. The main goal of this effort is to significantly improve the purity of the RFP discharges. A new segmented alumina torus will be installed with only 24 instead of the present 90 Viton O-rings. Use of vacuum grease during the assembly will not be permitted. The present pumping stand will be replaced by a new, oil-free, vacuum system and the effective pumping speed will be increased from 17 to 60 ℓ/s. The gas fill system will be entirely rebuilt to permit accurate mixing of a variety of gases for impurity studies.

The reduction in the number of torus O-rings will be made possible by the use of a glass sealing technology developed at LASL for ZT-40. Four-degree ceramic segments will be sealed in sets of five and six at a temperature of 1260°C. The surfaces of the remaining circumferential joints will be coated with a thin layer of the same glazing material to help ensure hermeticity of the O-ring seals.

Viewing and pumping sections will be made of quartz. This mixing of alumina and quartz torus segments and the ensuing mismatch of expansion coefficients can be tolerated in ZT-S because of its small size, and since there is no plan to bake the discharge torus in situ.

The present 14-mm-diam pump ports (3 of which are either closed off or occupied by magnetic probes) will be replaced by a single 44.5-mm-diam side tubulation. Measurements on a replica of the primary conductor indicate a toroidal field error of ~ 35% for a 57.5-mm-diam hole. To reduce this perturbation, the new pump port will be fitted with a movable conducting plug which will be moved into position just prior to the firing of the discharge.

One of the benefits of the improved vacuum technology will be a reduction of the base pressure in the discharge chamber. This pressure is important since it affects the rate at which layers of impurity build up at the wall of the torus during the interval between gas fill and firing of the experiment.

The base pressure in the present configuration has been determined indirectly by interpretation of remote pressure gauge readings. A computer code solving 20 coupled equations has been written for this purpose. Known values of conductance, pumping, and outgassing rates are entered in the program and unknown values of these parameters are adjusted to give the best possible fit with available pressure readings. Proceeding in this fashion a base pressure of 4×10^{-6} torr has been calculated for the present ZT-S configuration.

After adjustment of the codes for the new pumping configuration and the reduced number of O-rings, a base pressure of 6×10^{-7} torr is predicted for the new torus, a factor of 6.5 lower than obtained previously.

b. Improved Circuitry. Another facet of the ZT-S upgrade will be the use of a power crowbar system, which together with a modification of the toroidal field banks, will allow more flexibility in the setting up of the RFP discharges. The power crowbar has recently been installed and typical current waveforms with passive crowbar only and with both passive and power crowbars are shown in Fig. II-9.

c. Improved Diagnostics. Whereas new Faraday rotation techniques are under development for ZT-40, the ZT-S experiment will have to rely on internal magnetic probes for the measurement of magnetic field distributions. These data are of utmost importance since they form the basis of our diffusion, energy content, and ideal and resistive MHD stability calculations.

The present magnetic probes have a rather large outer diameter of 10 mm. Smaller probes will be available on ZT-S with a jacket diameter of the order of 4 mm. The integrity of the vacuum will be ensured by the use of newly designed bellow-sealed probe mechanisms.

The electron density distribution in ZT-S will be measured with a multichord interferometer operating at a wavelength of 3.9 μm. In order to acquire complete data for Abel inversion on each discharge, the integrated electron density will be measured along five parallel chords simultaneously. A device has been developed to do this using only one laser, by means of Bragg diffraction heterodyne techniques.[6] The phase detection is in quadrature[7] so that an accurate, unambiguous, and uniform record of interferometric phase is obtained in each channel.

The optical layout is shown in Fig. II-10. The scheme is basically a Mach-Zehnder arrangement with the acousto-optic cell serving as a beam-splitter and with each of the five scene beams each traversing the plasma twice. The Bragg cell not only splits the scene and reference beams but also shifts the reference beams' infrared frequency by 40 MHz with respect to the frequency of the scene beams. Therefore the detected power contains an oscillating component at 40 MHz due to interference between a reference beam and its corresponding scene beam. The plasma refractivity along the scene paths then phase-modulates this 40-MHz carrier.

The modulation/demodulation electronics is shown in Fig. II-11. All five receivers derive their local oscillator signals from the 40-MHz oscillator which also drives the Bragg cell via a burst amplifier. In Fig. II-11 only one receiver is shown; all five are identical. The Bragg cell must be driven in burst mode because the required RF power for reasonable diffraction efficiency in the infrared is more than can be safely applied CW to the cell. The quadrature signals $\sin\phi$ and $\cos\phi$ will be digitized by ADC's and analyzed unambiguously and sensitively by computer, facilitating the calculation and display of radial electron

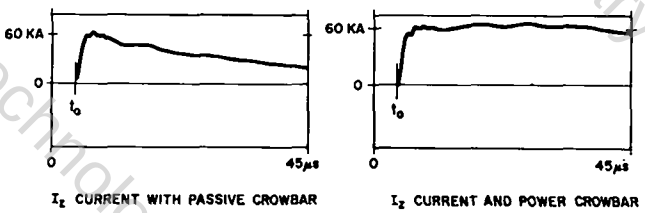

Fig. II-9.
Comparison of ZT-S current waveforms with and without power crowbar.

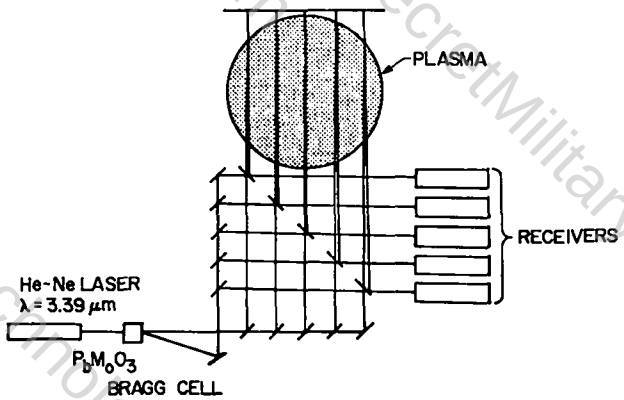

Fig. II-10.
Schematic of the five-channel interferometer.

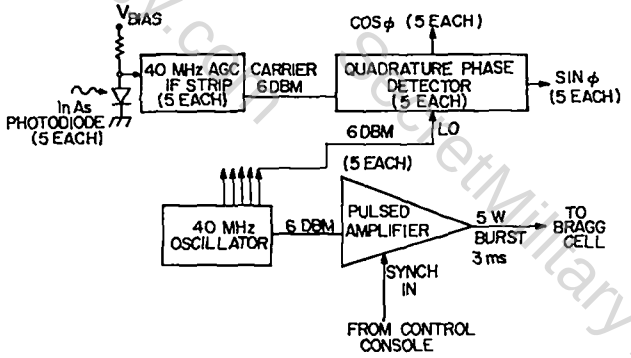

Fig. II-11.
Block diagram of the interferometer electronics.

density profiles within seconds of the plasma discharge.

Several milliwatts of laser power are required due to the low sensitivity of room-temperature InAs photodiodes to 3.39-μm radiation modulated at 40 MHz. To achieve this, a Spectra Physics model 125 gas laser, modified for 3.39-μm operation, is used. The longitudinal mode beats at 85 MHz are not detectable with the 10 MHz passband of the 40-MHz IF strips; however, photometric mixing on the detectors translates this 85-MHz beat down to 45 MHz, within the receiver passband. The solution consists of removing the mirrors from both ends of the model 125 laser, and of using it as an amplifier. The laser is excited by a short oscillator whose mode beat is in the hundreds of megahertz.

The apparatus has been tested successfully on the bench with a resolution of $\leq$ 1/50 of a fringe. It is felt that the problems and their solutions have been well identified.

In addition, it is intended to interface the present Thomson scattering diagnostic with the existing data acquisition system. The technique under consideration has been used successfully on Scyllac. It has not yet been implemented on ZT-S because of the low level of radiation detected by the scattered-light analyzer. Random variations of the background signal make it difficult for the computer to subtract plasma light from the scattered laser light. Part of the effort will be to improve the photon count at the detector.

C. ZT-40

1. Objectives. The ZT-40 experiment is the next step up from ZT-S in the Reverse-Field Pinch program at LASL. The initial objective of ZT-40 will be to demonstrate confinement time scaling from the results of ZT-I and ZT-S. If the confinement time scales as the square of the minor bore, ZT-40 should be stable for at least 150 to 200 μs. A second objective will be to operate in a regime clean enough to overcome the impurity radiation barrier and raise the temperature to $T_i = T_e \sim 100$ to 200 eV. In addition ZT-40 will be used to determine the ranges of the current and electron densities which allow the production of stable configurations. Another objective will be to extend the duration of the current to milliseconds and operate with reduced rates of rise of current in order to establish the time scale over which control of the stability can be effected by programming of external currents. Finally ZT-40 will be used to investigate the self-reversal mode of operation. A general goal of the project is to determine which of the potential advantages of the reversed-field pinch concept can be brought to a practical realization with a direct application to an energy-producing fusion reactor.

It is projected that the first plasma experiments on ZT-40 will begin in the calendar year 1979.

2. Description. ZT-40 has a 40-cm minor-bore torus with plasma aspect ratio of 5.7. The torus is fed at 12 points and has 12 magnetic cores equally spaced about the torus. The ZT-40 facility is shown in Fig. II-12 and a sketch of the front end is shown in Fig. II-13. The number of feedplates was determined by the requirement that the initial risetime of the current be the same as ZT-S (2.5 μs). The current risetime is lengthened to ~ 20 μs by removing feedplates and shorting the respective toroidal feed points, and by series-paralleling the poloidal field windings. Very slow operation (40 μs to 1 ms) can be attained by removing all feedplates and inducing the toroidal current by means of toroidal windings on the outside of the primary or by energizing the field only with the power crowbar banks.

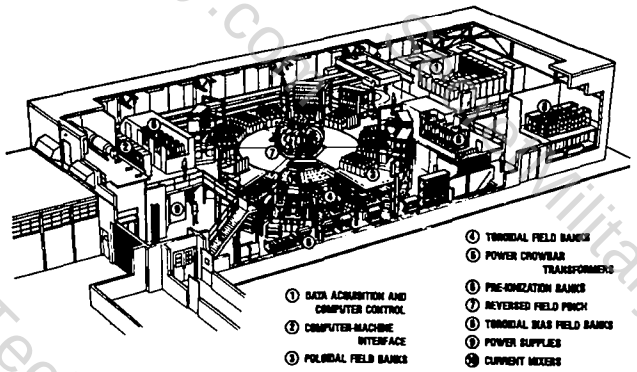

Fig. II-12.
ZT-40 Facility.

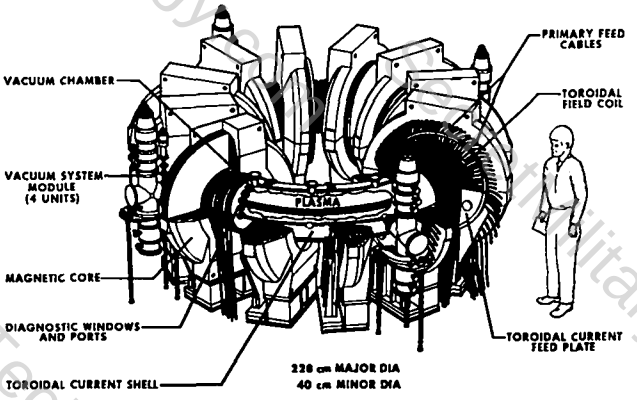

II-13.
Artist's sketch of the front end of ZT-40.

The currents obtained from a numerical calculation for the 12-feedplate design and a single-feedplate design are shown in Figs. II-14 and II-15. Figure II-16 shows the current obtained with the power crowbar bank and the single-feedplate design.

The initial experiments on ZT-40 will utilize a ceramic discharge tube. Further experiments with quartz and metal tubes are planned if their use will lead to cleaner discharges. The discharge tube is located inside a 2-cm-thick aluminum shell which serves as the primary conductor of a transformer with the plasma as the secondary and also as the conducting wall for stabilization of the plasma.

The vacuum system is designed as a four-point pumping system on the torus. The four stations will each have a single, large aperture with a

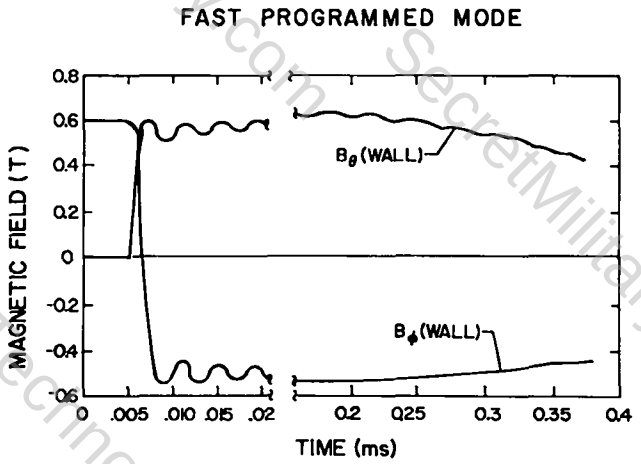

Fig. II-14.
Numerical calculation of toroidal and poloidal currents vs time for a 12-feedplate design.

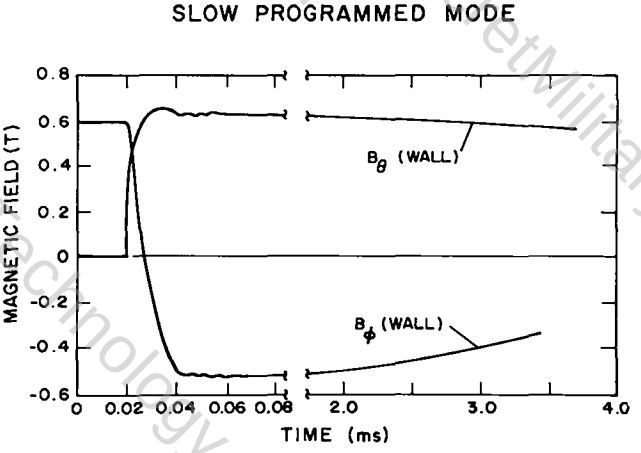

Fig. II-15.
Numerical calculation of toroidal and poloidal currents vs time for a single-feedplate design.

removable plug to prevent large field perturbations inside the torus. The 900-ℓ volume is pumped at a combined pumping speed of 450 ℓ/s for the four stations. The pumps that are used (cryogenic pumps, titanium sublimation, and air-bearing turbomolecular pumps which exhaust directly to atmosphere) are completely oil free. The initial roughing of the torus from atmospheric pressure is done with a Roots-type vane pump in series with an oil seal roughing pump. These systems are trapped and will be switched off the experiment while still in the pressure range where viscous flow predominates.

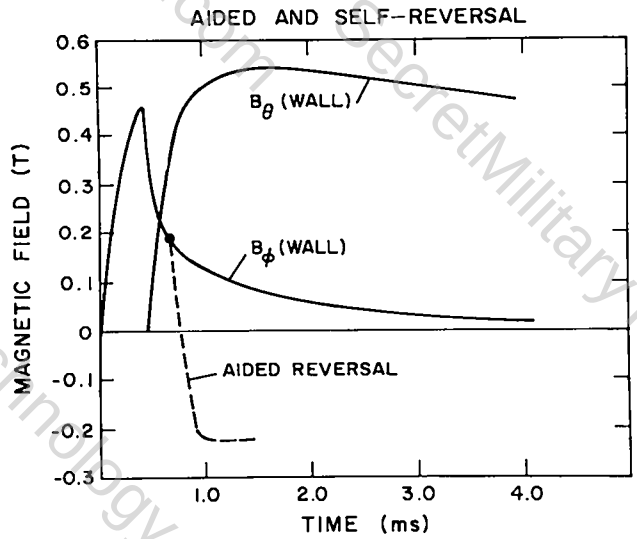

Fig. II-16.
Numerical calculation of toroidal and poloidal currents vs time for a single-feedplate design using the power crowbar banks to drive the currents.

The basic machine parameters for ZT-40 are given in Table II-I.

TABLE-II-I

ZT-40 PHYSICS DESIGN PARAMETERS

Major Radius	R = 114 cm
Minor Vacuum Chamber Radius	a = 20 cm
Gas Fill (D_2)	p = 5-30 mtorr
Electron Density	$n_e = 10^{14}$-10^{16} cm^{-3}
Confinement Time (assuming a^2 scaling)	τ_c = 150-200 μs
Electron, ion temperature	$T_e \sim T_i$ = 100-200 eV
Toroidal Current	$I_\phi \sim$ 150-600 kA
Mean Toroidal Current Density	$J_\phi < 2$ kA/cm^2
Initial Toroidal Field	B_ϕ = 0.2 - 0.6 T
Reversed Toroidal Field	$B_{\phi R} = < -0.5$ T
Poloidal Field	$B_\theta = < 0.6$ T
Range of Plasma Current Risetime	τ = 2.5 μs to 1 ms
Base Pressure	$p_o \sim 10^{-8}$ torr

3. Engineering and Construction. Approval for the ZT-40 experiment was given in late 1976. Although much of the preliminary design was complete at that time, most of the final design remained to be done. Completion of the ZT-40 design, along with development and construction activities, was the primary activity of the engineering and development groups as well as numerous other staff in the Controlled Thermonuclear Research program. A summary of activities during 1977 is given below. Some of them are reported in more detail in Secs. XII, XIV, and XVII.

a. Structural. Beginning in May 1977, the experimental area was cleared. The steel support structure was then installed. The only activity in this area which remains is the fabrication and installation of the blast walls.

b. Capacitor Banks. The location of the principal capacitor banks is shown in Fig. II-12. During 1977, the 50-kV poloidal field, I_ϕ, and toroidal field, I_θ, capacitor banks were installed and cabled as far as the crowbar spark gaps. All the capacitors, start spark gaps, and cables were tested before installation. Construction of the bias capacitor bank was about half completed. Design of the charge, air, and trigger systems was completed and installation of these systems was begun. The subassembly work required for the completion of the capacitor banks was largely completed, partly as a result of a slowdown in construction caused by a two-month delay in the delivery of the new crane for the experimental area. This freed the construction crew for subassembly work.

Before the design of the 50-kV start and crowbar switches was finalized, extensive tests were conducted to determine their performance and reliability. These included changes in geometry and materials to see the effect of these changes on operating parameters and gap lifetime and collection of data on prefire rates. Tests were also made on a mockup of the current mixer which will be installed between the capacitor banks and the current feeds to the front end. The mixer will equalize voltages at the various current feeds and will facilitate the changing of the number of current feeds. A satisfactory

electrical design was developed for the mixer. Final mechanical design was completed and parts were ordered.

c. Power Supplies. The design of the power supply system for ZT-40 was finalized and installation of components in the power supply room (see Fig. II-12) was 70% completed. After the installation of the saturable reactor controllers was finished, initial performance tests of the units were conducted. A screen room for the power supply controllers was built. This room had some special features not readily available in commercial units so it was constructed by LASL personnel.

d. Control System. Control and data acquisition functions on ZT-40 will be provided by a Prime 400 computer. During 1977, the computer was delivered and checked out and software development was begun. In collaboration with representatives of the computer manufacturer, two existing programs were combined so that the Prime 400 can now operate in a timesharing mode while at the same time always keeping the experiment as the top priority user. The screen room for the computer and other data acquisition equipment was purchased and installed. A light-coupled interface, which will electrically isolate the computer from the experiment, was designed and construction begun.

Work was started on a time delay system for controlling the capacitor bank and diagnostics. A light-coupled 8-kV pulser was built and tested in a test bay and on the electrical prototype (see Sec. k). This system allows the pulser to "float" at the electrical potential of the system it is triggering and eliminates feedback of electrical noise through the pulser cables.

e. Vacuum System. The vacuum system for ZT-40 consists of four high-vacuum pump stands which mount near the plasma chamber (Fig. II-13) and roughing and gas-fill systems. A major part of the design and procurement of these systems was completed. Turbomolecular, cryogenic, and titanium sublimation pumps were purchased and evaluated. They were found to be satisfactory for use on ZT-40.

The design of the protection and control logic for the vacuum system was largely completed. Protection interlocks will be hardwired so they remain in operation even when the control computer is down.

f. Ceramic Torus. The 40-cm minor-diameter ceramic torus will be constructed from 60 straight sections. Each 30° sector will consist of four 6° sections which will be glass-sealed together to form a 24° sector and one 6° diagnostic/pump port sector. Figure II-17 shows the position of the various tubulations and sapphire windows. It also shows the projected location of the various diagnostics.

During 1977 procurement of the ceramic sections was begun. Glass seals for sealing the sections together and for sealing in windows and tubulations were developed by LASL Group CMB-6. Two options for vacuum pump ports and diagnostic tubulations were developed. The simpler one, which does not require a metal-to-ceramic seal was chosen as the final design. The glass-sealing methods developed were tested on 20-cm and 30-cm minor-diameter sections. A photograph of an assembled 30-cm minor-diameter torus which has been glass-sealed together into sectors is shown in Fig. II-18. The figure also shows a section which has had holes for the sapphire windows ground out.

g. Metal Primary Shell and I_ϕ Feedplates. The metal primary shell for the experiment was designed and procurement was begun. Electrical insulation of the I_ϕ feedplates is a difficult

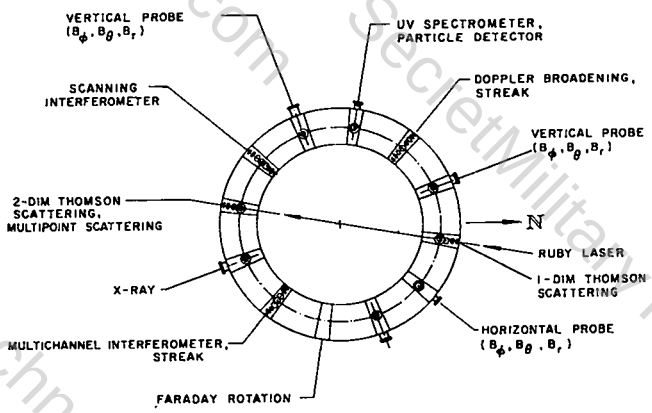

Fig. II-17.
Diagram of ZT-40 torus showing location of tubulations and sapphire windows. Location of projected diagnostics is also shown.

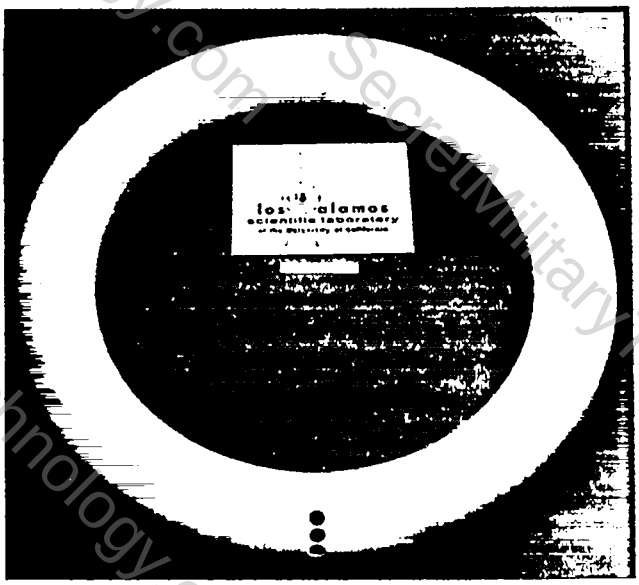

Fig. II-18.
Photograph of 30-cm minor-diameter ceramic torus.

problem because of their complicated geometry. Two options were investigated. The first has the metal conductors molded inside an epoxy casing. In this design the epoxy is cured under high pressure. Tests on molded samples showed this method leads to high electrical strength, at least a factor of 2 higher than obtained by previously used techniques. The second option uses a combination of coated metal pieces, polyethylene hats and sheet insulation. After a series of tests on both approaches, the epoxy-molded design was chosen for use on ZT-40.

h. Magnetic Cores. In ZT-40, magnetic cores are used in the I_ϕ circuit to increase the coupling between the metal primary and the plasma secondary. The cores used are tape-wound from 0.05-mm-thick iron tape and are larger than cores previously manufactured in this manner. During 1977, all of the cores were wound and stacked. Some of them were completed and personnel from LASL visited the vendor and performed acceptance tests. The cores performed as anticipated. Delivery of all the cores is expected in early 1978.

i. Electric Circuit Simulation. Work with the circuit analysis program continued during 1977. The code was updated to reflect changes in circuit parameters caused by mechanical design constraints. The different operational modes were examined in detail with particular attention being given to power crowbar requirements. The magnetic field waveforms shown in Figs. II-14, II-15, and II-16 are a product of these studies.

j. Power Crowbar. The ZT-40 power crowbar will be connected into the I_ϕ and I_θ circuits with a variable-turn ratio transformer. Preliminary tests of the transformer design, which uses parallel plate windings in order to reduce leakage inductance, were made. The tests showed that the design would work, so design and procurement of a prototype was started. The power crowbar circuits will also require the development of a switch with high Coulomb capacity. Development was started on an improved spark gap. A model was built but no tests were conducted. Also, some conceptual design work was done on a mercury-wetted spark gap. This switch would not be available for initial power crowbar operation but may be required for operation of ZT-40 with magnetic fields which last for milliseconds.

k. Electrical Prototype. An electrical prototype of one-twelfth of one of the two high-voltage banks was constructed and checkout of the system was begun. It will be used to determine trigger system performance, to examine available operating ranges, and to conduct tests to determine how well electrical transients can be suppressed using RLC shunts across the mixers. Later the prototype will be used to test power crowbar components.

l. Diagnostics. The potential diagnostics for ZT-40 were identified and the primary shell and ceramic torus was designed to accommodate them. The location of the various diagnostics is shown in Fig. II-17. Work was begun on the design of both internal and external magnetic probes. Three methods of making Faraday rotation measurements are being investigated. Probably only the most promising one will be used on ZT-40. Four approaches which use lasers to make density measurements are being pursued. Considerable work was done on two of them. A multichannel interferometer has worked well on the bench. It is being installed on ZT-S and its performance will be evaluated. A scanning interferometer which

gives a density profile every 5-10 μs has been evaluated on the bench through mediocre windows and works well. Only conceptual studies have been performed on the other two approaches. Two methods of using Thomson scattering to measure electron temperature and density are being worked on. One is a conventional arrangement which gives data at two spatial and one temporal point. The other would use a mode-locked ruby laser to give density and temperature as a function of time. Work also continued in other areas which would extend the diagnostics currently used on ZT-S to ZT-40.

REFERENCES

1. "LASL Controlled Thermonuclear Research Program, January-December 1976," Los Alamos Scientific Laboratory report LA-7082-PR (1978), p. 58.
2. S. Costa and S. Ortolani, "Study of the Impurity Radiation Losses in a Pinch Discharge," UPEE 75/06, University of Padova, Italy (December 1975).
3. R. W. P. McWhirter, "Spectral Intensities," in Plasma Diagnostics Techniques, Richard H. Huddlestone and Stanley L. Leonard, Eds. (Academic Press, 1965), Chap. V., pp. 201-263.
4. Newsletter, DMFE, Atomic Data for CTR, July 1975.
5. L. Oren and R. J. Taylor, "Trapping and Removal of Oxygen in Tokamaks," Nuclear Fusion 17, 1143-1151 (1977).
6. A. R. Jacobson, "A Novel Interferometer for the Measurement of Plasma Density," Los Alamos Scientific Laboratory report LA-6727-MS (1977).
7. C. J. Buchenauer and A. R. Jacobson, "Quadrature Interferometer for Plasma Density Measurements," Rev. Sci. Inst. 48, pp. 769-774 (1977).

III. SCYLLAC FEEDBACK STABILIZATION EXPERIMENTS

R. R. Bartsch, E. L. Cantrell, R. F. Gribble, G. Miller,
K. J. Kutac, L. E. Handy, and R. E. Siemon

A. INTRODUCTION

The final experiments on the Scyllac feedback stabilization project have been completed, and the experiments have been terminated.

Details of the experiments leading up to the ℓ=1,2 results are presented in a paper accepted for publication in Nuclear Fusion titled "Feedback Stabilization of an ℓ=0,1,2 High Beta Stellarator." Also, a letter published in Nuclear Fusion, "Observation of Propagating m=1 Waves in Scyllac," contains pertinent results of previous sector work. In preparation is a journal paper discussing in detail the final results on the ℓ=1,2 sector experiment. Finally, some of the results are presented in more detail in the 1977 Quarterly Progress Reports.

The last experiments differed from previous efforts in several important aspects. First the equilibrium configuration was changed from the ℓ=0,1 combination of stellarator fields to ℓ=1,2 stellarator fields. Secondly, the helical plasma perturbation was much larger on these final experiments than on the previous Scyllac experiments giving a plasma helical radius of about 3 vs the value of 1.4 cm used in the earlier experiments. Also the wavelength of the fields was increased from 0.62 m to 1.0 m.

The feedback system in the final series of experiments was also much different than in the previous cases in that the output of the position detectors was processed in such a manner as to drive the power amplifiers in response to the modal structure of the plasma instability rather than the displacements as seen by the individual detectors.

B. EXPERIMENTAL ARRANGEMENT

The experimental apparatus was essentially the same as that described in detail in Ref. 1. In this experiment the ℓ=0,1 shaped compression coil was replaced by a compression coil with an ℓ=1,2 shape and the sector length was extended to be 7/15 of a full torus. The compression coil produced a pure ℓ=1,2 vacuum magnetic field characterized by $b_1 = 0.133$ and $b_2 = -0.0132$ (a = 1 cm) with a helical wave number $h = 0.06$ cm^{-1} and wavelength $\lambda = 2\pi/h = 104.7$ cm. Plasma radius is a and the radial field parameter b_1 and b_2 normalized to the compression field E_0 are defined by

$$B_r/B_0 = b_1 \sin(\theta - hz) + b_2 \sin(2\theta - hz) \quad .$$

A vertical field given by $b_v = -b_1 b_2/ha$, which resulted in centered flux surfaces, was also present.

The conducting wall shape is accurately given by the following parametrical representation,

$$x = x_0 + b\Delta_1 \cos(hz) + b[\cos\phi - \Delta_2 \cos(\phi - hz)]$$

$$y = b\Delta_1 \sin(hz) + b[\sin\phi + \Delta_2 \sin(\phi - hz)] \quad ,$$

where z is the longitudinal coordinate along the minor axis of the 4-m-radius torus, x is the horizontal coordinate increasing toroidally outward, y is vertical, and the parameter ϕ is an azimuthal angle. Values are b = 10.6 cm, $\Delta_1 = 0.235$, $\Delta_2 = 0.265$, and x_0 = 1 cm. This describes a helically rotating ellipse with major radius $b(1 + \Delta_2)$ and minor radius $b(1 - \Delta_2)$, the center of which is helically displaced by b/Δ_1.

The quartz discharge tube was formed into a toroidally curved helix with a radius of 3.2 cm corresponding to the expected equilibrium helical shape of the plasma. The positions of the discharge tube and conducting wall relative to the minor axis of the torus are shown in Fig. III-1.

Because of the smaller average coil bore, the magnetic field was larger in this configuration than in the ℓ=0,1 configuration. The magnetic field was initially 16 kG with a risetime of 3 μs, falling to 12 kG in 40 μs. Additional ℓ=2 fields were produced by equilibrium adjustment windings and feedback driven windings mounted on the

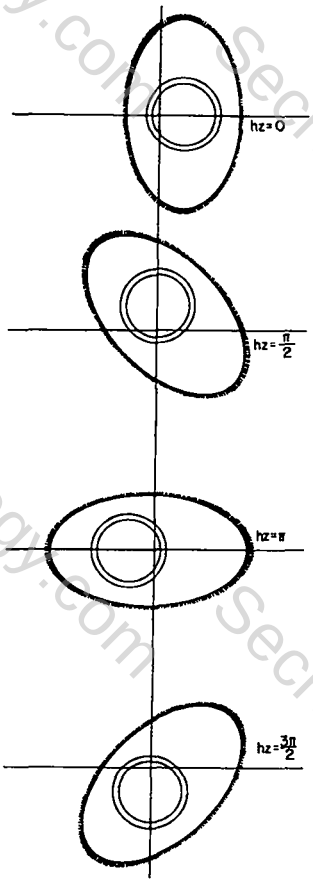

Fig. III-1.
Discharge tube position relative to conducting wall.

discharge tube in the same manner as described in Ref. 1.

The feedback system utilized twenty 16-segment photodiode position detectors[2] viewing the plasma motion from the top and front of the discharge tube to determine the horizontal and vertical motions. These signals fed into a fast analog processor which mode-analyzed the information about plasma position as a function of longitudinal position into five longitudinal mode signals for the horizontal and vertical planes. The mode-analyzer output consisted of the sum of the mode signal and its time derivative for additional damping. The gain for each mode signal and its derivative were individually adjustable.

Each power amplifier was driven by a summing amplifier with properly weighted mode signal inputs to transform the mode signals, effectively interpolating between position detectors. For all 10 modes, it was necessary to rotate the coordinates from the horizontal-vertical of the position detectors 45 degrees to correspond to the orientation of the $\ell=2$ feedback coil system. There were 44 modules, each driving one-half wavelength, corresponding to 11 wavelengths in all and two orthogonal force directions.

The longitudinal mode structure in an open ended sector is not known unless the boundary conditions at the ends are known. Two sets of modes that might be expected on physical grounds were considered, corresponding (1) to the plasma ends being fixed, and (2) the plasma having no curvature at the ends (an elastic bar model). The second set of modes agreed best with the data in that it allowed the full motion near the ends that was observed. However, that these modes are not orthogonal leads to very undesirable features, and thus a third set of orthogonal Fourier modes was selected.

These modes, illustrated in Fig. III-2, are not intended to represent the time eigenmodes of the sector plasma. The function of the mode analysis procedure is to interpolate the position detector information as a function of z, providing a short wavelength cutoff on the response of the feedback system. The mode analyzer approach thus circumvents undesirable oscillations arising from the system response to otherwise stable short wavelength motions. Orthogonal mode signals have the convenient property of being the best fit values (in the least squares sense) for a fit of a sum of modes to the position detector data as a function of z.

The layout of the $\ell=1,2$ sector is shown in Fig. III-3. The location of the Thomson scattering apparatus, the excluded flux loop probe, and the two orthogonal 16-channel luminosity apparatus are indicated. The top viewing position detectors were located at $hz = 0$ in every wavelength except at $z = 0$ (the left end in Fig. III-3) and $z = 2\lambda$ (10 in all), and the front viewing position detectors were located at $hz = \pi$ every wavelength except at $z = 2.5\lambda$ (10 in all). Other diagnostic information was obtained from 5 streak cameras, viewing the plasma in different locations, and a coupled cavity interferometer which determined the preionized plasma density.

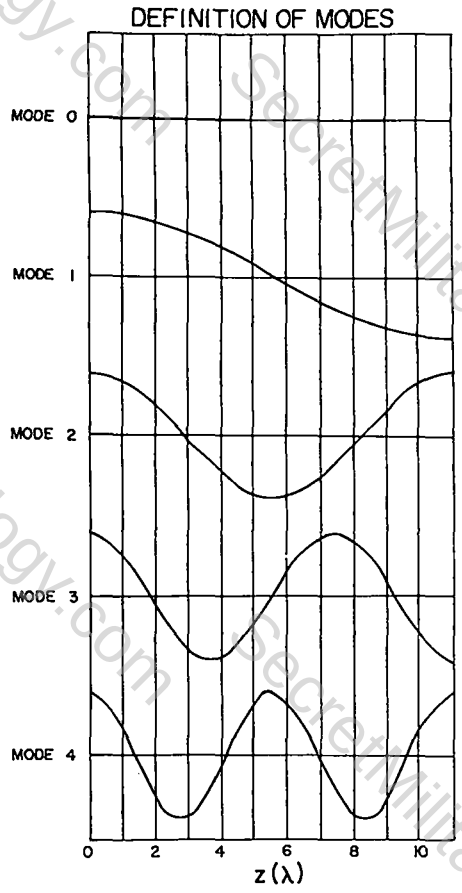

Fig. III-2.
Modes controlled by feedback system.

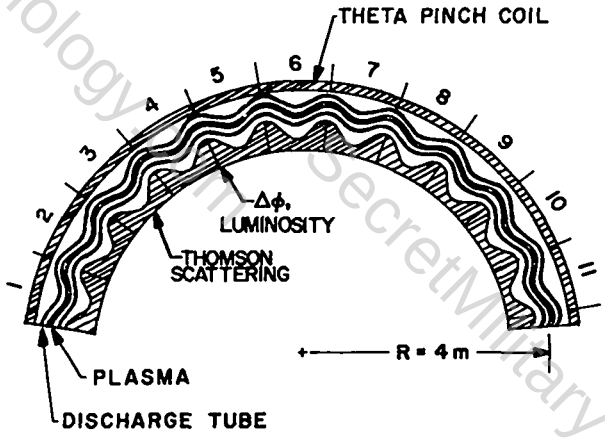

Fig. III-3.
Experimental arrangement.

C. RESULTS

1. Toroidal Equilibrium. The toroidal equilibrium was studied qualitatively with streak cameras and quantitatively with use of the feedback position detectors and the multichannel luminosity apparatus.

The streak photographs showed less dynamic plasma behavior than in the ℓ=0,1 experiment and a surprisingly long time, even without feedback, before strong wall hits were indicated by lighting up of the discharge tube. A typical streak photograph is shown in Fig. III-4.

The m=1, k=0 instability growth rate from small-δ theory is $\gamma = 0.27\ \mu s^{-1}$ (v_A = 17 cm/μs, β = 0.7) and three growth times is about 10 μs. The streak photographs suggest that the plasma, although m=1 unstable, gently rebounds from the wall.

The plasma behavior shown in Fig. III-4 was approximately the same over a wide range of filling pressures, from 12-96 mtorr. This is in sharp contrast to the ℓ=0,1 experiment where the filling pressure strongly influenced the inward or outward motion of the plasma. The lower pressure limit was mainly due to the decrease of the plasma luminosity to the point where there was insufficient light for observation by position detectors and streak cameras.

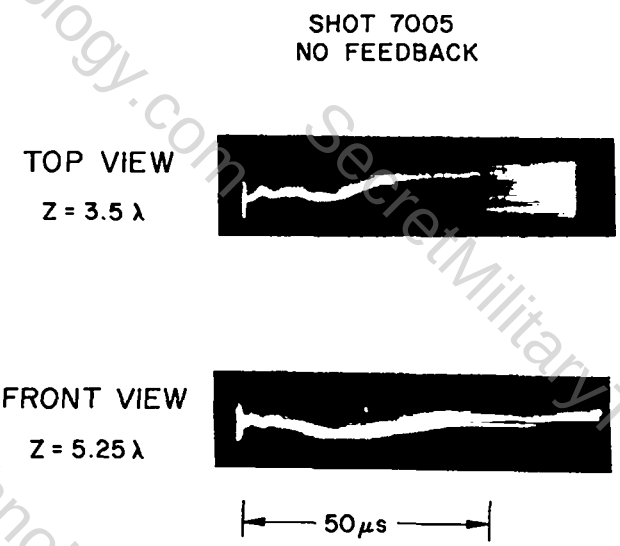

Fig. III-4.
Streak photographs of plasma without feedback.

At high filling pressures there was a tendency for the column to bifurcate, evidently due to an m=2 instability. The onset of the instability was not sharply defined as a function of pressure since above threshold the instability had a slow growth. Below about 70 mtorr there was no evidence of an m=2 instability. The filling pressure threshold for the m=2 instability calculated from sharp-boundary small-δ theory is 8 mtorr, thus it is apparent that the theory is very pessimistic, as has already been observed.[3]

As in the ℓ=0,1 experiment ℓ=2 windings were used for adjustment of the equilibrium. These were driven with Jones-Weibel[4] circuits that were designed to provide a step waveform. However, in this experiment such a waveform was not suitable. The plasma had an initial tendency to move outward, striking and rebounding from the wall at the locations $hz = \pi$.

If a step ℓ=2 current beginning at main bank time was applied with sufficient amplitude to prevent this outward motion, the plasma would move rapidly inward at late times. As an ad-hoc procedure the slow ringing capacitor in the Jones-Weibel circuit was not fired, changing the output waveform from a step to a pulse. This pulse was initiated 3 μs before the main bank. The average plasma trajections in the horizontal plane (average over five central wavelengths) together with the ℓ=2 field waveforms for the step and pulse cases are shown in Fig. III-5.

Ideally the equilibrium adjustment waveform would be such that a small change at late times, after initial transients had died away, would produce a change in the trajectory from inward to outward. In the limited time available to perform this experiment it was not possible to provide such a waveform. However, using the feedback system in the programmed mode to produce a current pulse at late times, it was possible to experimentally demonstrate nearness to equilibrium.

The data are shown in Fig. III-6, which gives the average trajectory in the horizontal plane together with the total ℓ=2 field (equilibrium adjustment plus programmed pulse from the feedback amplifier system).

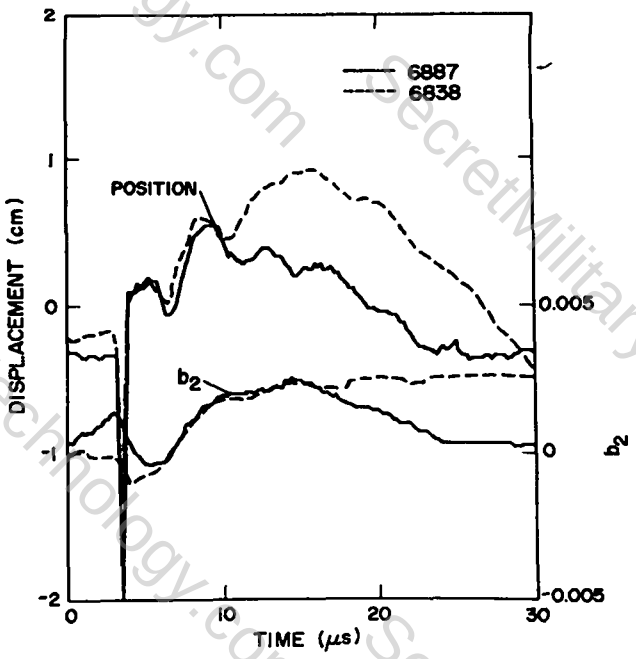

Fig. III-5.
Position and trimming circuit waveforms.

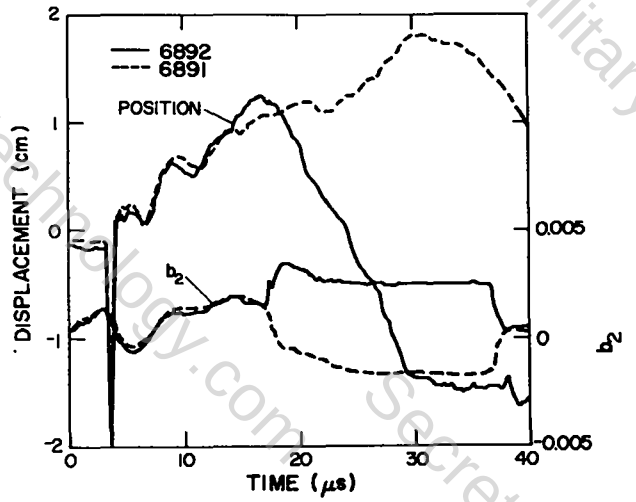

Fig. III-6.
Sensitivity of equilibrium.

Small-δ diffuse profile equilibrium theory[5] tends to require slightly larger helical fields than observed in the experiment to give equilibrium (theory: $b_2 = 0.018$, exp: $0.012 < b_2 < 0.016$, for $\beta = 0.7$, $a = 1$ cm).

Using a streak camera that superimposed views of the plasma one-half helical wavelength apart, the helical deformation of the plasma as a

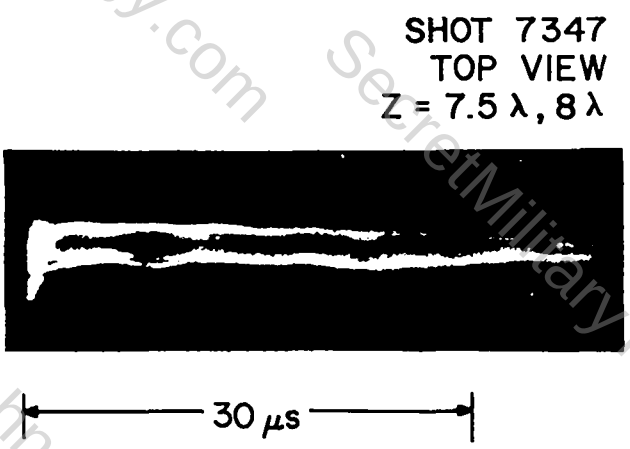

Fig. III-7.
Streak photograph measuring helical shift.

function of time was studied. A streak photograph is shown in Fig. III-7. Markers centered on the plasma image (poorly visible in Fig. III-7) indicated the plasma helical radius to be approximately 3.2 cm which was the helical radius of the quartz discharge tube and also the helical radius given by small-δ sharp-boundary theory (for β = 0.6).

2. Excluded Flux. The excluded flux traces were not strongly correlated with whether or not a wall hit occurred, as observed with streak cameras. This is remarkable in that the excluded flux is directly related to the plasma energy ($B\Delta\phi$ proportional to energy per unit length) and therefore the time for radial energy losses is long even when the plasma is in apparent contact with the wall. Because of this the excluded flux depended little on whether or not the equilibrium adjustment field or feedback were applied.

In Fig. III-8 is shown a comparison of the excluded flux traces obtained in this experiment with those obtained in the previous experiment involving ℓ=0 fields. The excluded flux, in this case, is quite different at the field maximum (hz = 0) and field minimum (hz = π) locations of the ℓ=0 field. A strong transient behavior associated with ℓ=0 oscillations of the plasma is also present. The shorter time scale erratic behavior of the excluded flux in the ℓ=0 case is due to pick up of the time varying feedback magnetic field.

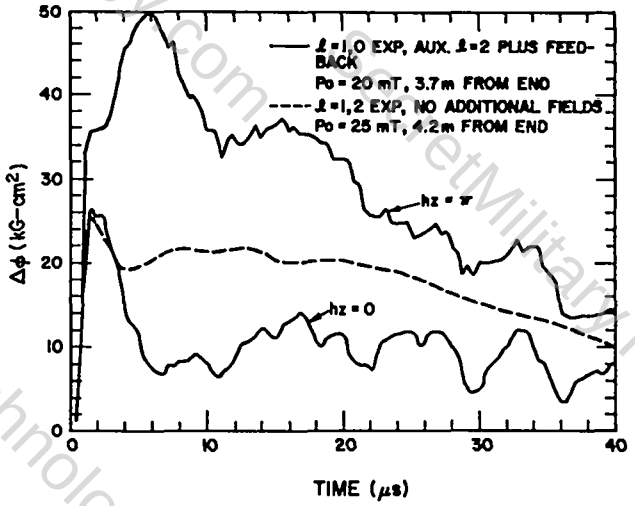

Fig. III-8.
Excluded flux for ℓ=1,2 compared with ℓ=0,1 fields.

A common feature of the excluded flux behavior from the two experiments is a fall-off beginning about 20 μs. This is due to end-loss as shown in Fig. III-9. The theoretical curve is based on two-dimensional end-loss computations by Brackbill.[6] Other small effects (such as the fall off of the main B_z field) are included by incorporating the particle loss due to magnetohydrodynamic flow as calculated by Brackbill into a one-dimensional calculation describing the radial evolution of a theta pinch.[7] The calculations show that particle loss begins after a time delay approximately equal to the Alfven propagation time ($v_A = B_{outside}/\rho$) while loss of temperature on

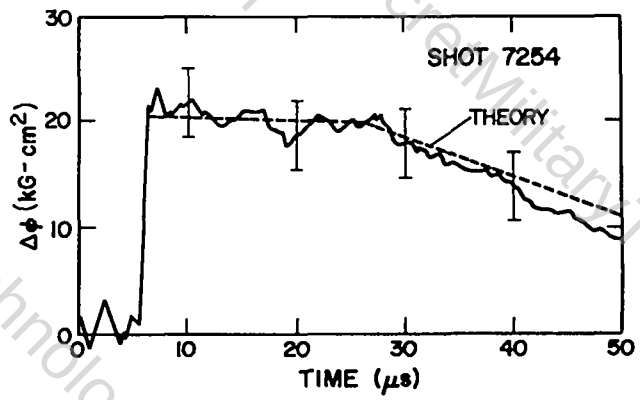

Figure III-9.
Excluded flux decay compared with end-loss theory.

axis begins after a longer time equal to the cusp propagation time

$$v = \left(\frac{1}{c^2} + \frac{1}{v_A^2}\right)^{-1/2},$$

where c is the sound speed. The good agreement between theory and experiment clearly shows that the fall-off of excluded flux observed both in this experiment and in the ℓ=1,0 experiment is due to end loss.

3. Thomson Scattering. Thomson scattering, with the same apparatus as in the ℓ=0,1 experiment,[8] was used to determine the electron temperature. The results are given in Fig. III-10. The data points were obtained on different shots with and without feedback (no difference was evident) with the laser pulse occurring at different times. Measurements at early time with the laser beam displaced sideways showed a definite non-constant temperature profile. The spread in the measurements is at least partly due to the temperature profile and the variation in plasma position at the time the laser was fired. Also shown in Fig. III-10 is a theoretical curve based on the two-dimensional end-loss calculations already discussed. There seems to be agreement with the upper envelope of the data.

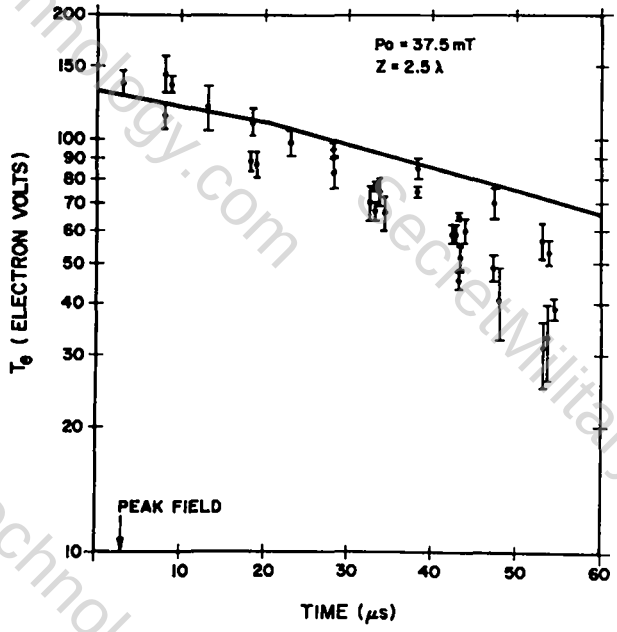

Fig. III-10.
Thomson scattering temperature measurements vs time.

The calculations show an "onion-skin" effect with the outer plasma cooling more rapidly than the plasma on axis and this seems consistent with the larger data spread at late times. Energy loss due to radiation, not included in the calculation, may also become important as the plasma temperature drops.[9]

4. Luminosity Measurements. Two orthogonal 16-channel luminosity devices were used to determine the luminosity profiles of the plasma. At the location of the luminosity apparatus (hz = 0, see Fig. III-3) the elliptically shaped plasma was oriented so that it appeared narrow when viewed

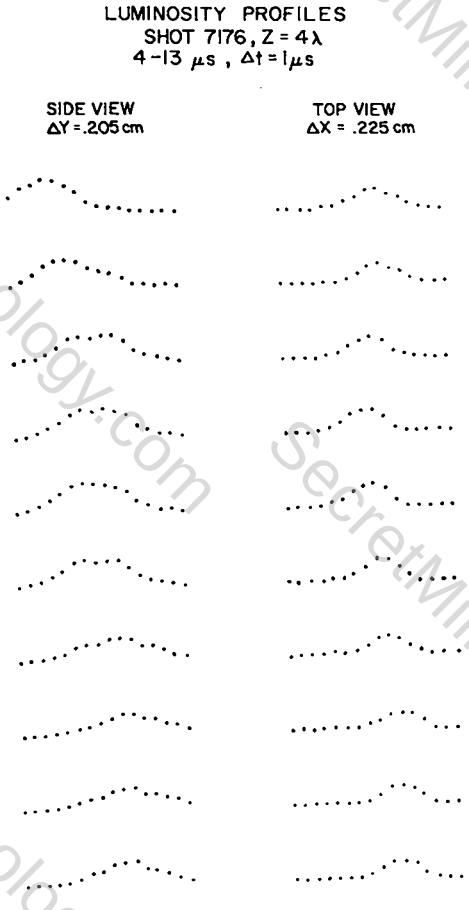

Fig. III-11.
Luminosity data showing profiles.

from the top and broad when viewed from the side. Raw data are shown in Fig. III-11.

The luminosity profiles were fit with a Gaussian ($\sim \exp[-2(x - x_0)^2/a^2]$, assuming luminosity $\sim n^2$), to determine the plasma radii a_1 and a_2. Results are given in Fig. III-12. These data are consistent with the sharp-boundary small-δ theory, $a_1 = a(1 - \delta_2)$, $a_2 = a(1 + \delta_2)$, with $\delta_2 = 2b_2/[ha(2 - \beta)]$, only if a rather low beta value is used, $\beta \sim 0.2$.

Oscillations of δ_2 were not observed. However, the luminosity measurements did show a regular oscillation of the peak luminosity, approximately in phase in the two views. The oscillation was also present in the peak luminosity signal available from the feedback position detectors, as seen in Fig. III-13. The feedback position detectors' spectral response was 350-650 nm and as in the ℓ=1,0 experiment the absolute plasma luminosity was within a factor of two of pure bremsstrahlung.

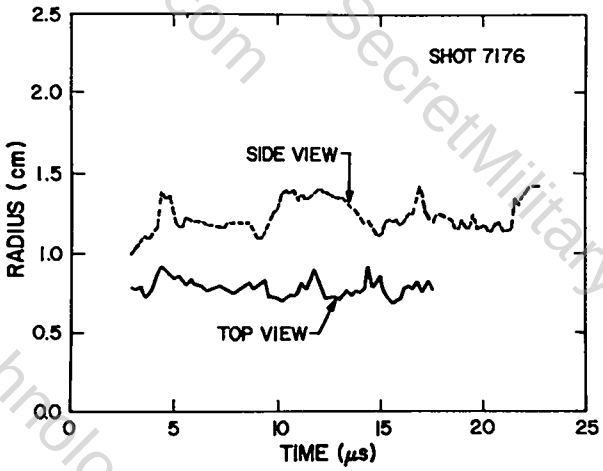

Fig. III-12.
Plasma ellipticity from luminosity.

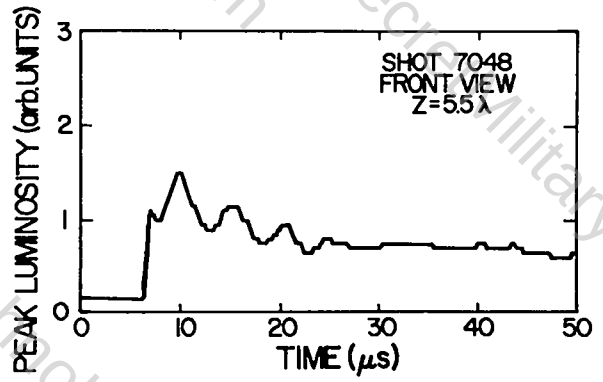

Fig. III-13.
Position detector peak luminosity signal.

The plasma radius obtained from the luminosity measurements together with the exoluded flux information allow the determination of the plasma pressure, or β, ($\beta \sim 0.1 + 0.5\ \Delta\phi/(a^2B)$, $\beta > 0.2$). Assuming a Gaussian pressure profile with 1/e radius a = 1 cm and using the measured values $\Delta\phi$ = 20 kG-cm^2, and B = 16 kG, the plasma beta value is 0.7.

The electron and ion temperature equilibration time is a few microseconds at these densities and temperatures. Assuming $T_i = T_e$ = 120 eV and β = 0.7 the plasma density is determined to be $n_e \simeq 2 \times 10^{16}$ cm^{-3}.

5. Axial Current. In a high-beta stellarator an axial electric field is produced by the change in azimuthal flux between the outer boundary of the plasma and the conducting wall that occurs as the magnetic field initially rises.[10-12] In the ℓ=0,1 sector the ends were electrically isolated to prevent the flow of external current.

However in the ℓ=1,2 configuration, to avoid a large induced voltage with the larger helical fields, a current return was provided between the metallic vacuum valves at the ends of the sector. Normally a loop linking the main B_z field and a resistance of 1 Ω were placed in the return circuit to partially cancel the current and to damp out the remainder. The return wires had an inductance of 2.2 μh while the plasma inductance was about 5.5 μh.

The measured axial current is shown in Fig. III-14 for cases with the resistors and cancellation loop in the circuit and with them shorted out. The azimuthal flux calculated from the sharp-boundary small-δ mode[11] is ~ 40 kV-μs (independent of a and β) from the ℓ=2 field and ~ 15 kV-μs for β = 0.65 (7 kV-μs for $\beta \simeq 0$, 40 kV-μs for β = 1, independent of a) from the ℓ=1 field.

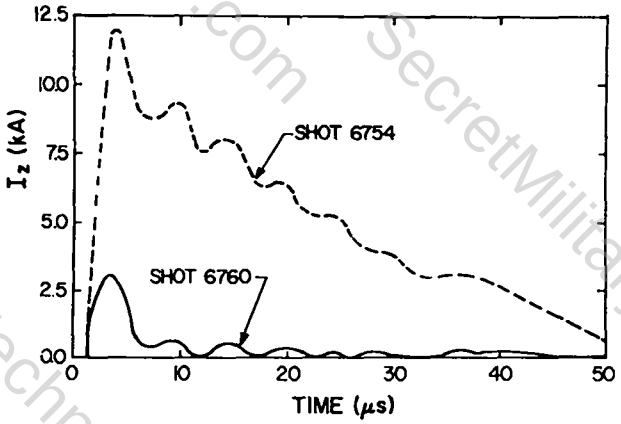

Fig. III-14.
Axial current with and without cancellation circuit.

The cancellation loop reduced the current to ~ 0.29 of its original value with a flux of ~ 60 kV-μs implying a azimuthal flux of 80 kV-μs. The initial current of 12 kA (see Fig. III-14) and the circuit inductance of 7.7 μh gives a value of 92 kV-μs. This discrepancy between theory and experiment is most likely due to the small-δ assumptions of the theory.

6. Effect of Feedback. In Figs. III-15 and III-16 are shown the mode signals (see Fig. III-2 for a definition of the modes) and feedback currents for a typical shot with feedback.

The effect of feedback was only to stabilize the plasma m=1 motion since the energy confinement was dominated by end loss with or without feedback. All modes had a velocity gain τ_1 = 3 μs, $\left(b_2 \sim \xi + \tau_1 \frac{\partial \xi}{\partial t}\right)$ and an overall gain for the ℓ=2 current of about 500 A/cm and about 50 G/cm for the ℓ=2 field (at a = 1 cm).

In Figs. III-15 and III-16, an improvement for all modes with feedback is apparent. An independent determination of the effectiveness of feedback is the sixteen-channel luminosity device discussed in a previous section. Shown in Fig. III-17 are two successive plasma discharges where all experimental parameters are held constant except that in case (a), the feedback system is turned off while in (b) it is active. In the first case (a), the plasma moves rapidly to the wall of the discharge tube (indicated by the dashed parallel lines). In case (b), the feedback system controlled the instability and held the

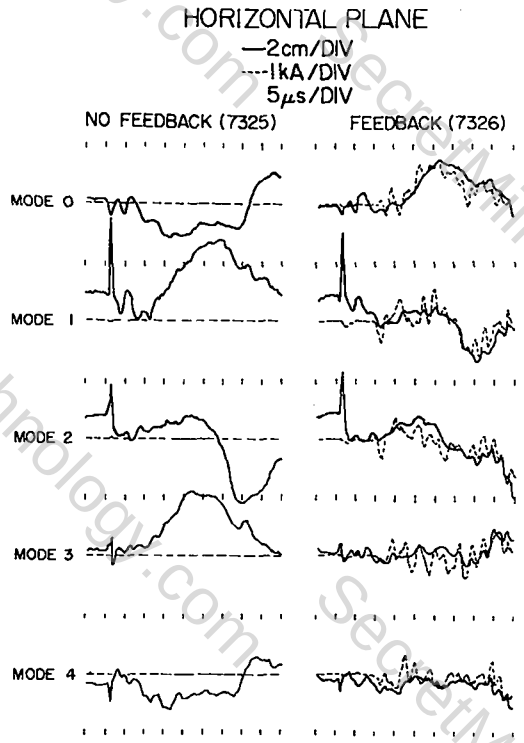

Fig. III-15.
Horizontal mode amplitudes controlled by feedback.

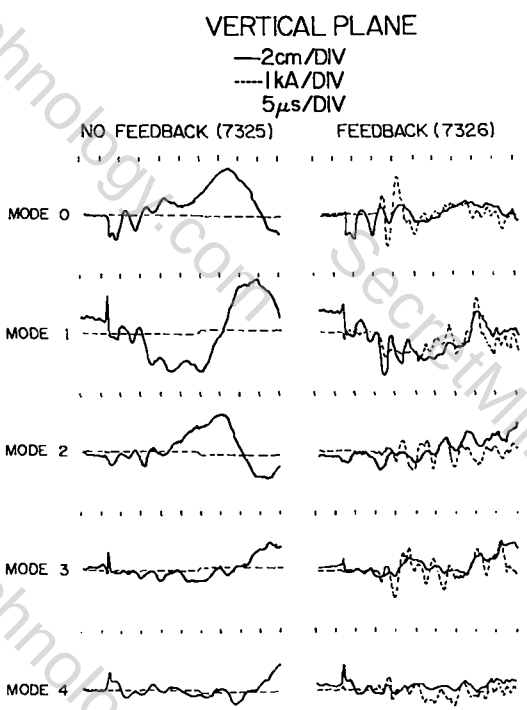

Fig. III-16.
Vertical mode amplitudes controlled by feedback.

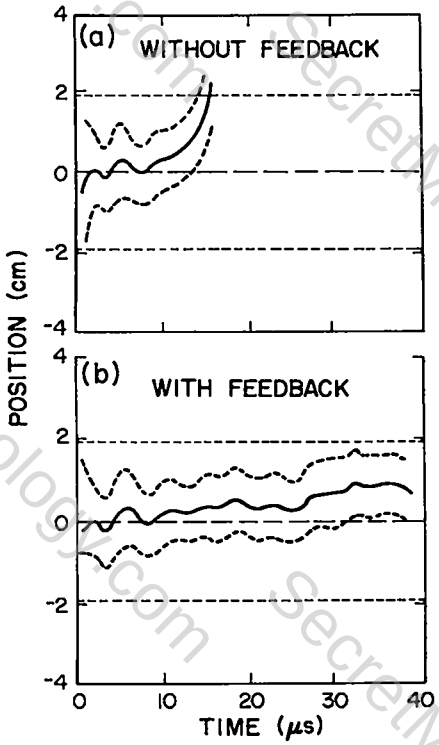

Fig. III-17.
Luminosity position data showing feedback control.

plasma near the center of the discharge tube. In Fig. III-18, the quantity $(\int \xi^2\ dz/L)^{1/2}$ averaged over 10 shots with feedback and 10 shots without feedback is plotted. This shows a definite decrease in the magnitude of the plasma excursions

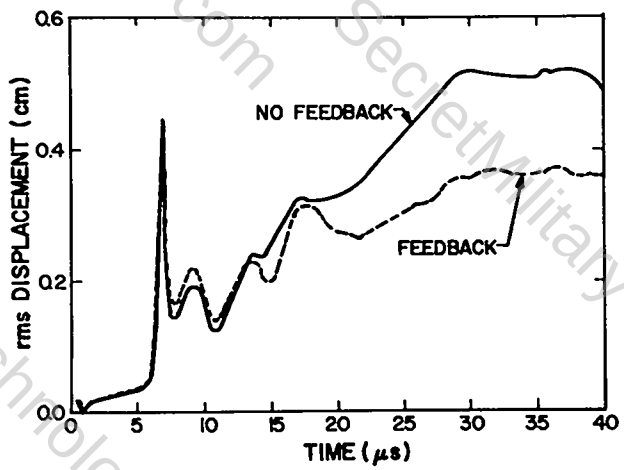

Fig. III-18.
Averaged rms displacements with and without feedback stabilization.

of axis with feedback. However, even without feedback, the average plasma excursions were quite small.

An unexpected oscillatory behavior with a frequency approximately equal to the helical oscillation frequency was present and in fact varying the velocity gain setting, which mainly governed the amplification of these oscillations, had little effect. Without feedback the helical oscillations were observable with both the top viewing position detectors and those looking from the front implying that both spatial phases were present. The tendency for the feedback system to oscillate at the helical frequency is probably due to direct coupling of the feedback $\ell=2$ field to the plasma $\ell=1$ shape as observed in Ref. 1, aggravated by the weak damping of the helical oscillations in this case.

In no case was the confinement limited by the presence of these small oscillations.

D. CONCLUSIONS

The experiments using the modal feedback system were uniformly successful. Many interesting features of the system were unable to be experimentally studied due to time restrictions. In general, the feedback system improved the stability of the plasma column in all cases. The experimentally obtained confinement times were clearly limited by particle loss and thermal conduction to the open ends of the sector.

The m=1 instability which accompanies high-beta stellarator equilibrium has been shown to be amenable to feedback stabilization. Furthermore, it has been demonstrated that the equilibrium obtained with the $\ell=1,2$ stellarator fields is qualitatively superior to the $\ell=0,1$ system in that the transient behavior occurring as the plasma assumes its equilibrium shape is minimal. The use of modal control in the feedback system resulted in improvement in its performance. Present technology exists that could reduce the amount of feedback energy loss by a factor of 20.

Further experiments in a complete toroidal geometry would be necessary to determine the upper limits of confinement time.

REFERENCES

1. R. R. Bartsch, E. L. Cantrell, R. F. Gribble, K. A. Klare, K. J. Kutac, G. Miller, and W. E. Quinn, Nucl. Fusion (1978), to be published.

2. R. Gribble and G. Miller, Rev. Sci. Instrum. 48, 778 (1977).

3. J. Neuhauser, M. Kaufmann, H. Rohr, and G. Schramm, Nucl. Fusion 17, 3 (1977).

4. E. S. Weibel and I. R. Jones, Rev. Sci. Instrum. 32, 972 (1961).

5. D. C. Barnes and J. U. Brackbill, Nucl. Sci. and Eng. 64, 18 (1977).

6. J. U. Brackbill, Los Alamos Scientific Laboratory, personal communication (1977).

7. G. Miller, Los Alamos Scientific Laboratory unpublished data (1977).

8. R. E. Siemon, Appl. Optics 13, 697 (1974).

9. F. C. Jahoda, Los Alamos Scientific Laboratory, private communication (1977).

10. E. Funfer, M. Kaufmann, W. Lotz, J. Neuhauser, G. Schramm, and U. Seidel, "Linear ℓ=1 Stellarator Experiments Using a Shaped Coil," Garching Laboratory report IPP 1/130 (1973).

11. G. Miller, Phys. Fluids 18, 1704 (1975).

12. P.C.T. Van der Lann, "Effects of Flux Conservation on the Field Configuration in Scyllac," Los Alamos Scientific Laboratory report LA-6767-MS (1977).

IV. SCYLLA IV-P LINEAR THETA-PINCH EXPERIMENTS

R. J. Commisso, C. A. Ekdahl, K. B. Freese, R. F. Gribble,
K. F. McKenna, G. Miller, and R. E. Siemon

A. INTRODUCTION

The ability of linear theta-pinch devices to generate high-energy plasmas of fusion interest has clearly been established. This fact combined with the additional advantages of simple geometry, high plasma beta and density, demonstrated plasma equilibrium and neutral stability properties, and ease of plasma heating make the linear theta pinch an attractive alternate approach to a pure fusion reactor and a prime candidate for a fusion-driven fissile fuel producer (hybrid). The fundamental problem encountered in the adaptation of the linear theta pinch to reactor applications is the loss of plasma energy containment due to particle streaming through the ends and axial electron and ion thermal conduction along the open magnetic field lines. A significant reduction in the magnitude of these losses is necessary for the successful development of a linear theta-pinch fusion reactor. The main objective of the Los Alamos Scientific Laboratory (LASL) linear theta-pinch program is the investigation of end-loss physics and the development of end-stoppering techniques which enhance the plasma confinement in these devices.

The principal experiment in the program is the 5-m-long Scylla IV-P linear theta pinch. The peak theta-pinch plasma parameters are $n = 1.5 \times 10^{16}$ cm^{-3}, $T_e + T_i \simeq 3.2$ keV, $\beta \simeq 0.9$, and plasma radius $\simeq 1$ cm. With the reduction of end losses as the ultimate objective, the following experiments have been carried out on Scylla IV-P: (a) an investigation of the characteristic end-loss times, and plasma flow processes near the theta-pinch coil ends, and (b) material end-plug end-stoppering experiments designed to eliminate axial particle flow.

B. THETA-PINCH EXPERIMENTAL ARRANGEMENT

The Scylla IV-P theta pinch has a maximum energy storage of 2 MJ at 60 kV primary bank voltage. Six hundred 1.8-μF capacitors feed the 500-cm-long, 11.2-cm-diam single-turn compression coil. Primary bank operation at 45 kV generates a vacuum E_θ of 0.6 kV/cm at the inside wall of the 8.8-cm-i.d. quartz discharge tube and a peak compression field of 50 kG is obtained 3.0 μs after discharge initiation. A Scyllac-type crowbar system extends the magnetic field in time with an L/R decay of 110 μs. The experimental results discussed below were obtained at 45 kV primary bank voltage and with a theta-pinch fill pressure of 10-mtorr deuterium.

In order to minimize plasma-wall interactions at the discharge tube ends and provide access for optical and internal plasma diagnostics, each end of the theta-pinch discharge tube is terminated, 4.5 cm beyond the coil ends, within a quartz expansion chamber. The chambers are 20 cm in diam, 50 cm long, and end-supported by 20-cm-diam metal vacuum tees.

Gas preionization is accomplished, in the theta-pinch mode, with a preionization capacitor bank consisting of ten 0.7-μF, 75-kV capacitors charged to 55 kV. The preionization bank oscillates at 500 kHz and produces a peak field of 2kG.

C. EXPERIMENTAL RESULTS WITHOUT END PLUGS

In order to determine the plasma parameters and end-loss characteristics, which establish reference conditions for end-stoppering studies, experiments were conducted with the theta-pinch ends unobstructed. End-on interferograms are used to determine the time history of the plasma column particle inventory, peak density, radius, and, in conjunction with the excluded flux measurement, the plasma beta and total temperature.

1. Plasma Parameters at Peak Magnetic Field. Figure IV-1 presents a time sequence of end-on plasma column interferograms obtained with a 30-ns pulsed holographic ruby laser interferometer. Each interferogram was obtained on a separate plasma discharge and the entire 8.8-cm diam of the discharge tube was illuminated by the interferometer laser light. The fringe pattern on each interferogram was digitized and reduced with software developed for the CTR-PDP-10 computer.

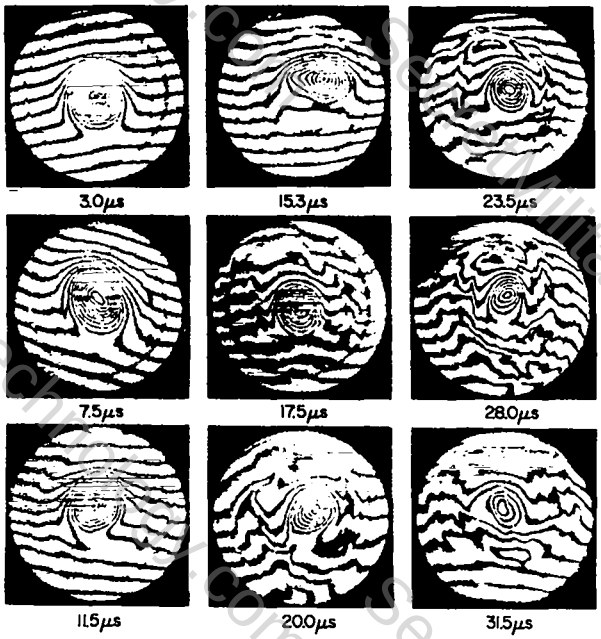

Fig. IV-1.
Time sequence of end-on plasma column interferograms.

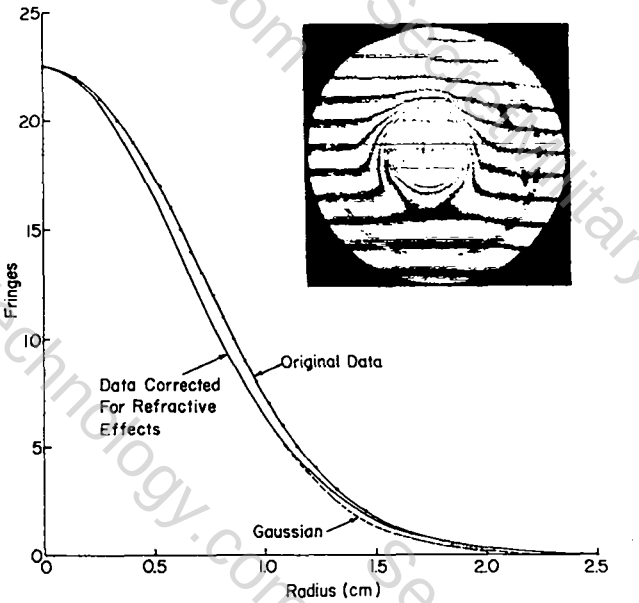

Fig. IV-2.
End-on interferogram obtained at t = 3.5 μs and corresponding reduced fringe shift profile.

The plasma parameters derived from analysis of the interferograms are most accurately determined near peak field time when the plasma column is highly symmetric and instability free. However, refractive bending of the interferometer laser light in the strong radial plasma density gradients existing near peak field time can complicate the interpretation of the interferograms. In order to assess these refractive effects and to determine the peak plasma parameters as accurately as possible, several interferograms obtained at $t \simeq 3.5$ μs were hand-analyzed; the interferogram computer reduction program does not account for ray-bending effects. Figure IV-2 shows a typical near-peak field time interferogram and the corresponding corrected and uncorrected fringe shift profiles. The maximum correction due to refractive bending[1] typically amounts to about 1.5 fringes.

Since the corrected fringe shift profiles for the hand analyzed interferograms are not exactly Gaussian, the peak plasma beta, β_a, was determined by numerically integrating the exact equation

$$\pi r_\phi^2 = \int_0^b 1 - \sqrt{-[f(r)/f_a]\beta_a}\; 2\pi r dr \,, \qquad (1)$$

where r_ϕ is the excluded flux radius (discussed below), b is the tube radius and f_a is the peak number of fringes. Equation (1) is derived from the definition of excluded flux and the pressure balance equation, assuming that the plasma temperature is independent of radius. From analysis of all the hand-analyzed interferograms an averaged β_a of 0.90 ± 0.02 was obtained. The peak plasma density, n_a, was determined from the expression

$$n_a = 3.24 \times 10^{17}\, f_a/L \ \text{cm}^{-3} \,, \qquad (2)$$

where L was taken to be equal to the theta-pinch coil length (500 cm). From the hand-reduced interferograms a peak n_a of $(1.49 \pm 0.03) \times 10^{16}$ cm^{-3} was obtained. From pressure balance,

$$n_a k(T_e+T_i) = \beta_a \frac{B_z^2}{8\pi} \,, \qquad (3)$$

the above values of β_a and n_a yield a total plasma

temperature at $t \simeq 3.5$ μs of $T_e + T_i = 3.25 \pm 0.15$ keV.

The total electron inventory, N_e, was determined from the equation

$$N_e = 3.24 \times 10^{17} \int_0^b f(r) 2\pi r dr \quad . \qquad (4)$$

From analysis of both the corrected and uncorrected fringe shift profiles, a maximum error in the total particle inventory of about 7% was attributed to interferometer refractive ray-bending effects. From the corrected fringe shift profiles a particle inventory at $t \simeq 3.5$ μs of $(1.96 \pm 0.04) \times 10^{19}$ was determined. This value compares well with the initial theta-pinch particle fill of 2.1×10^{19} at 10-mtorr D_2 fill pressure.

2. Time History of the Plasma Parameters.

The time history of the plasma parameters was determined using the results of the PDP-10 computer analysis of the end-on interferograms. This approach is justified since the errors introduced by refractive ray-bending effects are small and occur only near-peak field time when the density gradients are large. The low density plasma "halo," observed to surround the central plasma column for times $t \gtrsim 10$ μs (Fig. IV-1), was not included in the interferogram computer analysis data used to determine the plasma parameters. The halo plasma is generally believed to originate from wall-plasma interaction near the theta coil ends, however, this has not been verified experimentally.

The plasma radius is determined from the equation

$$a = \left(\frac{N_e}{Ln\pi} \right)^{1/2} \quad , \qquad (5)$$

where again N_e is the total number of particles evaluated from the end-on interferograms neglecting the plasma halo, and n_a is the peak density. It should be noted that n_a can be higher than indicated from the interferograms if the plasma column contains an axial curvature generated by the observed m = 1 wobble instability[2] which onsets ~ 5 μs after discharge initiation. In addition, the appropriate length, L, which should be used to describe the time-dependent axial dimension of the plasma column is unknown. Accordingly, the plasma radius obtained from Eq. (5) can consider only a best approximation. The time evolution of the plasma radius obtained from

The plasma excluded flux radius, r_θ, measured with the diamagnetic loop-probe system located at the center of the theta-pinch coil is shown in Fig. IV-3(b). The presented curve is the average of 44 data shots, taken simultaneously with the end-on interferograms, and the error bars represent ± one standard deviation from this average. The magnitude of the error bars, especially at late times, results more from limitations in the data acquisition system than from shot-to-shot plasma irreproducibility.

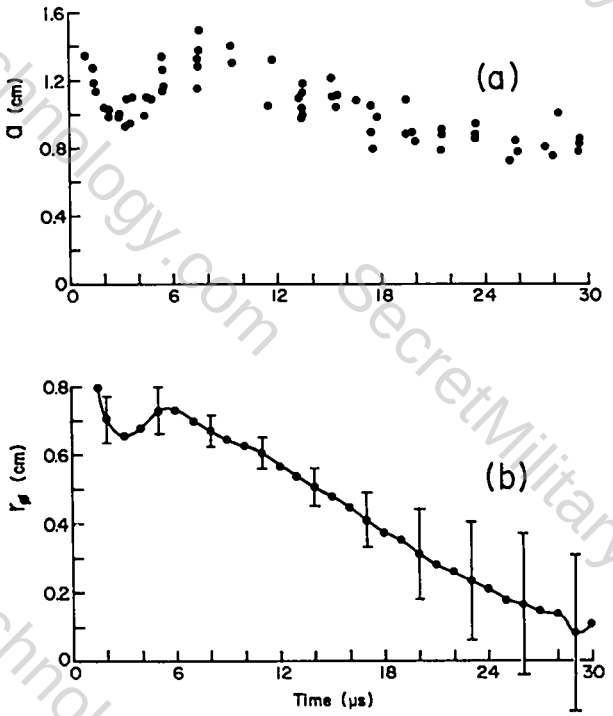

Fig. IV-3.
(a) Time history of plasma radius, a, and (b) averaged excluded flux radius, r_ϕ.

Specifically, the excluded flux data was recorded on a 6-bit SEC unit which, it has recently been found, is insufficient to resolve the large excursions in the excluded flux signal, particularly the low-level (~1-bit magnitude) signals existing at late times during the discharge. More recent data have been recorded on an oscilloscope in order to eliminate the problem.

Assuming a Gaussian density profile at all times during the plasma lifetime, the plasma peak beta, β_a, is calculated at a given time using the plasma radius obtained from the individual interferograms, and the averaged value of r_ϕ (Fig. IV-3b). The time history of β_a is shown in Fig. IV-4b.

The time history of the total plasma temperature is determined from pressure balance in Eq. (3) using n_a evaluated from the end-on interferograms (Fig. IV-4a), the measured magnetic field B_z, and the calculated values of β_a. The resulting time evolution of the central plasma column temperature is shown in Fig. IV-5. Neglecting the data obtained during the first 6 μs of the column life time, when the main magnetic field undergoes its maximum oscillation before the crowbar becomes effective at $t \simeq 6$ μs, a characteristic temperature decay time, τ_T, of 12.8 ± 0.9 μs is obtained from a least squares fit to the data of Fig. IV-5.

3. Plasma End-Loss Measurements. As in previous high-energy theta-pinch experiments, the central plasma column particle containment time was obtained from analysis of the end-on interferograms, neglecting the low-density plasma halo surrounding the main column. The time history of the central column electron inventory is presented in Fig. IV-6. The initial period ($t < 6$ μs) of constant electron inventory, also observed in previous experiments,[3-5] has been shown on Scylla IV-P to result from radial confinement of the plasma in the end expansion chambers;[2] the axially ejected plasma remains collimated (little radial

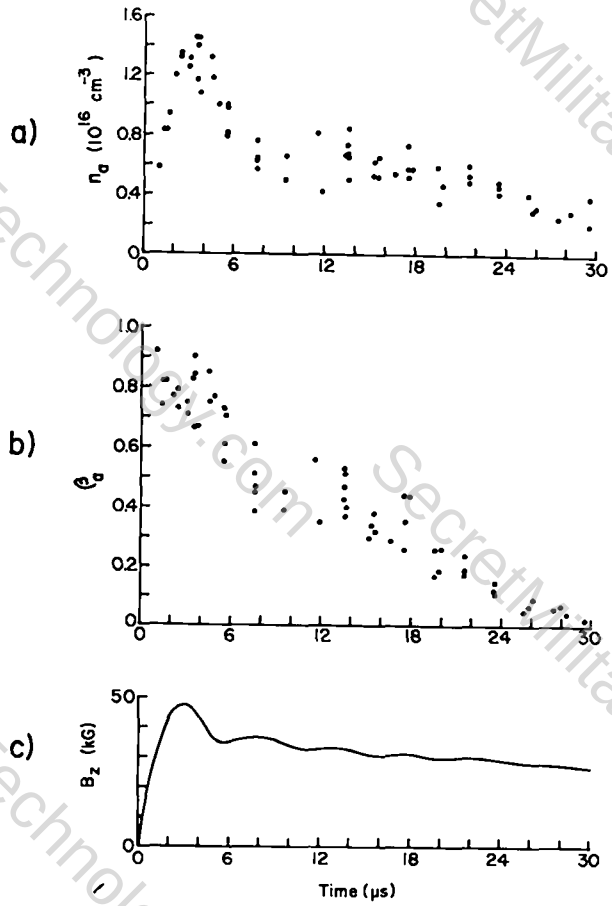

Fig. IV-4.
(a) Time history of plasma peak density n_a, (b) peak beta, β_a, and (c) main magnetic field waveform, B_z.

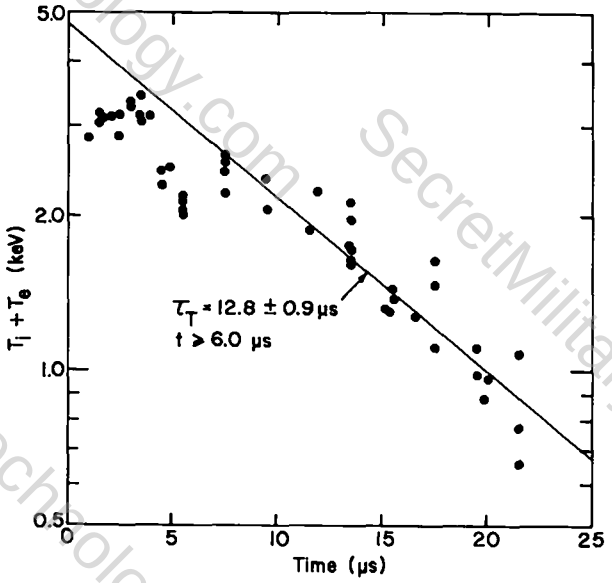

Fig. IV-5.
Time history of total plasma temperature determined from pressure balance.

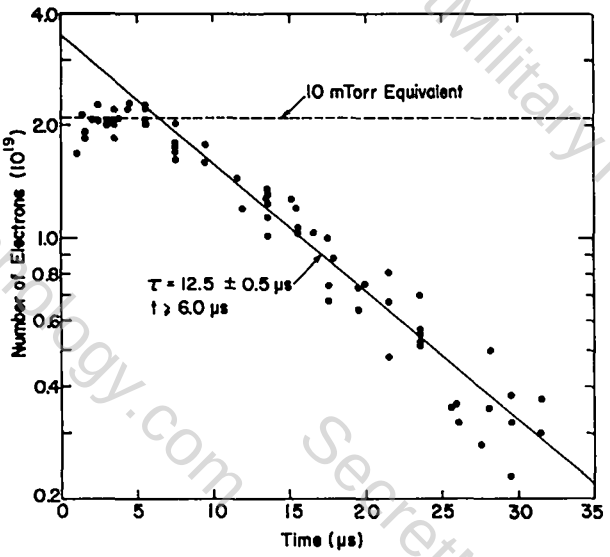

Fig. IV-6.
Time history of the central plasma column electron inventory.

expansion) for tens of centimeters after flowing out the ends of the theta-pinch coil. A least squares fit to the data of Fig. IV-6, for $t \geq 6$ μs, yields an e-folding end-loss time of 12.5 ± 0.5 μs. In order to obtain a consistent comparison with the present experimental results, the electron inventory data from previous experiments[4,5] have been re-analyzed so that only the data following the initial period of constant inventory are used in the particle end-loss time determination.

The particle end-loss time can be defined in terms of thermal transit times as

$$\tau = \frac{L}{2}\left(\frac{m_i}{2T}\right)^{1/2} \eta \quad , \qquad (6)$$

where L is the theta-pinch coil length, T the total plasma temperature, and η is a normalizing parameter, which is theoretically found to be a function of the plasma β; the possible dependence of η on other plasma properties is unknown. In Fig. IV-7, η is plotted against β. The solid

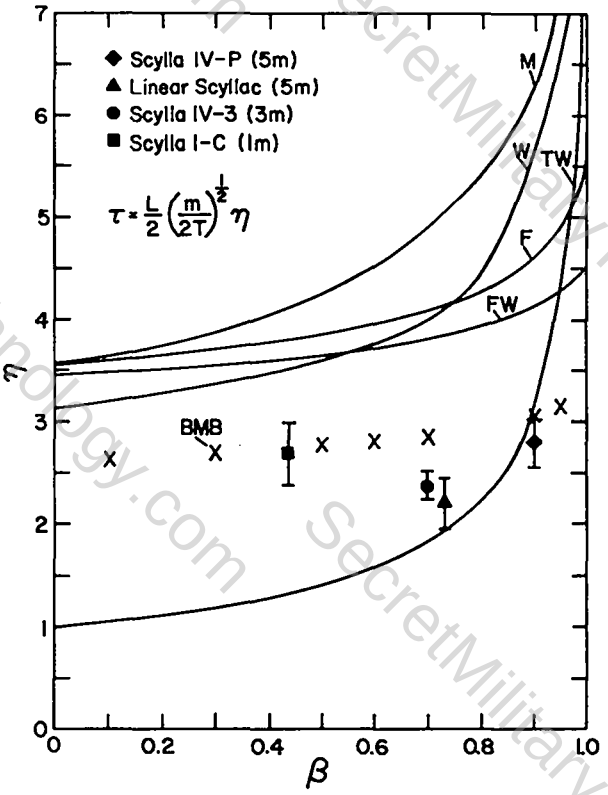

Fig. IV-7.
Theoretical and computational results for ηvβ and experimental data points.

curves represent existing particle end-loss theories which are discussed by Freidberg and Weitzner.[6] The x's mark the results of a recent numerical magnetohydrodynamic treatment of the end-loss problem by Brackbill et al.[7] The data points are from the Scylla IV-P, Scylla IV-3,[4] and Linear Scyllac[5] experiments which generated high energy collisionless plasmas, and the low-energy collision dominated Scylla I-C experiment.[8] In determining the experimental points, the peak values of β and total plasma temperature obtained in each experiment were used. The data from Scylla IV-[13] were excluded from Fig. IV-6 because the magnetic field was not crowbarred and β was not determined.

From examination of Fig. IV-7 the following major results can be identified, (a) For all the experiments the plasma particle end-loss time is between 2.2 and 2.8 thermal transit times. (b) Experimentally, the normalized end-loss time

appears to be independent of the plasma β. (c) The parameter η is independent of the plasma collisionality, and (d) The Brackbill et al., two-dimensional unsteady MHD code best describes the observed experimental results.

D. END-LOSS CALCULATIONS

It was pointed out by Siemon that the longitudinal temperature profile in a theta pinch is probably very near the form $(1-(z/L)^2)^{2/7}$ given by the constant pressure model.[9,10] A simple calculation of theta-pinch heat loss is therefore possible since the end-cooling term $\partial/\partial z(\kappa \partial T/\partial z)$ is then $-4\ \kappa T/(7L^2)$ (using $\kappa \sim T^{5/2}$). The equations take their simplest form if entropies rather than temperatures are used as the dependent variables. If s_e, s_i are the entropy per particle for electrons and ions at r = 0 and z = 0 (i.e., on axis in the center of the machine), the equations describing cooling are

$$\frac{ds_e}{dt} = \frac{3}{2}\left(\frac{T_i/T_e - 1}{\tau_{eq}} - \frac{1}{\tau_{ce}}\right) \tag{7}$$

$$\frac{ds_i}{dt} = \frac{3}{2}\left(\frac{T_e/T_i - 1}{\tau_{eq}} - \frac{1}{\tau_{ci}}\right) , \tag{8}$$

where, e.g., $\tau_{ce} = 21L^2\ n/(8\ \kappa_e)$. From Braginskii[11] (using $\ell n\ \Lambda = 10$),

$$\tau_{eq}(\mu s) = 6 \times 10^{-3}\ T_e(eV)^{3/2}/n(10^{16}\ cm^{-3}) , \tag{9}$$

$$\tau_{ce}(\mu s) = 1.4 \times 10^{6}\ L(m)^2\ n(10^{16}\ cm^{-3})/T_e(eV)^{5/2} , \tag{10}$$

$$\tau_{ci}(\mu s) = 5 \times 10^{7}\ L(m)^2\ n(10^{16}\ cm^{-3})/T_i(eV)^{5/2} . \tag{11}$$

Pressure balance is used to relate entropy and temperature. If N(t) is the line density at z = 0 and B(t) the external magnetic field, then the plasma area A is determined from the pressure balance relation,

$$\left(\frac{N}{A}\right)^{5/3}\left[\exp(2s_e/3) + \exp(2s_i/3)\right] + \frac{\phi^2}{2A^2} = \frac{B^2}{2} , \tag{12}$$

where $\phi = \pi a_0^2 \sqrt{1 - \beta_0}\ B_0$ is the flux inside the plasma. The temperature is obtained using $T_e = (N \exp(s_e)/A)^{2/3}$, $T_i = (N \exp(s_i)/A)^{2/3}$. Equations (7), (8), and (12) constitute a closed set of equations for s_e and s_i, which can be solved numerically.

Figure IV-8 shows a comparison of the energy line density calculated from the above equations (using the correct $\ell n\ \Lambda_{ee}$, $\ell n\ \Lambda_{ie}$, $\ell n\ \Lambda_{ii}$ factors) with experimental observations for cases with and without end plugs. The data were essentially fit

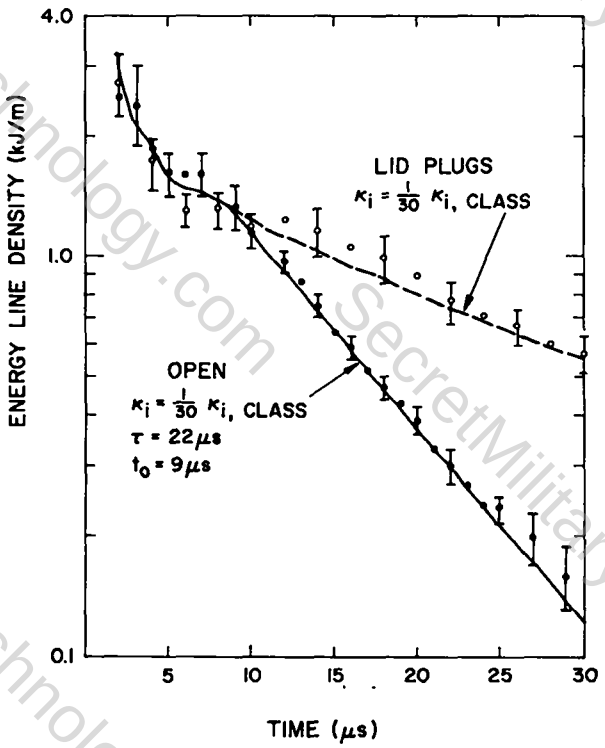

Fig. IV-8.
Measured and calculated values of excluded flux times magnetic field.

using the ion thermal conductivity (uncertain because of long mean free path), and particle end loss (i.e., N(t)) as adjustable parameters. For the plugged case N(t) was taken as constant and κ_i varied to give the fit shown in Fig. IV-8. In the unplugged case, using the value of κ_i determined, and assuming the simple form $N(t) = N_0 \exp(-(t - t_0)/\tau)$ (for $t > t_0$), the parameters t_0 and τ were varied to obtain the fit shown.

E. EXPERIMENTS WITH SOLID END PLUGS

Exploratory experiments performed in 1976 on the Scylla IV-P theta pinch using silicon dioxide (quartz) end plugs[12] demonstrated that plasma flow past the plugs and out of the ends of the pinch could be stopped. In addition, the stability of the plasma column was improved with the plugs inserted. Ablation of the plug surface was slight, with only about 0.1% of the plasma energy invested in the ablation process. However, these initial experiments indicated only a slight increase in energy confinement. It appeared that plasma flow to the end-plug region and energy loss by atomic processes in this region of ablated plug material dominated the energy confinement at the center of the pinch.

Recent experiments have been carried out with end plugs constructed of lower Z materials in an attempt to reduce the energy loss by atomic processes. Tabulated in Table IV-I are all the materials used in the Scylla IV-P end-plug experiments, along with their atomic numbers (Z), and the ionization potentials from their ground-state hydrogen-like (single-electron) configurations.

TABLE IV-I
MATERIALS USED FOR END PLUGS

Name	Elements	"Z"	I.P. (Hydrogen-like)
SiO_2 (Quartz)	Si	14	2.67 (keV)
	O	8	0.87 (keV)
BN (Boron Nitride)	N	7	0.55 (keV)
	B	5	0.34 (keV)
LiD (Lithium Deuteride)	Li	3	0.12 (keV)
	D	1	0.01 (keV)

In addition, new diagnostics have been implemented in these experiments that have provided a more detailed characterization of the processes in the end-plug region.

1. Density Measurements in the Plasma-Plug Interaction Region. Side-viewing ruby laser interferometery was used to observe the high-density ablated plasma near the end-plug surface. Interferograms of the end-plug region exposed at two different times in the discharge are shown in Fig. IV-9 for the boron nitride (BN) end plugs. Since the plasma column diam in Scylla IV-P is of the order of 2 cm, it is evident from Abel inversion of these holograms that the high electron density resulting from ablation and subsequent ionization is concentrated at the periphery of the column resulting in a annular radial density profile, Fig. IV-10. This hollow radial profile does not, however, extend axially to the surface of the plug. The density very close to the surface is characterized by a more nearly Gaussian radial distribution, Fig. IV-11, with

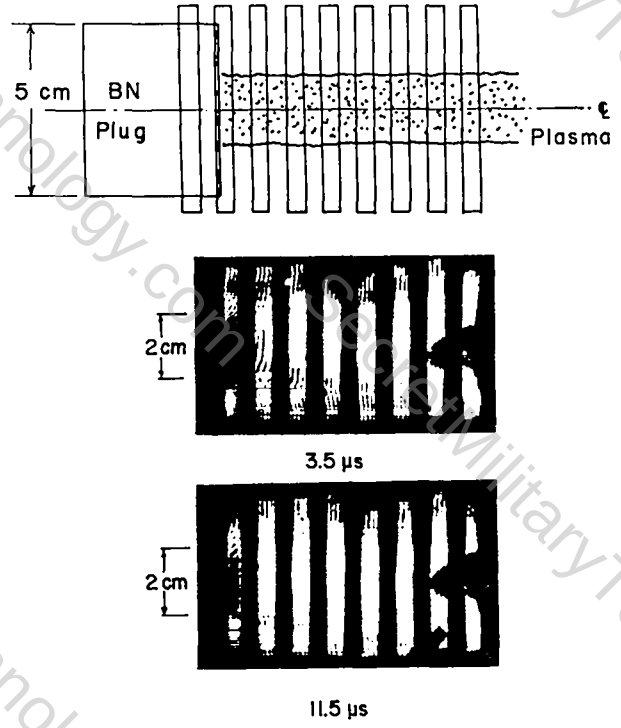

Fig. IV-9.
Side view interferograms in the vicinity of boron nitride end plugs.

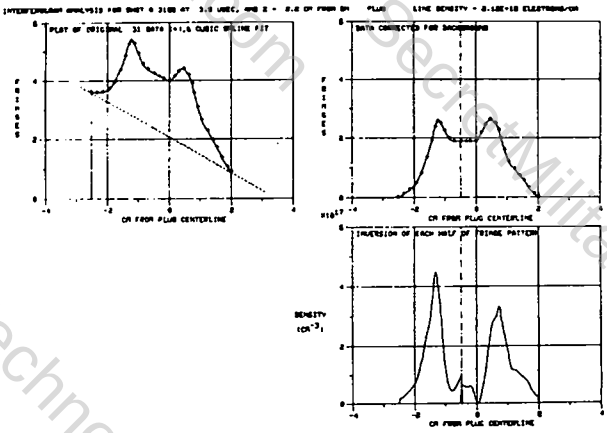

Fig. IV-10.
(Upper left) Plot of the fringe count taken in a plane perpendicular to the plasma column axis. (Upper right) Fringe count corrected for the linear shift introduced by the background fringes. (Lower right) Abel inversion of the corrected fringe count.

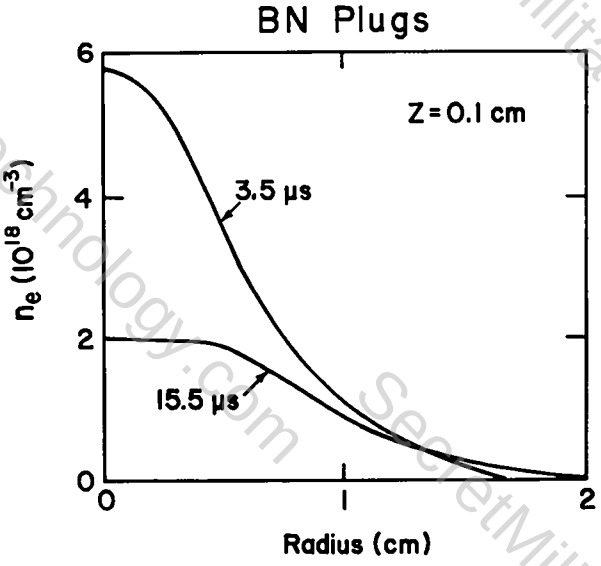

Fig. IV-11.
Radial density profiles obtained by Abel inversion of fringe counts in a plane 0.1 centimeters from the boron nitride plug surface.

maximum electron densities in excess of 5×10^{18} cm^{-3}. This suggests that although the ablation is well distributed over the contact region of the high-energy plasma column on the plug surface, the flow of ablated material toward the midplane of the theta pinch is less inhibited near the edge of the plasma column where the axial pressure is less. The axial variation of the number of electrons per cm of column length, plotted at various times in Fig. IV-12, decreases rapidly with distance from the plug surface, with an e-folding distance of about 1 cm or less. The formative time for the ablation layer is about 1-1.5 μs, and after about 10 μs, the electron line density begins to decrease.

At 3-5 μs the line density is a substantial fraction of that predicted by computer simulations in which flow of the deuterium plasma to the plug is stopped (also shown in Fig. IV-12), however, as noted above, most of this density is near the edge

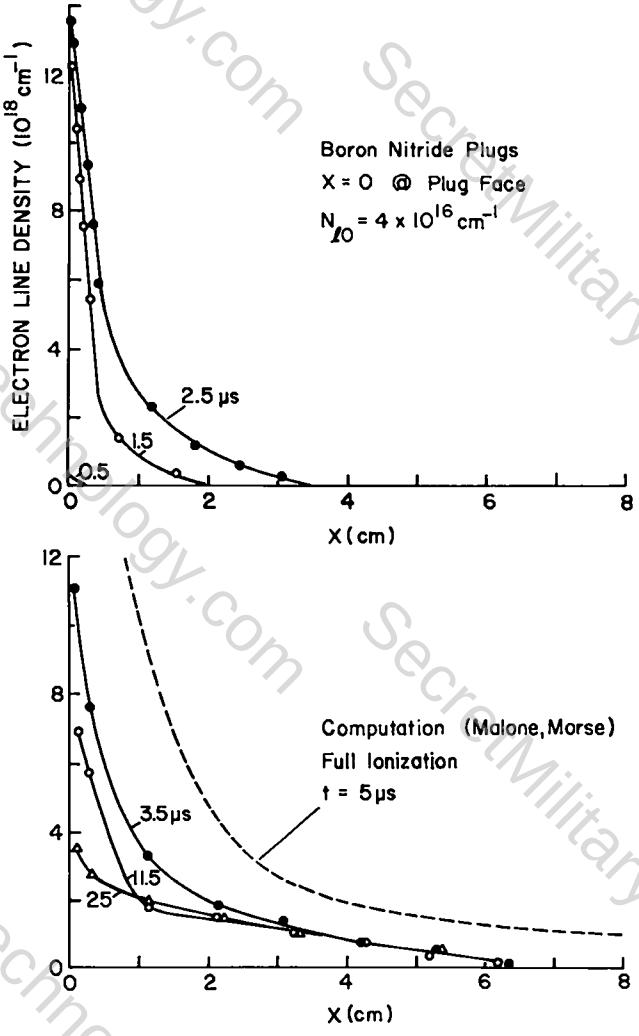

Fig. IV-12.
Axial electron line density inferred from side-view interferograms. Also shown is the line density predicted by computer simulations.

of the column and can have little effect on flow in the main body of the deuterium plasma. Furthermore, diamagnetic loop measurements of the energy confinement at the pinch midplane were much the same for these BN plugs as for the SiO_2 plugs, i.e., no substantial improvement over an open geometry was measured. Apparently even with the lower Z of the BN plugs, atomic processes acted as a major energy sink preventing the ablation and ionization of sufficient plug material to impede the deuterium plasma flow and associated energy loss.

Lithium deuteride (LiD) is the lowest Z solid end-plug material available at room temperature, and the line radiation from this material should be completely burned through at an electron temperature of 100 eV. Side-viewing interferograms obtained with the LiD plugs (Fig. IV-13), indicate much higher density of ablated plasma. Indeed, so much material is ablated and ionized in the first 2 μs that the fringes in the first centimeter from the surface are obscured. It is also evident that, unlike the BN plugs, there is little radial confinement of the ablated material near the plug

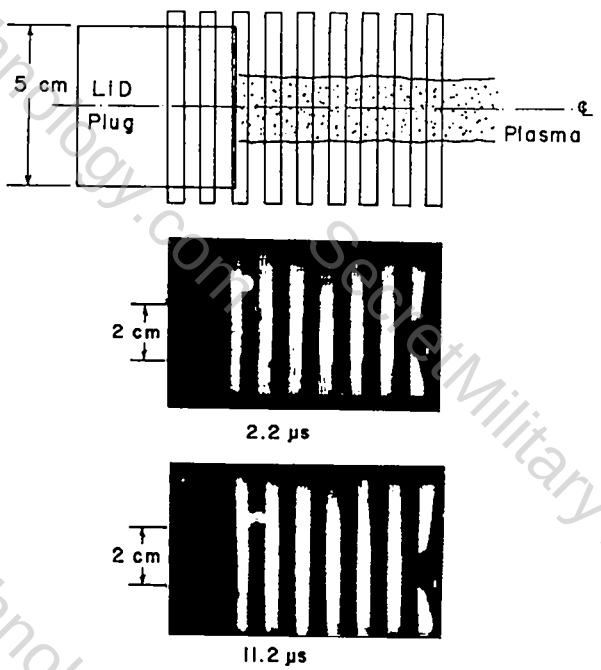

Fig. IV-13.
Side-view interferograms in the vicinity of lithium deuteride end plugs.

surface. Radial density profiles obtained from Abel inversion of the interferograms, Fig. IV-14, is characterized by a high electron density near the column edge, however, with these plugs there is now a significant increase of density in the interior of the column. The line density, Fig. IV-15, at distances far from the plug surface is very close to that predicted by Malone and Morse's[13] simulation of a plugged column with Z appropriate to these plugs, but again it must be remembered that much of this plasma density is outside of the outer radius of main plasma column.

2. Luminosity and Spectroscopic Measurements. Streak camera photographs taken in the region of the end plug indicate that a luminous front initially propagates away from the surface with a velocity of about 1.4×10^6 cm/sec (see Fig. IV-16). Later in time and at positions closer to the midplane, spectroscopic measurements of continuum radiation show a propagation away from the plug with a velocity of $2\text{-}4 \times 10^6$ cm/sec, Fig. IV-17. These velocities are less than half those predicted for the ablation front in the computer simulations. No such propagation could be identified spectroscopically with the BN plugs.

3. Energy Line Density Measurements. With the LiD plugs, diamagnetic loop-probe measurements at the pinch midplane show a significant increase

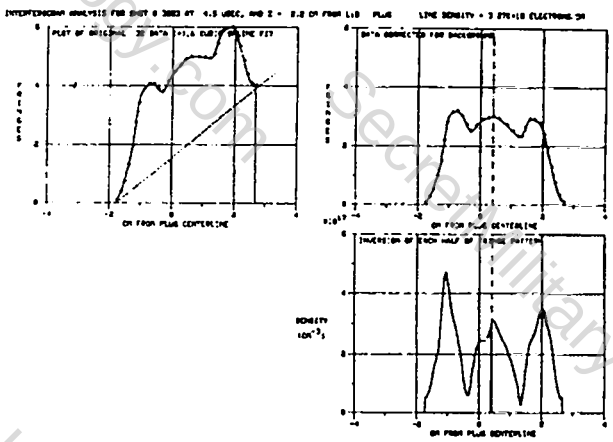

Fig. IV-14.
(Upper left) Plot of the fringe count taken in a plane perpendicular to the plasma column axis. (Upper right) Fringe count corrected for the linear shift introduced by the background fringes. (Lower right) Abel inversion of the corrected fringe count.

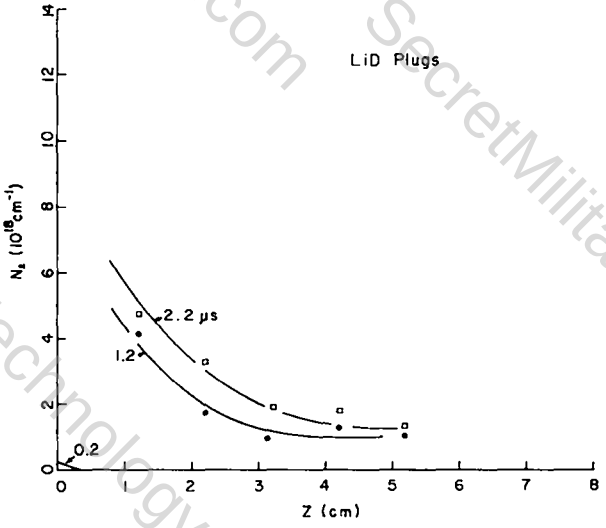

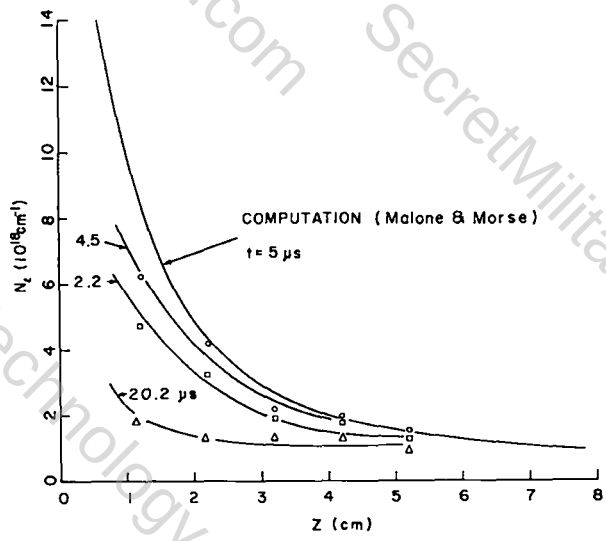

Fig. IV-15.
Axial electron line density inferred from side-view interferograms. Also shown is the line density predicted by computer simulations.

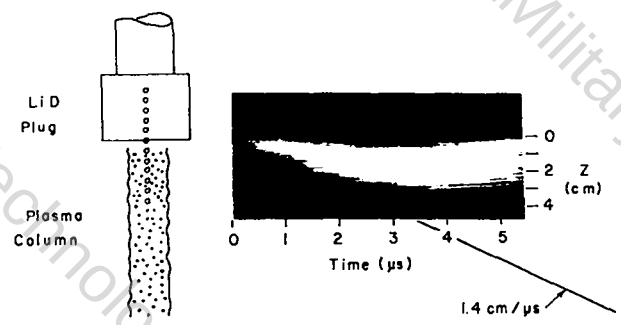

Fig. IV-16.
Side-viewing streak camera photograph showing the axial propagation of a luminous front away from the lithium deuteride plug.

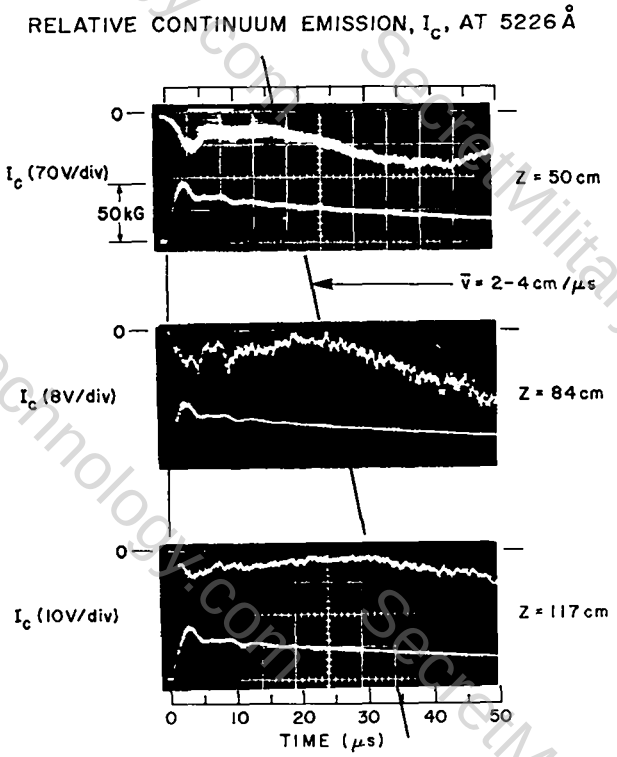

Fig. IV-17.
Oscillograms of monochromator-photomultiplier continuum monitor signals. The velocity of the luminous front inferred from the increase in these signals is indicated by the diagonal line.

in energy confinement over that obtained either in open geometry, or with higher Z end plugs. As shown in Fig. IV-18, the energy confinement time has been increased by a factor of three (from 9 to 29 μs) over the open geometry by use of the LiD plugs, which is significantly better than the improvement observed using the higher Z end plugs. This encouraging result is in excellent agreement with computer calculations by Siemon and Miller (Sec. D) of the expected energy confinement in a column in which flow is stopped and the losses are dominated by electron thermal conduction to the ends and decay of magnetic fields.

4. Discussion. Differences in energy confinement using plugs of different materials suggests that a comparison of measurements for these experiments may yield clues to the improved performance of LiD plugs. Streak camera photographs indicate that both high-and low-Z materials have a stabilizing influence on the column (Fig. IV-19), but that there are qualitative

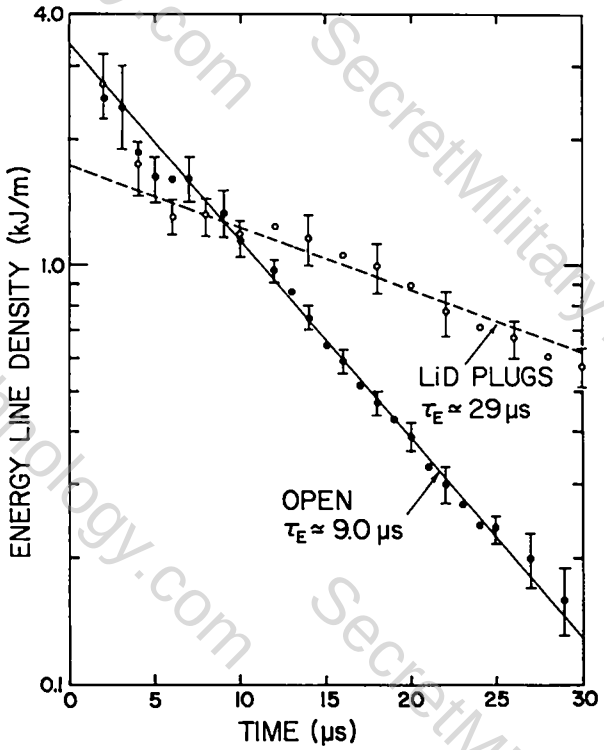

Fig. IV-18.
The energy line density inferred from diamagnetic loop measurements in the theta-pinch midplane. The straight lines and time constants shown result from least squares fitting exponential decays to the data for times greater than six μs.

differences in the column behavior when plugged with different materials. An apparent "blooming" of the column at late times with LiD plugs is observed, the reason for which is not yet understood. Comparison of the energy line density (measured at several axial positions with diamagnetic loops) for high- and low-Z plugs (see Fig. IV-20) shows the strong cooling effect of the higher Z plasma near the plugs. With LiD plugs, on the other hand, the axial energy distribution early in time is much nearer to that characterizing the open geometry. Comparison of axially resolved continuum radiation measurements for open-ended and plugged geometries show that the continuum emission near the plug surface is lower for LiD than for BN (Fig. IV-21). This is probably attributable to the lower effective ionic charge of LiD and the lower temperature with BN. The continuum radiation should not be an important energy loss mechanism compared with the line radiation. Finally, a comparison of radial density profiles extracted from side-viewing interferograms (Fig. IV-22) indicates that there is a much higher density of ablated material propagating away from the plug surface with the LiD plugs. These observations strongly suggest that the performance improvement of LiD over higher Z materials results, at least in part, from less plasma energy deposition in atomic processes in the ablated material, leaving sufficient energy flux on the surface to efficiently ablate the material required to retard the deuterium plasma flow into this region.

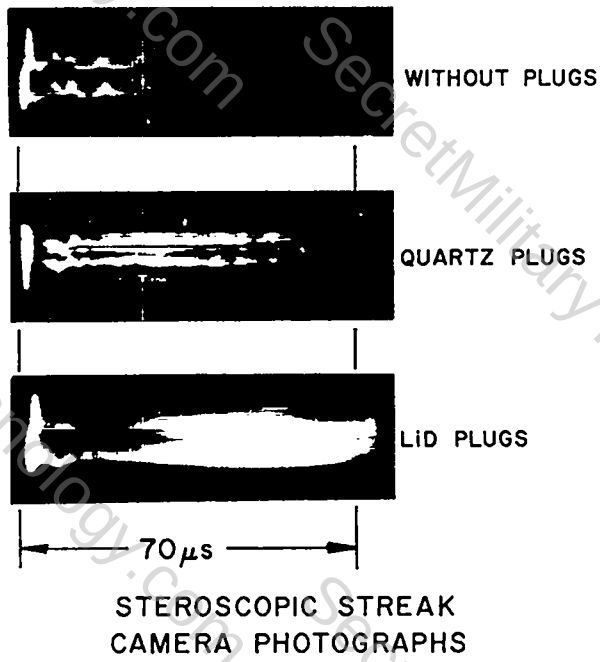

Fig. IV-19.
Stereoscopic streak camera photographs taken with an open geometry and two different end-plug materials.

In summary, the use of LiD end plugs gives a dramatic increase in energy containment as compared with the higher atomic number SiO_2 and BN plugs. For plug materials with Z greater than three, atomic processes do not allow the buildup of plasma density in the ablated layer necessary for expected plug behavior. By using LiD end plugs, we have succeeded in improving the energy confinement time of a thermonuclear plasma by a factor of three, in excellent agreement with theory.

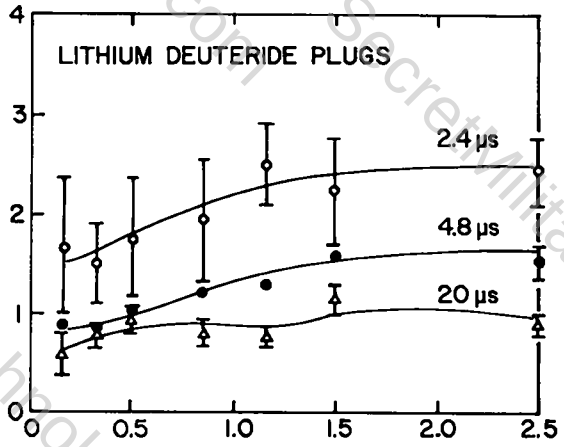

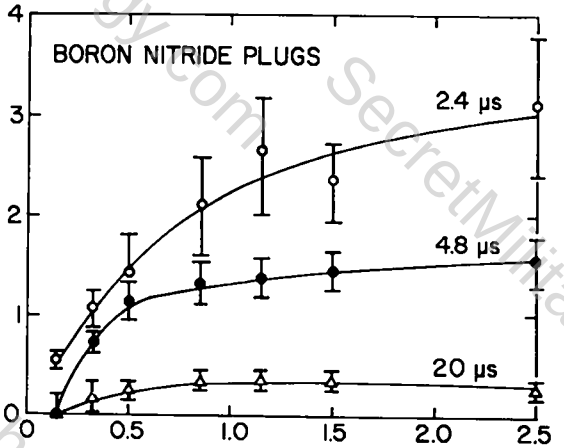

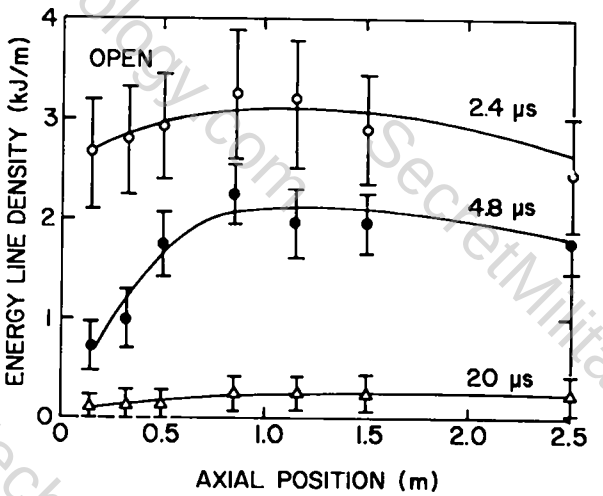

Fig. IV-20.
Diamagnetic loop measurements of the plasma energy line density. (The axial coordinate zero corresponds to the end of the compression coil.)

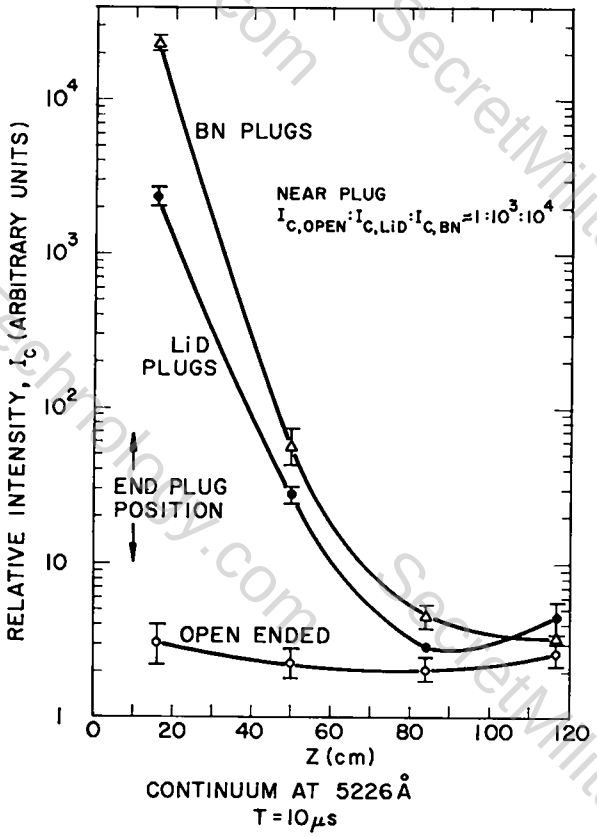

Fig. IV-21.
Measurements of continuum radiation near the end of the compression coil at 10 μs after primary bank initiation.

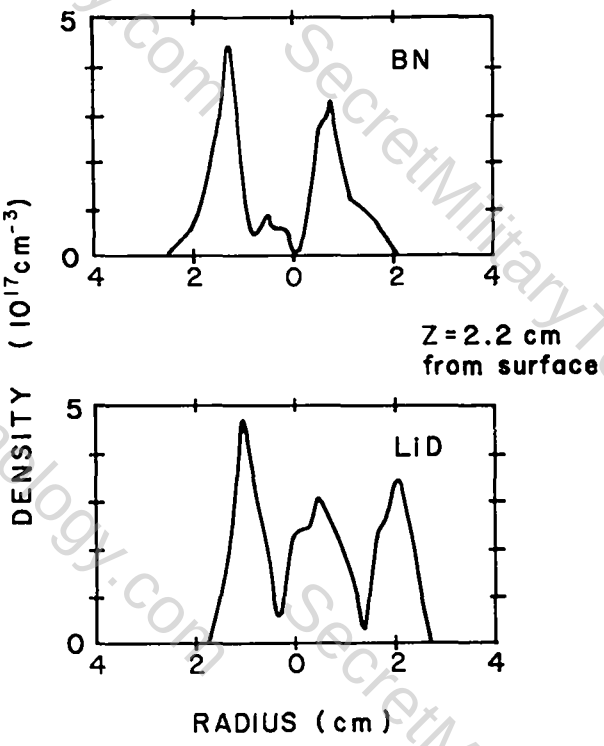

Fig. IV-22.
Radial density profiles 2.2 centimeters from the plug surface.

REFERENCES

1. F. C. Jahoda and R. E. Siemon, "Holographic Interferometry Cookbook," Los Alamos Scientific Laboratory report LA-5058-MS (1972).

2. "LASL Controlled Thermonuclear Research Program January--December 1976," Los Alamos Scientific Laboratory report LA-7082-PR (1978), p. 67,87.

3. E. M. Little, W. E. Quinn, and G. A. Sawyer, "Plasma End Losses and Heating in the Low-Pressure Regime of a Theta Pinch," Phys. Fluids 8, 1168 (1965).

4. R. F. Gribble, W. E. Quinn, and R. E. Siemon, "Plasma Experiments With a Three- Meter θ-Pinch," Phys. Fluids 14, 2042 (1971).

5. K. S. Thomas, H. W. Harris, F. C. Jahoda, G. A. Sawyer, and R. E. Siemon, "Plasma Experiments on the Linear Scyllac Theta Pinch," Phys. Fluids 17, 1314 (1974).

6. J. P. Freidberg and H. Weitzner, "Endloss from a Linear θ-Pinch," Nucl. Fusion 15, 217 (1975).

7. J. U. Brackbill, M. T. Menzel, and D. C. Barnes, "Numerical Studies of the Linear Theta Pinch," Third Topical Conference on Pulsed High-Beta Plasmas, Culham, England (1975).

8. K. F. McKenna and T. M. York, "End Loss from a Collision Dominated Theta Pinch Plasma," Phys. Fluids 20, 1556 (1977).

9. A. W. DeSilva, "Thermal End Loss from a Plugged Theta Pinch," Los Alamos Scientific Laboratory report LA-6980.

10. T. K. Chu and L. C. Johnson, "Conduction Heat Loss Scaling in Open Field Line Geometries," Phys. Fluids 20,1684 (1977).

11. S. I. Braginskii, "Transport Processes in a Plasma," Reviews of Plasma Physics 1, 205 (1965).

12. R. J. Commisso, C. A. Ekdahl, K. B. Freese, K. F. McKenna, and W. E. Quinn, "Solid-End-Plug Experiment on a θ-Pinch," Phys. Rev. Lett. 39,137 (1977).

13. R. C. Malone and R. L. Morse, personal communication, 1977.

V. STAGED THETA PINCH

C. J. Buchenauer, J. N. Downing, A. R. Jacobson,
E. M. Little, K. S. Thomas

A. INTRODUCTION

The Staged Theta Pinch (STP) is a 4.5-m-long, 22-cm-bore theta pinch designed to study the physics and technological problems associated with using separate capacitor banks for implosion heating and adiabatic compression. The STP uses a low-energy, high-voltage capacitor bank (PFN I) to produce the plasma and a lower voltage, high-energy capacitor bank to provide a variable amount of adiabatic compression. A second low-energy, high-voltage capacitor bank (PFN II) is available to shape the implosion magnetic field and to assist in containing the plasma before it contacts the wall of the discharge chamber. The experiment produces high-temperature plasmas with a much larger ratio of plasma radius to discharge tube radius than conventional theta pinches which utilize a single capacitor bank for both shock heating and adiabatic compression.

A complete description of the Staged Theta-Pinch experiment and a summary of results through 1976 was given in the last annual report.[1] The period covered by this report was spent constructing, checking out, and collecting data with a Thomson scattering apparatus. Data were collected at two axial positions, one near the center of the main compression coil and one near the end. At the center of the coil, data were taken at three radial positions; at the end, data were taken at four radial positions. Measurements were made as a function of time with initial D_2 fills from 3 to 15 mtorr. (At the end the range was 5-15 mtorr because of the rapid decrease of density with time at this position.) The results of these measurements, as well as a description of the experimental apparatus, are given below.

B. THOMSON SCATTERING APPARATUS

A schematic layout of the Thomson scattering experiment is shown in Fig. V-1. The ~ 3-J ruby laser beam was expanded before being focused by the lens shown in the left of the figure. Pyrex windows were required because of plasma damage to the lens and beam dump when these were part of the

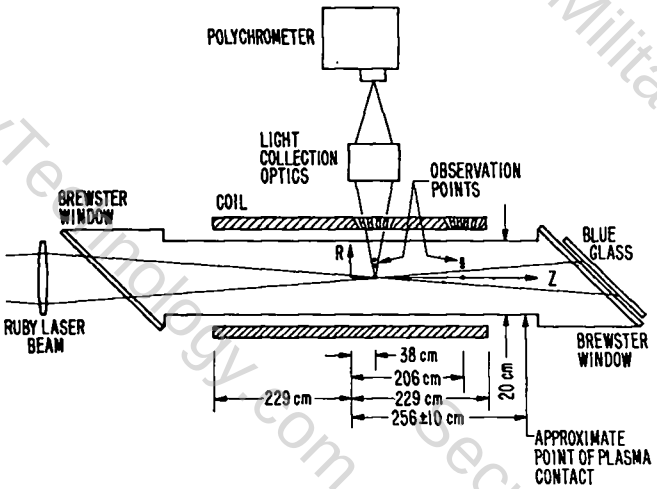

Fig. V-1.
Schematic layout of the Thomson scattering experiment.

vacuum chamber. The Pyrex windows were mounted at the Brewster angle to reduce reflections. (The windows are shown 90° from their actual mounting position.) Scattered light was collected with a five-channel polychrometer. The system was aligned using a wheeled carriage (called the "lowrider") which could be moved along the discharge tube inside the vacuum chamber by means of external magnets. The same magnets caused a movable vane to be raised when the "lowrider" was in its alignment position. When not in use, the "lowrider" was stored in a stainless steel "cross" at the end of the vacuum chamber.

The outputs from the five polychrometer channels were displayed on oscilloscopes. The height of the signals from the channels used for a plasma discharge was measured on a digitizer and a background, which was obtained from the average background over several shots, was subtracted. It was then analyzed as indicated in the following paragraph.

The five polychrometer channels had bandwidths of 692-688 nm, 688-681 nm, 681-670 nm, 670-659 nm, and 659-644 nm, respectively. The measured spectral response of each channel was

used to compute the relative intensities which would be observed for different electron temperatures with 694-nm excitation and 90° scattering. Curves were constructed from the computed relative channel intensities using the normalization that the sum of the squares equals unity for each temperature. The observed scattered intensities were fitted by computer to these calibration curves to give a least squares fit.

C. EXPERIMENTAL CONDITIONS

All data were taken with voltages of 100 kV - PFN I, 90 kV - PFN II, and 20 kV - Staging bank. These conditions were chosen because they allowed control of the plasma over a wide range of initial D_2 fills. The magnetic field waveform for 10-mtorr fill is given in Fig. V-2. The waveform for other cases was approximately the same except for the lowest fills where the first dip was filled in by plasma-circuit interactions. Table V-I gives expected plasma parameters for 5-, 7-, 10-, and 15-mtorr fills. The parameters, except T_e, were taken from data collected in the fall of 1976. Figure V-3 shows measured radial density profiles taken at the peak of magnetic field. The profiles become more diffuse at lower fills and, although data were not available, the trend probably continues at fills below 5 mtorr. This trend may be related to some of the results presented in the next section.

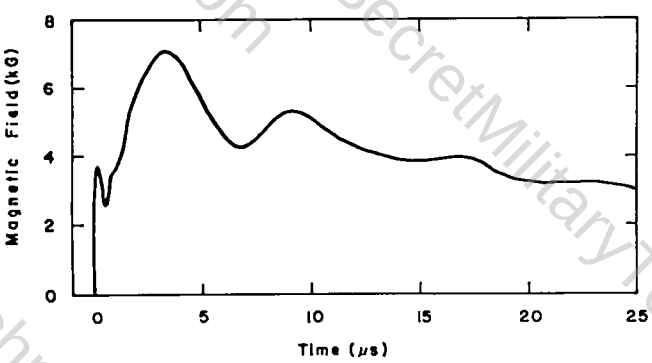

Fig. V-2.
Magnetic field vs time.

TABLE V-I

PLASMA PARAMETERS - STP

Fill (mtorr)	5	7	10	15
Density (10^{15} cm^{-3})	1.5	2.3	3.5	6.0
Magnetic field (kG)	7	7	7	7
Ion temperature (eV)	683	416	254	132
Electron temperature (eV) (measured)	137	114	96	73
Electron temperature (eV) (calculated)	102	108	110	90

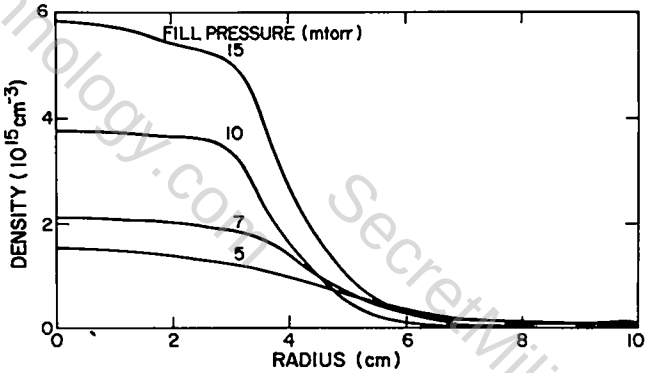

Fig. V-3.
Radial plasma density profiles for different D_2 fill pressures.

D. PLASMA RESULTS

Figures V-4 and V-5 show the time dependence of the electron temperature for different initial fills at the two different axial positions, Z = 38 cm and Z = 206 cm. (Z = 0 cm is the center of the compression coil and Z = 229 cm is the end.) All measurements were made on axis with the exception of the Z = 38 cm, 4-mtorr case where data were included for R = 3.3 cm because of the lack of data on axis. Electron temperature time histories for other off-axis cases were the same as measured on axis.

In many cases T_e was measured out to 50 μs after discharge initiation. During this period the temperature showed a slow decay to 0.5-0.7 of its peak value. The early time behavior of T_e was as follows: At all radial positions T_e rose rapidly (< 100 ns) to a value approximately one-half of its peak value. This occurred at a time which corresponded to the arrival of the implosion density front. The temperature then rose

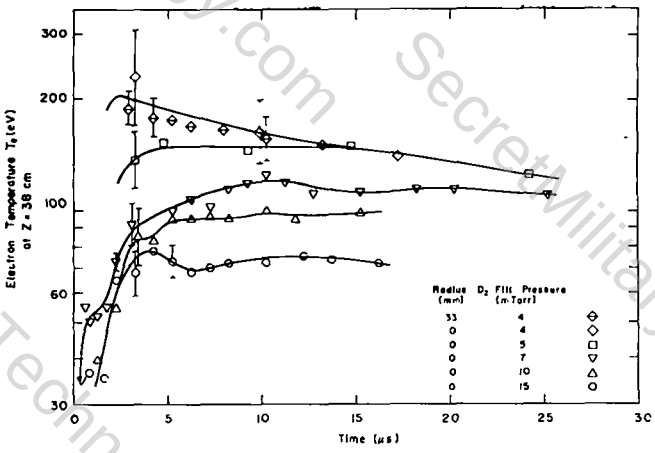

Fig. V-4.
Electron temperature vs time for five D_2 fills at an axial position near the center of the compression coil.

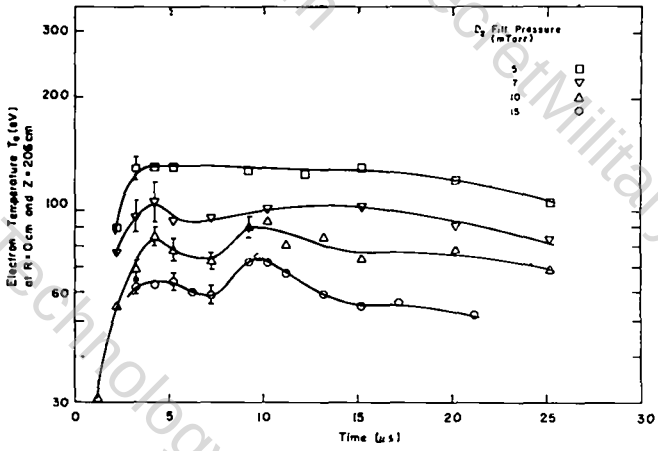

Fig. V-5.
Electron temperature vs time for four D_2 fills at an axial position near the end of the compression coil.

slowly as the compression magnetic field increased. In some cases at higher fills the peak temperature occurred after peak magnetic field. This is interpreted as an impurity effect because its behavior was related to the cleanliness of the discharge conditions.

Figure V-6 shows the dependence of T_e on initial D_2 fill. The open circles are the temperature measured at peak magnetic field. For those cases where the peak temperature occurred later, the peak temperature is plotted as dark circles. As can be seen from the figure, the electron temperature increased rapidly for D_2 fills below 5 mtorr. A correlation was found between the rate of magnetic field diffusion as measured by the excluded flux apparatus and the electron temperature; the faster the field diffusion, the higher the temperature. Higher electron temperatures could also be produced by lowering the preionization capacitor bank voltage.

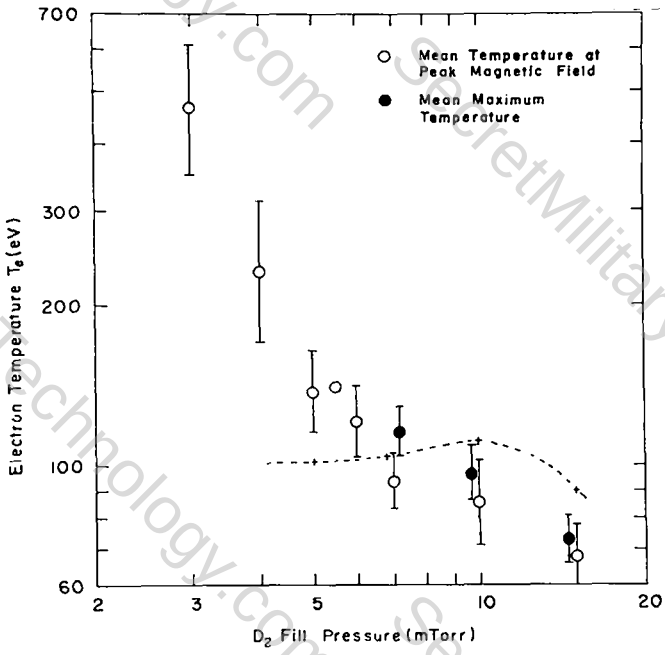

Fig. V-6.
Electron temperature vs initial D_2 fill. Dashed line is prediction of a computer model.

The predicted electron temperatures, assuming heating of the electrons by the ions and classical thermal conductivity out the ends of the experiment, were calculated using a code written by R. Siemon. The temperatures predicted by this code are plotted as a dashed line in Fig. V-6. Below 5 mtorr the plasma parameters were not known so the code could not be used. Reasonable assumptions about the parameters would, however, predict a slight decline in T_e at lower fills. The higher measured temperatures at lower fills are, therefore, probably due to anomalous heating of the electrons by the rapid magnetic field diffusion at early times. To test the effect of extra heating during the implosion, the code was run with the measured electron temperature as the initial condition. The code predicted a rapid

approach (< 5 μs) to the computed values given in Fig. V-6.

For five cases, two at Z = 38 cm and three at Z = 206 cm, sufficient data were available to study the radial dependence of T_e. The results are plotted in Figs. V-7 and V-8. As can be seen from Fig. V-8, the temperatures drop off rapidly around R = 5 cm near the ends but not at the center of the compression coil. (The extent of the radial scan was limited to 5 cm at the center because of the geometry of the apparatus.)

The ratio of peak electron temperature at Z = 38 cm and Z = 206 cm was calculated for 5, 7, 10, and 15 mtorr and the results were compared with a theoretical model of T. K. Chu.[2] The result is shown in Fig. V-9. The position of plasma contact with the ends of the machine is uncertain. The assumed point is shown in Fig. V-1. The horizontal error bars indicate the range of possible contact points.

When the initial calibration of the polychrometer was set up, the gain of the various channels was adjusted to give an output proportional to the channel width. Therefore, the sum

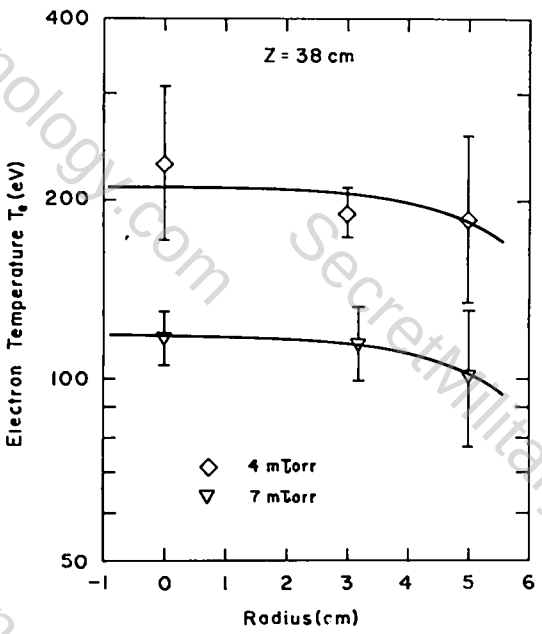

Fig. V-7.
Electron temperature vs radius for two initial D_2 fills at an axial position near the end of the compression coil.

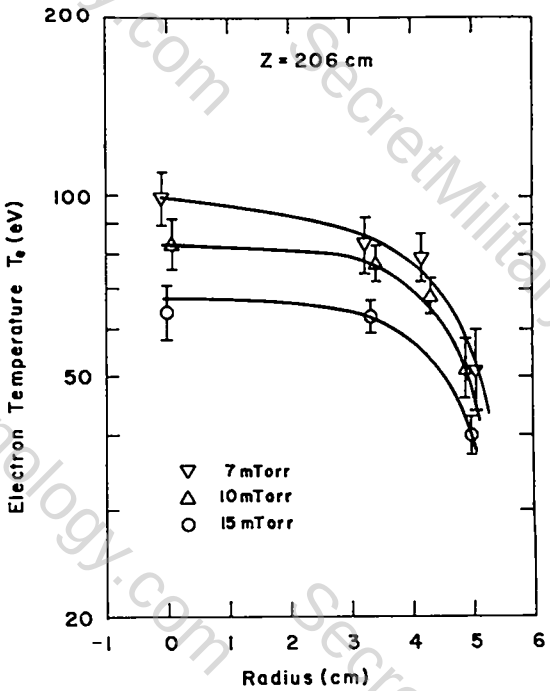

Fig. V-8.
Electron temperature vs radius for three initial D_2 fills at a position near the end of the compression coil.

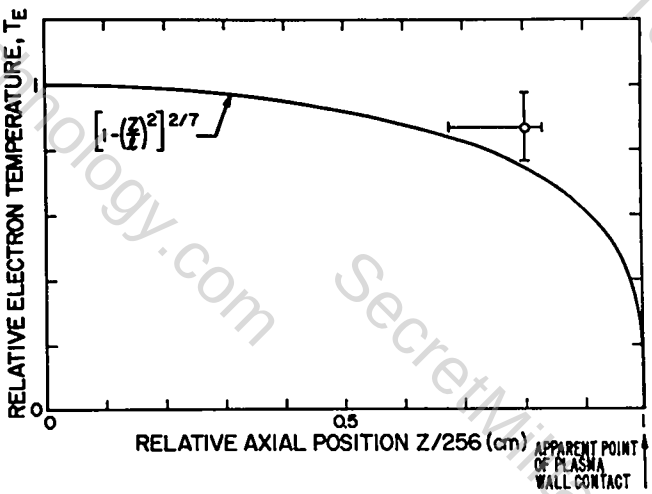

Fig. V-9.
Axial temperature profiles - theory and experiment.

of the intensities of the channels was a measure of plasma density. When it was discovered that the plasma column near the end had a different density time dependence from what it had at the center of the coil, the sums were plotted as a

function of time. This gives a qualitative measurement of density vs time. Data were included only when a lengthy data run was available at a particular D_2 fill. The data for Z = 206 cm are probably more accurate than for Z = 38 cm because more care was taken to make the data meaningful after the density variations were observed. The results are plotted in Figs. V-10 and V-11 for data taken on axis. The time dependence of the density was the same at other radii. The drop in density is particularly noticeable for the Z = 206 cm, 5- and 7-mtorr fill cases.

E. SUMMARY

The electron temperature measurements on the STP experiment yielded the following results:

1. The functional dependence of T_e on plasma parameters (see Fig. V-6 and Table V-I) was different from the one predicted by a theoretical model which assumes that T_e is dominated by classical energy input from the ions and classical thermal conductivity out the ends of the compression coil. The lower measured temperatures at the higher initial fills may be an impurity radiation effect which would be expected to increase with higher plasma densities if the number of impurity ions is constant. The higher measured temperatures at lower fills can be explained by anomalous heating during the implosion phase. The slow decay in temperature requires, however, either continued anomalous heating or reduced thermal conduction at the lower D_2 fills.

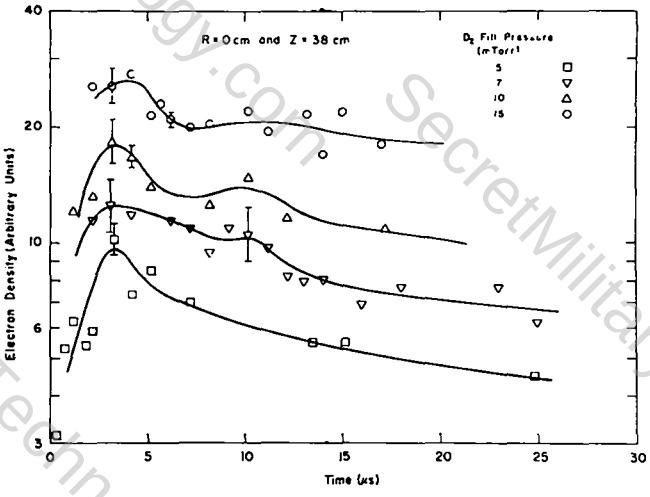

Fig. V-10.
Density vs time, as measured from the scattered light signal, for four initial D_2 fills at a position near the center of the compression coil.

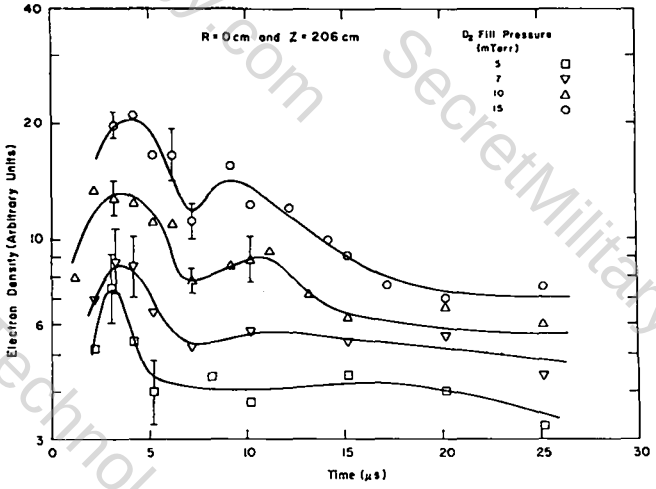

Fig. V-11.
Density vs time, as measured from the scattered light signal, for four initial D_2 fills at a position near the end of the compression coil.

2. T_e as a function of radius decreases more slowly at the center of the machine than at the ends. This is probably a result of radial heat flow. If electron heating is proportional to n^2 (ion-electron collisions) radial heat flow could give the observed results. Because of the high beta of the plasma, radial heat flow is expected to be an important consideration.

3. The time dependence of plasma density is different at the ends of the machine from what it is in the center. The decrease in density at the ends after peak field is particularly noticeable at lower D_2 fills. A detailed study of this phenomemon will require much more accurate density measurements than is possible with a Thomson scattering measurement.

REFERENCES

1. K. S. Thomas, compiler, "LASL Controlled Thermonuclear Research Program, January-December 1976," Los Alamos Scientific Laboratory report LA-7082-PR (1978).

2. T. K. Chu and L. C. Johnson, Phys. Fluids 20, 1684 (1977).

VI. FIELD-REVERSAL EXPERIMENT (FRX)

R. K. Linford, D. A. Platts, and E. G. Sherwood

A. INTRODUCTION

Two theta-pinch systems FRX-A and FRX-B are being used to study the stability and confinement properties of the reversed-field configuration (RFC) shown in Fig. VI-1. In this configuration the plasma is confined by closed poloidal field lines supported by the toroidal plasma current. If sufficiently stable, this RFC could be used to increase the energy confinement in open-ended plasma devices such as mirrors, theta pinches, and liners.

The FRX-A and FRX-B facilities were produced by modifying other experiments during the latter half of 1976. The 1976 Annual Report describes these facilities and provides the historical motivation for initiating the research.[1] (Note: The name of the experimental program has changed from Field-Reversal Theta Pinch (FRTP) to the present FRX.) The FRX-A system was completed, and initial experiments performed in 1976. This system also produced the majority of the results presented in this report. The FRX-B system was completed in the spring of 1977, but certain deficiencies, discussed below, were discovered in the plasma it produced. The concentrated efforts of the small staff on FRX-A have prevented rapid progress on FRX-B. However, full operation of this larger system is expected in the first half of 1978.

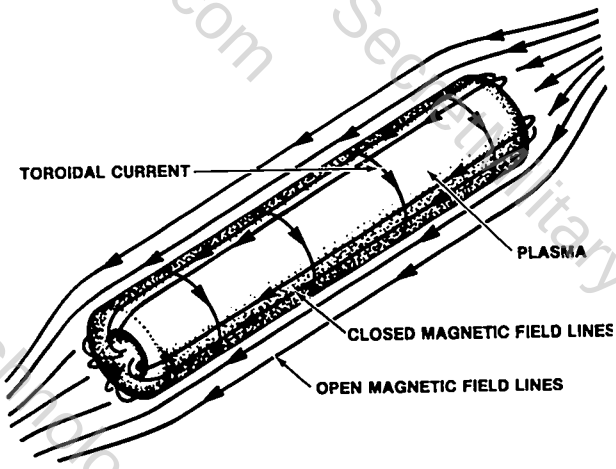

Fig. VI-1.
Reversed-field configuration.

B. DIAGNOSTICS

The only diagnostics used during 1976 that continued to prove useful were the external B-field probe and the side-on streak camera. Several new diagnostics have been added, and two of them were new developments. These diagnostics are briefly described in this section and most are shown schematically in Fig. VI-2.

1. End-On Framing Camera. Initially, a single-frame Beckman-Whitley camera was used in conjunction with an image intensifier (see Fig. VI-2). Two Corning Glass filters (#4-76, and #3-70) were required to reduce the atomic and molecular deuterium line radiation from the cold plasma in the ends of the discharge tube outside the compression coil.

Later, the single-frame camera was replaced with a multiframe Imacon camera. A 1-MHz framing plug-in was modified to frame at the rate of 6 per

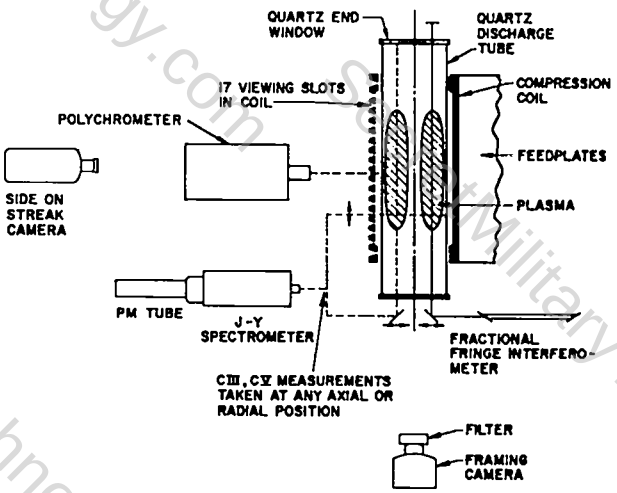

Fig. VI-2.
Diagnostic arrangement on FRX-A.

10 μs. The previous filters were replaced by more efficient filters.

2. Internal B-Field Probe. A thin-wall, 6.35-mm diam, stainless tube was positioned along the axis of the system (see Fig. VI-3) to house the internal field probe. The probe coil and an electrostatic shield were attached to the end of a solid-copper-shielded coax cable, and the whole probe structure was insulated. This probe assembly (identical to the external probe) was inserted into the stainless tube until the coil reached the desired axial position. To prevent a breakdown of the probe insulation, it was necessary to attach a series-tuned RLC network between the stainless tube and ground. This network damped a 40-kV transient that occurred during the initial breakdown of the preionized plasma.

3. J-Y Spectrometer. A quarter-meter J-Y spectrometer has been used in conjunction with an EMI 6256B photomultiplier to monitor the C III 2297-A and the C V 2271-A lines from the naturally occurring impurity. As shown in Fig. VI-2, the spectrometer is used to make shot-by-shot scans of the axial and radial plasma profiles. It is also used to monitor the total light of the C V line radiated from the same plasma location that is being monitored by the polychromator described in the next subsection.

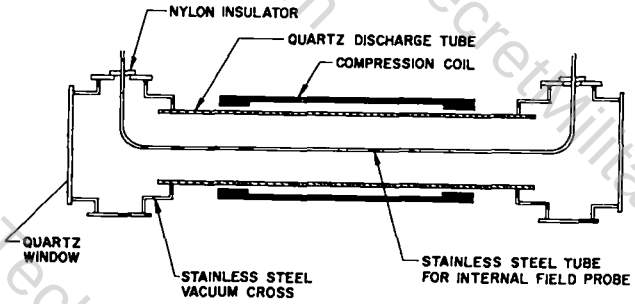

Fig. VI-3.
Axial cross section of the system showing the position of the stainless tube for the internal field probe.

4. Polychromator. A half-meter Jarrel-Ash monochromator has been used in developing a 7-channel polychromator to measure the Doppler broadening and shift of the C V 2271-A line. The seven channels produce the line shape as a function of time on a single shot. By moving the mirror shown in Fig. VI-4 on subsequent shots, various chords of the plasma can be scanned (1-cm steps, 1-cm resolution). If the plasma rotates as a rigid rotor, the component of velocity (or Doppler shift) along a given chord will be independent of the position along the chord. Hence, the line shape is undistorted so that accurate measurements of carbon rotation and temperature as a function of radius and time can be obtained.

The polychromator is very similar to one developed by Scott, et al.[2] This one uses a cylindrical quartz lens to increase the dispersion so that an array of seven 1P28/V1 photomultiplier tubes could be used as the detector. The entrance slit is adjusted to 40 μm by the usual micrometer adjustment as an optimum compromise between intensity and resolution. The exit slit, however, is fixed at 400 μm with a 440-μm-diameter quartz fiber cradled in the slit. This defocusing lens disperses the light so that when the tubes are positioned 10° apart (staggered about an average

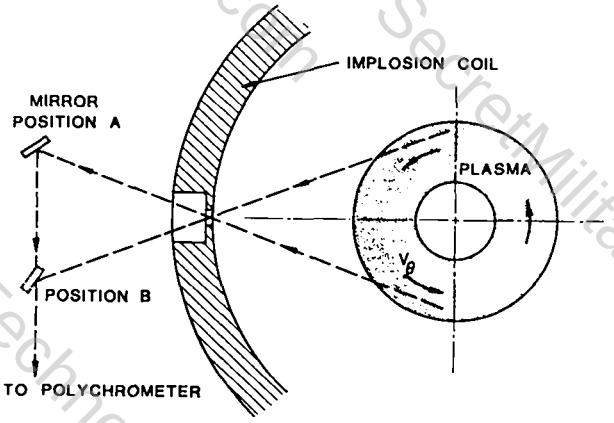

Fig. VI-4.
A transverse plasma cross section showing 2 of the 15 possible mirror postions for measuring ion temperature and rotation.

arc with a 12.4-cm radius) and when the grating is used in second order, the polychromator resolution is 0.355 A between channels. The angular blurring due to the finite f number of the monochromator is only 2.9°.

The plans are to feed all seven outputs to A/D converters and have a computer reduce the data. At present, the outputs are sequentially sampled every 2 μs by a multiplexer circuit designed by C. J. Buchenauer. The result is a marker pulse followed by a sequence of seven pulses, which plot out the shape of the C V line. This pattern is repeated every 2 μs during the plasma discharge as is shown in Fig. VI-5.

5. Feedback-Stabilized Fractional-Fringe Interferometer. The density measurements obtained from the fractional-fringe interferometer shown in Fig. VI-2 were not very useful because these axial measurements included the density of the cold plasma in the ends of the discharge tube. To avoid this problem, a double-pass, Michelson interferometer was designed by D. A. Platts to look transversely through the plasma diameter (see Fig. VI-6). The apparent problem of a small phase shift (< λ/8) for the 6328-A line (HeNe laser) was turned to an advantage by using feedback to stabilize the interferometer at the most sensitive phase position. The output signal is then proportional to the density.

The feedback amplifier and speaker-coil system, designed by C. J. Buchenauer, has a high-frequency cutoff of about 2 Hz. The higher frequency vibrations are damped by using a rigid, compact construction and by using acoustically absorbing materials around the beam paths and optical components.

A sample output of the device is shown in Fig. VI-7 along with the magnetic field trace. By comparing these traces, several effects are readily observable including the plasma formation by the ringing preionization field, the fast density increase during the implosion, and the slower increase during the axial compression phase. The sharp density spikes near the end of the plasma life are caused by the rotational m=2 instability discussed later in the report. The sag in the base line that is evident at the end of the plasma life is not yet understood, but it is under study. It does not occur if the machine is fired without gas so that no plasma is produced.

6. Pressure Probe. A pressure probe has been inserted into the end of the system through a ball joint so that the pressure of the plasma leaving axially from the compression coil region can be measured as a function of radial and axial

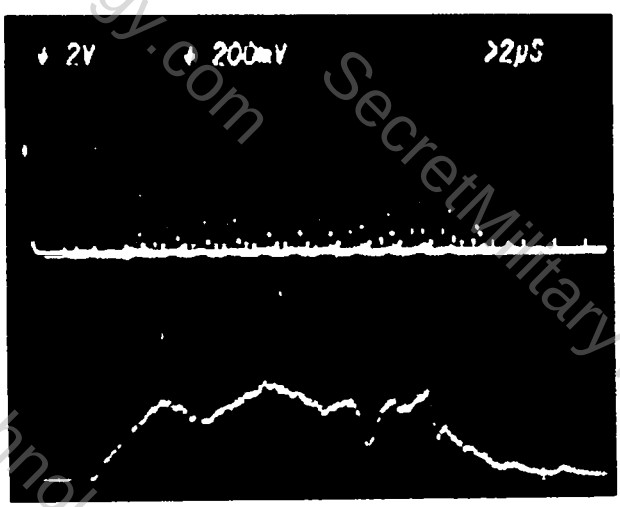

Fig. VI-5.
A comparison of the multiplexed polychromator output (top trace) and the J-Y spectrometer output (bottom trace) for a chord at a 3-cm radius.

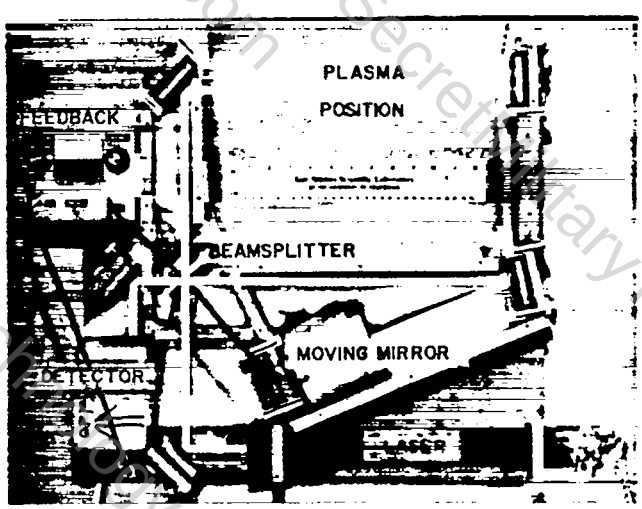

Fig. VI-6.
Transverse Michelson interferometer design.

position. The probe was designed and constructed by T. M. York, based on previous work,[3] as well as some initial tests on the system with existing probes. The final design, shown in Fig. VI-8(a), uses a 2-mm-diam, 0.5-mm-thick piezoelectric crystal. The entire probe is housed in an 8-mm-diam quartz tube and the front is capped with a 0.25-mm-thick quartz disc.

The probe output is sent through a line driver for impedance matching. A test trace from a shock tube is shown in Fig. VI-8(b). The signal shows the step-function response of the probe. Probe calibration indicates a sensitivity of 0.41 V/atm.

C. EXPERIMENTAL RESULTS

Three major topics have been addressed during 1977. The first topic is the accidentally discovered connection between impurities and two modes of plasma behavior, which are typified by the disparate results of Bodin and Newton[4] and Eberhagen and Grossmann.[5] The second topic is the attempted duplication of the 50-μs of stable confinement reported by Kurtmullaev et al.[6] The third topic is the diagnostic study of the rotational m=2 instability, which presently limits

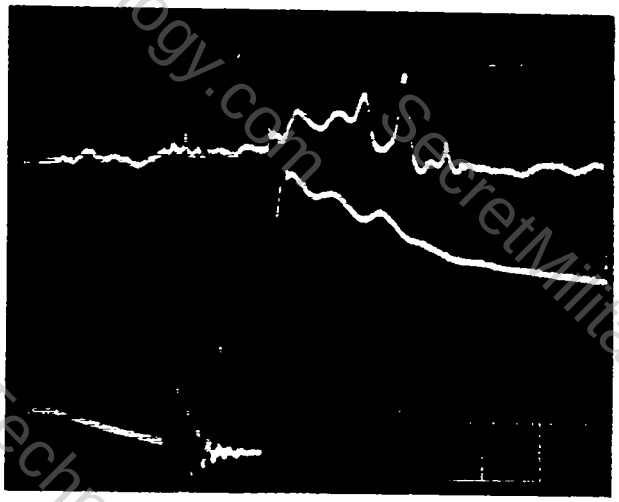

Fig. VI-7.
A comparison of the temporal behavior of the transverse line density from the fractional-fringe interferometer (top trace) with the external magnetic field (bottom trace).

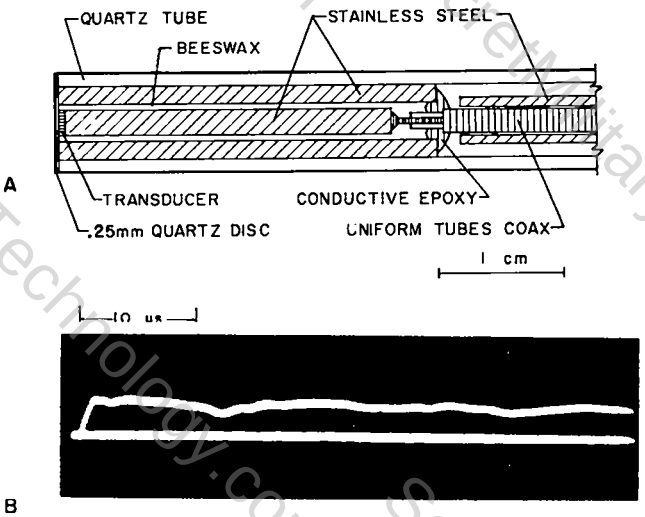

Fig. VI-8.
Pressure probe (a) cross section, and (b) shock tube response.

the lifetime of the RFC. The experimental results associated with these three subjects are summarized in this section.

1. Impurity Effects. Two distinct modes of plasma behavior have been observed in FRX-A. The only two parameters that appear to determine the mode are vacuum cleanliness and the power input to the plasma. This effect is shown qualitatively by the graph in Fig. VI-9. The curve represents the sharp boundary between the "clean mode" and "dirty mode" behavior.

Initially FRX-A was constrained to operate in the dirty mode because of limitations in the vacuum system and main bank. The bearings on the turbine vacuum pump were changed from oil lubrication to grease in order to improve the reliability. This modification also lowered the base pressure from about 4×10^{-7} to 5×10^{-8} torr. As a result, the clean mode of operation could be achieved at 19.5 kV on the main bank (20 kV full charge), but the dirty mode was produced at 19.0 kV.

This discovery of the clean mode motivated a series of improvements to the vacuum system and the main bank. These modifications decreased the

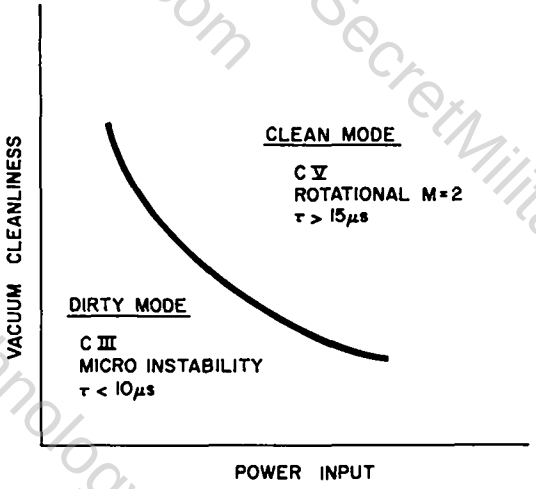

Fig. VI-9.
Effect of impurities on plasma behavior.

critical voltage that separates the modes from the 19.2 kV to less than 10 kV.

The horizontal axis is labeled "power input," instead of "bank voltage," because the capacitance and inductance of the system have been varied to demonstrate that the product $B\dot{B}$ is the important parameter. The boundary between the modes cannot only be traversed "horizontally" by varying $B\dot{B}$ (usually by the voltage) but also "vertically." The transition from dirty to clean mode is observed each day during the first few clean-up shots. Unfortunately, the lack of a gas analyzer prevents the quantitative labeling of the axes.

The differences between the clean and dirty modes are partly summarized in Fig. VI-9. The behavior of the C III and C V radiation following the implosion indicates that $T_e \sim 10$-30 eV in the dirty mode and 70-150 eV in the clean mode. This large jump in T_e arising from small changes in $B\dot{B}$ is indicative that an impurity radiation barrier may play an important role.

The other major difference between the modes is that the RFC is terminated much sooner in the dirty mode, and the field annihilation is caused by an unknown instability. This mode is called a "microinstability" in Fig. VI-9 simply because no macroscopic distortion of the plasma is observed, and therefore, the wavelength is probably small compared with the plasma size. In contrast, the RFC destruction in the clean mode is caused by a rotational m=2 instability at later times. The side-on-streak and end-on-framing camera pictures in Fig. VI-10 illustrate these differences. Note the sudden annihilation of the central hole in the dirty mode followed immediately by increased plasma luminosity and loss of axial confinement. Note also the effect of the m=2 mode on axial confinement in the clean mode.

There are striking similarities between the plasma behavior indicated in Fig. VI-10 and the behavior observed in other experiments. The dirty mode is very similar to the results of Bodin and Newton,[4] and the majority of the other early experiments (before 1964). The clean mode results are almost identical with those reported by Eberhagen and Grossman.[5] Thus, these results from FRX-A help to provide a link between the long-lived results of more recent experiments[5,6] compared with earlier experiments. Although a correlation with impurity radiation barriers is indicated, some difficult questions still remain:

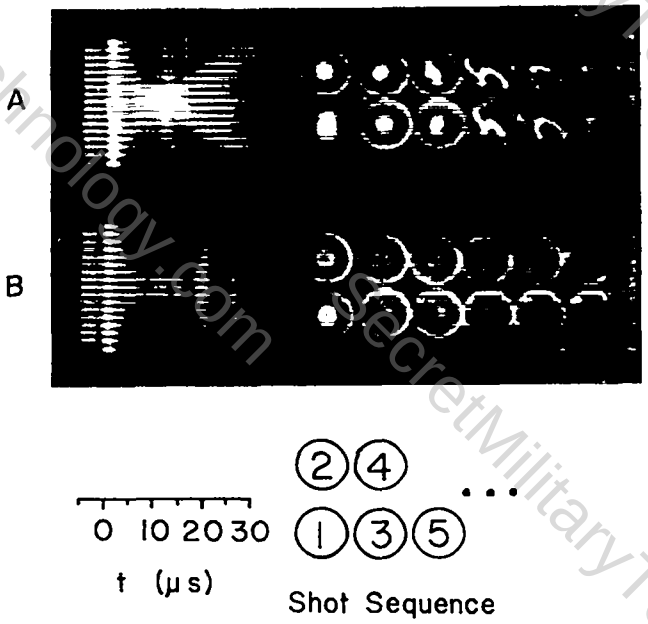

Fig. VI-10.
Side-on-streak and end-on-framing pictures illustrating the difference between (a) the dirty mode, and (b) the clean mode. The time of the implosion corresponds to t=0. The framing pictures were taken at 1.6-μs intervals with first frame at t=2 μs.

(1) What is the "microinstability" and what is its connection with radiation barriers? (2) Why did Eberhagen observe clean mode behavior with $T_e \sim 60$ eV, and Bodin observe dirty mode behavior at $T_e \sim 150$ eV?

2. Attempted Duplication of Kurtmullaev's Results. The FRX-A system operates in the same filling pressure and B-field range as reported by Kurtmullaev[6] and has a very similar main coil and vacuum chamber geometry. The details of the preionization and bias fields were not described in the paper. The major differences between the Kurtmullaev system and FRX-A appeared to be: (1) the multipole barrier field, (2) the axial-implosion-coil system, and (3) the operation of the main bank in the "second-half-cycle" mode.

In spite of these similarities, the resulting plasma properties are quite different as indicated in Table VI-I. The large difference in the ratio of T_e/T_i is consistent with theta-pinch and belt-pinch experiments at low density ($< 10^{14}$cm^{-3}). However, the low plasma densities are inconsistent with the filling pressures quoted in Ref. 6 unless the percentage of ionization is low.

Recent personal communication between Kurtmullaev and A. R. Sherwood resulted in new information. The fill pressure is now claimed to be less than in Ref. 6 (< 1 mtorr), and the preionization is essentially 100%. This high degree of preionization is achieved by either a Z-pinch PI or by two successive bursts of theta-pinch PI, one at the beginning of the bias field and one just before implosion. Thus two additional differences between FRX-A and the Kurtmullaev system are now known.

TABLE VI-I.

COMPARISON OF REVERSED-FIELD PLASMA PARAMETERS

SYSTEM	ℓ cm	R cm	Δ cm	N 10^{13}cm^{-3}	T_i eV	T_e eV	τ μs	CAUSE OF TERMINATION
EBERHAGEN: REGULAR	20	1.3-1.7	0.5-1	30-80	35-80	35-80	25	M=2
COAXIAL	50	18	2	5	15-25	15-25	30	TEARING
KURTMULLAEV	35	7	5	0.1	100	1000	50	L/R DECAY
FRX-A (CLEAN MODE)	35	2.5-6.5	2-3	1	150-400	100	25	M=2
NRL-RED SYSTEM	40	4	2	10		4-6	5	DIFFUSION

The initial attempt to duplicate the Kurtmullaev results were performed before this latest information was known. This attempt consisted of removing two of the three originally known differences listed above. A hexapole barrier field was added to the system and the system was modified to operate second-half-cycle.

Numerous experiments were performed to exhaust the possible combinations of first- or second-half-cycle operation with a variety of barrier-field conditions. The temporal behavior of the barrier field was varied between a single sinusoidal pulse of 30-μs duration to a typical crowbarred waveform, depending on the timing of the crowbar. The timing of the barrier field was varied from the beginning of the bias field to after the implosion, and the amplitude was varied from zero to 400 G at a radius of 7 cm (950 G at 9 cm).

In general, only minor differences were observed in the plasma behavior. The major effect was to increase the optimum fill pressure (< 40%) for maximum plasma lifetime. The strength of the effect increased according to the strength of the barrier field at the time of implosion. At the optimum pressure the RFC life time was still 20-25 μs and the termination was still caused by the rotational m=2 instability. The end-on framing camera also showed a hexagonal pattern in the "halo" around the main plasma, but the main plasma remained circular until the onset of the m=2 instability.

No more detailed results are given here because of the lack of positive results. This lack of success may be associated with either the differences that still exist between the experiments or because of the comparatively small size of the barrier field. Under the present design, the barrier field cannot be increased substantially without the risk of crushing the quartz vacuum chamber that supports the conductors.

The modification of the barrier field and the removal of the other differences are being considered; however, each one requires a substantial amount of effort. For example, the lowering of the filling pressure would require a major modification of the preionization system and the development of new diagnostics compatible with the lower density. In addition, there is not much interest in a plasma with as high a ratio of T_e/T_i as is obtained at these low densities. Future attempts to duplicate the Kurtmullaev experiment will be made only if the expected gain in understanding warrants the required effort. The focus of the present research is to understand, and hopefully control, the rotational m=2 instability.

3. Rotational m=2 Instability. The recent theoretical work on rotational instabilities, including finite-Larmor-radius (FLR) effects, has accurately predicted the m=1 mode (wobble) in the Scylla IV-P experiment.[7] J. P. Freidberg is modifying the code to study the RFC. The diagnostic study described in this section will be correlated with this theory in an effort to understand the m=2 instability.

The theory assumes that the temperature is independent of radius and that the rotation is rigid rotor. This allows the equilibrium ion equation to be written in the following form.

$$\frac{E_r}{rB_Z} + \frac{V_{\theta i}}{B_Z} = \frac{T_i}{ZerB_Z}\frac{1}{n_i}\frac{\partial n_i}{\partial r} \quad . \tag{1}$$

where each term is an angular frequency independent of radius.

$$-\Omega_E + \Omega = -\Omega^* \quad . \tag{2}$$

The rigid rotor profiles are given by

$$B = B_\infty \tanh K \left(\frac{r^2}{R^2} - 1\right) \quad \text{and}$$
$$n = n_m \operatorname{sech}^2 K \left(\frac{r^2}{R^2} - 1\right) \quad , \tag{3}$$

where

$$K \equiv \tanh^{-1}\left(\frac{B_i}{B_\infty}\right)$$
$$B_i \equiv -B(r=0) \text{ for } B(r=0) < 0$$
$$B_\infty \equiv B(r \gg R) \tag{4}$$
$$n_m \equiv n(r=R) \quad ,$$

where R is the major toroidal radius. The parameter K can also be shown to be approximately equal to half the toroidal aspect ratio. If an effective minor radius a is defined by

$$n_m \, 2\pi R(2a) \equiv \int_0^\infty n \, 2\pi r \, dr, \tag{5}$$

then

$$\frac{R}{a} = \frac{4K}{1 + \tanh K} \quad . \tag{6}$$

Thus the choice of two parameters R and K completely determine the profiles including aspect ratio and degree of field reversal. Density profiles are plotted in Fig. VI-11 for several values of the aspect ratio.

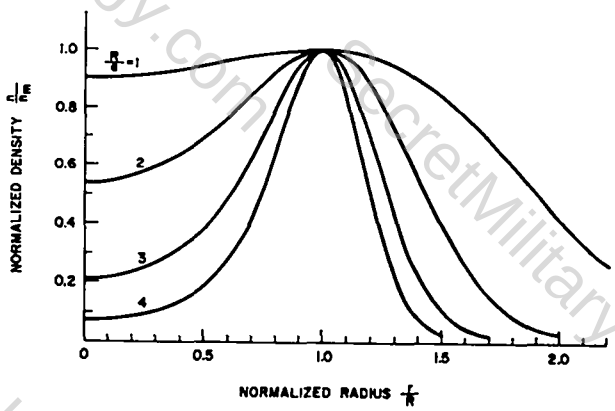

Fig. VI-11.
Rigid rotor density profiles.

The stability analysis for an ordinary theta pinch[7] for $\beta=1$ indicates that the plasma is stable to the m=2 for rotations given by

$$-0.30 < \alpha < 1.45 \quad , \tag{7}$$

where $\alpha = -\Omega / \Omega^*$. For the RFC rigid rotor profile, the pressure gradient drift velocity is given by

$$\Omega^* = \frac{4K}{B_\infty R^2 Z} \frac{kT_i}{e} \quad . \tag{8}$$

In addition, the theory predicts that the real part of the m=2 mode frequency at the critical $\alpha = 1.45$ is

$$\omega_r \simeq -\Omega^* \quad . \tag{9}$$

Although these critical values of α and ω_r are for a normal theta pinch, it is expected that qualitatively similar behavior will exist for the RFC.

The following measurements have been made to characterize the plasma in general and to determine the values of ω_r, Ω, and Ω^*.

a. ω_r. The critical value of ω_r can be obtained from the fractional-fringe interferometer, J-Y spectrometer, side-on-streak, or end-on-framing pictures. However, the end-on pictures give the best measure of ω_r at the onset of the m=2. The major inaccuracy of this measurement arises from the very rapid growth of the mode. The ellipticity grows from a barely detectable value ($\sim$1.2) to about 4 in a time corresponding to half a revolution, $t=\pi\,\omega_r^{-1}$ (see Fig. VI-10(b)). This corresponds to a growth rate $\sigma \simeq \omega_r/2$, which is so fast that the mode becomes nonlinear in the time needed to accurately determine the value of ω_r. From the evidence so far, it does not appear that ω_r changes more than 50% during this time, so that an approximate value can be obtained from the duration of the first period from any of the diagnostics mentioned above. A complete parametric study has not been made, but ω_r normally increases with increasing B and the range $8 \times 10^5 < \omega_r < 2 \times 10^6$ has been observed.

b. Ω. The rotational velocity of the C V ions has been measured by the polychromator described above. For ion temperatures $T_i < 300$ eV, the rotation appears to be rigid rotor and the temperature is independent of radius. Thus the experiment satisfies the assumptions of the previously described theory. The results consistently show that the C V does not rotate significantly for the first 8-10 μs, but then it accelerates until the onset of the m=2 instability.

Within the accuracy of available measurements, all of the results can be summarized by the normalized rotation plotted in Fig. VI-12. This behavior is in qualitative agreement with theory because the critical velocity for instability scales with Ω^*. However, the theoretical value of the normalized critical rotation given by Eq. (7) is $\alpha_c \simeq 1.45$ instead of the observed $\alpha_c \sim 0.4$. This numerical difference may be associated with the difference between the RFC and the standard theta pinch, or it might be associated with a possible difference in rotational velocity between the C V and deuterium. As stated above, the code is being modified to handle the RFC to remove that possible source discrepancy, and the possible difference in rotational velocities is briefly discussed here.

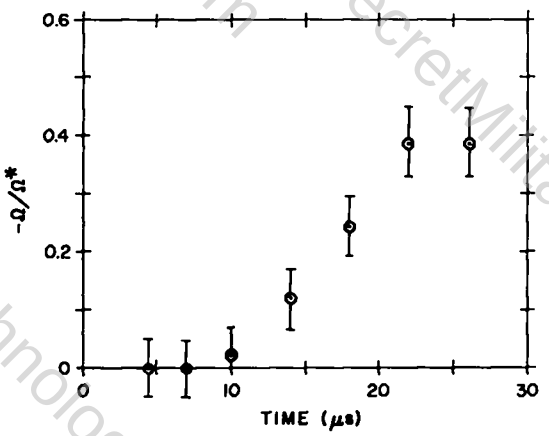

Fig. VI-12.
Normalized C V rotation as a function of time.

The process of rotational equilibration between impurities and deuterium is more complex than the thermalization process. The azimuthal drag force arising from a difference in the rotational velocity causes the impurity to drift radially in the $-\nabla B^2$ direction. This drift continues until the narrowing density profile of the impurity compensates for the higher Z, i.e., until the Ω^* of the impurity and the deuterium are equal (see Eq. (1) and Eq. (2)).

The relaxation time has been calculated by assuming that the drag force is proportional to the ratio of the azimuthal velocity difference to the classical slowing-down time, $(v_{\theta D}-v_{\theta C})/\tau_s$, and by assuming that initially the C V and D^+ have the same rigid rotor profile. The result yields

$$\tau_r = 1.39 \times 10^{-2} \left(\frac{2}{M_D}\right)^{1/2} \frac{T_D^{3/2} \left(1 + \frac{T_e}{T_D}\right) \delta^2}{\left(1 + \frac{M_D}{M_C}\right) Z_C^{1/2} \left(Z_C^{1/2} + 1\right) \ln\Lambda} , \quad (10)$$

where τ_r is in μs, M in amu, T in eV, and δ in cm. The density gradient scale length δ is essentially 1.18 a (the minor plasma radius) for the aspect ratios of interest (see Fig. VI-11). Using the M and Z values of C V and D^+ yields the following comparison between τ_r and the energy equilibration time τ_E.

$$\frac{\tau_r}{\tau_E} = 0.094 \left(\frac{\delta}{\rho_D}\right)^2 \simeq 0.13 \left(\frac{a}{\rho_D}\right)^2 . \quad (11)$$

The ratio of these relaxation times is approximately 1 for the observed plasmas (ρ_D is the deuterium thermal gyro radius in the external B field).

The calculated values of τ_E have been confirmed experimentally. Polychromator data like Fig. VI-5 show that the C V temperature is independent of time when T < 300 eV. This is consistent with the calculated τ_E < 4 μs because data cannot be obtained from the polychromator for about 5 μs after the implosion (because of a combination of rapid light increase and the sampling technique of the multiplexer). When T > 300 eV the expected decrease of line width is observed at early times.

Since τ_E is known to be short compared with the plasma lifetime, Eq. (11) indicates that the C V should be rotating at the same speed as the D^+. In other words, the polychromator measurement should yield the correct value of the critical Ω.

c. Ω^*. It is apparent from Eq. (8) that four independent parameters are necessary to evaluate Ω^*, i.e., T_i, B_∞, R, and K. The ion temperature can be determined within ±40 eV by the polychromator measurements described above. Except for the previously mentioned C V equilibration effects, the ion temperature is independent of time and radius. The magnitude of T_i scales in the expected ways with B and the filling pressure and the observed range of values is 150 <T_i <400 eV.

The value of B_∞ is measured by a calibrated probe located outside the quartz tube at r=11 cm. Because of the finite plasma length, this value of B may be slightly smaller than the field just outside the plasma. Most of the data have been taken for values of B between 4 and 6 kG.

With the existing diagnostics, the best method of determining the major radius R is from the end-on-framing pictures. If the luminosity is assumed proportional to some power of n, then R can normally be determined within less than 1 cm error.

The most difficult parameter to determine is the profile parameter K. A rough estimate of the aspect ratio R/a can be made from the end-on photographs, but the nonlinearity of both the film and the luminosity dependence on the density and temperature prevent an accurate determination. The result of such an estimate yields 2 < R/a < 3, or 0.8 < K < 1.4 by using Eq. (6).

The definition of K given by Eq. (4) provides another method of determining K. The ratio of B_i/B_∞ is usually about 0.85 as determined by the internal probe described above. The stainless tube that houses this probe was not left in the system after these measurements were made because the hot plasma boiled substantial material off of the tube resulting in a premature loss of the RFC. Thus, the internal field measurements

were only taken for a limited number of plasma conditions. However, the typical value of 0.85 corresponds to K=1.26 and R/a=2.8, which supports the values obtained from the end-on pictures (see Fig. VI-10 and Fig. VI-11).

The profile was also investigated by measuring the intensity of the C V 2271-A line as a function of radius with the J-Y spectrometer (see Fig. VI-2). The results for two different bias fields, but the same B_∞, are plotted in Fig. VI-13. These curves appear to correspond with an aspect ratio $R/a \sim 1.3$ instead of the 2 to 3 range obtained by visible light and internal field measurement. The C V profile may appear artificially broad because of a slightly higher T_e in the sheath region compared with the peak density region. This slightly higher T_e could result from the ohmic heating in the sheath. Since T_e is much less than the 305 eV needed to excite the 2271-A line, slight increases in T_e would result in large increases in light intensity. For example, if $T_e(r=R)=100$ eV and $T_e(r=R\pm a)=130$ eV, the fraction of the electrons capable of excitation would be 10% at r=R and 20% at $r=R\pm a$, which is more than sufficient to explain the broader profile in Fig. VI-13.

In spite of the general agreement between these three profile measurements, there is still a substantial uncertainty in the value of K. Some other diagnostic such as Thomson scattering is needed to accurately determine the radial profile.

The probable range of Ω^* using compatible combinations of the parameters T_i, B_∞, R, and K is $7 \times 10^5 < \Omega^* < 4 \times 10^6$. This is essentially the same range as the observed critical value of ω_r. Thus the observed values of ω_r/Ω^* are compatible with Eq. (9), even though it is for the standard theta-pinch model.

d. Plasma loss. When the measured values of B_∞, T_i, and T_e are used in the pressure balance relation, the resulting peak density n_m is 2 to 3 times smaller than would be obtained if all the initial D_2 fill inside the implosion coil were compressed to the size indicated by the side-on-streak camera and the end-on-framing camera. The uncertainties in the radial profile are not enough to explain it, and the axial profile obtained from streak photographs is

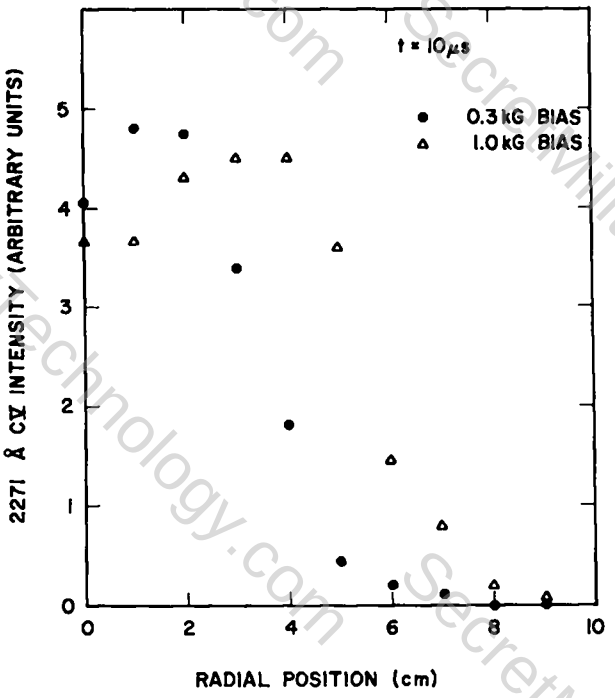

Fig. VI-13.
Radial profiles of the C V 2271-A radiation.

confirmed by C V scans such as the ones shown in Fig. VI-14.

Since C V is only present in relatively hot plasmas ($T_e > 70$ eV), the C V profiles would not include cold plasma that might exist. To determine whether substantial density exists in the form of cold plasma, C III scans were made. No detectable C III (2297-A) radiation was observed anywhere inside the coil region after the implosion was complete. Similar radial scans indicated substantial C III radiation originating from the ends of the discharge tube outside the coil region.

When the transverse fractional-fringe interferometer was developed, line density measurements were made through a plasma diameter at the mid-plane of the system (z=0). The results confirmed the low density implied by pressure balance. For a 5-mtorr fill, the peak density is about 1.5×10^{15} when $R \sim 4$ cm. Unfortunately, an axial scan with the interferometer has not yet been made to further confirm the axial profile.

To better understand this apparent loss of plasma, a pressure probe has been used to measure the flow of plasma out of the end of the system.

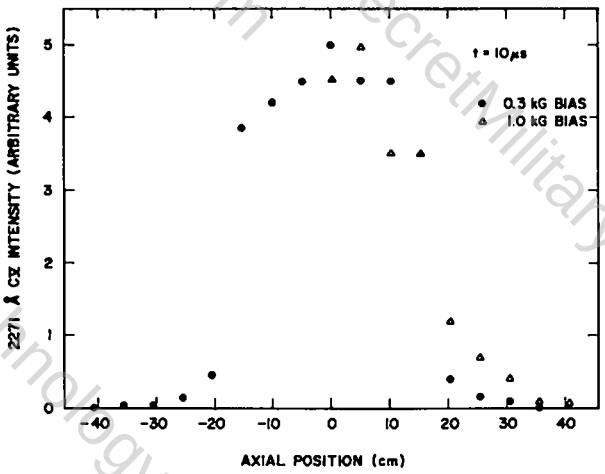

Fig. VI-14.
Axial profile of the C V 2271-A radiation.

A typical trace with the probe on axis and 8 cm from the end of the coil is shown in Fig. VI-15. The slight sag in the base line is caused by a plasma-generated acceleration or thermal strain of the probe. The pressure associated with the PI and the fast 2-μs spike at the time of implosion is observed at all radii. However, the long ($\sim$10 μs) pressure signal just following the implosion, and the second long burst following the m=2 breakup of the RFC are only observed for $r < 3$ cm if the probe is within 6 cm of the coil. These jets of plasma spread radially and hit the wall about 15 cm from the coil.

Preliminary time-of-flight measurements indicate that the first long pressure burst is caused by a plasma of comparable temperature and slightly larger mass than that which causes the second burst. It also appears that the initial loss occurs during the axial contraction phase of the plasma. Even though these pressure measurements help explain the low plasma density, they apparently conflict with the density increase observed in Fig. VI-7 during axial contraction. One possible explanation is that ionization is taking place during the axial contraction process. More detailed density and pressure probe studies should help to determine the origin of the plasma loss and resolve the apparent conflict with the density measurement.

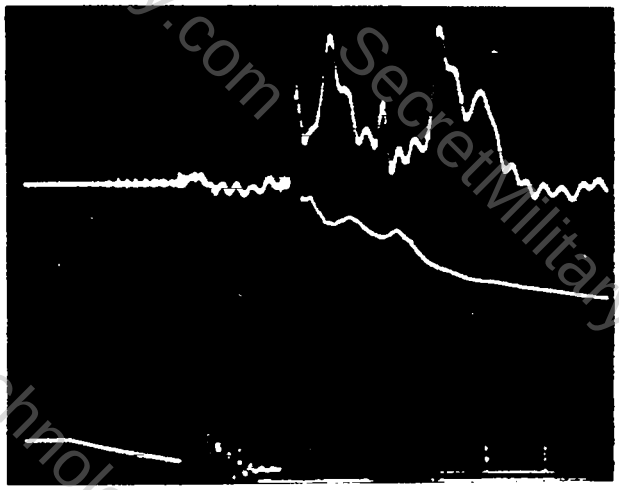

Fig. VI-15.
A comparison of the pressure probe signal obtained on axis 8 cm from the end of the coil (top trace) and the external magnetic field (bottom trace).

D. CONCLUSIONS AND DIRECTION OF FUTURE WORK

A radiation barrier appears to divide the plasma behavior into two distinct modes of operation. This result provides a link between the early short-lived experiments[4] and the recent longer lived experiments.[5,6] The "microinstability" that terminates the RFC in the short-lived dirty mode needs to be identified and studied.

The longer lived clean mode is typified by almost constant plasma pressure being confined for up to 25 μs, when an m=2 rotational instability destroys the RFC. The typical parameters of $n \sim 1.5 \times 10^{15}$ cm^{13}, $T_e \sim 100$ eV, and $150 < T_i < 400$ eV correspond to a sound speed $C_s \sim 12$ cm/μs. Thus even with the instability, the plasma is confined for 6 times longer than it would be in an open-ended system.

More theoretical work is needed to explain the absence of tearing and MHD instabilities. In particular the recent work on the tearing mode, which has included the effects of diffusion,[8] flow,[9,10] and other nonlinear effects,[11,12] need to be examined in light of the FRX-A results. Most of these effects tend to be stabilizing. The MHD modes also need to be studied. The sausage mode is stabilized by the appropriate diffuse profile, which may be satisfied by the rigid rotor profile. The kink mode may have a substantially reduced growth rate due to the highly elongated

cross section of the torus (see Fig. VI-1). It can easily be shown that an infinitely long torus is neutrally stable to the kink. Thus the geometry-modified growth rate may be too slow to see during the 25-μs lifetime. FLR effects may also be important. It is also possible that the motion associated with the axial contraction, bouncing, and/or rotation may have a stabilizing effect. All of these possibilities need careful theoretical consideration. Experimental investigation may become more practical in the future if the stable plasma lifetime can be extended long enough to observe these modes.

The major thrust of the present research is to study and, hopefully, control the m=2 instability. The existing theory[7] for rotational modes is only valid for normal theta-pinch columns. It is being modified to describe the RFC. The two major deficiencies in the diagnostics are the lack of accurate information about the density and electron temperature profiles. More careful use of existing diagnostics and the eventual addition of Thomson scattering should solve the problem. This correlation between theory and experiment is necessary to clearly identify the mode.

If the mode is the rotational m=2, as it now appears, then it can be stabilized by preventing the plasma from accelerating past the critical velocity. At least two plausible explanations exist for the observed angular acceleration. One, due to Eberhagen and Grossmann,[5] relies on plasma leaving the confined region carrying away angular momentum as a result of diffusing across the B field in the presence of a radial E field. The reaction force causes the confined plasma to spin in the opposite direction. The second argument, due to A. H. Boozer, is very similar to the source of rotation in a standard theta pinch. Line-tying of the open field lines shorts out the radial electric field (see Eq. (1)) causing the plasma on open field lines to rotate as in a standard theta pinch. This rotating plasma then causes the confined plasma to rotate by ion viscosity. More careful theoretical consideration and diagnostic measurements are needed to determine whether either of these models is correct.

If either model were correct, increased particle confinement would delay the onset of the instability. For this reason, a careful analysis of the end loss, observed by the pressure probe, is imperative. As previously mentioned, this loss may result from poor preionization or from some anomalous process that allows particle loss while the plasma is contracting to its equilibrium length. The obvious remedies are to improve the PI system if that is at fault or add axial implosion coils to drive the plasma more rapidly toward its equilibrium shape. Both of these changes would increase the similarity between the FRX systems and the Kurtmullaev experiment, thus increasing the motivation to make these changes.

If the line-tying argument is correct, then modifying the boundary conditions for the open-field lines by some type of end plug may limit the rotation to the stable regime. This approach was successfully used in Scylla IV-P to stabilize the related m=1 wobble,[13] and will be investigated in FRX-A.

REFERENCES

1. "LASL Controlled Thermonuclear Research Program, January-December 1976." K. S. Thomas, Compiler, Los Alamos Scientific Laboratory report LA-7082-PR (March 1978).

2. F. R. Scott, E. N. Ducas, and R. G. Tuckfield, Jr., Rev. Sci. Instrum. 33, 1001 (1962).

3. T. M. York, Rev. Sci. Instrum. 41, 519 (1970).

4. H. A. B. Bodin and A. A. Newton, Phys. Fluids 6, 1338 (1963).

5. A. Eberhagen and W. Grossman, Z. Phys. 248, 130 (1971).

6. A.G. Es'kov, O.A. Zolotovsky, A.G. Kalygin, R.Kh. Kurtmullaev, Ya.N. Laukhin, A.I. Malyutin, A.P. Proshletsov, V.N. Semenov, "Plasma Confinement in a Pulsed System with a Compact Toroidal Configuration," in Proc. Seventh European Conf. Controlled Fusion and Plasma Physics, Lausanne, 1975 (CRPP, 1975) Vol. I, p. 55.

7. J. P. Freidberg and L. D. Pearlstein, to be published in Phys. Fluids.

8. D. Dobrott, S. C. Prager, and J. B. Taylor, Phys. Fluids 20, 1850 (1977).

9. A. I. Shestakov and J. Killeen, "The Effect of Equilibrium Flow on the Resistive Tearing Mode," Bull. Am. Phys. Soc. 22, 1156 (1977).

10. A. Kalek, unpublished numerical calculations including plasma rotation.

11. P. N. Hu and H. Grad, "Nonlinear Analytic Tearing Evolution," Bull. Am. Phys. Soc. 22, 1136 (1977).

12. Y. Y. Lau, personal communication.

13. R. J. Commisso, C. A. Ekdahl, K. B. Freese, K. F. McKenna, and W. E. Quinn, "Solid-End-Plug Experiment on a Theta Pinch," Phys. Rev. Lett. 39, 137 (1977).

VII. IMPLOSION HEATING EXPERIMENT (IHX)

T. Jarboe, I. Henins, A. Sherwood, C. Swannack

A. INTRODUCTION

The Implosion Heating Experiment was a 40-cm-diameter, 1-meter-long high-voltage linear theta pinch designed to study the implosion phase of conventional theta-pinch heating. The implosion coil was fed at four places by low-impedance pulse-forming networks (PFNs) designed to produce a flat-topped current pulse. The effective impedance of the four PFNs was approximately equal to that of the imploding plasma, thus the circuit behavior was strongly coupled to the plasma dynamics. The PFN circuits and other details of the apparatus have been described previously.[1,2] This experiment was terminated near the end of the year in favor of the Fast Liner Experiment.

The experiment operated reliably in 1977 with no major changes in the hardware. The results of the density measurements made with a four-beam fractional-fringe interferometer have been presented previously.[3] This interferometer was used in almost all data-taking to check consistency of machine operation. The first part of the year was spent finishing a more detailed measurement of the magnetic field as a function of time and radius using magnetic probes and Faraday rotation. Detailed descriptions of the probe and Faraday rotation apparatus are available elsewhere[3,4] and will not be discussed here. The additional information about the magnetic field improves but does not substantially change the results which are shown in Ref. 3. The major part of the year was spent taking temperature and density data using Thomson scattering at four radial positions. These radial positions are R = 16, 12, 8, and 4.6 cm, where R = 0 corresponds to the axis of the theta pinch. The operating conditions for most of these data correspond to a flat-topped 6.5-kG driving field and 7.0-mT fill pressure. We also took data with filling pressures of 3.5 mT and 14 mT, but only at R = 12 cm.

The Thomson scattering apparatus was designed such that the laser beam was parallel to the axis of the theta-pinch coil with the viewing angle about 10° off the beam. The laser beam could enter from either end of the vacuum chamber, thus allowing measurements of either forward or back scattering. In our case, near-angle scattering had some advantages over 90° scattering. For example, it was possible to use a viewing dump to help eliminate stray light. In fact, we were able to measure Rayleigh scattering from N_2, and thus we were able to make absolute density measurements. Also, the small angle between the laser beam and the viewing system allowed us to measure both $T_{e\parallel}$ and $T_{e\perp}$ depending on whether we did forward or back scattering, respectively. Finally, we did not have to modify the driving coil for the viewing optics or the laser input and we were able to use good quality viewing optics.

The scattering volume was about 1 mm in diameter and 40 mm long and it was located at the midplane of the theta pinch. The light source used for this scattering measurement was a Korad K1500 ruby laser. The beam was expanded to about 35 mm and focused with a 1.2-meter focal length lens system to give a focal spot of less than 1 mm in diameter. The pulse width (full width at half max) was about 20 ns. Since electron temperatures in excess of 1 keV have been measured on lower density implosion heating experiments,[5] the polychrometer was designed to measure electron temperatures from 2 eV to 2 keV for $T_\parallel$ and from 250 eV to 250 keV for $T_\perp$. This was an adequate design because for temperatures less than 250 eV $T_\perp$ should be nearly equal to $T_\parallel$ at densities on the order of $10^{15}/cm^3$. To achieve this large range of temperatures we used 10 channels of detectors. As it turned out only the first eight channels were used and maximum temperatures (both $T_\perp$ and $T_\parallel$) of around 300 eV were observed. The ratio of each channel width to its difference from the laser frequency was about 1:3. The background light was fairly large in the wider channels and was changing rapidly as the sheath went by, but fortunately it was quite repeatable from shot to shot. Because of this large amplitude fluctuation it was not adequate to simply subtract the light level which was present before the laser was fired to account for the background. Instead it was necessary to observe the discharge without firing

the laser to measure the ratio of the plasma light at the time of the laser pulse (if the laser were fired) to that which was present 70 ns earlier. This ratio was then used to determine the background level during the scattering time from the light level measured earlier. The gates for the measurement of the background and laser pulse were each 70 ns wide. The jitter of the laser was only about 10 ns, so the gates were triggered at a set time after a signal was sent to Q-switch the ruby laser. However, the time of arrival of the peak of the signal from the laser output was compared with the timing of the gate on each shot to check that the light signal appeared near the center of the gate.

The results of the density measurements from Thomson scattering at R = 8 cm are shown in Fig. VII-1. These data are for the 7.0-mT fill pressure condition. The solid curve is the density as measured by the interferometer, assuming a constant density along the 90-cm path of the measurement. The two methods agree to within experimental errors, but the density from scattering data appears somewhat higher. It may be that the density in the center of the theta pinch is higher than at the ends. Had time allowed, this possibility would have been checked by doing scattering measurements out near the ends of the theta pinch. At 16 and 4.6 cm Rayleigh scattering was not done but the shape and timing of the density deduced from the Thomson scattering agree very well with the interferometer data at these positions.

The temperature data are shown in Fig. VII-2 for R = 16-, 12-, 8-, and 4.6-cm positions. The temperatures were deduced in the usual manner by finding the least squares fit of a Gaussian function to the time-integrated signal collected in each channel. The large variations seen in the data are mostly due to shot-to-shot variations in the measurement. Where the temperature is a rapidly changing function of time a small variation in the time of arrival of the sheath could account for some of the variations in temperature and density. It could also be that the sheath region has macroscopic inhomogeneities which could give a scatter in temperature and density. There

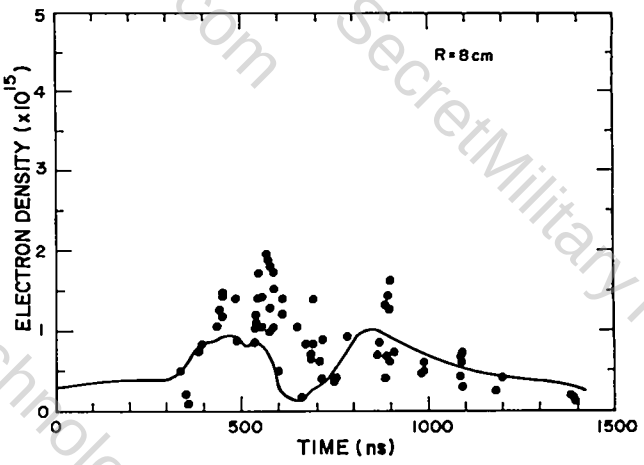

Fig. VII-1.
Thomson scattering density measurements at R=8 cm. The solid curve is the interferometric density measurement at the same radius.

are also some shot-to-shot differences in the density as measured by the interferometer, but these variations are not nearly as large. This could be a consequence of the larger volume sampled (2-mm diameter and 900-mm length). All of the temperature data shown here fit a Gaussian with a normalized rms deviation (NRD) of less than 0.15. NRD is given by the following expression:

$$\mathrm{NRD} \equiv \frac{1}{F(o)} \sqrt{\frac{\sum_{n=1}^{N} \left[F(x_n) - S_n\right]^2}{N}} ,$$

where F(x) is the Gaussian function that is used in the fit, x is the frequency shift from the laser frequency, S_n is the signal of the n^{th} channel centered at x_n, and N is the number of channels used in the fit. Figure VII-3 shows a fit when NRD = 0.080.

The results of the data taken at 3.5-mT and 14.0-mT fill pressures were not much different than those at 7.0 mT. The temperatures at 3.5-mT fill were somewhat higher than the 7.0-mT data, and the 14.0-mT data were somewhat lower but by less than a factor of two in either case.

The temperatures measured here are in reasonably good agreement with the numerical simulations of A. G. Sgro.[6] The solid curves in

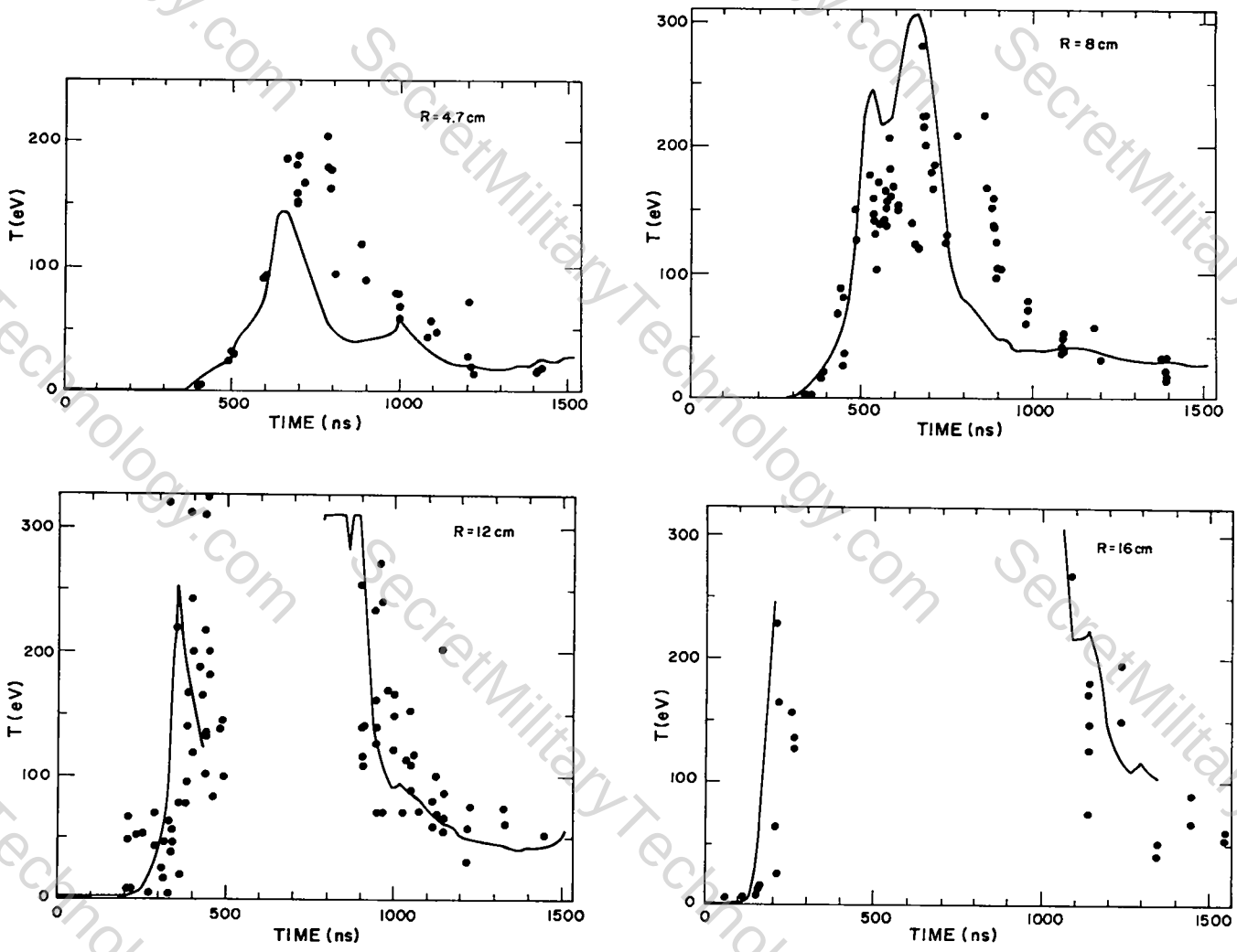

Fig. VII-2.
IHX temperature data at R=4.6-, 8-, 12-, and 16-cm. The solid curves are the results of numerical simulations by A. G. Sgro.

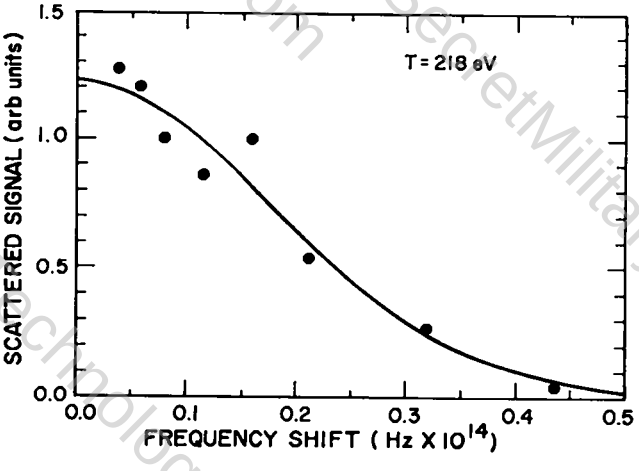

Fig. VII-3.
Typical scattered signals for a single shot. The solid curve is the Gaussian fit.

Fig. VII-2 are the results of these simulations for the IHX experimental parameters. The code does not contain end loss which makes the agreement somewhat surprising.

B. SUMMARY

In this experiment the implosion and first expansion were studied most extensively. The vacuum E_θ was 4 kV/cm, and plasma E_θs of 1.5 kV/cm were observed. Detailed measurements of the density and magnetic field as a function of time and radius were made using a four-beam interferometer, a single-beam Faraday rotation measurement, magnetic probes, and calibrated Thomson scattering. The electron temperature as a function of radius and time was measured using

Thomson scattering and double foil soft x-ray techniques. Neutron production rates were measured using a scintillator counter.

The implosion speed, the expansion speed, the radius of the sheath at turnaround, the density jump at the sheath, and the peak neutron production rate agree quite well with that predicted by the simple bounce model.[7] The actual width of the sheath and the electron temperature in the sheath are not predicted by this model, but the measurements agree with calculations done by Sgro and others. This temperature agreement is somewhat surprising since end losses are not included in these models. These results show that within the parameters of this experiment implosion heating is an effective means of heating plasmas to kilovolt temperatures and that the level of ion heating can be predicted reasonably well by the simple bounce model.

REFERENCES

1. I. Henins, J. E. Hammel, T. R. Jarboe, J. Marshall, and A. R. Sherwood, Pulsed High Beta Plasmas (Pergamon Press, Oxford and New York, 1976) pp. 203-207.

2. J. E. Hammel, I. Henins, J. Marshall, and A. R. Sherwood, "The Design of a High Voltage Generator for the LASL Implosion Heating Experiment," Proc. Fifth Symposium on Engineering Problems of Fusion Research, Princeton (1973) IEEE Pub. No. 73 CH0843-3-NPS, 1974, p. 664.

3. K. S. Thomas, compiler, "LASL Controlled Thermonuclear Research Program, January-December 1976," Los Alamos Scientific Laboratory report LA-7082-PR (March 1978), p. 106.

4. T. R. Jarboe, "Measurement of Faraday Rotation in the Implosion Heating Experiment," J. Appl. Phys. 48, 557 (1977).

5. K. Hothker, "Plasma Dynamics and Current-Sheath Structure in a Collision-Free Theta Pinch," Nucl. Fusion 16, 253-261 (1976).

6. A. G. Sgro, to be published in Phys. Fluids, 1978.

7. R. R. Bartsch, C. J. Buchenauer, E. L. Cantrell, J. N. Downing, F. L. Freeman, K. B. Freese, R. F. Gribble, I. Henins, F. C. Jahoda, T. R. Jarboe, R. Kristal, G. Miller, W. E. Quinn, F. L. Ribe, A. R. Sherwood, R. E. Siemon, K. S. Thomas, "Plasma Experiments on the Staged Theta Pinch, the Implosion Heating Experiment, and Scyllac Feedback-Sector Experiment," Plasma Physics and Controlled Nuclear Fusion Research (IAEA, Berchtesgaden, 1976) Vol. II, pp. 193-200.

VIII. FAST LINER EXPERIMENT

A. R. Sherwood, E. L. Cantrell, I. Henins, T. R. Jarboe, J. Marshall, C. E. Swannack

Early in the year a proposal to do an imploding liner experiment at LASL was prepared and presented to DMFE. This proposal[1] was eventually approved, and preparations for the liner experiment began after the termination of the IHX experiment in early December. Substantial contributions to the proposal were made by R. Gerwin, R. Malone, B. Suydam, R. Krakowski, R. Miller, R. Moses, and others.

The general concept is to explore the liner approach to fusion in the 10^6 cm/s liner velocity regime, where wall-confined plasma configurations are a possibility. As shown in Fig. VIII-1, a thin, nonrotating, cylindrical, metallic liner driven by a magnetic field in the theta direction is employed. The liner carries its own implosion current. The plasma needs an embedded magnetic field to inhibit thermal losses to the walls. A B_θ field, shown in the figure, has the advantage of providing insulation against both axial and radial heat flow. The initial plasma must be warm and dense. Theoretical guidance for the initial plasma conditions comes from numerical models which include liner physics and plasma losses. The following parameters for the initial plasma conditions are representative for reactor-like exeriments: $n_o = 5 \times 10^{17}$ cm^{-3}, $T_o = 200$ eV, and $B_{\theta o} = 5$ T. Relaxed conditions would still allow interesting experiments. The production of the initial plasma is a challenging task and is one of the most important goals of the experiment.

The approach being pursued in this experiment thus involves inertial confinement of the plasma particles and magnetic confinement of the energy. In this and other respects (e.g., B_θ liner drive field) it is similar to the LN-20 exeriment of Alikhanov[2] in the USSR, and it is a complementary approach to slower liner compression experiments such as the NRL LINUS program[3] and the experiments of Kurtmullaev.[2] In the latter experiments magnetic fields are used for plasma containment as well as insulation.

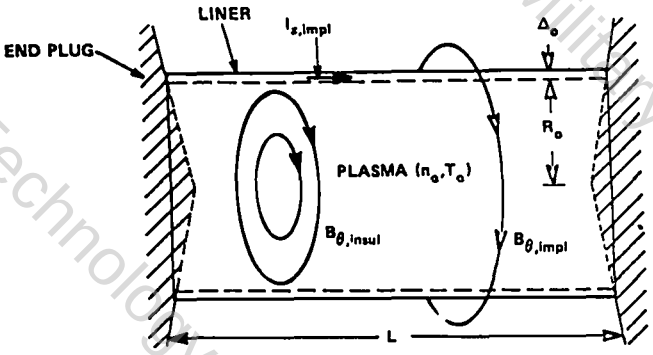

Fig. VIII-1.
Geometry of the Fast Liner Experiment. Material end plugs are employed, and the implosion is driven by an axial current carried within the liner itself.

The basis for optimism in the Fast Liner Experiment stems from the scaling law for DT fills optimized for maximum gain (derived in the proposal).[1]

$$Q' = 7\sqrt{\frac{\rho_o}{2\pi}\,E_\ell} \quad ,$$

where Q' is the ratio of the thermonuclear energy to the liner energy, ρ_o is the initial density of the liner (cgs) and E_ℓ is the liner energy per unit length (GJ/m). The coefficient in this equation depends somewhat on the exact model employed, and other factors of order unity are introduced if one considers such effects as liner compressibility. From this equation we see that reasonably high Q's might be obtained from the Scyllac bank (8 MJ) for a 10-cm-long aluminum liner. It is important to note, however, that this equation assumes that the plasma energy loss rate is small compared to the rate at which energy is supplied from the liner. Simple theoretical estimates make this assumption plausible, but more detailed calculations and (especially) some experimental results are necessary to check the concept.

There are two major elements to the experiment, namely plasma preparation experiments and liner implosion experiments. Initially these two elements will be separate, but they will be combined as soon as it is practical. The initial goal of the plasma preparation experiments is to produce a suitable initial plasma in an implodable geometry. Here "suitable" depends on geometric factors such as the length and diameter of the liner, but in general what is desired is a plasma with enough density, temperature, and embedded magnetic field that it should be heated during the liner implosion. The first plasma preparation experiments will be based upon coaxial plasma flow systems, that is plasma guns or modifications thereof. These experiments will be done on the same facility as was used for the Gun Injection Experiment (300-kJ bank operated at 180 kJ). At the end of the year this facility was being modified for the new experiments. At least to begin, the existing 30-cm-o.d. coaxial plasma gun will be used with geometrical changes at the muzzle.

The liner implosion experiments will be done initially without plasma on three racks of the Scyllac bank (1.75 MJ at 55 kV). The initial goals of these experiments will be to develop diagnostics, to check the symmetry and velocity of the implosions, to learn how to make current contact to the imploding liner, to compare the efficiency of coupling of energy from the bank to the liner with numerical calculations, etc. As is illustrated in Fig. VIII-2, it happens that with only a minimal addition to the existing collector plates four more racks of the Scyllac bank can be added. Assuming the seven racks can be run at 50 kV, about 3.5 MJ would then be available for the liner implosion experiments. It is planned that collector plate additions to accommodate the four additional racks will be ordered, but the initial experiments will be done on three racks (out of a total of 15 for the whole bank). The three racks chosen for the first experiments have not been operated for 2-1/2 to 3 years. At the end of the calendar year they were being checked out and brought back into operable condition.

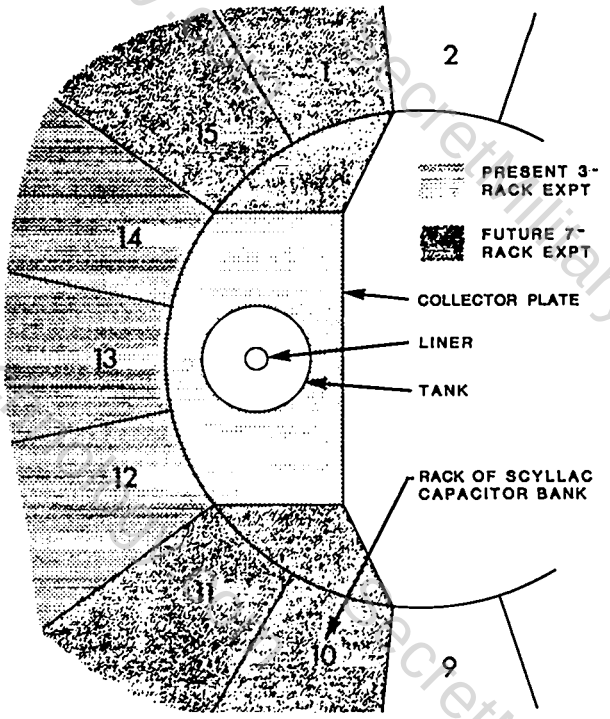

3-RACK AND 7-RACK LINER EXPERIMENTS

Fig. VIII-2.
Initial and future liner implosion experiments on the Scyllac bank. The initial experiments will use three racks (12, 13, and 14), but with only small additions to the collector plates four more racks could be added.

As this new experiment begins to get under way it appears quite possible that collaborations will be established with other elements of the CTR community. Candidates for such collaborations are a) parallel plasma preparation experiments to be done at other US institutions so that several possible paths towards the required initial plasma can be followed, and b) a joint experiment with the Soviets in which cooperative liner implosion and liner/plasma experiments are conducted, and in which the Soviets would conduct further plasma preparation experiments following the approach used in the LN-20 experiment (roughly--plasma injection from electromagnetic shock tubes). The latter collaboration was initially suggested by E. P. Velikhov in May 1977. A team of five US scientists, including three from LASL, visited Moscow in October to review the Soviet liner program and to explore the possibility of joint

LASL-Kurchatov liner experiments. The meetings were fruitful and the prospects for such joint experiments appear promising.

REFERENCES

1. A. R. Sherwood, B. L. Freeman, R. A. Gerwin, T. R. Jarboe, R. A. Krakowski, R. C. Malone, J. Marshall, R. L. Miller, B. Suydam, "Fast Liner Proposal," Los Alamos Scientific Laboratory report LA-6707-P (August 1977).

2. S. G. Alikhanov, V. P. Bakhtin, Wm. M. Brusnikin, I. S. Glushkov, R. Kh. Kurtmullaev, A. L. Lunin, A. D. Muzychenko, V. P. Novikov, V. V. Pichugin, V. N. Semenov, G. E. Smolkin, E. G. Utyugov, and I. Ya. Shipuk, "Study of Models of Liner Thermonuclear Systems" (translated by D. L. Book), Proc. 6th Int. Conf. on Plasma Physics and Controlled Nuclear Fusion Research Berchtesgaden, FGR, October 1976, (IAEA, Vienna, to be published), Paper No. E-19-2.

3. A. E. Robson and P. J. Turchi, "The NRL LINuS Program," Proceedings of the 3rd Topical Conference on Pulsed, High Beta Plasmas, Culham, 9-12 September 1975.

IX. GUN INJECTION EXPERIMENT

I. Henins and J. Marshall

A. INTRODUCTION

As reported in the last annual report, this experiment was undertaken as part of the Scylla IV-P program to develop a plasma injector for a linear theta pinch. The 1.5-m-long coaxial gun has an inner electrode diameter of 10 cm and a 30-cm-diameter outer electrode. A fast-acting valve admits a gas load at the middle of the electrode space, and a Scyllac-type 185-μF capacitor bank with an approximate inductance of 8 nH is used to power the gun. For all the experiments the bank has been charged to 45 kV, corresponding to a stored energy of 187 kJ.

During the previous year the experiment was assembled and the first measurements were made. The initial measurements were of the properties of the gun plasma itself. These were followed by an investigation of plasma injection into a short (50-cm-long) solenoidal guide field having a typical strength of about 10 kG (maximum was 17 kG). The diagnostics employed included single beam and holographic interferometry, fast-framing photography, neutron measurements, magnetic flux exclusion measurements in the guide field, and calorimetric measurements of the streaming plasma energy both upstream and downstream of the guide field coil. Two distinct gun operation modes were selected. In Mode 1 the gun is fired 300 μs after 50 cm^3 atm of deuterium gas is injected by the fast valve. The maximum gun current in this case is about 800 kA and the resulting plasma stream is rather broad. In the second, Mode 2, operation the gun is fired 360 μs after injecting 63 cm^3 atm of D_2 gas. In this case the gun current reaches 1.3 MA and the plasma stream forms on axis in front of the gun with a diameter of only a few centimeters. Calorimeter measurements showed that over 80% of the stored electrical energy emerges as plasma energy from the gun. The tighter plasma stream of the Mode 2 operation was better able to penetrate a 10-kG B_z guide field.

During the present year the calorimeter measurements were extended to measure the plasma stream divergence without a guide field, and a 2-m-long guide field coil was installed in place of the shorter 50-cm one. Plasma diamagnetic measurements at three positions have been used to determine plasma stream velocity and the transverse energy of the β=1 plasma stream. Probing of the magnetic field inside the plasma at the midplane of the 10-kG guide field coil also has shown flux exclusion out to a 12-cm diameter, which is comparable to that calculated for β=1 plasma from diamagnetic measurements.

The progress of the experiment was slowed because of manpower shortages in CTR-5. Work was suspended on the Gun Injection Experiment for about five months so that we could concentrate on finishing the measurements on the Implosion Heating Experiment and preparation of the proposals for the Fast Liner Implosion Experiment. At the end of this year the Gun Injection Experiment has been closed down and the experimental facility will be used for plasma preparation studies aimed at providing a suitable preplasma for the Fast Liner Experiment.

B. EXPERIMENTAL RESULTS

1. Plasma Injection into a 2-m-long B_z Guide Field.

a. Magnetic Field Coils. A new guide field coil assembly to replace the short 50-cm-long "see through" coil was made in two 1-m-long sections by wrapping a single layer of insulated #2 AWG copper cable with 2-cm turn-to-turn spacing on a 23-cm-diameter stainless steel cylindrical form. Then a layer of fiber glass and epoxy was applied to hold the windings in place. A stainless steel can was welded over the windings to provide a vacuum-tight coil case. The current is fed coaxially through a metal tube attached to the coil case. One end of the coil is attached to the coil form which serves as the current return.

The coil assembly is mounted 40 cm from the gun as shown in Fig. IX-1. The end nearest the gun has six turns spaced 1 cm apart to minimize the B_z decrease near the of the coil. There is a 2-cm gap between the two coils; one extra turn

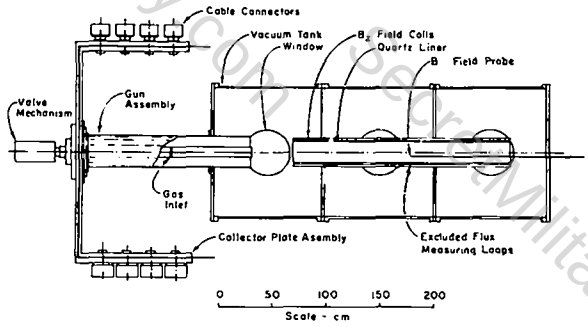

Fig. IX-1.
Schematic diagram of coaxial gun experiment with 2-m-long B_z guide field coil.

near each end of the coils here provides an average 2-cm turn spacing. The coil near the gun has a total of 56 turns, and the other 52.

Each of the coils is energized by a 3000-μF, 10-kV capacitor bank. The risetime of the B_z field in the coils is 800 μs. The coil current and the B_z are not in phase because the L/R time of the stainless steel shell is about 550 μs. Maximum B_z at 10 kV bank voltage is 16 kG.

b. Excluded Flux Measurements. These measurements were made with three loops placed near the inside walls of the B_z coils at 60 cm, 150 cm, and 220 cm from the gun muzzle. Each loop is approximately 0.5 cm wide and 65 cm long and completely surrounds the plasma to eliminate off-axis effects. A 20-cm-i.d., 200-cm-long, 0.5-cm-thick quartz tube liner inside the loops protected them from direct plasma bombardment.

During the short time of plasma injection the stainless steel coil form acts as a good flux conserver; therefore the total flux excluded by the plasma can be derived from the measurement of the change in magnetic field strength near the coil wall. If diamagnetic features of the plasma stream can be identified, then plasma velocity in the stream can be measured as the plasma progresses through the three loops.

Figure IX-2 shows the diamagnetic plasma energy for the long delay mode (Mode 2) as the plasma is injected into a 10-kG guide field. The maximum areas of the plasma, assuming it to be $\beta = 1$, calculated from the excluded flux measurements at each of the three loop positions are 110 cm^2, 50 cm^2, and 25 cm^2. The time-varying

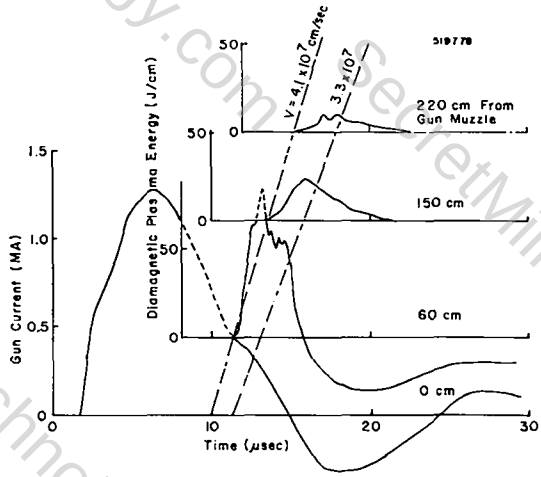

Fig. IX-2.
Diamagnetic energy and velocity of plasma injected into a 10-kG guide field. Mode 2 gun operation.

areas at each loop position were multiplied by the external magnetic field energy density to give the diamagnetic plasma energy plotted in Fig. IX-2. These curves, together with a velocity distribution can be further integrated over time to give the total diamagnetic energy. These values for the data in Fig. IX-2 are 4.6 kJ, 2.1 kJ, and 0.6 kJ for the loops 60 cm, 150 cm, and 220 cm from the gun muzzle, respectively. Extrapolation of the plasma position to the gun muzzle indicates that the plasma emerges at approximately 10 μs after the gun current starts. It appears that the paramagnetic signal observed at later times, as seen in Fig. IX-2, is caused by plasma bombardment of the quartz liner and is confined to the region near the entrance of the coil. Secondary plasma, derived from evaporation of the quartz wall, apparently entrains magnetic flux and carries it inward, so as to decrease the flux between the quartz liner and the inner coil wall. The paramagnetic component was therefore not included in the total energy calculation. When the gun is operated in the short delay mode (Mode 1), a diamagnetic plasma appears to emerge from the gun as a short pulse with a velocity distribution from 2×10^7 to 9×10^7 cm/s as shown in Fig. IX-3. There are well-defined features that allow measurement of velocity throughout the duration of the diamagnetic signals. The peak values of the excluded flux areas at the three loop positions in

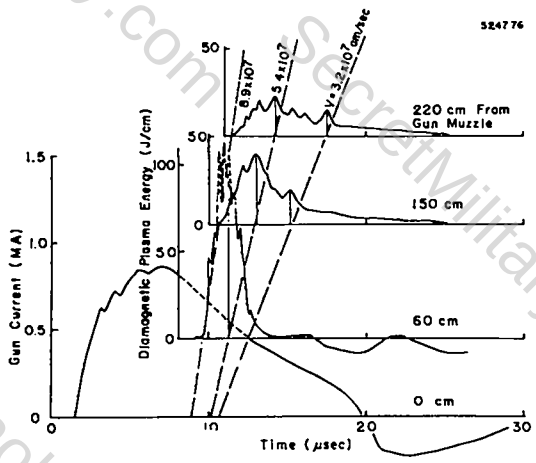

Fig. IX-3.
Diamagnetic energy and velocity of plasma injected into a 10-kG guide field. Mode 1 gun operation.

this case are 130 cm^2, 70 cm^2, and 45 cm^2. The integrated total plasma diamagnetic energies are 8.7 kJ, 6.5 kJ, and 4.8 kJ. Thus it appears that the short delay mode of gun operation produces more diamagnetic plasma which retains its diamagnetism as it travels down a B_z guide field. The velocities observed in the 2-m-long guide field are higher than the ~ 20 cm/μs velocities reported last year. The reason for this is not clear; it may have something to do with the length of the guide field and the more accurate measurement this allows.

An effort was made to maximize the diamagnetic plasma by varying the gun delay and amount of gas injected. It appears that the 300-μs delay with 1.4 x 10^6 Pa plenum pressure is near optimum.

2. Magnetic Field Probing. A magnetic field probe was inserted into the B_z guide field as shown in Fig. IX-1. The axial position was kept at 150 cm from the gun muzzle (the #2 diamagnetic loop position) and the probe was moved radially. The gun was operated with the short (300-μs) delay. The probe coil had an area of about 2 cm^2 and was inserted in a 9-mm outside-diameter alumina tube. Quartz envelopes were also tried but they could not withstand the plasma bombardment. The insertion of the probe in the plasma stream disturbed the signals in the diamagnetic loops, even upstream from the probe position. Usually the duration of the diamagnetic signals was shortened and the later paramagnetic signal was enhanced.

Typical smoothed magnetic probe data for several radii are shown in Fig. IX-4. On axis the signal shows complete flux exclusion lasting about 8 μs, after which the flux penetration (or disappearance of plasma) takes place. At larger radii the maximum flux exclusion lasts only a couple of microseconds, as is shown in the figure. However, nearly complete flux exclusion occurs out to a radius of 6 cm.

The 6-cm-radius outer limit of complete flux exclusion as observed by the B_z probe can be compared to the 70 cm^2 flux exclusion area measured by the diamagnetic loop at 150 cm, which corresponds to a flux exclusion radius of about 5 cm.

3. Plasma Stream Divergence. A rough estimate of the plasma stream spread in the absence of external magnetic fields can be obtained by observing how much energy is collected by a calorimeter at various distances from the gun muzzle. To make these measurements a large calorimeter (50 cm diameter, 91 cm long) was mounted behind a 60-cm by 60-cm copper plate containing a 30-cm-diameter aperture. The plasma energy passing through the aperture was measured at distances of 30, 60, and 110 cm from the gun muzzle. The gun input energy was kept constant at 187 kJ (185-μF bank charged to 45 kV).

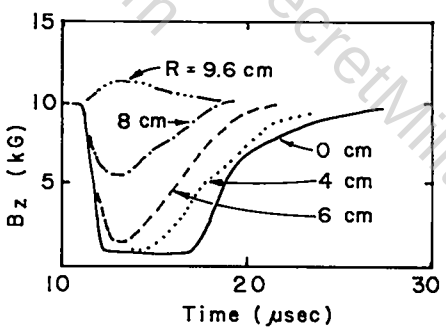

Fig. IX-4.
Magnetic field exclusion from plasma stream 150 cm from gun muzzle.

For the long delay case (Mode 2), the collected amounts of energy were 135 ±8, 108 ±5, and 98 ±8 kJ for the above calorimeter positions, respectively. When the gun was operated with the short delay (Mode 1) the amounts of energy collected were 161 ±10, 110 ±6, and 54 ±3 kJ, respectively. The uncertainties are the standard deviations calculated from four to five gun shots for each calorimeter position. From these data it is seen that for the longer delay and larger gas loading the plasma stream is confined closer to the axis of the system than in the other case.

When the calorimeter is placed behind the 2-m-long guide field coil, about 40 kJ of energy is collected in the Mode 2 operation of the gun, essentially independent of the strength of the magnetic field up to 10 kG. The energy of the more divergent and more diamagnetic plasma stream of Mode 1 operation, however, does not flow down the guide field as well. The energy collected at the end of the guide field coil is only 2, 14, 22, and 13 kJ with B_z equal to 0, 5, 10, and 15 kG, respectively.

C. SUMMARY

This coaxial plasma gun has been the largest and highest voltage gun operated at LASL so far. Its operation has been fairly typical compared to other previous plasma guns. We have again demonstrated that a coaxial plasma gun is very efficient in converting electrical energy into plasma energy. With the limited effort available for this experiment we were not able to demonstrate plasma injection suitable for replacing the implosion heating phase of a theta pinch. There were two principal deficiencies in the system investigated. One of these was severe bombardment of the entrance end of the fused silica liner. The other was the small diamagnetic energy of the injected plasma relative to its translational kinetic energy.

Plasma bombardment of the quartz liner at the entrance to the coil is presumably due to an insufficient barrier of flux separating the plasma from the liner and the end of the coil. It should be possible to alleviate this problem by using a larger diameter coil, by increasing the current density just at the end of the coil, and by reducing the thickness of passive material covering the end turns. Previous experiments with smaller guns did not show this behavior. In those experiments the gun was of smaller diameter than the coil, whereas in the present the gun is larger in diameter than the inner liner surface by 50%. This probably means that there is relatively more high-energy plasma streaming directly at the end of the coil than before. Bombardment of the liner is undesirable because it introduces large amounts of impurity by evaporation of the liner material and because it can mechanically destroy the liner.

The small diamagnetic energy of the injected plasma (~ 10% of the total plasma energy measured calorimetrically) is unsuitable as a theta-pinch filling for subsequent adiabatic compression because, with its low initial transverse temperature, it would require excessive compression to reach thermonuclear temperatures. In addition, the high streaming velocity would lead to excessive losses through the far end of the theta pinch. The difficulty might be alleviated by using a long, gradually increasing field entrance section to the solenoid. This approach has been investigated by Skvortsov et al. at the Kurchatov Institute. Another possibility is injection from both ends of the theta pinch, allowing the two plasmas to thermalize by Coulomb scattering against one another.

While gun injection of the precompression plasma into a theta pinch might successfully replace implosion heating, and thus eliminate the need for fast high-voltage power supplies, it appears to be limited to relatively short systems, because of the finite axial velocity of the injected plasma. This implies that, if this were to be used in a reactor, it would have to have very effective end-stoppering, or else the plasma would have to be compressed to very high densities, as in an imploding liner system. It is not obvious how gun injection could be used in reactors based on conventional theta - pinch parameters.

X. EXPERIMENTAL PLASMA PHYSICS

H. Dreicer, Martin E. Banton, J. C. Ingraham,
R. S. Massey, F. E. Wittman, and B. L. Wright

A. SUMMARY

The primary efforts of the Experimental Plasma Physics Group are directed toward the study of high-frequency plasma resistivity, plasma heating, and heat flow in the presence of plasma turbulence, electron drifts, and other effects likely to be present in plasmas of current fusion interest.

During the past year we have continued our study of the effect of a strong dc electron drift on the high-frequency plasma resistivity. We have taken a great deal more data and refined our techniques of data collection and analysis. Our findings confirm our preliminary results reported last year[1] that the high-frequency plasma absorption becomes negative if the electron drift velocity exceeds the electron thermal velocity. We plan to extend this work in the future to the case where turbulence is simultaneously present in the plasma, in which case an experimental test of the concept of the Plasma Wave Laser[2] may be possible.

We have continued to use our Dual-Mode Resonator to study the absorption experienced by a weak test microwave field in the presence of turbulence generated by parametric instabilities that are excited by a strong microwave driver field. Our recent test-field resistivity measurements as a function of the test-driver frequency separation support our earlier hypothesis that the enhanced test absorption occurs through nonlinear beating between some portion of the unstable wave spectrum and the weak test signal in such a manner that additional energy is transferred from the test field to the plasma through this beat oscillation.

We have also used the Dual-Mode Resonator to study weak test-field absorption in the presence of a strong driver field, but in the absence of parametric instability turbulence. Here we observe a reduction of the test-field absorption that is identical to our earlier reported measurement of the reduction of the driver absorption.[3] This reduction is caused by the effect of the large driver-induced oscillatory velocity of the electrons on the electron-ion collision cross section. Such a frequency-independent reduction of this cross section implies that any transport coefficient that is a function of the electron-ion collision cross section could be modified by strong electron oscillatory velocities induced, for example, in the heating of a tokamak using high-frequency power, or in the heating of a long linear plasma column by an intense CO_2 laser beam.

The above experimental studies, which were being done on our Q-machine, were temporarily suspended on May 25, 1977, so as to allow dismantling of our equipment to make room for the construction of a large toroidal reversed-field pinch (ZT-40). Relocation of our experiment into a new area was begun in late December, and we plan to be in operation by June 1978. This delay has made it necessary to postpone our planned studies of plasma heat flow until the Q-machine is operating again. A considerable amount of time in the past year has been devoted to planning for the dismantling and relocation of our experiments.

Testing has continued on a new experiment to study nonlinear interactions between a plasma and a travelling electromagnetic wave. Primary emphasis will be on the study of the beat-heating of a plasma using two electromagnetic waves separated in frequency by a natural-mode frequency of the plasma, and on the study of the decay of a single strong electromagnetic pump into two electron plasma waves.

B. PLASMA AC RESISTIVITY STUDIES

Our studies of the ac plasma resistivity have continued, primarily on our single-ended Q-machine. This device provides a fully ionized magnetized potassium plasma column ($T_e \approx T_i \approx 2250$ K, $n \approx 1\text{-}5 \times 10^{10}$ cm^{-3}, diameter ≈ 2.5 cm, $B \approx 5$ kG, length ≈ 200 cm) on which to study plasma resistivity using high-Q ($\approx 20\,000$) microwave resonators and movable high-frequency Langmuir probes. The experimental setup is shown schematically in Fig. X-1.

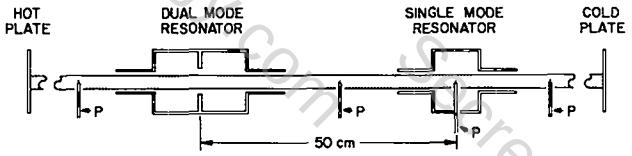

Fig. X-1.
Experimental setup of Q-machine experiments.

The ac plasma resistivity is determined from measurement of the microwave energy absorption rate of the plasma. This absorption is determined from the measured rate of decay of microwave energy stored within a high-Q resonator containing a portion of the plasma column. The difference between this rate of decay and that obtained in the absence of plasma yields a measurement of the plasma absorption rate.

1. Observation of Negative Inverse Bremsstrahlung Absorption Due to Strong Electron Drift Speed. We have continued our study of the effect of a strong dc electron drift on the plasma ac resistivity or microwave absorption. In this experiment a short ($\sim$ 0.4-μs) positive voltage pulse is applied to the cold plate of our Q-machine (Fig. X-1) in order to induce a uniform electron drift in the plasma column. The electron drift velocity is determined from simultaneous measurements of the electron current in the circuit external to the plasma, and the electron density. Measurements of the radial profiles of electron density and drift current density using small probes show that the drift velocity is independent of radial position in the plasma.

The change of plasma absorption as a result of the application of the electron drift is measured using our high Q-microwave resonator techniques. Since the electric field of the resonator mode is parallel to the strong dc magnetic field of the Q-machine, the absorption measured is a result of electron-ion collisions alone (inverse bremsstrahlung) rather than electron cyclotron effects.

To achieve large electron drift velocities, in the face of the limited electron current emission of the Q-machine hot plate, it was necessary to lower the electron density, n, and perform observations in the range $0.35 \lesssim \omega_{pe}^2/\omega^2 \lesssim 0.5$. This has the advantage *of reduced ohmic heating* due to the electron current flow, but it also reduces the sensitivity of our measurement of the plasma absorption in the resonator, since this quantity is proportional to n^2. Another way to avoid ohmic heating is to use a short pulse length for the electron current and to measure the microwave absorption rate during this short time interval. This also insures that the Buneman instability[4] cannot grow sufficiently to influence the electron drift speed and the microwave absorption. The price paid for gaining these advantages is the increased difficulty of accurately measuring the slope of the microwave energy decay from our oscilloscope traces during such a short time interval.

Previously[1] we have reported preliminary measurements showing that if the electron drift velocity, v_D, exceeds the electron thermal velocity, $v_T = \sqrt{2kT/m}$, the microwave absorption actually becomes negative, that is, Negative Inverse Bremsstrahlung Absorption occurs. In the past year we have refined our analysis techniques and taken a great deal more experimental data which confirm our previous conclusions.

The refinements have included efforts to reduce any possible systematic errors that might occur from measurements of resonator decay rates taken from the oscilloscope-trace photographs. Each oscilloscope trace picture was a composite of four traces: a baseline and three resonator decays. Two of the decays, spaced by about one cm on the photograph, were for the resonator without plasma and the third decay, located between the first two decays, was for the resonator with plasma in the presence of electron drift. These four traces were all made within a period of less than 30 s so as to minimize effects of baseline and gain drifts of the oscilloscope. The traces were positioned as close together as possible on the photograph so as to minimize errors arising from variations of oscilloscope gain and sweep-rate with position on the oscilloscope face when comparing resonator decay rates with and without plasma. Trace measurements were made using an optical digitizing system having an equivalent resolution on the oscilloscope photograph of $\pm$ 0.005 cm. In addition, we recalibrated the

microwave power response of our fast (0.01-μs response time) microwave crystal detectors several times during each data run, and at each frequency for which data was being taken. (For example, the empty resonator frequency was 1992 MHz. With plasma at $\omega_p^2/\omega^2 = 0.35$, the frequency was 2023 MHz.)

Our experimental results are shown on Fig. X-2 and indeed, it can be seen that Negative Inverse Bremsstrahlung Absorption corresponding to a negative plasma resistivity does occur at larger drift velocities. The vertical axis in the figure is the measured plasma ac resistivity normalized to its measured value in the absence of electron drift. The horizontal axis is the electron drift velocity, normalized to the electron thermal velocity, $v_{TO} = \sqrt{2kT_o/m}$, prior to the application of the electron drift. Each data point corresponds to the average of measurements taken from at least ten oscilloscope photographs, and the vertical error bars are equal to the rms deviation of these measurements about the average. The horizontal error bars correspond to the variations during the current pulse of the measured electron current about its average. The solid line is our theoretical computation based upon the Oberman-Dawson formalism[5] of the resistivity of a drifting Maxwellian electron velocity distribution

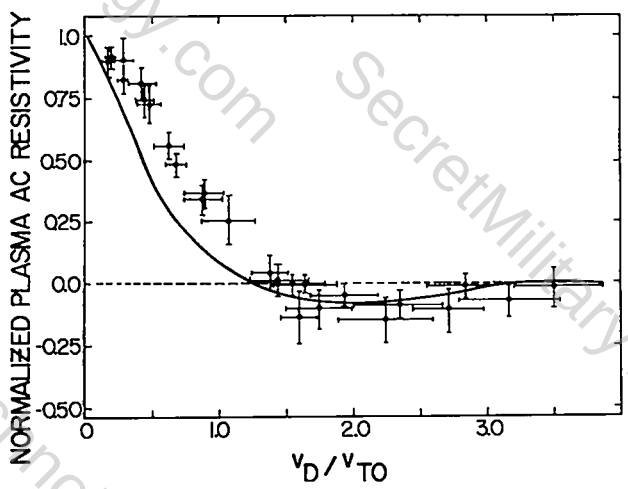

Fig. X-2.
Normalized ac plasma resistivity vs electron drift velocity; comparison of theory and experiment.

and including the effect of a dc magnetic field parallel to the drift. (Our computation is in good agreement with the earlier results of Musha and Yoshida,[6] who utilized the Boltzmann-Fokker-Planck equation to evaluate the resistivity of a plasma having a drifting Maxwellian.) Experiment and theory are seen to agree well, especially at higher drift velocities where the negative absorption occurs.

In order to compare theory and experiment we have corrected the theoretical computation for the ohmic heating of the electrons that occurs during the time of the absorption measurement. The electron ohmic heating was computed using the Fokker-Planck equation and assuming the electron velocity distribution was a drifting Maxwellian.[7] As a check on our electron ohmic heating computations, we have performed microwave measurements of the electron temperature during the period that follows termination of the electron current pulse, and these measurements support the computed electron heating results.

We plan in the future to study the effect of electron drift on microwave absorption in a turbulent plasma.

2. Weak Field AC Resistivity Enhanced by Plasma Fluctuations. Our past studies of parametric instabilities near the plasma frequency have treated the case in which a microwave electromagnetic "pump" field of frequency ω_o and long wavelength ($k_o \simeq 0$) exhibits a strongly enhanced absorption rate as its energy is drained by the unstable growth of electron plasma waves (ω_1) and ion fluctuations (ω_2). The process is a nonlinear one in which frequency and wave-number matching conditions are satisfied ($\omega_1 + \omega_2 = \omega_0$, $\vec{k}_1 + \vec{k}_2 = 0$) and which can only occur when the pump field amplitude, E, exceeds the threshold level, E_T, required to overcome natural damping mechanisms. For $\omega_o \approx \omega_p$, two distinct instabilities are recognized: the parametric decay instability in which ω_2 corresponds to an ion acoustic wave, and the oscillating-two-stream instability in which ω_2 is zero. For the case $T_e = T_i$ and $\omega_o \gtrsim \omega_p$, our experiments[1,8-10] have verified details of these phenomena including absolute measurement of instability thresholds in agreement with theory, transient observations of pump depletion

consistent with computed growth rates, verification of appropriate structure in the electron fluctuation spectrum (corrected for ion drift), and analysis of "bump-in-tail" fast electron beams created by large amplitude electron plasma waves.

With the nonlinear mechanisms of pump-field absorption well established, the question arises whether such driven plasma fluctuations could also affect the absorption rate (or equivalent ac resistivity) of a microwave field at a frequency other than that of the pump field that generated them. The topic addressed by this question is the enhancement of the weak-field ac resistivity of a plasma by nonthermal fluctuations. The mechanisms responsible can be nonlinear couplings similar to those of parametric instabilities but for which (because the fluctuation levels are externally maintained) the observed resistivity is associated with a first-order current and is therefore independent of the amplitude of the weak ac sampling field. Theoretical treatment of this problem[11] suggests that electron (or ion) waves in a plasma can enhance the resistivity of an external ac field, providing that the mode produced by field-wave coupling lies in the resonant region of the plasma's dielectric response that is associated with ion (or electron) motion. Thus the enhancement of weak-field ac resistivity by plasma fluctuations involves matching conditions that can lead to frequency dependence from both the resonant behavior of the dielectric response and the spectral distribution of the fluctuations involved.

In the case of the experiment described below, interpretation of the data is not immediate: both strong electron waves and strong ion waves are generated by the pump field. There are thus two major possibilities for the source of the enhanced weak-field ac resistivity that we measure. One can argue that ion fluctuations are unimportant because their parametric origin and the Manley-Rowe relations give them small amplitudes in comparison with the cogenerated electron waves. On the other hand, the enhancement of ac resistivity caused by electron waves depends roughly on the derivative of the spectral intensity.[11] As the pertinent spectrum appears to be quite broad in some of our work, we cannot conclude immediately that electron waves are dominant. It is worth noting that the two regimes in which we see the strongest effects are those to which conventional theories of steady-state weak turbulence may not apply. These regimes are (a) the transient period of rapid growth of the fluctuations in which the parametric growth rates are comparable to the ion plasma frequency, ω_{pi}, and (b) the steady state maintained by a pump, well above threshold, in which nonlinear saturation has produced considerable spectral broadening and the resulting turbulence has doubtless caused radical changes in the plasma's dielectric behavior.

The experiment is performed with a dual-mode microwave resonator (Fig. X-1) that is capable of supporting two nearly degenerate modes (even and odd symmetry) with overlapping fields of the TM_{010} character and frequencies near 2000 MHz. We use one of these modes as a strong driver field. When the driver field is above threshold ($E > E_T$) it acts as the pump field described above and generates and maintains electron and ion plasma waves. The other mode of the resonator is then used as a weak, subthreshold test field to monitor the ac resistivity at a somewhat different frequency. By switching off the external, pulsed, microwave sources at suitable times, we can measure and compare the simultaneous absorption rates of both fields. In accord with expectations, the effective resistivity of the driver field is governed by the nonlinear processes studied previously; the resistivity of the test field is found to be independent of test-field amplitude, but noticeably affected by the (driver produced) plasma fluctuations.

We have already reported[1] the results of experiments performed over the density range $0.65 \leq \omega_p^2/\omega^2 \leq 0.90$ with a test-driver frequency difference, $f_{test}-f_{driver}$, of $\pm$ 15 MHz. Those experiments investigated the absorption of test and driver fields both during the period of transient growth of parametric instabilities and during the subsequent saturated steady state. We have now extended our work to include test-driver frequency separations of $\pm$ 11.6, $\pm$ 27, and $\pm$ 86 MHz. These more recent experiments have shown phenomena that are qualitatively similar to

those found at ± 15 MHz but that indicate a decreasing influence of the plasma fluctuations on the test-field resistivity as its frequency becomes more distant from that of the driver. For comparison, the ion plasma frequency, $\omega_{pi}/2\pi$, is near 7 MHz. Thus, all our work has involved test frequencies that are outside the range of the initial, unstable electron wave frequency: $f_{e\text{-wave}} = f_{driver} - f_{ion\text{-wave}}$.

Figures X-3 through X-6 illustrate the frequency dependence of the enhancement of test-field resistivity during the growth of driver-produced parametric instabilities. Figures X-3 and X-4

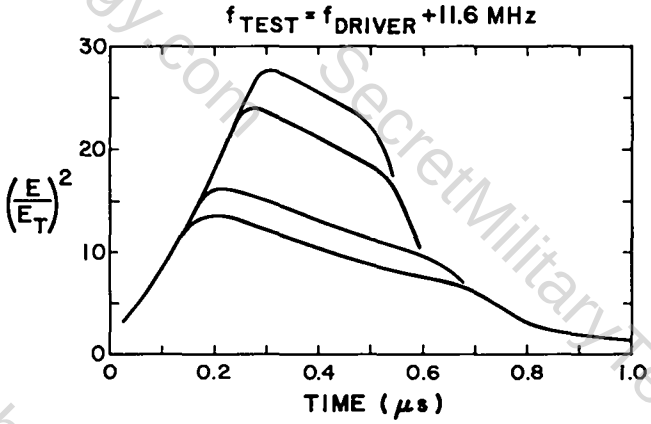

Fig. X-3.
The four driver-field time histories used in the transient resistivity measurements of Fig. X-5.

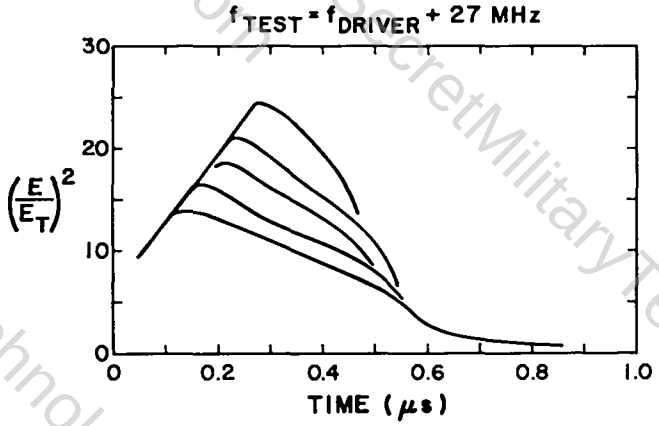

Fig. X-4.
The five driver-field time histories used in the transient resistivity measurements of Fig. X-6.

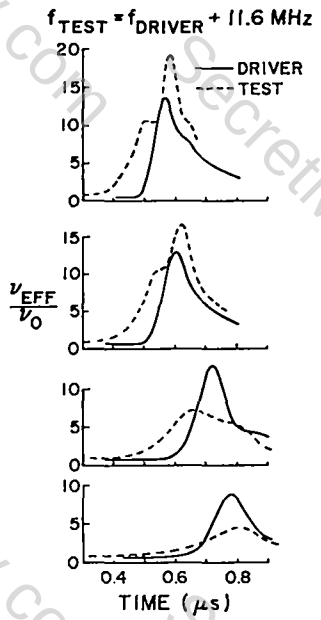

Fig. X-5.
Normalized resistivity of test (---) and driver (——) fields corresponding to Fig. X-3 in order (top to bottom) of decreasing driver power.

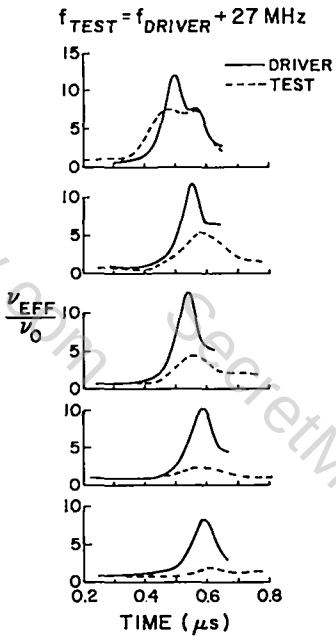

Fig. X-6.
Normalized resistivity of test (---) and driver (——) fields corresponding to Fig. X-4 in order (top to bottom) of decreasing driver power.

show how the driver time history was controlled for $f_{test} - f_{driver}$ = 11.6 and 27 MHz. The quantity

plotted is the square of the driver field amplitude, E, relative to the threshold level, E_T, required to excite instabilities. In each of the several cases shown, the driver field in the resonator passes through three stages:

(a) During the application of an external, pulsed, microwave source, the driver amplitude rises rapidly to a maximum level controlled by the time of termination of the pulse.

(b) The above-threshold field decays slowly by means of electron-ion collisional absorption (and resonator wall losses) while the unstable plasma fluctuations continue to grow from noise.

(c) A sudden decrease (pump depletion) of the driver field occurs when the fluctuations reach sufficient amplitude to draw substantial energy from it via nonlinear mechanisms.[1]

Figures X-6 and X-7 compare the absorption rate exhibited by the driver field in these cases with that shown simultaneously by a freely decaying test field. The quantity plotted is the effective resistivity (indicated here as an effective collision frequency, ν_{eff}) normalized to the electron-ion collisional value measured with weak fields (ν_o). The plots show that the strongly enhanced resistivity of the driver field is accompanied by a strong influence of the growing fluctuations on the resistivity of the test field. For a higher average driver power (faster growth of unstable plasma waves) there is a greater enhancement of the test-field resistivity with an earlier onset in time (relative to that of the driver). Comparing the behavior of a test field 11.6 MHz above the driver frequency with that of one 27 MHz above, one easily sees that the enhancement of ac resistivity becomes more pronounced as the two frequencies come closer together. Note that we are here speaking of $f_{test} > f_{driver}$ while the unstably growing electron waves satisfy $f_{e\text{-}wave} \leq f_{driver}$. In these transient studies we found noticeable (factor of 3) enhancement of the test-field resistivity even at the largest frequency separations: $f_{test}-f_{driver} = \pm 86$ MHz.

One should not ascribe particular importance to the heights reached by the absorption peaks in Figs. X-5 and X-6. The maxima in ν_{eff} occur because the fluctuations that enhance the absorption rate grow rapidly at first but then decay away upon depletion of the driver field that generates them. Thus the maximum values attained are determined more by the time history of the driver field following pump depletion than by inherent limits on the absorption process. Of greater interest are the differences observed between the times of <u>onset</u> of enhanced absorption in the test and driver fields. A rough explanation of the behavior of these differences is as follows. The onset of enhanced absorption occurs when the pertinent fluctuations reach a sufficient, critical amplitude, $\mathcal{E}_c$, to compete noticeably with electron-ion collisional absorption. The absorption rate of the test field is independent of test-field amplitude and therefore, $\mathcal{E}_c$(test) is roughly constant for a given test frequency. By contrast, our computations of parametric absorption rates[1] show that, for the driver (pump) field, $\mathcal{E}_c$(driver) is an increasing function of driver power. Thus as the average strength of the driver field is increased, the difference $\mathcal{E}_c$(driver)-$\mathcal{E}_c$(test) becomes more positive. Because the fluctuation amplitude at all frequencies grows with time during this period, the time delay between onsets, t(driver)-t(test) is likewise an increasing function of driver strength. This behavior is readily noticed in the figures.

When a sufficiently wide pulse of microwave power is supplied by the external source, the driver field in the resonator can be maintained at a fairly constant level after pump depletion. The result is a steady-state regime in which (for $E > E_T$) the unstable fluctuations have saturated. By varying the driver power relative to threshold, $(E/E_T)^2$, we can control the level of plasma turbulence produced. Again we compare the resistivities of test and driver fields under these conditions.

Figures X-7 and X-8 show such a comparison of steady-state data with f_{test} both above and below f_{driver} by about 27 MHz. The quantity plotted is the normalized resistivity measured with either field as a function of the driver field strength. The figures show the characteristic jump in driver-field resistivity as its amplitude exceeds the instability threshold ($E/E_T = 1$), but only at

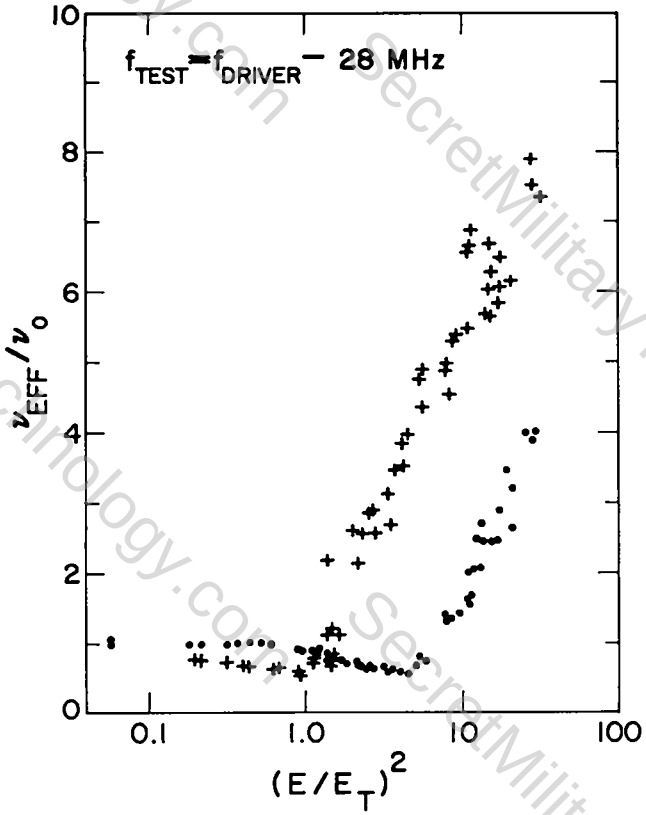

Fig. X-7.
Normalized resistivity of test (●) and driver (+) fields in the steady state.

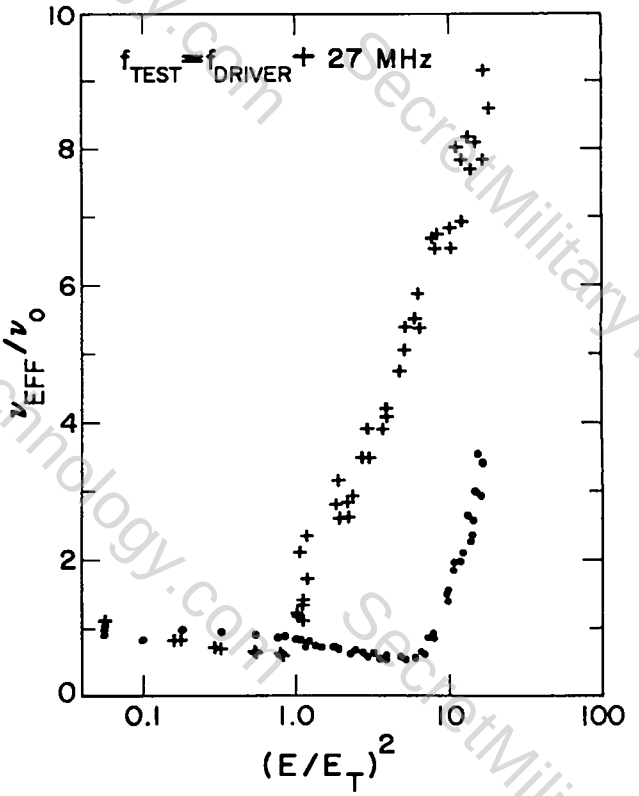

Fig. X-8.
Normalized resistivity of test (●) and driver (+) fields in the steady state.

the higher powers does the test-field resistivity show any enhancement. Presumably we see here the effects of a broadening of the pertinent wave spectrum (ion or electron) that occurs when the fluctuation amplitudes are well saturated. The nearly identical appearance of these two plots further suggests a frequency dependence of the enhanced test-field resistivity that is symmetric about the driver frequency.

In an attempt to document the above features we can plot, as a function of $f_{test}-f_{driver}$, the normalized driver power, $(E/E_T)^2$, required to generate a fluctuation level that doubles the test-field resistivity ($\nu_{eff}/\nu_o = 2$). Such a plot (Fig. X-9) indicates that the enhancement of test-field resistivity, as a function of f_{test}, has symmetric structure about f_{driver} in the saturated steady state and that more driver power (stronger turbulence) is needed to produce a given enhancement as $|f_{test}-f_{driver}|$ increases. A notable exception is the case $f_{test}-f_{driver}$ = -11.7 MHz which shows much more sensitivity than the case $f_{test}-f_{driver}$ = +11.6 MHz. This strong influence seen on a test field just below the driver in frequency is reminiscent of the less saturated, more concentrated, parametric decay spectrum that occurs at lower driver powers. One is tempted to suggest that the enhancement of test-field resistivity seen in these steady-state experiments scales directly with the intensity of electron waves at f_{test} and that we are seeing the effects of symmetric spectral broadening (possibly via four-wave processes[12]) as the driver power is increased. But such an interpretation discounts the conventional theoretical result that it is instead the derivative of the spectrum that should determine the contribution of electron waves to ac resistivity.

We are convinced that the enhancement of weak-field ac resistivity that we have measured can be attributed to the presence of fluctuations in our plasma. However, without further modeling

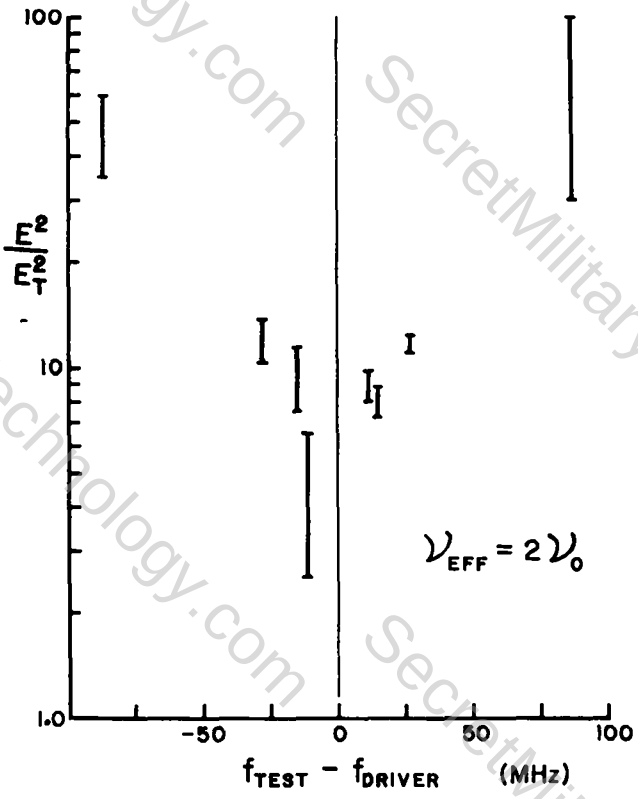

Fig. X-9.
Dependence on test frequency of the driver field required to double the test-field resistivity.

of the processes involved, the data by themselves do not suggest whether electron waves or ion waves make a dominant contribution. Because of the implied frequency and wave-number matching requirements it is probable that in either case the properties of the plasma (e.g., fluctuation levels, dielectric response) at both electron and ion frequencies are important. From the experiment we have obtained a fairly complete picture of the phenomena involved in both the transient and the steady-state regimes. We have documented their dependence on (a) the test and driver frequency separation, (b) the field amplitudes, and (c)[1] the plasma density. In the process we have identified many general features that can serve as tests of theoretical models for ac resistivity enhancement.

3. Modification of Electron-Ion Collision Rate by Intense RF Fields. The dual-mode resonator has also been used to confirm earlier work on high-field effects that do not involve parametric instability. We have already reported[3] measurements taken under conditions for which the plasma was parametrically stable but for which the oscillatory velocity of an electron in the rf field, $V_E = eE_0/m\omega$, was comparable to the random thermal velocity, $V_T = [2kT/m]^{1/2}$. A pronounced reduction of ac resistivity was observed in this case, a reduction attributed to the strong modification of electron orbits as they interact with the screened potentials of nearby ions. Through use of the dual-mode resonator, we have now applied simultaneous weak and strong fields at a frequency separation of 28 MHz. Figure X-10 shows a plot of the normalized collision rates of both the strong field (crosses) and the weak field (spots) as functions of the ac amplitude parameter, V_E/V_T, associated with the strong field. The modification of electron orbits by the strong field is seen to affect the absorption of the weak field so that indeed both fields show identical reductions in collisional resistivity. This observation supports the idea that an intense ac field can produce a genuine, frequency-independent reduction of the electron-ion collision rate of the sort

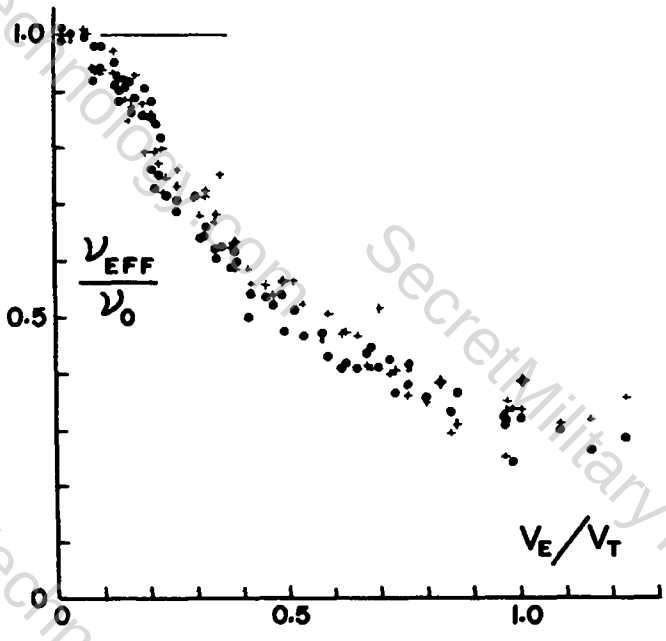

Fig. X-10.
Normalized collision rates of weak (●) and strong (+) fields as functions of the strong-field amplitude.

that might affect other collision-dependent transport properties as well.

4. Progress on an Experiment to Study Nonlinear Interactions Between Plasma and Traveling Electromagnetic Waves. In addition to the Q-machine research, work is in progress on another plasma source. This is a cylindrical, permanent magnet multipole-confined argon plasma device of the type developed by MacKenzie and coworkers[13] at UCLA. Experiments presently planned for this machine include an investigation of the decay of a photon into two plasmons, (the "2 ω_p instability") and a study of heating a plasma by beating two electromagnetic waves whose frequencies are separated by a natural-mode frequency of the plasma. These experiments involve traveling electromagnetic waves, in contrast to the Q-machine studies, and they take place in a region of essentially zero magnetic field. To achieve this a 100-cm-long cylindrical mesh waveguide, transparent to plasma, is mounted coaxially with the plasma source in the field-free region of the plasma, and is used to contain the plasma-microwave interaction.

Our research during the past year can be divided into three categories:

(a) Characterization of the plasma in the presence of the mesh waveguide.

(b) Investigation of the plasma noise near ω_p in the absence of microwaves.

(c) Preliminary investigations of the effect of plasma on the propagation of subthreshold (for the 2 ω_p-instability) microwave signals.

Two different mesh waveguides have been investigated. The original waveguide, made of copper-plated copper wire, had a mesh spacing of 6.4 mm and a transparency of 62%. Representative axial and radial profiles of density and temperature can be seen in Figs. X-11 and X-12. The temperatures are obtained using the $\ell n(I)$ vs V characteristic of a Langmuir probe near space potential. Higher temperature tails were usually noted. The axial density profiles were measured using ion saturation current to a plane probe, and radial density profiles were inferred from electron and ion saturation current to a cylindrical probe. Although these data are for a discharge current of 1 amp at 40 volts with the mesh at

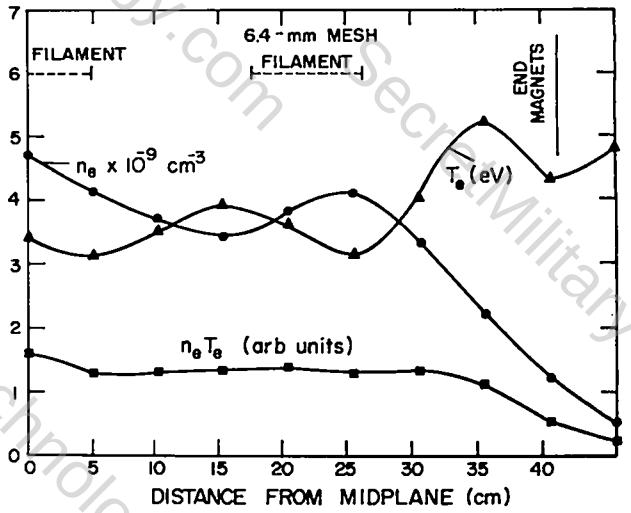

Fig. X-11.
Electron density and temperature on axis vs axial position measured from midplane for 6.4-mm mesh spacing. The product $n_e T_e$ is also shown. Mesh at floating potential ($\approx$ - 30 V), discharge voltage = - 40 V, discharge current = 1 A, gas pressure 8 x 10^{-4} torr.

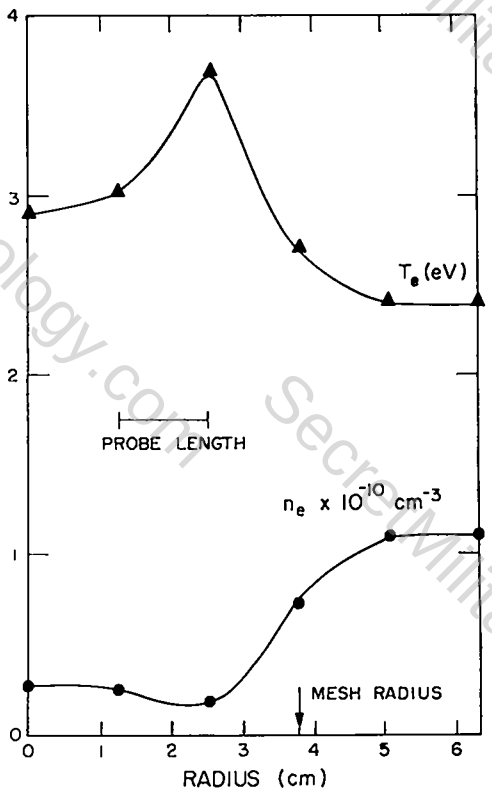

Fig. X-12.
Electron density and temperature at 30.5 cm. from midplane vs radial position for 6.4-mm mesh spacing. Same discharge conditions as Fig. X-11.

floating potential (≈ -30 V), these three parameters were varied widely. It was found that a more negative mesh potential gave higher interior densities, as, of course, did higher currents. However, sputtering became serious when either the filament bias (discharge voltage) or the mesh potential was more negative than - 40 V.

The main disadvantage of this mesh spacing was its relative lack of transparency to the plasma, reducing the plasma density inside the mesh to $\simeq 1/3$ that outside the mesh. For the investigation of the 2 ω_p instability, undesirably high discharge currents would be required to achieve the necessary density.

For this reason, the mesh was clipped to give 12.7-mm mesh spacing and a transparency of 82%. This resulted in much higher interior plasma densities but also caused a greater disturbance of microwave propagation in the waveguide. Axial and radial profiles of density and temperature for the same operating conditions as Fig. X-11 may be seen in Figs. X-13 and X-14.

Several checks on the density measurements have been made. Density in the waveguide can be inferred from microwave cutoff experiments, and average density may be deduced from microwave interferometry measurements using the mesh

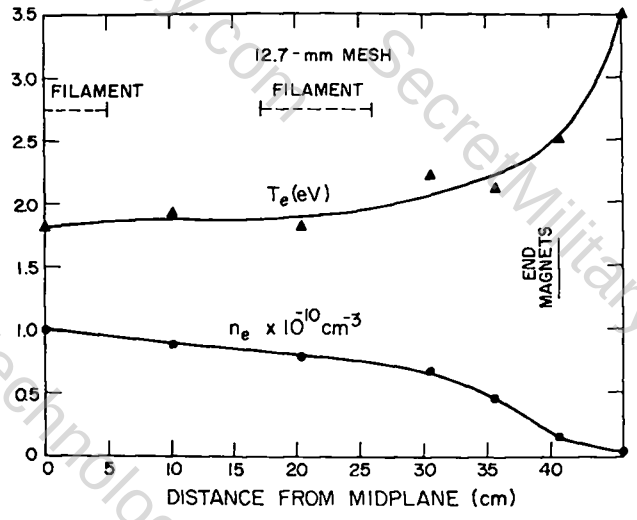

Fig. X-13.
Electron density and temperature vs axial position measured from midplane for 12.7-mm mesh spacing. Discharge parameters same as Fig. X-11.

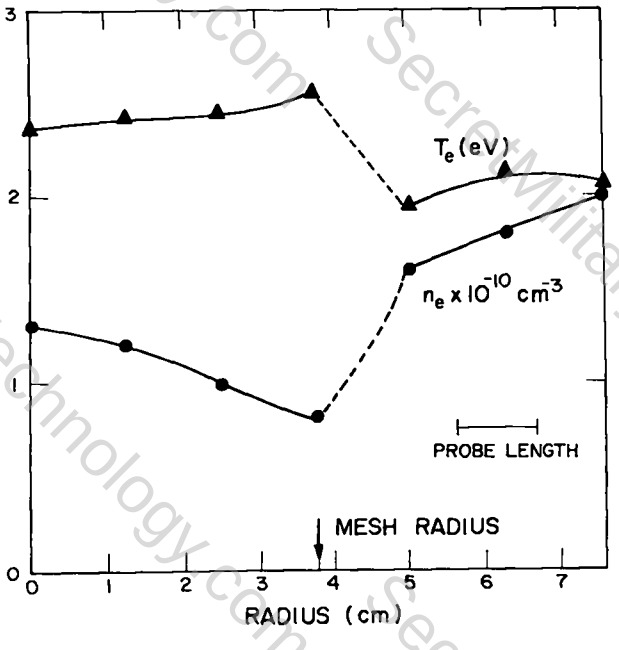

Fig. X-14.
Electron density and temperature at midplane vs radial position for 12.7-mm mesh spacing. Discharge parameters same as Fig. X-11.

waveguide. Density was inferred from the measured cutoff frequency by assuming the plasma uniformly filled the waveguide and using the relations $f_c = \sqrt{f_{co}^2 + (\omega_p/2\pi)^2}$, where f_c is the cutoff frequency, and f_{co} is the cutoff frequency in the absence of plasma. This determines ω_p and thus n_e. Because of the radial profile, however, this n_e is less than the density on-axis, which the axial probe measures. The interferometer measurements are also somewhat difficult to relate precisely to probe measurements because of the radial and axial profiles in density, but the phase shift predicted for the profiles of Figs. X-13 and X-14 agree with the measured shift within 10%.

Because the two phenomena to be investigated excite plasma waves near ω_p, noise around ω_p in the absence of microwaves is being examined. This noise is detected by a shielded probe having a 1.6-mm-long by 0.15-mm-diameter tip, amplified 20 db by a low-noise amplifier, and displayed on a spectrum analyzer. At the time these measurements were made, the ends of the waveguide had Mylar windows which had become heavily coated with metal

by sputtering. Several features of the noise were noted.

(a) For the one case where noise spectrum radial profiles have been measured thus far (discharge current ≈ 1A), the noise level was much greater (10-100 times) inside the mesh than outside.

(b) The noise frequency was essentially the plasma frequency corresponding to the peak density inside the waveguide over a wide range of density. Fig. X-15 shows, as a function of discharge current, the noise frequency, the plasma frequency calculated from probe density measurements, and the plasma frequency deduced from microwave cutoff measurements. The latter tend to underestimate the on-axis density, as mentioned before. Interferometer measurements (not shown) also tend to lie below the probe data by about 10%.

When the coated Mylar windows were removed, the behavior of the noise changed completely. The noise was much greater (~ 10 times) just outside the mesh than inside. That such a change at the end-boundaries inside the mesh should produce this change in noise distribution is somewhat surprising unless the conducting ends formed a "resonator" for the waves associated with the noise. It should be noted that electromagnetic noise at these frequencies would be far below the waveguide cutoff.

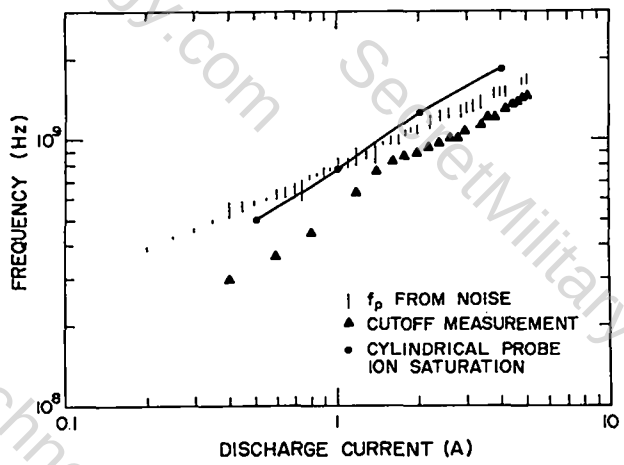

Fig. X-15.
Plasma frequency (Hz) vs discharge current (amps). Discharge voltage -40 V, mesh bias - 40 V, neutral pressure 4 x 10^{-4} torr.

Low-power ($\leq$ 100 W) microwave experiments have been done on the 12.7-mm mesh guide to establish the performance of the system in the linear regime. Investigations at higher powers will be carried out when our 1-kW TWT amplifier system is in operation. To reach powers higher than the 1-kW level we will either resort to a higher power microwave system, or utilize microwave resonator techniques to enhance the field levels of the traveling waves experienced by the plasma.

REFERENCES

1. "LASL Controlled Thermonuclear Research Program, January-December 1976," Los Alamos Scientific Laboratory report LA-7082-PR (1978), pp. 110-126.

2. A. T. Lin, P. K. Kaw, and J. M. Dawson, "A Possible Plasma Laser," Phys. Rev. A 8, 2618 (1973).

3. J. H. Brownell, H. Dreicer, R. F. Ellis, and J. C. Ingraham, "Influence of Intense AC Electric Fields on the Electron-Ion Collision Rate in a Plasma," Phys. Rev. Lett. 33, 1210 (1974).

4. O. Buneman, "Instability, Turbulence, and Conductivity in Current-Carrying Plasma," Phys. Rev. Lett. 1, 8 (1958).

5. J. M. Dawson and C. R. Oberman, "High-Frequency Conductivity and the Emission and Absorption Coefficients of a Fully Ionized Plasma," Phys. Fluids 5, 517 (1961).

6. T. Musha and F. Yoshida, "Negative Absorption Due to Coulomb Scattering of an Electron Stream," Phys. Rev. 133 A, 1303 (1964).

7. H. Dreicer, "Electron and Ion Runaway in a Fully Ionized Gas," Phys. Rev. 115, 238 (1959).

8. H. Dreicer, D. B. Henderson, and J. C. Ingraham, "Anomalous Microwave Absorption near the Plasma Frequency," Phys. Rev. Lett. 26, 1616 (1971).

9. H. Dreicer, R. F. Ellis, and J. C. Ingraham, "Hot-Electron Production and Anomalous Microwave Absorption near the Plasma Frequency," Phys. Rev. Lett. 31, 426 (1973).

10. "LASL Controlled Thermonuclear Research Program, January-December 1975," Los Alamos

Scientific Laboratory report LA-6582-PR (1976), pp. 100-110.

11. K. Nishikawa and Y. Ichikawa, "High-Frequency Conductivity of a Plasma with Fluctuations," Phys. Fluids 12, 2563 (1969).

12. S. Y. Yuen, "Saturation of Parametric Decay Instability by Nonlinear Four-Wave Coupling," Bull. Am. Phys. Soc. 22, 1122 (1977).

13. Rudolf Limpaecher and K. R. Mackenzie, "Magnetic Multipole Containment of Large Uniform Collisionless Quiescent Plasmas," Rev. Sci. Instrum. 44, 726 (1973).

XI. HIGH-DENSITY Z-PINCH

J. Hammel, C. Ekdahl, K. Hanks, L. Jones, W. Nunnally, D. Thomson

A. INTRODUCTION

An experimental program was set up in May of 1977 to investigate a very high density Z-pinch initiated by a small-diameter laser beam. The original proposal for such an experiment was made in January 1976 to the alternate concepts task force in CTR Division.[1] The experiment is a cooperative effort between CTR, P, and TD Divisions.

The experiment will be used to investigate a Z-pinch under the conditions of very high density ($n = 10^{20}$ to 5×10^{20} cm^{-3}) and very small radius (1×10^{-2} cm to 5×10^{-2} cm). With this small radius, the current density will be large and ohmic heating should take the temperature to many kilovolts for currents of 0.7 to 1.0 MA. The current will need to rise very rapidly for the pinch field to be able to maintain a small pinch radius. An idea of the required current rate of rise, under assumptions of a simple pinch model with classical behavior is presented in Ref. 1. For a pinch density of 10^{20} cm^3 and a radius of 350 μm the average rate of rise from initiation to 200 kA should be 5×10^{12} A/s or greater. The inductance of a 10-cm-long pinch 350 μm in radius in a close coupled pinch chamber is about 100 nH and for the above dI/dt implies a voltage of 500 kV across the pinch.

B. DESCRIPTION OF EXPERIMENT

1. Marx Power Supply. For the current source, a Marx generator has been designed to operate at 600 kV with coupling to the pinch load through a water transmission line. The supply consists of twelve 6-kJ Marx units fed in parallel to a 1-Ω, 90-ns water transmission line. The pinch chamber is then closely coupled to the transmission line in a manner which is similar to the diodes in an e-beam machine. The Marx module consists of 12 Maxwell 100-kV, 0.1-μF capacitors connected two in parallel at each level and erected six high. The spark gaps are Physics International 100-kV, 100-kA gaps.

The modular design has an advantage in allowing a one or more unit prototype to be built and tested before final construction of the full machine. A one-module prototype has been constructed with a 5-Ω, 60-ns line and test pinch chamber. This prototype has been used to check on the Marx triggering, voltage holdoff of the system and also a full voltage test of the pinch voltage breakdown in different geometries. The Marx has been operated at a full 600 kV into dummy loads.

Near full voltage, the erection time is about 80 ns with an observed jitter of about 30 ns. At low voltages the jitter becomes larger.

2. Plasma Initiation Laser. The laser purchased for the initiation of the pinch is a Holobeam neodymium glass and is specified to deliver 18 J in 18 ns with a beam divergence of 3 mrad. The actual performance of the laser does not meet specifications and is now being worked on by Holobeam. When the laser becomes operational, laser breakdown studies will be made prior to the actual pinch experiments on the full machine.

C. PROTOTYPE EXPERIMENTS

The prototype is in operation now for preliminary pinch experiments with currents up to 60 kA. For the initial experiments the initiating pulse will be from a ruby laser with an energy of 7 J in 25 ns.

The short-pulse breakdown voltage for H_2 in the pinch geometry was measured. At a H_2 pressure of 3 atm and a 5-cm electrode separation the breakdown was at about 300 kV for a pulse rising in 180 ns. The breakdown was apparently initiated at the point of highest stress which is 80 to 90 kV/cm.

The first pinch experiment with the prototype will be an initiation study using the ruby laser on the present gas chamber which has 5-cm electrode separation. It is desirable, if not essential, to put the laser pulse in a time window of about 30-ns duration just before spontaneous breakdown occurs. This means that the initiating laser pulse should be timed from Marx erection to

eliminate the jitter in erection time. This puts stringent demands on the electronics since the total time from erection to gas breakdown is about 240 ns. Fast spark gap triggering for laser and Imacon triggering is being tried. When these developments are complete we hope to have our first pinch experiments on the prototype.

REFERENCE

1. J. E. Hammel, "An Ohmically Heated High-Density Z Pinch," Los Alamos Scientific Laboratory report LA-6203-MS (January 1976).

XII. PLASMA DIAGNOSTICS

F. C. Jahoda, W. T. Armstrong, P. R. Forman, K. B. Freese
R. Kristal, and R. E. Siemon

A. INTRODUCTION

The scanning infrared heterodyne interferometer has been successfully bench tested with inclusion of a vacuum chamber in the plasma arm. Resolution of 25 spots over a 5-cm field of view in 0.25 μs with 0.1 fringe accuracy ($\int$ ndl ~ 3 x 10^{15} cm^{-2}) has been demonstrated. The system awaits installation of flat windows for side-on viewing on Scylla IV-P. A second system with larger field of view and capable of a trade-off of more resolution spots for slower total scan time for ZT-40 is under construction (Sec. B).

The insertion of end plugs in Scylla IV-P increased the electron density near the plugs sufficiently so that side-on ruby laser holographic interferometry became a very useful diagnostic. It has also renewed interest in a long-pulse ruby laser as a source for multi-frame interferograms from a single discharge. The activity under way to achieve such a ruby laser with adequate phase coherence is described (Sec. C).

A portable Thomson scattering apparatus is being constructed in order to measure electron temperature at several axial locations on Scylla IV-P. A more compact version of the three-grating polychrometer is combined with a special high-energy ruby laser oscillator on a single stand (Sec. D).

The spatially resolved Thomson scattering apparatus is being modified to increase signal-to-noise ratio. This entails extensive expansion of the automated read-out and computer assisted calibrations (Sec. E).

Some general-purpose computer codes relating (1) to ray tracing including phase errors due to beam bending and (2) to impurity radiation as an energy loss mechanism and as a temperature diagnostic, have been developed (Sec. F).

Analysis of previous data on CO_2 laser-theta-pinch plasma interactions has been completed, and a doctoral dissertation submitted to the University of Colorado. The thesis abstract and conclusion chapter are reproduced (Sec. G).

Three desirable diagnostics in an advanced conceptual or early design phase for ZT-40 are (1) far infrared Faraday rotation for poloidal field measurement, (2) short-pulse laser scattering for density profiles, and (3) mode-locked laser scattering for time history of electron temperature (Sec. H).

A substantial fraction of the Diagnostics Group effort centers on the use of minicomputers for data acquisition and for device control as well as adequate electromagnetic shielding between computer and plasma device. This activity is reported in Sec. XIV.

B. SCANNING INFRARED HETERODYNE INTERFEROMETRY

This project is concerned with measuring side-on plasma density profiles in the parameter range where visible interferometry is not sensitive enough ($\int$ ndl < ~ 10^{17} cm^{-2}). Of particular interest are

1. Obtaining sufficient phase and spatial resolution to enable accurate Abel inversions of interferometric data.

2. Obtaining multiple profiles during a single discharge to avoid the ambiguities of plasma irreproducibility. The concept was described previously.[1] During this year a system has been completely built and successfully bench tested. It is ready for installation on Scylla IV-P as soon as flat windows are available. A second system is under construction for ZT-40. A complete description and documentation for the existing system follows.

In standard (stationary beam) heterodyne interferometry the density time history is observed as a phase distortion of the beat (heterodyne) signal between two optical beams of different frequencies. The virtues of the technique include self-calibration, fractional - fringe resolution over a multi-fringe range, and

unambiguous sense determination. Also, the output is in electronic, rather than photographic, form which permits more rapid and automated data analysis.

By combining standard heterodyne interferometry with rapid spatial scanning, the temporal (heterodyne) fringes are converted to spatial fringes. By making the scan time short enough to "freeze" the plasma, multiple density profiles can be obtained during a single discharge using a single detector channel. The advantages of the technique accrue mainly with the lower density plasmas (area density $< \sim 10^{17}/cm^2$) where the highly developed photographic techniques available in the visible region of the spectrum are not sensitive enough, and hence the infrared wavelengths must be used.

The system layout is shown in Fig. XII-1. A cw He-Ne laser beam at 3.39 μm is focused inside a lead-molybdate acousto-optic cell. This generates a first-order diffracted beam, frequency shifted by ~ 100 MHz from the zero-order beam at the laser frequency. The zero order is used as the scene beam and the first order is the reference beam. The two beams are collimated and impinge side by side on a turbine driven rotating mirror, which provides the spatial scanning. Scanning the two beams in this way, in identical fashion, effects an enormous reduction in spurious differential phase shift that might otherwise occur, as well as optimizing signal-to-noise ratio.

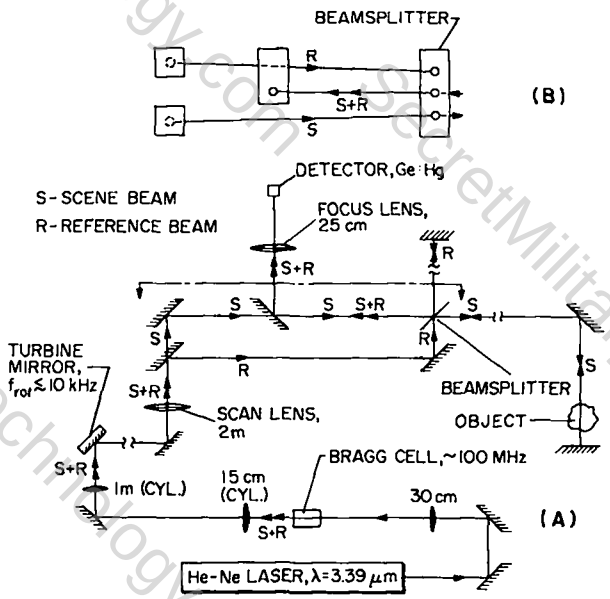

Fig. XII-1.
System optical schematic.

The angular scan off the rotating mirror is converted to a linear scan by placing the rotor at the front focal plane of the scan lens. The two beams scanning side by side are then easily separated into scene and reference arms. The far field spot forms at the back focal plane, at which point the return mirrors are placed, making the system double pass. The return beams are superposed on the beamsplitter and collected by the focus lens, which focuses the entire scan field onto the detector. Thus the rotor is imaged onto the detector, which insures a stationary spot on the detector during the scan. A new mirror scan occurs every time a new mirror facet of the rotating turbine sweeps by.

The scan field parameters are evident from Fig. XII-2. Scene beam scan waveforms (acousto-optic cell off) are shown with different resolution test grills in place of the object, for

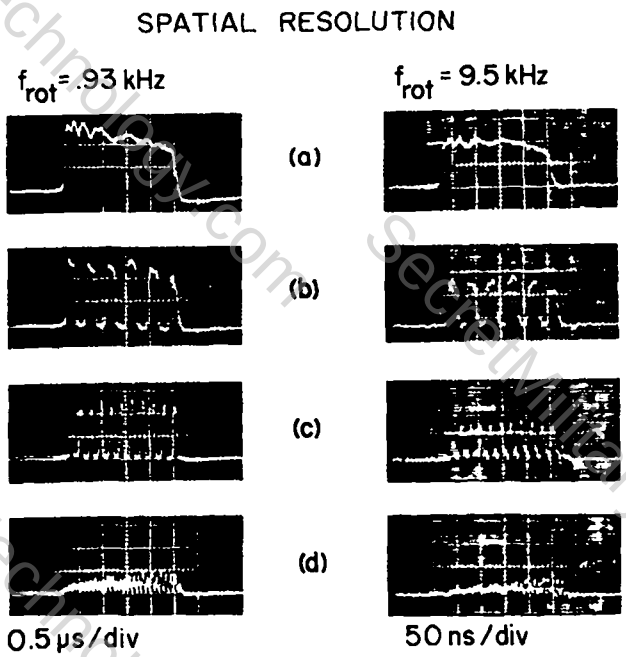

Fig. XII-2.
(a) Normal scene beam scans; (b) Resolution test grill in object plane, 10 mm/period (11 spots across field); (c) 5 mm/period (21 spots); (d) 2.2 mm/period (50 spots). Object plane is 17 cm from return mirror.

low and high rotor speeds. The scan field may be ~ 5.5 cm, in a time as short as 1/4 μs. Strong modulation due to the test grill is observed at 21 spots, even at top speed. The actual resolution is 25-30 spots, corresponding to a maximum scan rate of ~ 100 spots/μs.

Heterodyning while scanning at low speed is shown in Fig. XII-3. The heterodyne frequency is ~ 100 MHz, and so appears to fill in the waveform at the sweep speed used. The scanning without test grill [Fig. XII-3(a)], demonstrates the possibility of obtaining virtually 100% contrast. Figs. XII-3(b), 3(c), and 3(d) show resolution test results in agreement with Fig. XII-2.

High-speed heterodyning with a test cell with medium-quality quartz windows under vacuum in the plasma arm is shown in Fig. XII-4. Three linear phase objects are simulated by three different tilts of the scene beam return mirror. The heterodyne frequency may not be constant across the

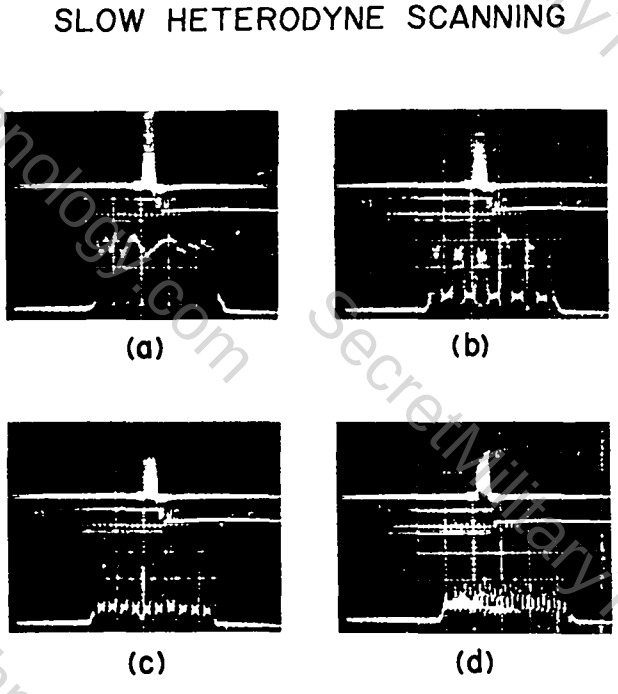

Fig. XII-3.
Lower trace: (a) *Heterodyne scanning at low speed* (f_{rot}-0.94 kHz) with quartz windows on vacuum chamber in scene beam; (b), (c), and (d) same resolution test grills as in Fig. XII-2. Upper trace - scan at low sweep speed; middle trace - acoustic burst.

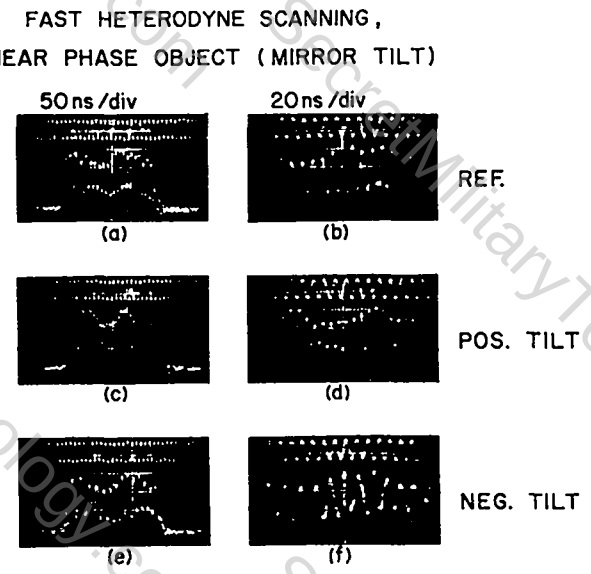

Fig. XII-4.
(a), (b) High-speed (9.6-kHz) heterodyne scanning through quartz windows under vacuum. Lower trace - *heterodyne scan; upper trace - acoustic* signal; (c), (d) scene beam return mirror tilted ~ 1/4 mrad; (e), (f) mirror tilted ~ 1/4 mrad in opposite direction.

scan, owing to slight phase differences between scene and reference optics. For this reason a reference exposure technique is used, whereby a scan made with the object (data) compared to a scan made without the object (reference). The difference in the two phase plots gives the object profile. The accuracy of this procedure may be found by comparing scans 4(d) and 4(f) against 4(b), in Fig. XII-4 since the differences are strictly linear phase profiles. The valleys in the fringe pattern have been digitized in each case and the differences appear in Fig. XII-5. Linear interpolation was used on the reference scan Fig. XII-4(b). The maximum deviation from the linear profile is ≈ 0.1 fringe for some points, the error being much better than that for many points. The error includes sources such as digitizer, scope, and camera optics, so that the basic system is capable of better than 0.1 fringe accuracy.

Multiple framing with the present system is limited to 100-μs frame interval (single facet at 10 kHz). A rotor is on order (from Cordin), which has 12 facets and rotates at the same top speed.

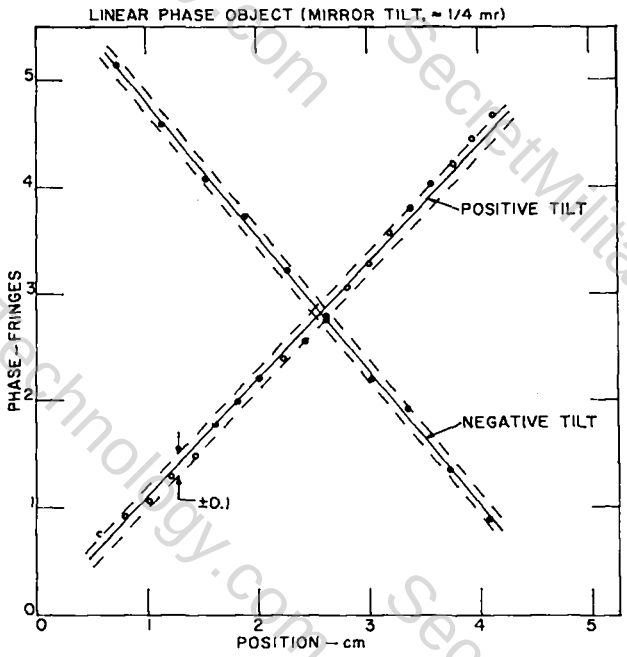

Fig. XII-5.
Measured phase profiles for Figs. XII-4(d) and -4(f) (data scans) using Fig. XII-4(b) as the reference scan.

When multiple framing is used, it is a simple matter to get four sequential scans on a single oscilloscope face. Therefore in the initial configuration, one scope is required for each four profiles during a discharge. Development work on electronic phase detection is under consideration.

The system as described above is suitable for Scylla IV-P, even with only one frame per discharge. It will be installed whenever flat window access is available.

In applying the concept to ZT-40, some changes are needed to accommodate the larger scan format. This will consist of X6 expansion optics in the scene beam (and shared with the reference beam if necessary) to increase the field from 5.5 to 33 cm, adequate to cover the ZT-40 plasma ($\approx$ 20-cm diam). If the scan time is kept constant, then the number of spots across the field will remain the same. However we will probably capitalize on the much slower dynamics anticipated in ZT-40, to allow a scan time of $\simeq$ 1 μs. This will permit a maximum resolution of ~ 100 spots across the field. It will also allow a reduction in the heterodyne frequency by at least a factor of two, thereby simplifying the data acquisition, storage, and analysis. Also, a stationary beam system will be incorporated on axis. This will allow normalization of the measured profile in case the density in the wings of the plasma profile is not negligible compared to the peak.

C. LONG-PULSE RUBY LASER FOR HOLOGRAPHIC INTERFEROMETRY

All previous ruby laser interferometry on theta pinches has been end-on because of the sensitivity limitation: at λ = 694 nm one fringe displacement is produced by $\int ndl = 3.2 \times 10^{17}$ cm^{-2}. [This fact was the motivation for the hydrogen fluoride laser interferometry (λ=2.9 μ, one fringe for $\int ndl = 7.7 \times 10^{16}$ cm^{-2}), successfully but painfully carried out on Scyllac in the past. Even for this wavelength the sensitivity is so marginal that, after considerable effort, it was abandoned as manpower-ineffective on Scylla IV-P.]

With the insertion of end plugs into Scylla IV-P, the density is greatly increased near the end plug and side-on ruby holographic interferometry becomes a useful diagnostic. This represents a happy circumstance in that the basics of the diagnostic were well developed before suitable circumstances for its application arose and it moved from the conception of the idea in the Diagnostics group to being a standard working measurement on an experiment within the reporting period of this report. The experimental results are outlined in the Scylla IV-P section. This development has also stimulated renewed interest in developing a long- (500-μs) pulsed ruby laser suitable for multiframe live fringe holographic interferometry,[2] since the dynamics are rapid in time, data shots are limited, and in some cases the window contamination problem is severe. Experimental effort was prompted by comment from some Soviet visitors to the effect that confocal cavity ruby lasers yield quasi-dc outputs with about 10% amplitude modulation suitable for interferometry.

Figure XII-6 shows a typical output pulse obtained from such a confocal cavity ruby laser. The laser consisted of two mirrors with 30% and 100% reflectivity each having a radius of curva-

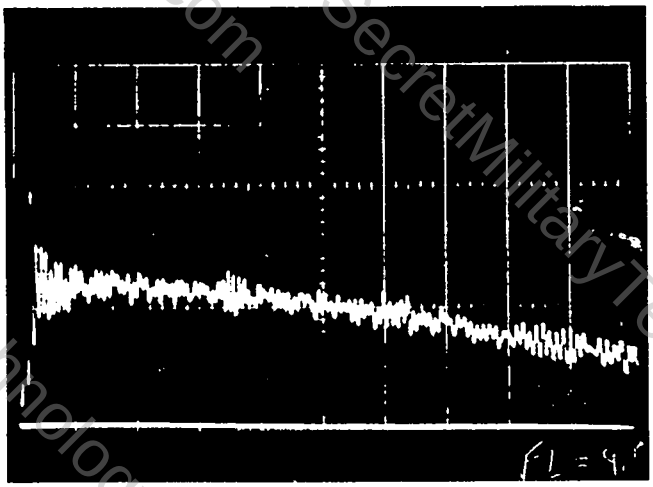

Fig. XII-6.
Output from long-pulse ruby laser with modest intensity modulation.

ture of 100 cm. The ruby was a standard 0.95-cm diam by 10-cm Korad laser head with flat anti-reflection coated end faces.

The cavity length was varied and it was found that a cavity length of 109 cm produced the smallest degree of oscillations, but this is far from a critical adjustment. During the set of tests, it was discovered that one must skew the laser head diagonally as much as possible to make the faces of the rod as far off from parallel with the mirrors as possible. If this is not done, many strong spurious reflections occur within the cavity and the output is dominated by very strong oscillations.

Positioning the laser head other than in the center of the cavity was tried. It was found that the farther off center the rod was placed, the worse the oscillations in the output became, probably due to the rod faces introducing more reflections as the beam walk-off between the rod and end mirror becomes less. The laser head must be placed somewhere close to the center of the cavity, but it is not a critical positioning.

Performance of the laser was studied as a function of pumping voltage. The threshold voltage was found to be 2.8 kV and a typical operating voltage was established at 4.8 kV. This pumping voltage gives a useful pulse of about 250 μs and contains 18 J energy.

The conclusions drawn from this series of tests is that while such lasers are adequate for simple interferometers, they are not adequate for holographic interferometry. In particular the variable transverse mode structure between the time-separated wavefronts that form the interferograms prevented high-quality results. Insertion of a pinhole into the laser cavity to achieve good transverse mode selection resulted in good holograms but changed the laser output from quasi-dc to irregularly spaced intermittent pulses that cannot be synchronized with framing camera recording. This result led to the abandonment of this approach.

The quasi-dc output from a confocal cavity results from the random superposition of many longitudinal modes of equal frequency and random phase. The resulting nearly uniform intensity does not provide the phase coherence needed in our application. This has forced us to consider single longitudinal mode operation which, however, generally suffers from longitudinal mode hopping due to gain profile hole burning. Two approaches to eliminate mode hopping even during long pulse operation are being investigated. The first method employs compensated phase modulation (CPM) and the second uses a ring laser.

The CPM method consists of driving two KDP crystals 180° out of phase, one at each end of the ruby rod, with a high-frequency sine wave generator.[3] This effectively moves the laser cavity standing wave pattern back and forth through the ruby rod, allowing more homogeneous depletion of the active medium. The use of this method was reported for a confocal cavity with a pumping voltage three times threshold and resulted in reducing the modulation to less than 10%.[3] Our initial attempts at such experiments have not proved as successful. We have applied 2 kV at 40 MHz to two longitudinal Pockels cells and as yet have not noticed any decrease in modulation depth of the random spiking.

A ring laser is currently under construction to test the second approach. A Faraday rotator using a 10-cm length of SF-6 glass has been built, which in conjunction with a half-wave plate determines the lasing direction. Having a traveling wave precludes the possibility of hole

burning. Negative feedback will be attempted to achieve constant amplitude. For this purpose part of the laser output is directed to a high-voltage photodiode (ITT 114 A). The signal from this diode is placed directly on a Pockels cell within the cavity to decrease the laser output. A similiar feedback arrangement using a Kerr cell has been reported in the literature.[4]

D. PORTABLE THOMSON SCATTERING

The interest in axial heat conduction in Scylla IV-P has generated a requirement for axially resolved electron temperature measurements. To do this, it is proposed that one Thomson scattering experiment be set up at the center of the theta pinch and another portable experiment be moved along its length, each making simultaneous measurements of the electron temperature. The fixed-location Thomson scattering measurement has been installed on the center section of the theta pinch and construction has begun on a small, compact, portable laser-detector system which can be moved to different axial locations.

Figure XII-7 shows the layout of this new system. It consists of a 5-J ruby laser (Korad K5Q) mounted in a stand below the theta-pinch coil. On top of this same stand is mounted a triple-grating polychrometer[5] to detect the spectrum of scattered laser light. This arrangement has the advantage that it may be aligned away from the coil and then moved into place, guaranteeing that the laser and detector see the same plasma volume.

The triple-grating polychrometer built for this experiment is a modification of Siemon's design suggested by Greenwald and Smith.[6] This new design requires one less mirror in the optical path than Siemon's design, and it is relatively easier to fabricate. However, it does introduce some astigmatism and chromatic abberation into the optical system. These problems can be reduced to a tolerable level.

Figure XII-8 is a schematic of the Greenwald-Smith design. Each stage of the polychrometer is essentially identical to the rest. Light entering the device through the entrance slit, S1, is collimated by lens L1 and falls on the first grating G1. The dispersed spectrum is then imaged onto a mask between the first and second stage. The dispersed light is recombined by the second grating G2 and imaged onto slit S2. The difference between Siemon's design and the Greenwald-Smith design is the way this second stage recombines the dispersed light. Figure XII-9 shows a detail of the first and second stages of the polychrometer. Light of wavelength λ incident on the entrance slit enters at an angle α_1, with respect to the normal of grating G1. The grating is used in a near Littrow mounting and the light leaves the grating at angle β_1 where

$$\sin \alpha_1 + \sin \beta_1 = \frac{\lambda}{\ell} \quad , \qquad (1)$$

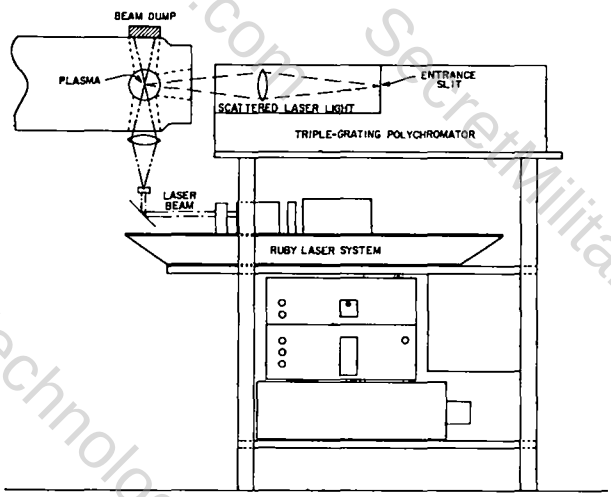

Fig. XII-7.
Portable Thomson scattering set-up.

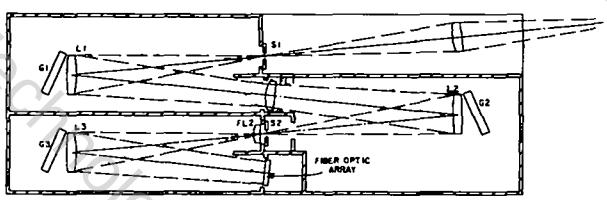

Fig. XII-8.
Triple-grating polychrometer.

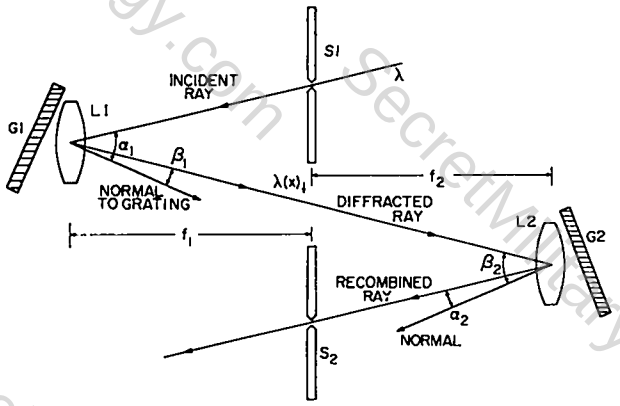

Fig. XII-9.
First two stages of triple-grating polychrometer.

and ℓ is the line spacing of the grating. The linear dispersion at the mask is given by

$$\frac{d\lambda_1}{dx} = \frac{1}{f_1}\,\frac{d\lambda_1}{d\beta_1} = \frac{\ell}{f_1}\,\cos\beta_1 \quad . \tag{2}$$

For the dispersed light to be faithfully recombined, the linear dispersion of the second stage must be identical to that of the first. It can be shown that when this is the case, the image of the recombined beam will fall on the entrance slit. This is the Siemon design and requires a turning mirror to avoid this complication. In the Greenwald-Smith design an alternative approximate solution is found by requiring that angle $\alpha_2 = \beta_1$ and $\beta_2 = \alpha_1$ for the central wavelength λ. In our system the mask transmits wavelengths from 6900 Å to 6100 Å, thus making the central wavelength 6500 Å. For the second grating G2 to faithfully recombine the light, the linear dispersion for the second stage should be

$$\frac{d\lambda_2}{dx} = \frac{1}{f_2}\,\frac{d\lambda_2}{d\alpha_2} = \frac{\ell}{f_2}\,\cos\beta_2 \quad . \tag{3}$$

For

$$\frac{d\lambda_2}{dx} = \frac{d\lambda_1}{dx} \quad \text{we must have} \tag{4}$$

$$\frac{f_2}{f_1} = \frac{\cos\beta_2}{\cos\beta_1} \quad , \tag{5}$$

i.e., the focal length of the second-stage lens L2 compensates for the differences in dispersion by effectively magnifying the mask image. Other design constraints require $f_1 = f_2$, thus making Eq. (5) impossible. The solution to this problem proposed by Greenwald and Smith is to move the field lens FL1 so that the combination of FL1 and L2 has an effective focal length f_2 as shown in Fig. XII-10. For $f_1 = 381$ mm, $f_{FL} = 189$ mm, and $f_2/f_1 = 0.918$ at $\lambda = 6500$ Å, the lens separations are a = 15.5 mm and b = 364.1 mm. When the spectrum $\lambda(x)$ at the mask is fairly linear, wavelengths other than the central wavelength are also recombined successfully. In Ref. 6, the design band-pass was only 300 Å, and there were no problems. We however, wanted a wider band-pass, 800 Å, and nonlinearities in $\lambda(x)$ produce a blurred recombined image at slit S2. What is required is a lens combination that has a variable focal length as a function of wavelength such that the two dispersions can be matched. The required focal lengths vs wavelength are summarized in Table XII-I. One way to approximate this is to tilt the field lens FL1 so that the combination of lenses FL1 and L2 magnifies the different parts of the spectrum appropriately. The required lens separations are also given in Table XII-I. A least squares linear fit was used to approximate a(x) and determine the amount of tilt for FL1.

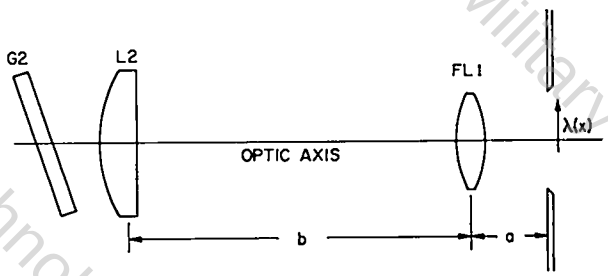

Fig. XII-10.
The use of the field lens FL1 to control the dispersion produced by the collimating lens L2.

TABLE XII-I

LENS SEPARATION PARAMETERS FOR DIFFERENT WAVELENGTHS

λ (Å)	x (mm)	$f_1 \frac{\cos \beta_2}{\cos \beta_1}$ (mm)	b (mm)	a (mm)
6900	-19.43	344.4	360.2	18.8
6700	- 9.69	346.8	361.7	17.6
6500	0.0	349.5	363.3	16.2
6300	9.66	352.1	364.1	14.87
6100	19.32	354.6	366.4	13.58

This method improves the image quality at S2 to an acceptable level.

E. SPACE RESOLVED THOMSON SCATTERING

The spatially resolved Thomson scattering experiment successfully measured electron temperatures in 1976,[7] but the signal-to-noise ratio was poor due to the small number (600) of spatial locations read on the SIT tube detector. The device has been taken off the Scylla IV-P experiment to effect changes both in method and hardware to increase the signal-to-noise ratio.

It was decided to increase the number of points read from 600 to approximately 10 000 and average over 16 points at each space-wavelength position in order to reduce the noise level by a factor of four. To accommodate this increase, the Prime 100 computer memory was also increased from 16k to 32k, and the time to read the data increased to ~ 0.5 s. During this amount of time, significant dark-current begins to build up on the detector, thus limiting its dynamic range. It was found that certain sections of the detector had more severe dark-current problems than other sections, so initially a scan pattern that reads the more sensitive zones of the tube first was used. This tended to equalize the dark-current irregularities across the tube, but it also produced anomalous readings at the zone boundaries. The problem was discovered by using the 3D graphics routines on the PDP-10 computer. (Before the data transfer link between the Prime 100 and the PDP-10, this effect had gone unnoticed.)

Being forced to return to a uniform master scan pattern, another method was sought to combat the dark-current buildup on the tube. The tube was cooled by passing chilled dry nitrogen through its enclosure, and it was found that cooling the tube below 20.6°C greatly reduces the dark current. This technique effectively eliminates the dark-current problem and permits multiple read scans after an exposure.

Each one of the 10 000 pixels read must be calibrated for accumulated charge vs integrated light intensity. The calibration data for each pixel can in principle be stored on the PDP-10 and used to normalize the data for analysis. However this would require approximately 10^6 words of data storage. Presently, ways are being sought to characterize the calibration curve of each pixel by a few (~ five) parameters, which would reduce the amount of storage to ~ 50 000 words.

Also, the triple-grating polychrometer and SIT tube detector must be jointly calibrated for wavelength vs spatial coordinate, again for 10 000 points. To simplify this procedure, a CAMAC-controlled stepping motor system has been developed to automatically determine the mapping of wavelengths and positions. This calibration data will occupy an additional 20 000 words of storage.

The large amounts of data storage and transmission required by this experiment make the use of a large computer facility like the PDP-10 a necessity. With a minimum of ~ 30 000 words of data gathered for each shot analyzed, high-speed data transmission will be required. The communications link between the Prime 100 and the PDP-10 has been upgraded to an eight-bit serial line, which can eventually be operated at 9600 baud. The 3D graphics capability on the PDP-10 will be useful for the proper display and understanding of the experimental results.

F. COMPUTER CODES

Some general purpose computer codes for problems that are common elements of various diagnostics have been developed.

1. Ray Trace Code. Starting from Fermat's principle, $\delta \int n ds = 0$, the eikonal equation for geometrical optics ray propagation can be derived

$$\frac{d}{ds}\left(n \frac{dr}{ds}\right) = \text{grad } n \quad ,$$

where n is the spatially varying refractive index, ds is the differential displacement along the propagation direction, and r is the spatial coordinate vector.

Several versions of one basic numerical code have been developed from this equation, given an analytic cylindrically symmetric density distribution, for ray propagation with initial conditions at specified displacements either parallel or transverse to the cylindrical axis. As is well known the refractivity has a λ^2 dependence on wavelength, and the motivation was to obtain a generally applicable formulation for any of the considerable number of laser wavelengths available from the visible to the far infrared, a range spanning more than three orders of magnitude in wavelength.

The focus of experimental interest may be on the angular or linear displacements of the rays themselves (Schlieren and related methods) or on the errors introduced by these effects on the interferometric fringe measurements that assume straight-line propagation. For the latter purpose, special double precision, small-integration-step versions of the code, sum the phase contributions over the actual trajectory and compare these with relevant quantities to give both total fringe count and the error that is made in the fringe count assuming rectilinear propagation. To obtain these relevant quantities the assumption is made that a lens positioned to image the plasma center on the detection plane equalizes the optical lengths of all straight-line paths emanating in a cone from the object point. The error count can have contributions both from the geometrical differences between the actual curved path and segmented rectilinear path and the fact that any deflection takes the ray through regions where the actual refractivity is less than along an extension of the initial path.

2. Impurity Radiation. Two related codes are available, both having at their core the time dependent solution of ionization and recombination rates for the ground state populations of various ionization stages of impurities.

The first code is suitable for radiation loss calculations and general predictions of temporal temperature behavior as a function of impurity concentration with ohmic heating and ion-electron equilibration terms included, starting from specified initial values. Only oxygen is included as a prototype for all low-Z impurities. No detailed spectral information is derived. A typical application is the prediction of ZT-40 heating previously reported already.[8] The ionization and recombination rate coefficients are taken from the Appleton Laboratory Tables and Graphs by H. P. Summers, and the electron excitation rates of averaged value resonance lines are taken as the general analytic expression of Seaton,[9] increased by a factor of 5 to bring it more into line both with recent detailed calculations on individual lines and fragmentary experimental results.

The second code is motivated as a temperature diagnostic. It iterates on solutions of the rate equations with successive guesses of the temperature history, given the density history, until a best fit is obtained to matching the appearance time and peaking of all the low-Z impurity spectral lines for which experimental data are available. This code uses analytical approximations of the various rate coefficients. The most serious error is an overestimation of the dielectronic recombination in a formulation given by Landini and Monsignori-Fossi[10] that is generally not valid for $n_e > 10^{12}$ cm^{-3}. However in a rising temperature, ionizing plasma (the specific situation for which the code is designed) the ionization coefficient is of dominant importance. For the latter the "exchange classical impact parameter" formulation due to Burgess[11] is used, which is generally regarded as the most accurate and agrees with extensive experimental data within a factor of two.

G. LASER-PLASMA INTERACTION STUDIES

The experimental data obtained during the interaction of a 150-J CO_2 laser with the cold dense mode of the one-meter-long Scylla I-C theta pinch were fully reported in the previous Annual report[12] shortly after termination of the experiment. During this year an extensive analysis, including a survey of relevant theory, was completed and resulted in the submission of a doctoral thesis (William T. Armstrong) to the University of Colorado. The abstract and concluding summary of the thesis are given below verbatim. For details reference is made to the thesis.

1. Abstract. Prompt stimulated Brillouin scatter (SBS) is studied on an experiment in which a high-power, pulsed CO_2 laser irradiates an independently produced, theta-pinch plasma. SBS does not significantly affect laser heating of the plasma.

The SBS signal consisted of a single, strong pulse occurring within $\pm$ 15 ns of the incident beam's peak power. The signal displayed some intermittency and shot-to-shot power fluctuation. Phase mismatching in the SBS coupling is attributed to a strong axial temperature gradient. A brief period of reduced temperature gradient, and corresponding enhanced SBS coupling, occurs near peak incident power. The constraint of significant SBS gain to this time period is consistent with the single-pulse characteristic and power fluctuations of the SBS signal.

The SBS signal was red shifted by ~ 51 A which corresponds to the ion-acoustic frequency. A theoretical fit of the SBS line shape gave a lower bound for the number of exponentiations of the backscattered signal from the noise level, $n_{ef} \geq 14$. SBS power measurements established an upper bound of $n_{ef} \leq 24$. With a gain length of 0.9 cm, these limits on n_{ef} correspond to an interaction length of 13 cm $\leq \ell_{int} \leq$ 22 cm. This interaction length is consistent with the high-power focus region where the SBS threshold is exceeded. The possible effects of Faraday rotation on SBS are discussed.

Measurements of density profiles and temperature histories permitted examination of laser refraction, local heating, and net absorption. Refractive containment of the CO_2 laser beam by an on-axis density minimum was observed at early times during the laser pulse. However, refractive containment was lost at late times due to the diffusive loss of the density minimum. Classical modeling of the expected heating required "bleached" absorption to account for the observed heating. A plasma absorptivity of ~ 46% was inferred from calorimetry measurements at 250 mtorr fill pressure. These results confirm that classical heating and refraction dominated the laser-plasma interaction.

2. Conclusions. Stimulated Brillouin Scatter:

a. SBS was observed with a signal characterized by a single pulse near the time of peak power.

b. The single pulse occurred in a time window of reduced axial temperature gradient.

c. SBS displayed the expected red-shift in frequency corresponding to the ion-acoustic frequency.

d. A theoretical spectral fit of the backscattered line shape agrees well with the measured temperature.

e. The spectral fit of the data and an absolute power estimate gave the SBS exponential gain value, n_e (number of e-foldings), to be 14-24 above the initial noise level.

f. This experimentally determined n_{ef} corresponds to an SBS interaction length consistent with the high-power density, focus region.

g. The constraints on SBS gain due to temperature gradients can account for the high thresholds and intermittent behavior of the SBS signal.

h. The SBS power was limited by a long gain length, low plasma noise level, and short laser focus region.

i. More detailed temperature measurements are needed to quantitatively study SBS dependence on the temperature gradient.

j. Single-shot spectral data with greater resolution is needed to study the theoretical spectral dependence in greater detail.

The most important feature of these results is the long SBS gain length. The SBS power was limited by the long gain length and short region in which threshold was exceeded. The SBS energy was apparently limited by the short time during which reduced axial temperature gradients allowed gain over a significant length.

Laser Beam Propagation:

a. Refractive containment of the CO_2 laser beam was observed at early times during the laser pulse.

b. Channeling of the laser beam in the programmed plasma density minimum was inferred from exit burn patterns.

c. Refractive containment was lost at late times.

d. Laser heating did not prevent diffusive loss of the density minimum.

e. Further study is needed to substantiate filamentation structure in the exit burn patterns.

Propagation through a long plasma was difficult. Improved containment of the laser beam requires a density minimum sustained through further magnetic-field programming.

Laser Beam Absorption and Plasma Heating:

a. Local absorption efficiency was high and consistent with classical theory for the portion of the laser beam contained in the plasma.

b. Net absorption efficiency was low due to a lack of refractive containment of the laser beam at late times during the laser pulse.

c. Temperature measurements at two axial stations showed substantial heating due to the initial laser spike.

d. Classical modeling of the expected heating is consistent with the temperature measurements.

e. Bleached absorption, i.e., an absorption coefficient incorporating the dynamically changing temperature, must be included in the analysis to account for the observed heating.

These results confirm that classical heating and refraction dominated the laser plasma interaction, and SBS caused only a minor change in heating efficiency.

H. FUTURE DIAGNOSTIC DEVELOPMENTS

There are currently three desirable diagnostic developments in an advanced conceptual or early design phase.

1. Far Infrared Faraday Rotation for ZT-40. The possibility exists to measure the poloidal field in ZT-40 with a Faraday rotation measurement on a far infrared laser beam on off-center transverse chords. For the 118-μ wavelength of CH_3OH, a central density of 5×10^{15} cm^{-3}, and a maximum poloidal field of 6 kG one obtains (a) up to about one radian linear polarization rotation in the longitudinal component of the poloidal field, (b) completely negligible rotation in the transverse field (B_ϕ and the orthogonal B_θ component), and (c) an only modest displacement of the laser beam at the exit window due to refractive bending. As in any Faraday rotation measurement the density must be known independently in order to determine the field, and for a proper measurement it is necessary to measure along several chords and use an Abel inversion-type unfolding to deduce a radial distribution. In principle, however, the density can be gotten from the same laser by interferometric techniques and, in view of the large rotation, some information could be derived from model fitting to just one or two chords.

Ideally one would use nonpolarizing, high-transmission windows on the machine diagnostic port and do all polarization analysis with independent external elements. However, given the desirability of using only sapphire windows on ZT-40, the extreme birefringence and differential absorption of sapphire to the two components of polarization can be used to advantage as having polarizer and analyzer fixed in place provided the correct crystal orientation exists in the windows. Calculations show that windows "crossed" in the absence of plasma will increase the transmission up to a factor of 5 for 90° plasma rotation. Commercially available lasers and cryogenic detectors can measure the "crossed" transmission

with a signal-to-noise ratio of at least 100, so that the measurement sensitivity of rotation angle should be approximately 0.2^{o}. Experimental tests of these predictions, for windows actually sealed into ceramic, will be made in the near future.

2. Short-Pulse Laser Thomson Scattering. An absolute density profile of a plasma, not requiring the inaccuracies of an inversion procedure, can be achieved, in principle, with laser scattering using only a single receiver, provided the light pulse is short enough so that its limited spatial extent provides the needed spatial resolution. An additional advantage of this technique is that much of the instrumental scatter at the entry and exit points to the vacuum chamber can be discriminated against by time-of-flight techniques.

For application to plasmas of diam $\geq$ 20 cm (e.g., ZT-40), a pulse width $\lesssim$ 0.1 ns is appropriate. The entire plasma is imaged onto the detector which is gated on for slightly more than the transit time of the pulse through the plasma (~ 1-2 ns). The plasma profile is obtained from the waveform of scattered intensity vs time (time corresponds to space in the plasma). Two modes may be considered, depending on detector risetime, τ_r: direct and integrated. In the direct mode (τ_r << scattered light pulse width) the instantaneous signal (suitably calibrated) corresponds to local density. In the integrated mode (τ_r >> scattered light pulse width) the waveform is essentially the integral of the profile, and would then be differentiated.

As a specific example we use ZT-40, with anticipated parameters: electron density, $n \sim 5 \times 10^{15}$ cm^{-3}, electron temperature, $T_e \sim 200$ ev, diam, D ~ 20 cm. We consider a ruby laser emitting one J in a single switched-out mode-locked pulse of 0.1-ns duration. We assume a photoemissive detector (photomultiplier or image dissector) with a quantum efficiency of 10% at 0.7 μm and an integration time of 2 ns. The spectral bandpass of the system is chosen to collect at least 95% of the scattered spectrum, which requires about $\pm$ 400 V under the assumed conditions (T_e = 200 eV, 90^{o} scattering). With a 2-mm beam size in the plasma, the receiver field of view is 2 mm by 20 cm. Thus the background radiation seen by the receiver comes from a slab of ~ 0.2 by 20 by 20 cm^3. Integrated over 800 V and 2 ns results in a background (free-free continuum) of 1.2×10^{-11} J. The scattered light from a 3 cm slug of plasma at the center would be $\sim 1.2 \times 10^{-10}$ J (for 0.1 steradian solid angle). Thus the peak plasma signal would be about 10 times greater than the background. Even more important is the signal-to-noise ratio, since it is the fluctuation in background during the transit that is of interest. With roughly 4.2×10^{7} photoelectrons of signal and 4.2×10^{6} photoelectrons of background, signal-to-noise ratio based on Gaussian statistics is better than 2×10^{4}. This is certainly optimistic since plasmas generally exhibit more continuum than pure bremsstrahlung and the detailed background fluctuation nature may well be nonthermal, a point which can only be decided by experiment. The extent to which the signal-to-noise ratio is more favorable than necessary is the extent to which parameters like laser energy can be compromised. A 0.1-J energy is considered readily achievable, and even 1-J should be below damage threshold.

The measurement would be flexible enough to be optimized for specific parameters, e.g., reducing the optical bandwidth if the temperature is lower. The measurement would be calibrated by Rayleigh scattering from a high-pressure gas fill as well as against interferometric data along the laser line of sight. Output recording would be on either a fast scope, or the Tektronix 7912 scan converter.

3. Laser Scattering with Sequential Mode-Locked Pulses. The prospect of having long-pulsed (500-μs) ruby lasers has stimulated interest in time-dependent Thomson scattering. At the densities contemplated for ZT-40 (5×10^{15} cm^{-3}) it is expected that the difficulty in observing scattered signals will not result from an inadequate number of scattered photons, but rather from an excess of light coming from the plasma. This then leads to the concept of phase-locked or signal-averaging techniques to extract the signal buried in the noise. We have recently become aware of successful experiments using such methods but operating on a vastly different time scale.[13]

The technique as envisioned at present involves taking a long-pulsed ruby laser and introducing an active mode-locking element within the laser cavity. The anticipated output would be a series of mode-locked pulses lasting for the full duration of the laser pulse, ~ 500 μs. Signal averaging would be done over as many pulses as necessary to obtain adequate signal-to-noise (e.g., for 5 μs) for repeated discrete sets of pulses over the full duration of the laser pulse train in order to give time-resolved electron temperature.

If 100 J are sustained over 500 μs in mode-locked operation, this average power of 200 kW will be sufficient for good time resolution. The shortest usable pulse will probably be about 500 ps. This limit is determined by the combined rise and fall time of the photomultipliers used to detect the scattered signals. Shorter times are certainly available from mode-locked lasers and faster detectors are commercially available, but photomultipliers with the required gain are limited to about this time duration. The maximum time separation between pulses will be bounded by the requirement to maintain a stable cavity configuration. To limit the cavity dimensions to something reasonable, this would suggest 20-30 ns between pulses or a duty cycle of 1/40 to 1/60, implying individual pulses of 8-12 MW. The output of the detector would be sent to a superfast boxcar integrator with an averaging time constant of several μs. The effective reduction of noise or equivalent effective increase in power will be proportional to the square root of the number of pulses averaged. For 1 μs this would be a factor of 5 to 7, or an effective laser power ~ 30 MW. This effective laser power is in the range that yields good results in current conventional scattering experiments on ZT-S. Clearly there is a trade-off between time resolution and effective laser power.

Initial efforts are aimed at seeing what can be produced in terms of a mode-locked long-pulse-chain ruby laser. A standing wave acousto-optic cell has been developed by bonding a lithium niobate transducer onto a quartz slab. Such a cell when antireflection coated should introduce sufficient periodic losses to produce mode locking.

REFERENCES

1. LASL Controlled Thermonuclear Research Program Report January-December 1976," Los Alamos Scientific Laboratory report LA-7082-PR (1978), p. 133-137.

2. F. C. Jahoda, "Submicrosecond Holographic Cine-Interferometry of Transmission Objects," Appl. Phys. Lett. 14, 341 (1969).

3. V. V. Antsiferov, K. G. Folin, V. S. Pivtsov, and V. D. Ugozhaev, "Ruby Laser with a Spherical Resonator with Smoothing of Spatial Inhomogeneities," Sov. Phy. Tech. Phy. Vol. 16, 2060 (1972).

4. F. R. Marshall and D. L. Roberts, "Use of Electro-Optical Shutters to Stabilize Ruby Laser Operation," Proc. IRE Vol. 50 (1962) p. 2108.

5. R. E. Siemon, "Polychrometer with Extreme Rejection of Stray Light," Appl. Opt., 13, 697 (1974).

6. M. Greenwald and W.I.B. Smith, "Triple Grating Polychromator for Thomson Scattering," Appl. Opt. 16, 587 (1977).

7. "LASL Controlled Thermonuclear Research Program Report January-December 1976," Los Alamos Scientific Laboratory report LA-7082-PR (1978) p. 132.

8. "LASL Controlled Thermonuclear Research Program Report January-December 1976," Los Alamos Scientific Laboratory report LA-7082-PR (1978), p. 64.

9. R.W.P. McWhirter, in Plasma Diagnostics Techniques, R. H. Huddlestone and S. L. Leonard, Eds., (Academic Press, New York, 1965), Chap. 6, p. 269.

10. M. Landini and B. C. Monsignori-Fossi, "A Simple Formula for the Total Dielectronic Recombination Coefficient," Solar Physics 20, 322 (1971).

11. H. P. Summers, "Ionization Equilibrium of Hydrogen-Like to Argon-Like Ions of Elements," Mon. Not. Roy. Astron. Soc., 169, 663 (1974); A. Burgess, "Semi-Classical Theory of Electron-Atom Collisions," AERE-R-4818, Sept. 14-16, 1964 (Meeting at Culham Lab), pp. 63-71, Proc. Symp. Atomic Collision Processes in Plasmas, Culham Report 4818, p. 63.

12. "LASL Controlled Thermonuclear Research Program Report January-December 1976," Los Alamos Scientific Laboratory report LA-7082-PR (1978) p. 132.

13. H. F. Dobele, K. Hirsch, and M.von Hellermann, "On Scattering Diagnostics with Periodically Pulsed Lasers to Follow the Continuous Evolution of Time Dependent Plasma Parameters," Preprint IPF 77-5, University of Stuttgart, April 1977.

XIII. THEORY

D. C. Barnes, J. U. Brackbill, T. Cayton, R. Y. Dagazian, J. P. Freidberg, S. P. Gary, R. A. Gerwin, D. W. Hewett, D. S. Lemons, H. R. Lewis, P. C. Liewer (Univ. of Maryland), R. C. Malone, D. Montgomery (Univ. of Iowa and College of William & Mary), C. W. Nielson, W. B. Riesenfeld, J. J. Sanderson (Univ. of St. Andrews), J. L. Schwarzmeier (Univ. of Wisconsin), A. G. Sgro, B. Abraham Shrauner (Washington Univ.), K. R. Symon (Univ. of Wisconsin), L. Turner, G. Vahala (College of William & Mary), D.Winske

A. INTRODUCTION

The work of the theory group is closely associated with and motivated by the experimental CTR program at LASL. For several years the problems and requirements of the Scyllac experiment provided the major motivation for research in the theory group. However, now that the Scyllac program has ended and the CTR effort at LASL has become directed toward alternate concepts, the variety of theoretical research has increased. This variety is reflected in the following description of theoretical work carried out in 1977 and it is expected to become greater in the future.

B. MHD STUDIES

1. Analytic and Numerical Studies of High-β Stellarators. An analytic formulation has been derived for calculating equilibria in a diffuse high-β stellarator configuration. Although analytic sharp-boundary equilibria have been known for some time, the extension to diffuse profiles is very nontrivial. The reason for this is as follows. Based on the sharp-boundary calculations, there is a strong suggestion that in a diffuse system one should expand about a basic θ-pinch field $B(r)\hat{e}_z$. Expansions of this type turn out to be incompatible with toroidal periodicity constraints and no such equilibria exist.

The expansion described here[1] overcomes this difficulty by considering the basic θ-pinch field to be of the form $B(r,\theta)\hat{e}_z$; that is, we must consider the leading order system to consist of noncircular flux surfaces with finite toroidal shifts. Under this assumption diffuse high-β stellarator equilibria can be found.

The leading-order field is the θ-pinch field just described. The first-order fields are helical fields, each one characterized by $\ell\theta + hz$. There can be an arbitrary number of helical fields with different ℓ values, but they must all have the same pitch number h. Also, no purely transverse fields are allowed in first order. The helical fields are determined from a potential function ϕ which satisfies the following second-order partial differential equation

$$\nabla^2\phi + \frac{\nabla\beta\cdot\nabla\phi}{1-\beta} = 0 \quad , \tag{1}$$

where $\beta(r,\theta) = 1 - B^2(r,\theta)/B_\infty^2$ appearing in coefficients. Toroidal effects are assumed to enter first in second order. To calculate the second-order fields, a periodicity condition (resulting from z independent terms) must be satisfied. This constraint imposes a second constraint between ϕ and β,

$$|\nabla\phi|^2 = g(\beta) - \frac{r\cos\theta}{R}(1-\beta)^2 \quad , \tag{2}$$

where g is an arbitrary function of β. Thus, the problem of finding high-β stellarator equilibria can be cast as two nonlinear, coupled partial differential equations for the unknowns ϕ and β.

These equations have been solved analytically for small but finite β. The result is a diffuse analog of the well-known sharp-boundary equilibrium relation with no toroidal shift. For high-β equilibria, a numerical code has been written. In this approach the solution is Fourier expanded in the azimuthal variable and a system of quasi-linear ordinary differential equations is

obtained. It is possible to obtain solutions with no toroidal shift when the appropriate helical field product is applied. Comparison of these results with earlier numerical and analytic work is proceeding.

Finally, a comparison has been made with the low-β stellarator. In both cases, helical fields are required to provide closed flux surfaces. However, in a high-β stellarator the toroidal drift force is balanced by the interaction of two helical fields: ℓ, ℓ+1. In a low-β stellarator a single helical field suffices. Here, the toroidal drift force is balanced, not by the helical fields, but by the interaction of a small applied vertical field with the small induced toroidal dipole current.

Numerical solutions of the diffuse, high-β stellarator equilibrium problem have been found by solving finite-difference approximations to the nonlinear, time-dependent equations describing ideal, magnetohydrodynamic flow in three dimensions.[2] Such solutions have provided answers to practical design questions associated with existing experiments; these design questions arise because, in contrast to tokamaks or even low-β stellarators, equilibria exist only for numerically correct helical field amplitudes. The solutions also have been used to study the equilibrium and stability properties of other configurations. Equilibria have been computed for existing experimental configurations with various plasma profiles, helical field combinations, and toroidal radii over a wide range of plasma β. From these results, the scaling of the helical field amplitudes with the principal parameters has been derived and summarized. Comparisons have been made between these scaling laws and recent experiments on Scyllac where the equilibrium fields were made adjustable. These comparisons confirm the accuracy of the numerical calculations, and demonstrate the improvement in confinement resulting from the improvement of the equilibrium.

Other configurations which have been studied numerically are: straight systems with combinations of helical fields characterized by ℓ=1,h and ℓ=3,3h; straight and toroidal systems with applied fields ℓ=0, ℓ=1, and ℓ=2 with the same pitch number h; and wall stabilized systems. It has been conjectured that the addition of an ℓ=3,3h field to an ℓ=1,h configuration can suppress MHD instabilities. The stability of straight systems with ℓ=1,h and ℓ=3,3h has been studied, and, at least for small helical field amplitudes, no stabilization by the ℓ=3,3h fields has been observed.

It would be desirable to reduce the dependence of the equilibrium fields on the plasma beta. One method by which this may be done is suggested by the much stronger dependence on β of the stellarator force produced by the interaction of ℓ=0 and ℓ=1 fields than by the interaction of ℓ=1 and ℓ=2 fields. By opposing these forces, the β dependence can be cancelled without cancelling the stellarator force. A possible problem arises because the ℓ=0 and ℓ=2 fields interact to produce a force with ℓ=2,h=0 dependences. Numerical studies of this interaction have been performed, and indicate that the resulting elliptical deformation of the plasma is not bounded to small amplitudes, but must be suppressed by an as yet undetermined external intervention.

Finally, wall stabilization of otherwise unstable equilibria has been computed with a plasma to wall ratio of 1:3. From the computations, a lower bound can be placed on the instability growth times which are much longer than the toroidal drift time.

In summary we now have analytic and numerical tools for studying high-β stellarator equilibria and can systematically examine new configurations with more desirable equilibrum and stability properties.

2. Simulation of Magnetohydrodynamic Instabilities. The 3-D MHD code used for studying high-β stellarators also has been used to study equilibria and stability of a straight, high-beta, $\rho = 0$ pinch configuration, as well as internal kink modes of a straight screw pinch. In addition to comparing the numerical results with analytic theories, the convergence of the numerical solutions was studied and the dependence of the solutions on various numerical parameters was examined.

3. Rigid-Drift Magnetohydrodynamic Equilibria for Cylindrical Pinches. The rigid-drift equations of magnetohydrodynamic equilibria in cylindrical geometry are:

$$(\vec{\nabla} \times \vec{B}) \times \vec{B} = 4\pi\vec{\nabla}p \quad ;$$

$$J_z \propto n \quad , \quad J_\theta \propto rn \quad ; \qquad (3)$$

$$p \propto n^\Gamma \quad ;$$

where $\vec{B}(r)$, $\vec{J}(r)$, p(r), and n(r) are the magnetic field, current density, pressure, and number density, respectively. Such magnetohydrodynamic equilibria have corresponding Vlasov equilibria.

When $\Gamma = 1$ (the isothermal case), these equations produce the Bennett profiles for the case of a pure Z-pinch.[3] The case of a pure θ pinch with $\Gamma = 1$ has been solved by Morse and Freidberg.[4] In both Z- and θ-pinch cases with $\Gamma = 1$, the pressure profiles drop to zero only at $r = \infty$.

For an arbitrarily pitched current density and $\Gamma = 2$, the equations have been solved analytically in terms of an infinite series of hypergeometric functions.[5] The condition $\Gamma = 2$ implies a local temperature that is proportional to the local number density. The shapes of the pressure and magnetic field profiles are completely determined by the model once two parameters are specified:

a. the local plasma beta on axis;
b. a quantity related to the pitch of the current density.

Particular profiles, plotted with the aid of the symbolic manipulation system, MACSYMA, have shown the possibility of occurrence of hollow profiles and reversed B_z fields simultaneously or independently. The pressure always falls to zero at a finite value of the radius.

This work may have relevance to understanding and manipulating ZT-40 equilibria.

4. Three-Dimensional Magnetohydrodynamic Turbulence and Pinch Stability. Nondissipative magnetohydrodynamic turbulence has been treated in a cylindrical region with a rigid, perfectly conducting boundary.[6] Canonical distributions have been constructed from three rugged invariants (magnetic helicity, cross helicity, energy) and two constraints have been imposed to simulate experimental conditions (fixed axial magnetic flux and an integral related to the poloidal flux). All fields were then expanded in Chandrasekhar-Kendall eigenfunctions of the curl operator.[7] All quiescent initial conditions led to finite mean-square expectation values for the expansion coefficients of the velocity field except those for which the magnetic helicity is extremal. These are force-free states which may involve field reversal. (Such symmetric states can exist only below certain current-to-flux ratios.)

Dual cascade situations sometimes can tend toward these extremal states. For example, in two-dimensional magnetohydrodynamics, excess energy can be cascaded to higher wave numbers and be dissipated there by resistivity and viscosity, while the inversely cascaded quantity (mean square vector potential) is not so readily dissipated. In three dimensions, energy and cross helicity can be cascaded to higher wave numbers and dissipated, whereas the magnetic helicity is less readily dissipated. This basic process (first suggested by Bretherton and Haidvogel for Navier-Stokes fluids[8]) provides a mechanism for the relaxation process to occur in three-dimensional (toroidal) Z-pinches in which the state of minimal energy to helicity is reached, as conjectured by J. B. Taylor.[9]

5. End-Loss Studies. Further numerical studies of plasma end loss have been obtained by solving finite-difference approximations to the time-dependent equations for ideal, magnetohydrodynamic flow in two dimensions. The results are found to compare well with new experimental data on mass lifetime in straight pinches, and with old data on the effect of simple mirrors on end loss from the linear Scyllac experiment.

A mysterious difference between the two-dimensional results and those obtained with a one-dimensional formulation which assumes radial pressure balance has been examined. By comparing the magnitude of those terms neglected in the

one-dimensional approximation with their actual value in the two-dimensional solutions, the source of the difference has been identified to be the magnetic field curvature term in the axial momentum equation. This term is found to be comparable with the axial pressure gradient, yet completely left out of the one-dimensional approximation.

The numerical method has been extended to incorporate the guiding center fluid equations, and will be applied to the study of multiple mirror confinement. The first step will be to recover both the guiding center and the magneto-hydrodynamic mass lifetime scaling with mirror strength. Next, energy anisotropy instabilities will be modeled by a simple relaxation process to examine how mirror strength, mirror separation, and relaxation time affect plasma end loss in a multiple mirror.

C. KINETIC EFFECTS

1. Gradient-driven microinstabilities. Two comparative studies of the family of instabilities driven by gradients perpendicular to a magnetic field were carried out. The first[10] included fully electromagnetic effects and propagation oblique to $\vec{B}$ for the high-frequency ($\omega \gg \Omega_{ci}$) modes associated with the relatively steep gradient of a perpendicular shock. The important results of this research were:

(a) At $T_e \gg T_i$, the ion acoustic instability is dominant, and its linear dispersion properties are unaffected by nonzero β_e and

(b) At $T_e \sim T_i$ and with density and magnetic field gradients pointing in the same direction, the instability of lowest threshold is the modified two-stream instability (with $k_z \neq 0$ rather than the lower hybrid drift instability ($k_z = 0$).

The second[11] study was restricted to electrostatic instabilities driven by density gradients, but considered modes of arbitrary frequency and generalized the work of Freidberg and Gerwin[12] to oblique propagation. The primary new results here were (a) a generalization of the Freidberg-Gerwin threshold criterion for the ion-cyclotron drift instability to arbitrary T_e/T_i ratio, and (b) detailed studies of the threshold and dispersion properties of the universal drift instability. Figure XIII-1 compares the growth rate of these two modes as a function of the diamagnetic drift. The threshold of the ion-cyclotron drift instability at zero beta is evident; it is also clear that the universal mode has no threshold in the electrostatic and local approximations and that further work on this mode is necessary to determine the conditions for its presence in a post implosion theta pinch.

The family of instabilities driven by a heat flux parallel to a magnetic field were also the subject of a comparative study. The threshold of the ion acoustic heat-flux instability, the mode considered most likely to lead to a heat-flux limit in $T_e \gg T_i$ laser fusion plasmas, was studied in detail. In the electrostatic ($\beta = 0$) limit, other instabilities (ion cyclotron, electron beam) are the first to go unstable at $T_e \lesssim T_i$, but these modes have relatively high thresholds and do not seem likely to lead to an effective heat-flux limitation.[13] However, at nonzero β and $T_e \sim T_i$, electromagnetic heat-flux modes have considerably

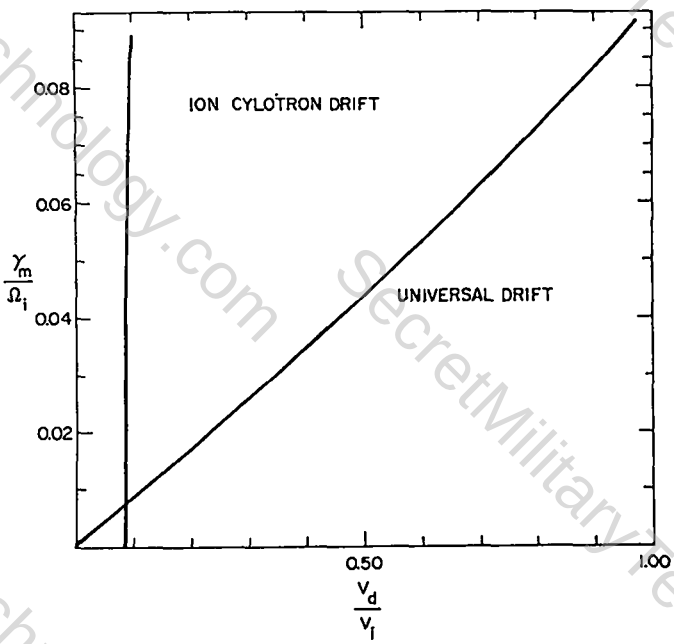

Figure XIII-1.
The growth rate maximized over wavenumber, ∂_m, of the universal and ion - cyclotron drift instabilities as a function density gradient drift speed v_d for Te = Ti. Here Ω_i = ion-cyclotron frequency and V_i = ion thermal speed.

lower thresholds than the ion acoustic instability;[14] therefore future studies will give more attention to electromagnetic modes.

In addition, a simple one-dimensional, one-fluid code has been written to model electron temperatures in a linear theta pinch and to study the possible effects of an anomalous heat flux limit.[15] The results indicate that near the end of a linear theta pinch the classical formula for the heat flux breaks down, due to the temperature scale length becoming shorter than the mean free path. If the flux is limited, in this region the temperature gradient over most of the profile is reduced and the energy confinement time is increased. Future work will concentrate on achieving a maximal increase in thermal confinement time. Current results indicate that an increase of at least an order of magnitude with respect to classical is possible.

A third type of instability studied was an electromagnetic mode driven by an ion beam.[16] This mode could be driven by thermonuclear alpha particles escaping in an axial direction from a linear reactor. The most important result here is that the growth rate of this instability is proportional to the 1/3 power of the beam density in contrast to the 1/2 power for many thermonuclear instabilities driven by isotropic alpha distributions.

2. A Nonlinear Theory for Electromagnetic Instabilities. In order to determine the anomalous transport associated with a given microinstability, an understanding of its nonlinear behavior is essential. A theory to describe the nonlinear state of transverse electromagnetic instabilities driven by anisotropic temperature distributions has recently been developed. The basis of the theory is an assumed distribution function based on two single particle integrals of motion for a charged particle in an electromagnetic wave field. This distribution function describes the instantaneous state of the wave-plasma system as it evolves in time and determines a nonlinear dispersion relation and two system energy constants. In the case of a zero frequency wave due to the Weibel instability driven by an initial electron temperature anisotropy, $T_{\perp o}/T_{\parallel o} > 1$, these relations are particularly simple and yield expressions for the energy in the wave magnetic field, the temperatures and the entropy of the system in terms of one unknown constant, $T_\perp/T_\parallel$, as the system evolves from $T_\perp/T_\parallel = T_{\perp o}/T_{\parallel o}$ to $T_\perp/T_\parallel = 1.0$. One important consequence of the theory is a simple expression for the maximum field energy. The theory has been verified by computer simulation of the Weibel instability. Extensions of the theory to magnetized plasmas appear to have wide application. These include: computing the collisionless absorption rate of magneto-acoustically heated plasmas, understanding the saturation level of the Alfven Ion Cyclotron instability (which is excited by perpendicular injection of neutral beams in mirror machines), and determining the reduction of heat loss in linear devices and the solar wind by high-beta electromagnetic heat-flux instabilities.

3. Linearized Analysis of Imhomogeneous Collisionless Plasma Equilibria: General Theory and BGK Equilibria. A generalized framework has been developed for analyzing the linearized equations for perturbations of inhomogeneous plasma equilibria in which there is a collisionless species, some properties of the solutions of the linearized equations have been described, and a basis has been given for numerical computations of the linearized properties of such equilibria.[17] The general approach has been applied successfully to some numerical studies of the stability of screw pinches within the framework of the Vlasov fluid model[18] and of the stability of Bernstein-Greene-Kruskal equilibria[19] When studying such inhomogeneous equilibria, it is useful to expand the perturbation potentials in eigenfunctions of the field operator which appears in the linearized equations and to define a dispersion matrix whose analytical properties determine the nature of the solutions of the initial-value problem. It is also useful to introduce auxiliary functions to replace the usual perturbation distribution functions, and to expand the auxiliary functions in eigenfunctionss of the equilibrium Liouville operators. By introducing the auxiliary functions, great freedom is achieved in the choice of the field operator, which appears in the linearized equations. This freedom can be used in some problems to define expansion functions for

the potentials that are particularly suitable for studying specific normal modes.

The general theory has been illustrated recently by using it as the basis for studying the stability of some large-amplitude Bernstein-Greene-Kruskal equilibria.[19] The stability properties of the BGK equilibria were determined independently by numerical particle-simulation studies for comparison with results of the general theory. An effective method was found for choosing an auxiliary function which yields a field operator particularly suitable for studying these equilibria. One of the eigenfunctions of the field operator is very similar to the unstable eigenmode of the equilibrium. This fact makes it possible to truncate the dispersion matrix severely. Excellent agreement with the numerical simulation results was obtained by using the truncated dispersion matrix.

4. Rotational Instabilities in a θ Pinch. A theory has been derived which attempts to explain the "wobble" instability observed in linear θ pinches. The instability corresponds to a gross m=1,n=0 mode (m is the azimuthal mode number and n the number of radial nodes) which rotates with a nonzero real frequency in the laboratory frame. Although rotation has long been thought to be the driving mechanism for the instability, none of the existing rotational instability theories provides a satisfactory explanation. In particular the m=1,n=0 mode is not found to be unstable in most theories; in those in which it is, the growth rate and real frequency predicted are far from the experimentally measured values.

In the present calculation, the high-β, finite Larmor radius equations for a rotating θ pinch are solved numerically subject to appropriate boundary conditions with particular attention focused on the m=1,n=0 mode. We find that this mode is unstable but that its maximum growth rate occurs not at $k^2=0$ (where it is neutrally stable) but at some finite $k^2>0$. The threshold for this mode is lower than that of any mode in the system and in this sense m=1,n=0 is the worst mode. However, typical growth rates are considerably smaller than m=2,n=0 growth rates when both modes are unstable. Good agreement with experiment is obtained assuming conditions corresponding approximately to complete end shorting. To get this agreement, we must assume that the plasma has a small positive charge which gives rise to an outward-pointing radial electric field (as arises from the ambipolar potential in a mirror machine).

5. Formulation of the Linearized Vlasov Fluid Model for a Sharp-Boundary Screw Pinch. A theoretical formulation has been derived for analyzing linearized equations appropriate to a straight, cylindrical, sharp-boundary screw pinch within the framework of the Vlasov fluid model.[20] This formulation has been applied to some computations relevant to finite-ion-gyroradius stabilization of MHD modes,[18] and it is being used to study magnetoacoustic heating in a collisionless plasma.[21] Surrounding the plasma is a cylindrical conducting wall, and there is a nonconducting vacuum between the plasma and the wall. By introducing a perturbation-dependent transformation of the phase space and linearizing about a zeroth-order state which depends on the perturbation, the linearized equations of Freidberg's Vlasov fluid model[22] are put into a form which would be correct for a hypothetical problem in which the plasma boundary is a rigid cylinder. The effects of the impulsive electric field at the actual perturbed boundary are taken into account in the zeroth-order state. The boundary conditions at the perturbed plasma boundary are continuity of the normal component of $\vec{B}$ and vanishing of the normal component of the net current density.

D. MAGNETOACOUSTIC HEATING

Magnetoacoustic heating is an attractive method for preferentially heating plasma ions when an appropriate dissipative mechanism exists at a convenient magnetoacoustic resonant frequency. Experimental evidence for the existence of a dissipative mechanism in a collisionless plasma is the observations by Grossmann, Kaufmann, and Neuhauser of collisionless damping of magnetoacoustic waves in a high-beta plasma.[23] Such a heating scheme may prove to be practical for reversed-field pinches; and, for a linear pinch, magnetoacoustic heating would not impose a limitation on end-stoppering schemes which have

been proposed. With a judicious choice of parameters, magnetoacoustic heating may allow the use of lower values of induced RF electric fields than are required when implosion heating is the sole method of heating.

Several aspects of resonant magnetoacoustic oscillations in high-beta, high-temperature plasmas have been considered, including energy balance, generalization of Poynting's Theorem to accommodate plasma motion, and various dissipation mechanisms for collisionless plasmas; also, the possible use of magnetoacoustic resonances as a plasma diagnostic has been considered. Most of these studies have involved the solution of linearized MHD or finite-ion-gyroradius equations; general screw-pinch equilibria have been considered for modes with finite axial wavelength. A numerical scheme for integrating the singular ordinary differential equations that occur with diffuse profiles has been devised.

The physics relevant to magnetoacoustic heating of a screw pinch in a collisionless plasma regime has been studied theoretically by two approaches and the results are being applied to cases of experimental interest. Heating times and associated induced RF electric fields have been computed. Both approaches are based on the Vlasov fluid model[22] in which collisionless ions and massless, fluid electrons are treated under the assumptions of quasi charge neutrality and negligible displacement current. The two approaches differ with respect to their ordering of small parameters and with respect to their treatment of the boundary region between the plasma and a surrounding vacuum.

1. Landau damping as a dissipation mechanism. In one approach, the techniques of earlier analyses of Turner[24] have been combined with a new ordering scheme, one which is adapted to the study of magnetoacoustic waves. The basic smallness parameter is the ratio of ion gyroradius to plasma radius; in terms of this parameter, the following quantities are assumed to be of order unity: local plasma beta, the ratio of plasma radius to any scale length of the wave, and the ratio of wave phase velocity along the magnetic field to the ion thermal velocity. This ordering scheme applied to the Vlasov fluid model provides a physical description of the plasma which contains kinetic effects along the magnetic field lines but retains only fluid-like effects transverse the the field lines; finite-ion-gyroradius effects do not contribute in leading order. A basic result of applying this description to a pinch configuration is the identification of ion Landau damping as a viable dissipative mechanism for converting magnetoacoustic wave energy into ion thermal energy.[25] The Landau damping causes a phase shift in the response of the plasma relative to the phase of an imposed oscillation of the confining magnetic field; this shift is responsible for the dissipation. At a magnetoacoustic resonance the amplitude of the plasma response and the associated rate of dissipation both peak. The total rate of energy dissipation is obtained by calculating the Poynting vector external to the plasma column. That the energy dissipated is converted completely into ion thermal energy is proved by use of a thermal transport equation derived from the ion Vlasov equation. In order to obtain the shortest doubling time, τ, for the plasma energy with the least induced RF electric field, E, it appears desirable to operate at a ratio of wave phase velocity along the magnetic field to ion thermal velocity approximately equal to 0.7. For example, $\tau \simeq 10^{-4}$s. has been obtained with E $\simeq$ 80 volts/cm.

2. Inclusion of finite-ion-gyroradius effects. In the other approach, the effect of finite ion gyroradius on magnetoacoustic heating of a sharp-boundary screw pinch is being studied. In order to take proper account of the sharp boundary, the starting equations are those derived by Lewis and Turner for applying the Vlasov fluid model to a sharp-boundary screw pinch.[18] Within the pinch the collisionless Boltzmann equation for the Vlasov fluid model has been solved analytically for small values compared to unity of kr_L and ω/ω_{ci}, where k is the largest relevant wavenumber, r_L is the ion gyroradius, ω is the frequency, and ω_{ci} is the ion cyclotron frequency. Finite-ion-gyroradius effects were kept to zero and first order and the solution is valid up to the sharp boundary. Because this approach uses a more general ordering, it also should be possible to determine whether dissipative mechanisms other

than Landau damping are operative for magnetoacoustic heating in a collisionless plasma. A differential equation for $\vec{u}$ ($\vec{A}^{(1)} = \vec{u}\times\vec{B}^{(0)}$) containing finite gyroradius effects was derived by substituting the solution of the collisionless Boltzmann equation into the transverse force-balance equation (the component perpendicular to $\vec{B}$ of the Maxwell $\vec{\nabla}\times\vec{B}$ equation). An analytical solution of the equation for $\vec{u}$ was used to calculate the heating of the pinch in the presence of an oscillatory driving electric field on a cylindrical surface in the vacuum region surrounding the pinch.[26] When there is a finite longitudinal wavelength ($k_z \neq 0$), significant additional heating can occur as a result of finite ion gyroradius. Computations relevant to specific experimental configurations are being carried out.

3. Relaxation processes as dissipative mechanisms. Finally, azimuthally symmetric and axially uniform magnetoacoustic heating of collisionless theta-pinch type plasmas was studied early in the year, and a phenomenological model was developed that showed how microturbulent-induced relaxation between the parallel and perpendicular ion temperatures could constitute a dissipation mechanism for such resonant heating.[27] Numerical methods for integrating the nonlinear partial differential equations of the model have been examined.

E. INTERNAL RING END STOPPER FOR OPEN-ENDED DEVICES

In open-ended magnetic confinement systems, it is desirable to reduce end loss of plasma because it constitutes the severest mechanism-limiting confinement. A scheme was proposed which could be employed in end-stoppering such devices and could be particularly suited to the needs of linear theta pinches.

The configuration that is proposed here is basically a multiply connected magnetic trap.[28,29] It is illustrated in Fig. XIII-2, where two ring conductors are shown inserted in a solenoid with a strong mirror at one end and connecting to a theta pinch on the other. Mirror coils can also be inserted in the regions between the rings. The cross-section area, the spacing, the total number of rings, and the strength of the solenoid and mirrors can all be varied to optimize the end-stoppering efficiency of the arrangement. The current in the internal rings flows in a direction opposite to that of the primary coil and is induced by pulsing the external solenoid. A magnetic configuration is generated which possesses a separatrix surface whose section is shown by the dashed line. On this line, the potential function[29] $U \equiv -\oint d\ell/B$ assumes a minimum tending to minus infinity on a circle inside each ring. The specific plasma volume $\oint d\ell/B$ (roughly equal to the average B^2) increases in all directions away from the separatrix surface. The integral is taken along a line of force, $d\ell$ being the length increment along this line. The plasma pressure distribution tends to peak on the separatrix, the plasma settling to a stable configuration as it enters the trap. These are low-beta arguments, but there is no reason to believe that they will be unfavorably modified in high beta. Kadomtsev has made simple arguments about the stability of $\beta = 1$ plasma in the region of bad curvature between the rings and the solenoid.

From the collisionless single-particle point of view, it is the isobars of B that play the important role in confinement. Particles executing adiabatic motion tend to be reflected at the points of intersection of the field lines with

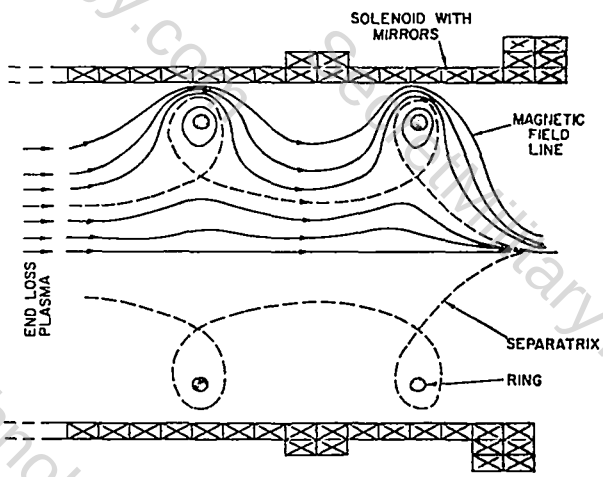

Figure XIII-2.
Schematic of magnetic field geometry of IRES.

isobars, the particular location of such reflection points depending on the particle velocity. The existence of a circular region inside each ring where the magnetic field strength is negligible causes a breakdown of the adiabatic motion. Nonadiabaticity in this region will produce scattering of the particles in velocity space. This may result in enhanced trapping of particles which are knocked out of the loss cone of the end mirror(s).

Denoting the fraction of particles trapped because of the presence of a single ring to the total number of particles going through the ring region in the absence of the ring by ϵ_R, the reduction of end loss is proportional to $f_R = (1+\epsilon_R)^{-n}$, where n is the number of rings. For simplicity, we have also assumed that only one final end mirror does the trapping and that it works stably. Figure XIII-3 shows f_R as a function of ϵ_R and n. It is seen that if $\epsilon_R = 0.3$, the end loss can be reduced by 75% if five rings are employed.

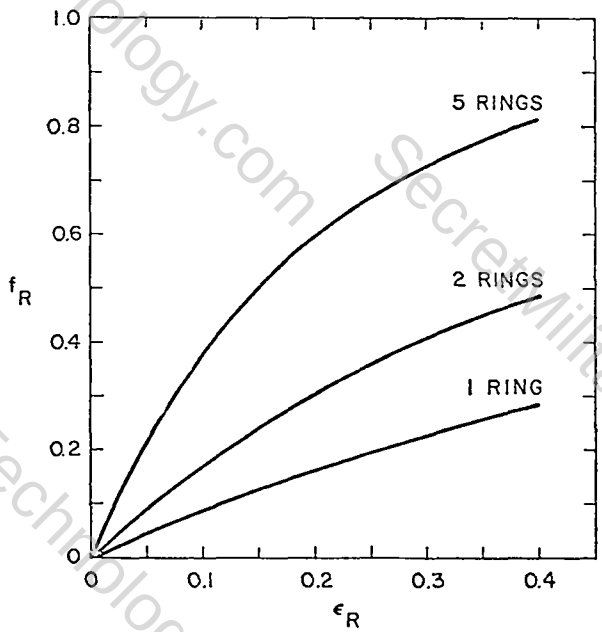

Figure XIII-3.
Percent reduction in end loss versus fraction of particles trapped by single end mirror as a result of nonadiabatic scattering by the rings.

It follows from these considerations that the internal ring conductors perform a twofold function:

1. They MHD stabilize the magnetic mirrors present in their vicinity; and

2. they introduce nonadiabatic behavior in a small but sizeable region inside the plasma which tends to shorten the spacing required between multiple mirrors. A device of the type being proposed here can be easily shaped into a cone by employing rings of diminishing diameter (Fig. XIII-4) providing for easy external mechanical support of the forces exerted by the plasma wind on the rings and the end coils. This conical internal ring confiner end (CIRCE) could also be viewed as a magnetically shielded solid end plug when it is looked at through the end of the theta pinch. A formal study of high-beta equilibria in the presence of internal conductors has been underway also. It will lead to a more realistic examination of the stability and confinement properties of internal ring end stoppers.

F. NUMERICAL SIMULATION

1. Two-Dimensional Finite-Electron-Mass Hybrid Simulation. The finite-electron-mass hybrid plasma simulation model of the lower hybrid drift (LHD) instability has encountered some numerical difficulties that have proved quite difficult to understand. Upon comparison of full PIC and hybrid simulation of the same problem, it is apparent that the physics required to simulate the

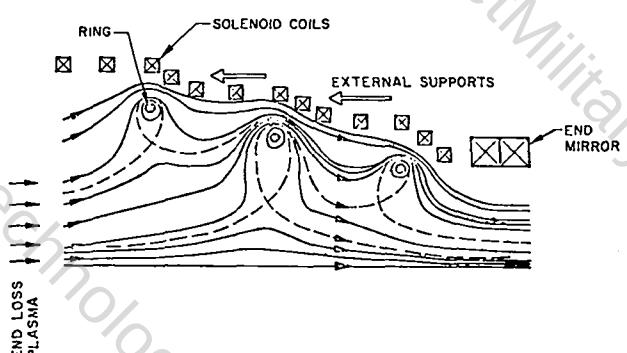

Figure XIII-4.
Schematic of magnetic field geometry of CIRCE. One half-section.

LHD instability is retained in the hybrid model. Figure XIII-5(a) shows B_z contours of this instability at various times and y-averages of these same contours are shown in Fig. XIII-5(b). Figures XIII-5(a) and XIII-5(b) were obtained from a PIC simulation and Figs. XIII-6(a) and XIII-6(b) show the comparable results of the hybrid simulation. Also evident is some enhanced diffusion (see Fig. XIII-6(b)) on the high magnetic field side of the sheath. This diffusion has proved to be numerical in origin, and consequently, the code as it now stands cannot be used for nonlinear studies. The numerical mechanisms underlying this phenomenon are quite complex and, in addition, have been obscured by a combination of random particle-like fluctuations due to the PIC treatment of the ions and recently discovered low-frequency oscillations of the inhomogeneous equilibrium.

It is now believed that a numerical instability has been identified which gives rise to the enhanced diffusion. The instability arises from the interaction between fluid electron and electrostatic field equations, which produces numerical turbulence in the electrostatic field. It is believed that this turbulent field then, through greater resistivity, produces the observed diffusion.

Progressing to this point has required the further expansion of this model to include the capability of treating the ions as well as the electrons as an Eulerian fluid. This has been

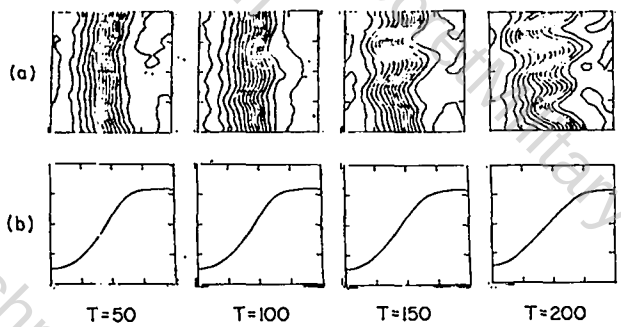

Figure XIII-5.
Full-particle simulation of the time evolution of the magnetic field component B_z. The x-y contours of B_z for $0 < -x < 10\ c\omega_{pe}^{-1}$ and $0 < y < 20\ c\omega_{pe}^{-1}$ are shown in (a) while the y-averaged profile of B_z is shown in (b).

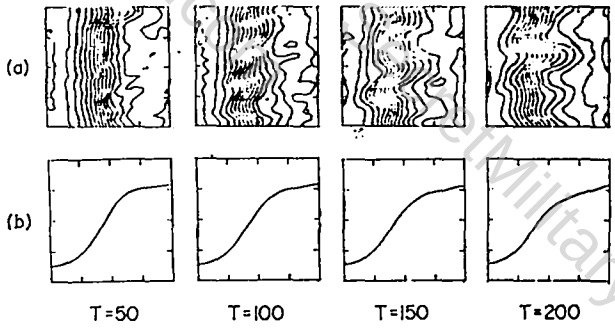

Figure XIII-6.
Hybrid simulation of the time evolution of B_z with all parameters the same as the full-particle simulation shown in Fig. XIII-5. Comparison of the results of the two simulation techniques reveals very similar wavelength and growth rate for the developing flutes.

necessary in order to eliminate the random PIC fluctuations already mentioned and has subsequently allowed the identification of a low-frequency ($\omega \simeq 240\ \omega_{pe}$) oscillation of the inhomogeneous equilibrium.

Finally, to insure that the instability could not result from some physical process still included in the model, a one-dimensional stablity analysis of this model has been completed. We find that for $\vec{k}\cdot\vec{B} = 0$, the model contains only Alfvén and ion acoustic modes, as expected. The dispersion relation for $\vec{k}\cdot\vec{B} \neq 0$ is

$$\omega^2 = (V_a^2 + C_s^2)k^2 \quad . \tag{4}$$

For configurations for which $\vec{k}\cdot\vec{B} \neq 0$, electron cyclotron motion must be followed but the relevant frequency for time-step restriction is determined only by the components of $\vec{B}$ parallel to $\vec{k}$. Thus the stability analysis has verified and exceeded earlier claims concerning the maximum allowable time step--further encouraging our belief in the ultimate utility of the model.

2. 1D Hybrid Simulation Results.

a. THOR Experiment. Several more simulations of the implosion phase of the Maryland Toroidal Device THOR were performed. Good agreement with the experimentally observed field profiles and neutron yields was found. The observed sequence of neutron pulses correlated with the most

compressed phase of each of several bounces indicated by the calculations. Furthermore, x rays corresponding to a plasma of 5 keV were found experimentally, which correlated in the calculations with a 3-to-5 keV low-density region on the outer edge of the plasma. A diagnostic that mimics the experimental x-ray detector is being included in the code and should allow a more meaningful comparison with the experimental temperatures.

b. Quasilinear Resistivity. The quasilinear perpendicular resistivity[30] model of Liewer and Krall has been included in the code as an alternate option to the quasiempirical Chodura resistivity.[31,32] This model requires a time step much smaller than required by the particle dynamics routines (which consume most of the time per cycle); therefore we are currently attempting to subcycle several field advances into one particle time step. When this is accomplished the running time of the code in the quasilinear mode should be increased by a factor of 3 to 10.

c. Pitch Programming of ZT-40. Mercier stable q(r) profiles which satisfy the global stability conditions $\infty < 0.5$, $\phi_z > 0$ (ϕ_z is the total Z flux) may be found from equilibrium theory. We have begun to consider how such profiles may be set up dynamically. One way is by proper programming of $q(r_{wall}, t)$. Thus we address the question of how to map $q(r_{wall}, t)$ into $q(r,\infty)$, the equilibrium q profile. This mapping depends on both plasma motion and field diffusion; indeed, some diffusion is required for q to penetrate the plasma. The low density region near the wall is represented by a force-free, wall-emitted plasma in which anomalous radial electron thermal conduction and other processes are assumed to keep the plasma isothermal and less than 100 ev. Figure XIII-7 illustrates one example of the transformation. In this case $\phi_z > 0$, but $\beta \sim 1$. Note that q(r) near the center falls from its programmed value due to resistivity. If a higher q is desired in this region q_{wall} must be larger at earlier times, or a bias field must be applied. A systematic search for stable q profiles on ZT-S is called for. These should then be compared with experiments, and predictions for ZT-40 should be made.

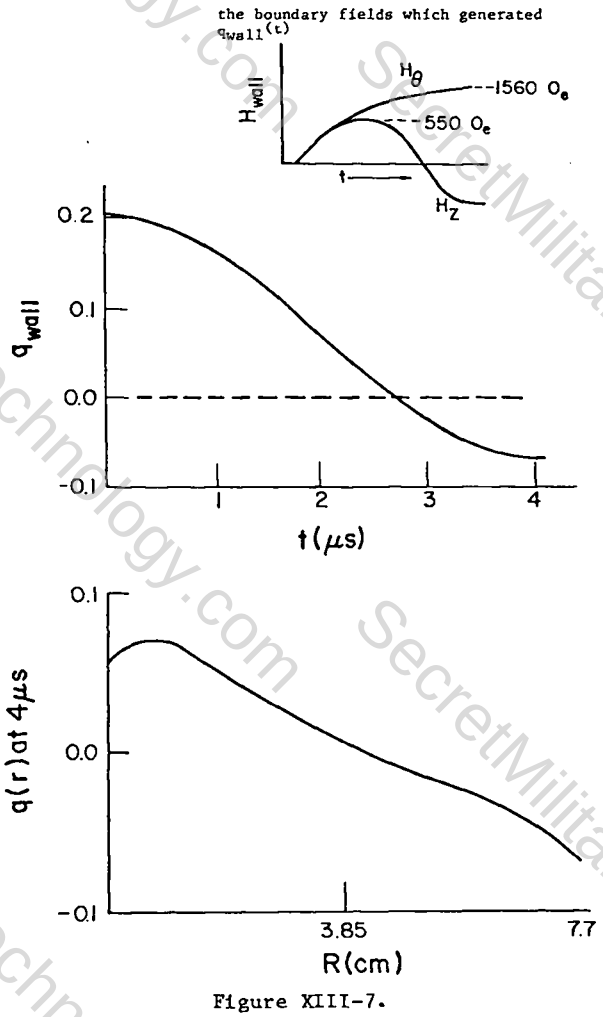

Figure XIII-7.
The q(r) profile resulting from the given $q_{wall}(t)$ profile.

d. Approach to Equilibrium and Anomalous Cross-field Thermal Conduction. Late-time (~ 3 ∂s) data from the Staged-Theta-Pinch experiment were used to test the approach of the code to an equilibrium. Unfortunately the calculated equilibrium was over-compressed. Better agreement was achieved when the electron temperature was limited to 100 eV and smoothed. This may be indicative of anomalous cross-field thermal conduction and/or the decrease of turbulence and anomalous resistivity (observed at the University of Maryland) below that used in the code. This work is still continuing.

3. Cylindrical Hybrid Code Development. Development of a 2-D cylindrical (r-z) plasma simulation technique which treats the electrons as a massless, neutralizing fluid has recently been initiated. Vlasov ions are represented by

standard PIC techniques and all components of both the electric and magnetic fields are retained but in the nonradiative limit. Our intentions are to apply this model first to the θ-pinch end-loss problem, but a great variety of problems can be addressed once the basic code is written.

The essential features of the algorithm are as follows. We assume density N, ion current $\vec{J}_i$, and magnetic field $\vec{B}$ profiles. Now the $m_e = 0$ limit of the electron momentum equation gives the self-consistent electric field

$$\vec{E} = -\frac{\nabla(NT_e)}{eN} + \frac{\vec{J}_e \times \vec{B}}{eNc} + \eta(\vec{J}_i + \vec{J}_e) \quad , \qquad (6)$$

where T_e and J_e are the electron temperature and current, respectively. T_e will be advanced in time from an initial value and $\vec{J}_e$ can be easily generated from Ampere's law given $\vec{J}_i$ in the quasi-neutral limit in which the irrotational electron and ion currents cancel.

The quasi-particle "ions" are given initial positions and velocities using weight factors so that by integrating over velocities the desired initial densities and ion currents are approximately recovered. The ions can now be advanced in time by particle-in-cell techniques, and the newly advanced density and ion currents calculated.

The remaining requirement to complete the time step is the recalculation or updating of the electric and magnetic fields so that they are consistent with the new density and ion currents. This is accomplished by using Faraday's law to update $\vec{B}$

$$\vec{B} = -c \nabla \times \vec{E} \quad ,$$

in which $\vec{E}$ is again produced by (5).

The most immediate problem is that (5) is not useful as $N \to 0$. In that many problems of interest in CTR do indeed have regions of comparatively low density, it is desirable to have the algorithm automatically detect and provide a field solution from Maxwell's equations in the low-density region. Currently we are attempting to treat this region as a vacuum.

G. FAST LINER DYNAMICS

The compressible fast cylindrical liner model of Shearer and Condit, namely the impulse-momentum approach,[33] was extended to more correctly treat cylindrical convergence of the liner. This extended model was then used to obtain analytical representations for the optimized neutron yield from an adiabatically compressed lossless DT plasma and analytical representations for the corresponding initial and final conditions. The analytical results agreed very well with the CHAMISA code, and a paper by R. A. Gerwin and R. C. Malone deriving and presenting these results has been written for submittal to Nuclear Fusion. As an example, one of the results is that the liner turn-around radius is a factor of order unity times the geometric mean of the initial liner radius and thickness.

More recently, the impulse-momentum approach has been further extended to include the effect of the driving electrical circuit on a liner magnetically imploded in a Z-pinch mode. (The earlier work assumed that the undriven liner possessed an initial kinetic energy.) In the earlier work, the results could be obtained by examining the dynamics near turn-around, so that a high-pressure approximation was appropriate (final plasma pressure larger than initial liner bulk modulus). In the new work, the results have had to be extended to include arbitrary pressures. A result based on dimensional analysis is that, for fixed final plasma temperature (~ 10 keV), and for fixed values of certain dimensionless ratios that are appropriate to the problem, the system gain (ratio of fusion energy to capacitor bank energy) scales as the square root of the initial charge on the bank. Thus, one has to optimize the device by adjustment of these dimensionless parameters. A code is being written to do this. The results will then constitute an upper bound on the gain of a real liner-plasma device, since plasma losses are still ignored.

During 1978, considerable effort was directed to the development of the fast liner implosion code, CHAMISA. At the end of 1978, the code had

the following capabilities: 1D Lagrangian implicit hydrodynamics; (2) tabular material equation-of-state covering all thermodynamic phases, ionization, and electron degeneracy; (3) a new analytic treatment of the electrical resistivity of aluminum and copper covering all phases; (4) nonlinear magnetic field diffusion (B_θ in cylindrical geometry only); (5) cross-field electron and ion thermal conduction; (6) bremsstrahlung loss; (7) nondepleting thermonuclear burn; (8) full coupling of liner to an external driving circuit (z-pinch only); (9) boundary condition options which simulate various physical entities (e.g., an adiabatic plasma, an incompressible liner, or B_θ or B_z adjacent to a perfect conductor), and thereby permit significant savings in computer time.

Development of this code is continuing in response to the needs of the Fast Liner Experiment at LASL.

The code has been used extensively to make comparisons with the analytic implosion model of Gerwin and to provide benchmarks for two reactor-studies codes. More recently the code was used to model the full time history of liner implosions on the two capacitor bank configurations planned for use in experiments at LASL. The results have been used as guides in preparing for the initial fast liner experiments.

Comparisons have been made of code calculations with data from Russian fast liner experiments. The agreement was quite good for older (circa 1967) experiments which are well documented in the literature. Efforts at comparison with the more recent LN-20 experiments have been frustrated by the difficulty of obtaining a complete set of experimental parameters and results from Russian preprints.

H. TRANSLATIONS OF RUSSIAN REPORTS AND PREPRINTS

During 1977, Russian Exchange Workshops were held at LASL on the prospects of high-beta systems and on feedback stabilization of plasma confinement systems. In addition, a USSR-LASL exchange workshop took place in the USSR on fast liner implosions, a meeting of the Joint Fusion Power Coordinating Committee was held at LASL in midyear, and LASL CTR Staff Members participated in Russian conferences on plasma diagnostics and superconducting magnet technology. As a result, much Russian material of programmatic interest was furnished to LASL scientists, and a considerable fraction of this material was translated into English either in its entirety or in title and abstract form.

Complete translations were made of the following preprints and reports.

"A study of the Dynamics and Stability of a Liner, Electromagnetically Accelerated on the LN-20 Device," S.G. Alikhanov, V.P. Bakhtin, V.G. Belan, V.M. Brusnikin, I.S. Glushkov, N.A. Karimova, A.D. Muzychenko, Yu.M. Senatorov

"Acceleration of Liners to High Velocities on the LN-20 Device," S.G. Alikhanov, V.P. Bakhtin, G.Yu. Lopatovsky, A.D. Muzychenko, V.A. Sibilyev

"A Study of the Outlook and Optimization of Energetic Electrodynamic Plasma Guns," V.I. Vasilyev, A.M. Zhitlukhin, V.G. Solovyeva, Yu.V. Skvortsov, N.M. Umrikhin

"A Theta Pinch with External Plasma Injection," V.P. Alipchenkov, V.I. Vasilyev, I.K. Konkashbaev, I.S. Landman, L.B. Nikandrov, Yu.V. Skvortsov, F.R. Ulinich, S.S. Tserevitinov

"Construction of the MK-200 Installation," R.G. Bikmatov, N.V. Goryacheva, A.M. Zhitlukhin, A.I. Kolchenko, A.P. Lototsky, A.D. Kiskin, A.M. Tikhonov, S.A. Sergeyev, Yu.V. Skvortsov, V.M. Strunnikov, S.S. Tserevitinov

"Calculation and Optimization of Plasma Guns," Yu.V. Skvortsov, N.M. Umrikhin

"A Study of the Neutron and X-Ray Output from the MK-200 Plasma Gun," R.G. Bikmatov, V.I. Vasilyev, V.V. Gavrilov, N.V. Goryacheva, A.D. Kiskin, N.M. Umrikhin, A.I. Yaroslavsky

"Passage of a Plasma along a Magnetic Field," A.M. Zhitlukhin, I.V. Ilyushin, B.Ya. Lyubimov, Yu.V. Skvortsov, V.G. Solovyeva

"Transport of Plasma Blobs with Energies of 100 kJ," A.M. Zhitlukhin, V.N. Lyashenko, S.A. Ravichev, Yu.V. Skvortsov, V.M. Strunnikov, S.S. Tserevitinov

"Processes Occurring the the Gap of a Coaxial Plasma Gun Fed from an Inductive Energy Store," E.A. Azizov, I.V. Kochurov

"A Study of Plasma Stream Parameters in Plasma Guns," V.I. Vasilyev, A.M. Zhitlukhin, A.P. Lototsky, V.G. Solovyeva, Yu.V. Skvortsov, N.M. Umrikhin

"Collision of Two Dense Plasma Streams," V.M. Alipchenkov, R.G. Bikmatov, V.I. Vasilyev, N.V. Goryacheva, A.M. Zhitlukhin, I.V. Ilyushin, A.D. Kiskin, I.K. Konkashbaev, V.N. Lyashenko, L.B. Nikandrov, S.A. Ravichev, Yu.V. Skvortsov, V.G. Solovyeva, V.M. Strunnikov, A.B. Titov, S.S. Tserevitinov

Translations of titles and abstracts (where available) were made of the following reports and preprints:

"Comprehensive Experiments on Plasma Compression in a Z-Pinch Liner System on the LN-20 Device," S.G. Alikhanov, V.P. Bakhtin, V.M. Brusnikin, I.S. Glushkov, G.Yu. Lopatovsky, A.D. Muzychenko, V.A. Sibilyev

"Technical Design of the LN-20 Device," S.G. Alikhanov, V.G. Belan, I.S. Glushkov, A.I. Kolchenko, I.K. Konkashbaev, V.A. Lanis, A.D. Muzychenko, E.N. Polyanskaya

"A Straight Z-Pinch-Liner Thermonuclear System," S.G. Alikhanov, V.P. Bakhtin, V.M. Brusnikin, I.S. Glushkov, A.D. Muzychenko

"A Study of Model Thermonuclear Liner Systems," S.G. Alikhanov, V.P. Bakhtin, V.M. Brusnikin, I.S. Glushkov, R.Kh. Kurtmullaev, A.L. Lunin, A.D. Muzychenko, V.P. Novikov, V.V. Pichugin, V.N. Semenov, G.E. Smolkin, E.G. Utyugov, I.Ya. Shipuk

"Production of Megagauss Fields by the Method of Magnetic Implosion," S.G. Alikhanov, V.G. Belan, G.I. Budker, A.I. Ivanchenko, G.N. Kichigin

"A Pulsed Thermonuclear System with Dense Plasma," S.G. Alikhanov, G.N. Kichigin, I.K. Konkashbaev

"The Generation of Intense Toroidal Fields Through Magnetic Flux Compression," S.G. Alikhanov, V.G. Belan

"Radiative Instability of a Bounded Plasma," S.G. Alikhanov

"Ohmic Heating of a Dense Hydrogen Plasma," S.G. Alikhanov, E.L. Boyarintsev, I.K. Konkashbaev, V.A. Kornilov

"Investigation of a Fast Pulsed Discharge in Hydrogen," S.G. Alikhanov, E.L. Boyarintsev, V.A. Kornilov, T.S. Melnikova

"Experiments with a High-Current Pulsed Arc," S.G. Alikhanov, I.K. Konkashbaev, B.S. Estrin

"A Theta Pinch with Liner and External Plasma Injection," Yu.V. Skvortsov

"Experiments on Heating of a Dense Plasma by a Strong, Fast-Rising Magnetic Field in a Straight Theta Pinch," V.A. Burtsev, A.P. Zhukov, B.V. Lyubin, V.A. Kubasov, V.N. Litunovsky, V.A. Ovsyannikov, V.G. Smirnov, V.P. Fedyakova

"Passage of a Plasma Through a Magnetic Nozzle," A.M. Zhitlukhin, I.V. Ilyushin, B.Ya. Lyubimov, Yu.V. Skvortsov, V.G. Solovyeva

"The Angara-5 Accelerator Complex," E.P. Velikhov, V.A. Glukhikh, O.A. Gusev, G.M. Latmanizova, S.L. Nedoseyev, O.B. Ovchinnikov, A.M. Pasechnikov, O.P. Pechersky, L.I. Rudakov, M.P. Svinyin, V.P. Smirnov, V.I. Chetvertkov

"A High-Current Electron Accelerator Producing Microsecond Beam Pulses," V.A. Glukhikh, O.A. Gusev, M.P. Svinyin, O.P. Pechersky, A.S. Perlin, E.M. Mellekh, E.P. Pavlov,

G.M. Latmanizova, V.S. Kuznetsov, M.I. Avramenko, V.B. Markov, L.A. Vykhodtsev, N.G. Beruchev, S.A. Kolyubakin

"A Fast-Acting Foil Disconnect Switch," A.B. Andrezen, V.A. Burtsev, V.M. Vodovozov, V.A. Dubyansky, N.P. Egorov, V.N. Litunovsky, V.A. Ovsyannikov, A.B. Produvnov, V.F. Prokopenko, I.V. Shestakov

"A Study of the Electrical Explosion of Cylindrical Foils in Air," V.A. Burtsev, V.A. Dubyansky, M.P. Kasatkina, A.B. Produvnov

"Aspects of a Pulsed Thermonuclear Reactor with Imploding Liner," G.A. Baranov, V.A. Glukhikh, O.A. Gusev, V.A. Zheltov, E.N. Izotov, Yu.K. Kalmykov, A.B. Komin, M.V. Krivosheyev, V.G. Kuchinsky, I.F. Malyshev, A.B. Mineyev, M.A. Gotovsky, V.V. Kantan

"A Two-Stage Electroexplosive Current Interrupter," V.A. Zheltov, A.V. Ivlev, A.S. Kibardin, A.V. Kromin, V.G. Kuchinsky, Yu.A. Morozov

"An Inductive Energy Store with Electromagnetic Current Multiplication," A.V. Ivlev, A.S. Kibardin, A.V. Kronin, V.G. Kuchinsky, K.M. Lobanov, I.F. Malyshev

"Pulsed Energy Sources Based on Inductive Energy Stores," V.A. Glukhikh, O.A. Gusev, A.I. Kostenko, B.A. Larionov, N.A. Monoszon, A.M. Stolov, G.V. Trokhachev

"Research and Development of a Homopolar Generator with Superconducting Excitation Winding," V.N. Artemov, V.A. Glukhikh, K.K. Dyachenko, V.V. Ivanov, B.G. Karasev, A.Yu. Koretsky, I.F. Malyshev, N.A. Monoszon, V.N. Skripunov, G.V. Trokhachev, G.F. Churakov, V.V. Kharitonov

"A Shock-Excited Hompolar Disc Generator," E.A. Bezgachev, V.A. Glukhikh, V.V. Ivanov, B.G. Karasev, I.F. Malyshev, V.V. Kharitonov

"Development of a Shock-Excited Homopolar Generator for Feeding a High-Current Electron Accelerator," V.A. Glukhikh, B.G. Karasev, V.V. Kharitonov, V.N. Skripunov

"Homopolar Generators with Superconducting Excitation Winding," V.V. Kharitonov, A.Yu. Koretsky

"Numerical Modeling of the Compression of a Magnetic Field by an Imploding Liner," R.A. Volkova, V.M. Goloviznin, F.R. Ulinich, A.P. Favorsky

REFERENCES

1. J. P. Freidberg and L. D. Pearlstein, "Rotational Instabilities in a Theta Pinch," submitted to Phys. Fluids (1978).
2. D. C. Barnes and J. U. Brackbill, Nucl. Sci. and Engr., 64, 18-32 (1977).
3. W. H. Bennett, Phys. Rev. 45, 89 (1934).
4. R. L. Morse and J. P.Freidberg, Phys. Fluids 13, 531 (1970).
5. L. Turner, to be published.
6. D. Montgomery, L. Turner, and G. Vahala, "Three-Dimensional Magnetohydrodynamic Turbulence in Cylindrical Geometry," to be published in Phys. Fluids.
7. S. Chandrasekhar and P. C. Kendall, Astrophys. J. 126, 457 (1957).
8. F. P. Bretherton and D. B. Haidvogel, J. Fluid Mech. 78, 129 (1976).
9. J. B. Taylor, in Pulsed High Beta Plasmas, ed. by D. E. Evans (Pergamon Press, Oxford, 1976) 59-67.
10. Don S. Lemons and S. Peter Gary, "Current Driven Instabilities in a Laminar Perpendicular Shock," J. Geophys. Res. (to be published) (1978).
11. S. Peter Gary and J. J. Sanderson, "Density Gradient Drift Instabilities: Oblique Propagation," Phys. Fluids (to be published) (1978).
12. J. P. Freidberg and R. A. Gerwin, Phys. Fluids 20, 1313-1315 (1977).
13. S. Peter Gary, "Electrostatic Heat Flux Instabilities," J. Plasma Physics (to be published) (1978).
14. S. Peter Gary, "Ion-Acoustic-Like Instabilities in the Solar Wind," J. Geophys. Res. (to be published) (1978).

15. S. Peter Gary, A. G. Sgro and A. W. DeSilva, "Axial Density Profiles and Nonclassical Thermal Conduction in Linear Theta Pinches," Phys. Fluids (submitted for publication) (1977).

16. S. Peter Gary, "The Electromagnetic Ion Beam Instability and Energy Loss of Fast Alpha Particles," Nuclear Fusion (to be published) (1978).

17. H. Ralph Lewis and Keith R. Symon, (submitted for publication in Journal of Mathematical Physics).

18. H. R. Lewis and L. Turner, Nuclear Fusion 16, 993 (1976).

19. J. L. Schwarzmeier, H. R. Lewis, B. Abraham Shrauner, and K. R. Symon, to be published.

20. H. Ralph Lewis and Leaf Turner, to be published.

21. H. R. Lewis, Proceedings of the Annual Controlled Fusion Theory Conference (May 4-6, 1977, San Diego, California), paper H8.

22. J. P. Friedberg, Phys. Fluids 15, 1102 (1972).

23. W. Grossmann, M. Kaufmann, J. Neuhauser, Nuclear Fusion 13, 462 (1973).

24. L. Turner, Phys. Fluids 20, 654 (1977) and Phys. Fluids 20, 662 (1977).

25. L. Turner, Proceedings of the Annual Controlled Fusion Theory Conference (May 4-6, 1977, San Diego, California), paper D20.

26. H. R. Lewis, Proceedings of the Annual Controlled Fusion Theory Conference (May 4-6, 1977, San Diego, California), paper H8.

27. T. E. Cayton, R. A. Gerwin, and L. Turner, Proceedings of the Annual Controlled Fusion Theory Conference (May 4-6, 1977, San Diego, California) paper PB8.

28. S. I. Braginskii and B. B. Kadomtsev in Plasma Physics and the Problems of CTR, Vol. III, p. 356.

29. B. B. Kadomtsev in Plasma Physics and the Problems of CTR, Vol. IV, p. 417.

30. P. C. Liewer and N. A. Krall, Phys. Fluids 16, 1953 (1973).

31. R. Chodura, Nucl. Fusion 15, 55 (1975).

32. A. G. Sgro and C. W. Nielson, Phys. Fluids 19, 126 (1976).

33. J. W. Shearer and W. C. Condit, "Magnetically Driven Metal Liners for Plasma Compression," in Energy Storage, Compression, and Switching, W. B. Bostick, V. Nardi, and O.S.F. Aucker, Eds., (Plenum Publishing Co., New York, 1976).

XIV. COMPUTERS

G. I. Chandler, R. Conrad, N. E. Greene, F. C. Jahoda, K. A. Klare,
J. W. Lillberg, L. W. Mann, C. W. Nielson, S. M. Ross, R. W. Wilkins

A. INTRODUCTION

The shortage of computer resources at LASL, coupled with the increased utility of the PDP-10 and MFE network, has made the USC facility a vital link in the LASL MFE effort. The PDP-10 has been used for scientific problems, administrative accounting, and inventory control. Many of the large particle simulation and MHD stability codes have been shifted to the network from the LASL computers. The yearly progress will be discussed in five phases: hardware enhancement (Sec. B-1) software enrichment (Sec. B-2), network development (Sec. B-3), experimental interfacing (Sec. B-4), applications of the USC computer and network, and future plans for augmentation of the computing facilities (Sec. B-6).

The preliminary design of the ZT-40 control and data acquisition system is outlined (Sec. C-1). The Scylla IV-P operating system was upgraded and routinely handles 60k bytes of data per discharge (Sec. C-2). A link between the experiment minicomputers and the PDP-10 is operational (Sec. C-3). The Sigma 2's have been improved by multiple terminals, serial CAMAC links, and a new graphics display system (Sec. C-4). Transient recorder linearity has been much improved with the aid of a computerized calibration system (Sec. C-5). Automated two-dimensional data acquisition has advanced with a completed algorithm for handling digitized Polaroid streak pictures and work is in progress on implementing a digital video frame grabber (Sec. C-6).

B. CTR USER SERVICE CENTER

1. Hardware. The items of equipment purchased this year are listed below together with a description of how each item is expected to increase the capacity and capability of the USC:

a) A terminal line concentrator (Digitial Equipment Corporation designation DN87) which handles higher speed lines for graphics and experimental data, provides capability for networking to minicomputers in the experimental program, and adds an additional 32 lines for time-sharing use. (The concentrator can be expanded to handle a total of 64 lines at a cost of approximately $21k.) This terminal handler is also expected to cut response time on the PDP-10. The former terminal concentrator requires the PDP-10 CPU to perform all character handling one at a time. The new device contains a small processor of its own which handles these functions and receives from and transmits to the PDP-10 in block mode.

b) A disk controller (DEC designation RH10) was ordered so that the traffic to and from the three disks on the system could be separated. This improvement to the system should make response time for time-sharing users much faster.

c) Memory Multiplexor (DEC designation MX10) was needed to give the terminal line-concentrator memory access. The existing memory has only four ports and those are needed for the network interface, the disk data channel, tape data channel, and the central processor. The multiplexor handles up to eight channels on one port thus allowing the channels with the least traffic to share a port and also providing room for expansion.

d) A microprocessor (Motorola 6800) and dual-headed printer (QUME) were purchased so that a sufficient character set could be put on line to do the word processing required for technical papers. The second head provides Greek letters and mathematical symbols in addition to the normal alpha-numeric symbols on the first head. The microcomputer uses software developed on the PDP-10 to drive the printer.

Although all of the items mentioned above were ordered early in the year they did not arrive until February 1978. In a field that is improving technically very rapidly it is unfortunate that one has to plan an acquisition so far ahead. It is wise to attend new product displays to aid in this planning but we have learned the hard way that delivery dates often slip badly especially on new products.

2. Software. The word-processing formatter was incorporated into the text editor and improved in the following ways:

a. Equation formatting for technical papers was made easier.

b. Double-column formatting was implemented.

c. Figure captions and figure placement in relation to the text were made to conform with Laboratory standards.

d. Footnote handling was made easier for the formatter.

e. Internal changes were made which decreased the editor response time as much as ten times on some commands and made the editor code much easier to maintain.

f. Commands were added which made FORTRAN programming, debugging, and execution easier and inadvertent file deletion was made more difficult.

The word-processing system is now used by all CTR-Division secretaries to do everything but small memos or letters. Each secretary in the Division has a word-processing terminal which produces exportable copy and it has been estimated that a trained secretary can produce a technical paper in one-third the time required by former methods. Papers produced by word-processing are also less likely to have errors and more likely to have revisions that improve content or conciseness because of the ease of modification.

The LASL USC text editor word processor has been exported to the other major nodes of the MFE network and has been found to be equally useful at these sites.

The access to the PDP-10 from experimental data-acquisition minicomputers has been enhanced by a special PDP-10 monitor software module added this year (in collaboration with a DEC software consultant). This module was designed to eliminate some of the drawbacks associated with connecting the minicomputers to the PDP-10 by asynchronous lines. The normal monitor treats asynchronous lines as terminal lines with a resulting high software overhead and severe restrictions on the nature of the data. The new monitor module bypasses the terminal handler with its high overhead and establishes a protocol with byte count and check sum which allows passing of arbitrary streams of eight-bit data bytes. An error correction protocol is also provided. The line speed was originally limited to 1200 baud but the new terminal line concentrator will permit it to be increased to 9600 baud.

This facility for handling data lines represents a reorientation of the USC staff thinking on how to handle data streams from the minicomputers. It was originally thought that the DA28, which handles traffic from the MFE network PDP 11/40 to the PDP-10, could be shared by another PDP 11/40 passing experimental data. It has become apparent that the software complexity of such a system would require one Staff Member working nearly full time for maintenance since the software would have to be modified for every DEC monitor and network change. Although sharing the DA28 appeared to be cost effective for us, it is apparent that the MFE network staff would not be able to support such a change. To go it alone, making our system nonstandard, was not cost effective for us. We plan to support higher baud rates than 9600 by buying synchronous lines for the DN87 which can pass up to 40 000 baud.

The PDP-10 utility library has been improved substantially throughout the year. The International Mathematical and Statistical Library was purchased to supplement our library of subroutines translated from the Los Alamos Central Computing Facility. Systematic testing of the accuracy of PDP-10 FORTRAN Library subroutines and other routines for simple functions is now under way because users have noted discrepancies between the PDP-10 solutions and solutions on other computers.

The system software is currently up to date with the latest DEC monitor and network software installed. There have been several machine language subroutines written to handle tape input-output, byte manipulation, and operational procedures.

3. Network. The MFE network has developed into a stable and reliable computing system for the local users. Due to the current saturation of LASL computing facilities, most users have found that the MFECC network provides better turnaround and produces rapid, high-quality graphics output via the Versatec printer/plotter. Unfortunately microfiche is still produced at LLL and arrives in the mail a week after it is run. The addition of

SLOPE (a simulator for the CDC operating system) and DBCTRL (an improved interactive debugging package) within the past year has made the system somewhat more flexible and easier to use, as well as provided a greater degree of compatibility with LASL computing facilities. We have found some difficulty in running large codes at night due to large core (LCM) limitations and the small LASL time allocation, so these codes are still run at LASL. Tape access time for archival files has been improved by the new FILEM (file manager) and the retrieval time of archival files should diminish even more with the new mass storage system that is being acquired for the network. With the addition of a CRAY computer to the network by early summer, it is expected that demands for network time will continue to increase.

4. Experimental Interfacing. The PRIME 300 on Scylla IV-P is connected to the PDP-10 via a 1200-baud line that employs the monitor module discussed under software. This line is used for shipping shot data for archival storage and subsequent data analysis on the PDP-10. The PRIME 100 has been tested on the same type of line. It is passing data to the PDP-10 for analysis of experimental diagnostics. Ports for the PRIME 400 (ZT-40 control and data acquisition minicomputer) and the Sigma 2 on ZT-S, will be available in the spring of 1978. The new terminal concentrator makes it possible to boost all these lines to 9600 baud if needed.

5. Application. Since many of our users are not experienced programmers, elementary manuals on how to use the PDP-10 and the MFE network have been prepared.

The USC now has 104 users and is near saturation during prime time. Often we have all eight dial-up lines in use and as many as 40 users on the PDP-10. The users are split about equally between network and PDP-10 stand-alone users. The network users are generally running particle simulation, reactor design, or MHD codes that are large production problems. The PDP-10 problem mix is more editing, word processing, and data analysis. Some 2-D MHD time-dependent and MHD equilibrium codes are run on the PDP-10 as background or at night. The USC staff has participated in the development of an Impurity-Radiation code and modifications to a MHD Equilibrium-Stability code so that it could be applied to ZT-40 and the High Beta Tokamak.

A cross compiler for the Motorola 6800 microcomputer has been purchased and installed to give users an easy method for generating 6800 code.

6. Future Plans. In order to satisfy the increased demands on the USC, the central processor is scheduled to be replaced in fiscal year 1980. It is hoped that the new processor will be four times as fast as the KI currently in use. The equipment being purchased in fiscal year 1978 and 1979 will be compatible with migration to the new configuration. The data channels will be replaced with a type that can access more than 256k of memory, the tape units will be replaced with higher density units, the memory will be upgraded to a more compact, reliable type that requires less maintenance, and higher density disks will be considered if user demand warrants it.

C. AUTOMATED DATA PROCESSING AND COMPUTER CONTROL

1. ZT-40. Preliminary design of the ZT-40 control and data-acquisition system was completed. A Prime 400 computer system was ordered and delivered for this task. It has a factor three to four speed advantage over the Scylla IV-P Prime 300, greater capacity for eventual extension of both fast memory and disk size, and capability for true multi-user time-sharing (RPRIMOS IV) in Real Time Operating System (RTOS)--i.e., while the Control Program is operating in a top-priority mode. The present hardware consists of 64k 16-bit words of main storage, two 3M word disk drives, two Tektronix 4014 terminals, TI 733 terminal for logging tasks, and a Versatek electrostatic printer-plotter. A CAMAC branch driver has been procured and integrated into RTOS for the interface to the experiment.

The computer will be located in a screen room which will also house much of the data acquisition equipment. As shown in Fig. XIV-1, the computer, via the CAMAC branch driver, communicates over a parallel highway with several CAMAC crates within

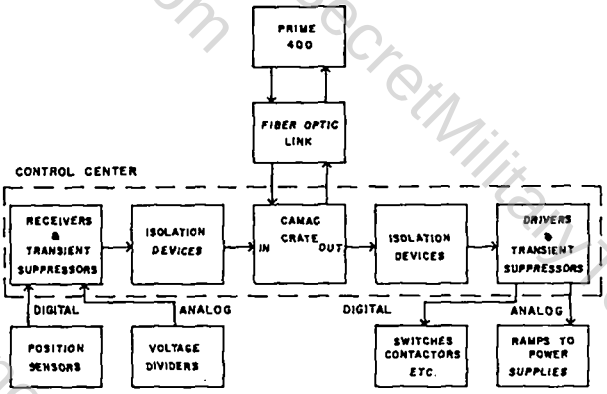

Figure XIV-1.
Conceptual design of ZT-40 control system. Dotted line encloses electronics located immediately above power supply room.

the screen room. Many of the individual CAMAC modules will be data acquisition devices connected to the external world through patch panels and signal conditioning units. A few modules are dedicated to control functions either for machine operation or diagnostics equipment. In particular, as shown, one module communicates with the fast timing pulse generators, which in turn, through fiber optics links, provide triggering signals both for the capacitor banks that energize ZT-40 and various diagnostic equipment. Two other modules, also through fiber optics links, serve the less critical timing control and monitoring functions of the diagnostics equipment and the crowbar gaps. Finally, there is shown in Fig. XIV-1, a CAMAC module serial highway driver that is optically coupled to the machine control center located in nine shielded relay racks near the power supplies. This control center contains additional CAMAC crates and interface circuitry designed to implement all the control functions except the fast triggering (operating and/or monitoring capacitor banks, interlocks, vacuum valves, etc.) while isolating the control circuitry from voltage transients generated by machine operation. More details of the screen room, the wiring, the optical coupling, the control center to machine interface, and the gap monitor development are described in Sec. XVII.

2. Scylla IV-P. The operating system on the Scylla IV-P Prime 300 computer was upgraded to the latest Prime revision (No. 11) and the disk controller converted from an 8-sector to 32-sector format, for compatibility with current releases of Prime software and with our other Prime computers. Prime's time-sharing system, PRIMOS III, was implemented to permit multiple users when the control program is not running.

Data acquisition devices currently being read by the computer include 52 Biomation 610's, two Biomation 8100's, 80 SEC 610's, 12 neutron scalers, and 62 ADC channels of the single-point Thomson scattering diagnostics--nearly 60 000 bytes of data per shot. A small auxiliary (6 ft by 5 ft) screen room is being installed, which, through optical coupling and serial CAMAC link to the computer, will accommodate as many as 100 additional diagnostic channels. The two Biomation 8100's were placed in tandem to extend the time scale of the coupled cavity data from 40 to 80 μs while maintaining 0.02-μs resolution.

3. Prime/PDP-10 Link. As discussed above, the Experiment Interface Computer (EIC) PDP-10 link concept has been abandoned. The new system is based on a high-speed serial terminal-type link with CAMAC teletype driver modules rather than a very high speed parallel link. At the present 1200-baud line speed all the data from a Scylla IV-P shot is shipped in two to four minutes. When the planned installation in early 1978 of 9600-baud input ports is complete, less than half a minute will be required and adaptation of the shipping program to the Real Time Operating System will cause this to occur automatically after each shot.

ASCII-formatted files can be shipped in either direction so that program development as well as data analysis can be run on either end of the link according to convenience. The same system is operational for the Prime 100.

4. Sigma 2. Our two Sigma 2's have again undergone several important improvements. These include support of an arbitrary number of terminals to edit and control programs, serial CAMAC instrumentation for support of remote terminals, and a new display system:

a. Terminals. The system monitor has been revised to permit connection of any number of terminals just as if they were the system console teletype. These terminals are interfaced through CAMAC modules having first-in first-out buffers as well as the necessary serializing. They communicate to a core resident program which recognizes and treats a number of control characters in a manner similar to the PDP-10. This program queues foreground tasks. The monitor structure itself limits the system to a single background user at any one time. Together with the new editor reported last year, this terminal capability has eliminated nearly all usage of the card reader and teletype.

b. Serial CAMAC. Serial CAMAC drivers have been implemented through individual modules in a standard (parallel highway driven) CAMAC crate. With the use of special adapters (U-ports) they can send and receive data over considerable distances with only one wire pair in each direction. The original motivation was to support Biomation 610 transient digitizers at the RFX experiment located over 500 feet from the computer screen room. The standard 200-s time period per 24-bit CAMAC operation was achieved. Currently one serial CAMAC driver replaces the previous noise-sensitive link to ZT-S for reading Biomations and another links the electronics shop to the Scyllac computer for general-purpose testing of new equipment or trouble shooting of defective devices.

c. New Display. The old four-channel video disk system used to display waveforms, text, and plots on standard TV monitors has become increasingly unreliable. A more modern digital electronic system to perform the same function has been purchased from Grinnell Systems. It has 512 x 512 display points for each of four screens. It was interfaced through CAMAC and is capable of generating alphanumerics, vectors, boxes, and more.

In the past the Sigma 2's have had their own limited plotting routines. For compatibility with the increasingly popular plotting package PLOT 10, used on the PDP-10, it was decided to make a smaller version of it (calendar plotting removed) for the Sigma 2's. The output character and control strings intended for storage displays, such as the Tektronix 4010, were converted by monitor overlay into commands for the Grinnell Systems unit. The result, although software-speed limited, is faster than a terminal operating at 9600 baud. The old routines for standard graphs remain available where the 8k word saving in core usage of this more limited package is necessary.

5. Transient Recorders. Doubts about the linearity of the Standard Engineering 610 E transient recorders initiated examination of their design. A method to quickly test linearity of a large number of units was required and devised. It uses a repetitive linear ramp waveform input, computer readout, and histogramming of the frequency of occurrence of each discrete output voltage level. With removal of certain resistors, glaring breaks in the frequency spectrum (output levels that almost never occurred) were also removed. The method measured the dynamic gain and also revealed that the divider string for the comparators has too little current, resulting in decreased gain at low frequencies and hence serious error if dc calibration is used. This deficiency is in the process of being corrected with installation of a special Zener diode. The cumulative error from the average gain measures the integral nonlinearity, i.e., deviation from straight line ramp. The circuit changes have improved this from more than $\pm$ 2.0 to about $\pm$ 0.4 in units normalized to 64 (six bits) full scale.

Solutions of problems with the CAMAC interfaced Biomation 610 transient recorders have resulted in a simpler and more reliable handshake procedure in the interface while reducing the commands needed to read each data word from four to one. Because the dynamic shift register that refreshes the Biomation memory operates on a faster cycle time (2 μs) than the data can be transmitted over a CAMAC line, consecutive words are read from the output register at 512 μs intervals, i.e., after one complete 256-word memory refresh cycle, when the next consecutive word again appears in the output register.

6. Automated 2-D Data Acquisition. In anticipation of obtaining a TV frame grabber, an algorithm was completed by Group M-8 for determining streak picture trajectories and trace widths from digitized Polaroid pictures. This algorithm was transferred to the MFECC network CDC-7600 and debugged, and a substantial inventory of Scyllac data shots accumulated, awaiting further detailed analysis.

The TV frame grabber, or video image processing system (VIPS), was acquired from Videology, Inc. It can digitize and store eight-bit information (256 gray levels) either for one 512 by 512 picture or for four-256 by 256 pictures. As customary with first models from a manufacturer, improvements have been necessary and [illegible] standard (parallel highway driven) CAMAC crate. With the use of special adapters (U-ports) they can send and receive data over considerable distances with only one wire pair in each direction. The original motivation was to support Biomation 610 transient digitizers at the RFX experiment located over 500 feet from the computer screen room. The standard 200-s time period per 24-bit CAMAC operation was achieved. Currently one serial CAMAC driver replaces the previous noise-sensitive link to ZT-S for reading Biomations and another links the electronics shop to the Scyllac computer for general-purpose testing of new equipment or trouble shooting of defective devices.

c. New Display. The old four-channel video disk system used to display waveforms, text, and plots on standard TV monitors has become increasingly unreliable. A more modern digital electronic system to perform the same function has been purchased from Grinnell Systems. It has 512 x 512 display points for each of four screens. It was interfaced through CAMAC and is capable of generating alphanumerics, vectors, boxes, and more.

In the past the Sigma 2's have had their own limited plotting routines. For compatibility with the increasingly popular plotting package PLOT 10, used on the PDP-10, it was decided to make a camera output and the frame grabber memory has been interfaced through CAMAC to the Sigma 2. A memory test program was written which writes the frame and then checks it, including various pattern lengths and random access. Failures after modification of the unit and replacement of some marginal components are down to about one bit per 100 frames.

Stored frames can be read on tape in the same format used for the digitized Polaroid pictures for transmission to the network 7600, enabling comparisons to be made as both line detection algorithms and spatial and intensity calibrations are developed. Eventually, sufficient simplifications are sought to do the entire analysis on a local minicomputer immediately upon data [illegible] frequency of occurrence of each discrete output voltage level. With removal of certain resistors, glaring breaks in the frequency spectrum (output levels that almost never occurred) were also removed. The method measured the dynamic gain and also revealed that the divider string for the comparators has too little current, resulting in decreased gain at low frequencies and hence serious error if dc calibration is used. This deficiency is in the process of being corrected with installation of a special Zener diode. The cumulative error from the average gain measures the integral nonlinearity, i.e., deviation from straight line ramp. The circuit changes have improved this from more than $\pm$ 2.0 to about $\pm$ 0.4 in units normalized to 64 (six bits) full scale.

Solutions of problems with the CAMAC interfaced Biomation 610 transient recorders have resulted in a simpler and more reliable handshake procedure in the interface while reducing the commands needed to read each data word from four to one. Because the dynamic shift register that refreshes the Biomation memory operates on a faster cycle time (2 μs) than the data can be transmitted over a CAMAC line, consecutive words are read from the output register at 512 μs intervals, i.e., after one complete 256-word memory refresh cycle, when the next consecutive word again appears in the output register.

XV. MAGNETIC ENERGY TRANSFER AND STORAGE

J. D. Rogers, E. M. Honig, C. R. King, J. D. G. Lindsay,
G. A Miranda, P. Thullen, H. Vogel, R. W. Warren, D. M. Weldon,
J. M. Weldon, D. H. Whitaker, K. D. Williamson, Jr., J. J. Wollan

A. SUMMARY

During the year the goal of the group changed from development of the superconducting magnetic energy transfer and storage (METS) system for use in future theta-pinch experiments to development of superconducting tokamak poloidal field systems (TPFS). The emphasis on the TPFS program is directed toward TNS requirements. The major objective of the program is to provide an integrated system demonstration by 1982 of a nominal 50-kA, 20-MJ, 7-T superconducting coil swung in a 2-s bipolar mode. With the METS program of the past few years as a basis, emphasis will be placed on three main technology development areas - superconducting coils, switching, and power supplies. In addition, studies are being performed for several conceptual tokamak TNS machines.

The METS program will be concluded with a demonstration METS-SFTR coupled superconducting prototype system which should be operable in late 1978 or early 1979. This system is to be composed of one 400-kJ, 25-kA superconducting energy storage coil and all associated charging and switching equipment. The coil will be charged in 300 s to a field level of 2.5 T at 25 kA through continuous duty leads and discharged in 0.7 ms through special coaxial pulsed-duty leads. The energy transfer is efficient, being determined by the storage coil inductance, transfer capacitance, and load inductance resonant circuit.

Major accomplishments during the past year include the following items:

1. Initiation of a preliminary conceptual engineering design for a 7-T, 20-MJ, 50-kA, superconducting TPFS coil.

2. Successful swinging of the 300-kJ, METS, Westinghouse coil in the bipolar TPFS mode ($\pm$ 12.1 kA, $\pm$ 2.72 T, 1.1 T/s).

3. Successful demonstration of commutated dc machines as pulsed power supplies for the TPFS.

4. Completion of several studies for the tokamak design group of General Atomic including the conceptual design of a 3-MA breaker and a 500-MJ homopolar.

5. Completion of the interrupter facility upgrade permitting a 60-kA, 60-kV test capability.

6. Successful testing of axial field interrupters to 37 kA and 38 kV.

7. Successful operation of two 17.8-cm vacuum interrupters in parallel at a total current level of 30 kA.

8. Near completion of the 6-T, dipole, superconducting magnet for use in the cable evaluation test facility.

9. Successful development of a 3-pin cryogenic disconnect capable of carrying 5 kA at a resistance of 15 nΩ.

10. Successful development and testing of a hybrid switch capable of carrying 25 kA continuously, interrupting this current and withstanding 60 kV.

11. Successful operation of Helix Corp., 700-W, 4.5-K refrigeration system.

12. Instigation of a Laboratory-wide helium conservation program.

B. 7-T, 20-MJ SUPERCONDUCTING TPFS COIL

1. Coil Design. A preliminary conceptual engineering design of a 7-T, 20-MJ superconducting energy storage coil has been initiated. The first magnetics and superconducting cable designs are complete. Energy loss calculations for a 1-s cosinusoidal magnetic field swing from +7 T to -7 T were made for a 50-kA, multistrand Roebel transposed cable. A cryostable 13:1, Cu to NbTi sub-bundle was designed. Minimal heat transfer calculations were made to assure stability. A similar design was also carried out for a 5.5-T, 20-MJ coil.

Proposals were received from industrial suppliers for development of a 50-kA NbTi superconducting cable. Two contracts are being negotiated for 7.6-m lengths of prototype cable

and various lengths of subcable components for testing. One such cable is to be built by Magnetic Corporation of America (MCA) working with a six-around-one first sub-bundle soldered together and insulated with double nylon wrap. Two configurations will be made. In the first, the sub-bundle will have two superconducting and four copper strands; in the second, three superconducting and three copper strands. Six of these first sub-bundles combine around a stainless cable to form the second sub-bundle. Twenty-four of these are then wrapped around a strap to make the cable. The second cable, which is to be made by Intermagnetics General Corporation (IGC), starts with a single, larger, polyamide-imide-film-insulated strand for the equivalent of the first sub-bundle. This strand has a complex copper, copper-nickel matrix with a copper-nickel spider segmenting the bulk of the copper in the outer periphery.

Preliminary analysis of the magnetically induced stress distribution in the proposed 20-MJ TPFS coil has been completed. Various mechanical models representing coil construction have been considered. Several analytical models representing stress distributions within the coil have been applied to the mechanical models and the less accurate discarded. Stress magnitudes and spatial variations have been determined. Peak magnitudes are on the order of 20 MPa.

2. 7- and 9-T Industrial TPFS Coil Design Study. Fabrication and testing of the first prototype TPFS coil are planned to be done in house. However, an assessment will be made of the time and cost involved for having an industrial supplier build such a prototype coil. To this end a contract was placed with Westinghouse Electric Corporation for an industrial study of both 7- and 9-T, 20-MJ, 50-kA prototype superconducting TPFS coil designs, costs, and schedules.

C. BIPOLAR TPFS COIL SIMULATION TESTS WITH THE 300-kJ METS COILS

1. Using Conventional Power Supplies. The LASL and Westinghouse 300-kJ energy storage coils have been tested to determine how fast the coil current could be swung from a positive to a negative value with the coils still superconducting.

The Westinghouse coil was "swung" in a ±12.1-kA bipolar operation without going normal. Peak swing in the magnetic field on the winding was from + to -2.72 T with an average rate of change of 1.1 T/s. These numbers are essentially limits of the test facility and not of the coil. Energy loss during the operation was 0.19% of the peak energy stored in the coils or 0.095% of the total energy transferred out of and back into the coil. This loss is equivalent to vaporizing 0.34 liters of liquid helium and was principally hysteretic in nature.

The LASL coil is a fully potted coil made with a monolithic conductor and its performance was not expected to be as good as the Westinghouse coil. The coil could be swung ±3 kA at a rate of about 0.34 T/s without going normal. Increasing the current swing to ±4 kA for the same time interval of 3.5 s caused a sizable increase in the losses indicating the coil was probably going normal. At a swing of ±5 kA the increased boiloff from the dewar caused by the energy transfer became very marked. In previous steady-state, nonpulsed tests, the coil had operated at 12.5 kA without going normal.

2. Using Rotating Machinery. A used 500-kW motor generator set, consisting of a synchronous motor and a commutated dc generator was acquired. The general characteristics of the dc machine make it suitable for reversing the current in the existing 300-kJ METS coil. The set has been operated with the dc generator as a motor, and preliminary measurements of its characteristics made. The set cannot conveniently be uncoupled so the synchronous motor will serve as a flywheel. Further measurements will be made before operation with the 300-kJ coil.

D. POWER SUPPLIES FOR TPFS

1. Commutated DC Machine Feasibility Tests. A 0.19-kW (0.25-hp) dc motor was operated as a pulsed power supply. This machine, rated at 2 A was capable of supplying 20 A into a direct short circuit at the terminals with no apparent damage. These tests showed the feasibility of this mode of operation of commutated dc machines.

2. TPFS, 20-MJ Homopolar.

a. Westinghouse. The design of a homopolar machine suitable for reversing current in the 20-MJ TPFS coil was completed by Westinghouse. It is based on the HETS 10-MJ work done previously. This machine uses superconducting field coils as the HETS machine did. It differs by having a six-turn drum-type rotor. The rotor has a solid iron core, which permits the increased energy storage. The machine has a terminal voltage of 2 kV, a current of 62.5 kA and a half-cycle (current-reversal) time of one second.

b. University of Texas at Austin. The Energy Storage Group at The University of Texas at Austin began work on a 20-MJ homopolar machine as an alternative to the design of Westinghouse. The machine will use superconducting field coils but an attempt is being made to simplify the overall mechanical construction details.

3. Traction Motors. It was determined that traction motors can serve as a current-reversing power supply for the TPFS 20-MJ coil. Traction motors are series dc commutated machines used to drive diesel-electric locomotives. As a current-reversing power supply 30 to 50 motors will be connected in a series-parallel arrangement to obtain 50 kA at 2.51 kV. In this configuration they will have a capacitance of 6.35 F and will store 20 MJ. Rebuilt traction motors cost 1.1 to 1.5 cents per J, and thus are economically attractive. Two units will be purchased and tested to determine over-current capability, capability for parallel operation and suitability for operation in the separately excited mode.

E. TNS STUDIES

Several separate but interrelated studies were undertaken in conjunction with the Center for Electromechanics of The University of Texas at Austin in support of the tokamak TNS design group of General Atomic at San Diego, California. The primary emphasis of the work has been to examine the feasibility of a homopolar machine as an energy transfer and storage element in the circuit of the TNS doublet, to address the related switching problems, and to consider the nature of the plasma shutdown at the end of the burn cycle.

Parameters supplied for the studies set the peak current and voltage at about 3 MA and 1 kV, respectively, with a 2-s startup for the ohmic-heating phase. The stored energy in the ohmic-heating coils was estimated to be 500 MJ and the total flux change to be 34 Vs. Of this amount, 20 Vs supplies the plasma inductive loading and 8 Vs the plasma resistive losses. The remainder powers the burn phase.

1. 3-MA Circuit Breaker for the TNS Doublet. A conceptual design of a 3-MA breaker having a recovery voltage of several kV was completed. Current interruption is achieved by a set of low-impedance circuit breakers, each with a capacity of 100 kA as shown in Fig. XV-1. The "water hammer" effect will be used to actuate or open the switch. Transformer oil will be used both as the actuating fluid and the arc-quenching fluid. A continuous flow of fluid will pass through the hollow electrodes prior to actuation. The switch will open under the influence of the inertial force of the oil column (water hammer) following closure of pilot and main valves. It is anticipated that shock loads on mechanical components will be

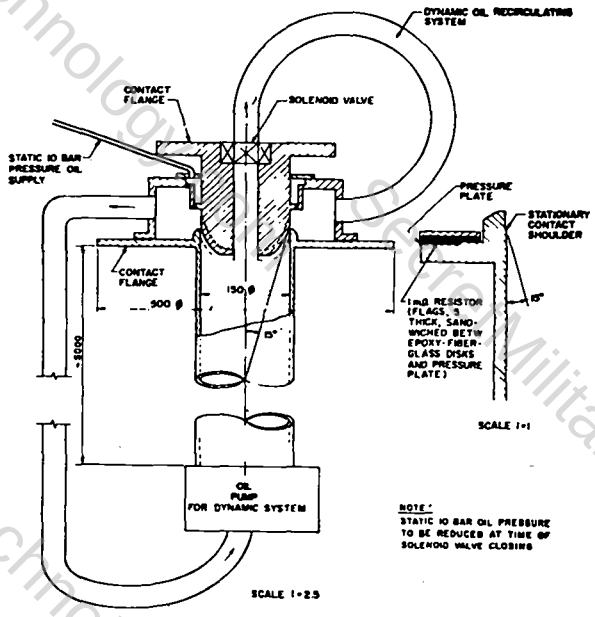

Fig. XV-1.
Hydraulically actuated oil circuit breaker for 100-kA intermittent duty and approximately 2-kA, 500-V interrupting capacity.

manageable in such a configuration. Because of the water-hammer application, the design is being considered for patenting. A literature survey showed that some of the same principles in arc extinction were developed in a European oil breaker for use in the European 400-kV dc transmission project.

The arc voltage drop in oil is higher than in any other standard medium; and, hence, is particularly useful for parallel operation and current transfer to a homopolar machine. A counterpulse circuit is proposed consisting of a capacitor bank for each of the parallel breaker units and a saturable reactor core enclosing the 3-MA bus.

2. 500-MJ Homopolar for General Atomic.

a. Machine Design. The design of a disc-type homopolar machine, undertaken for General Atomic Company (GA), was completed. The machine used two counter-rotating discs to store 500 MJ. Superconducting field coils supplied the main field and copper-graphite brushes were used to collect the current.

It was shown in this study that the cost of such a machine would be in the range of 1 to 2 cents per J. A parallel study of a 500-MJ copper-iron homopolar done by The University of Texas at Austin showed that the cost of copper-iron machines will be equivalent to that of superconducting machines. A preliminary written report and an oral presentation were given to GA.[1]

b. Circuit Analysis of a TNS Doublet Relative to a Variable Capacitance Homopolar Machine. A homopolar machine functioning as a capacitor in an LC circuit was studied where the current reversed within 2 s from negative to positive before continuing to increase for the 28-s burn period.

The differential equation for the series LCR circuit with a variable brush homopolar machine was integrated in current for two given flux functions describing the variable position of the brushes. To answer the question whether there is any continuous flux function that can provide for a monotonically increasing current over the period that includes current reversal and burn, the same differential equation was integrated in the magnetic flux for given monotonically rising current functions. From this study it was concluded that the moving brush feature was not useful for controlling the burn period. The results and details of the calculations were reported.[1,2]

3. Shutdown Problems in Large Tokamaks. The two types of shutdown considered were the normal shutdown at the end of the burn phase (soft shutdown) and a shutdown caused by a disruptive instability (hard shutdown). For a soft shutdown a cursory literature search was undertaken and methods for controlling the thermal wall loading were investigated. Since shutdown computer codes are not widespread, some of the differences between startup codes and shutdown codes were investigated, along with program changes needed to change a startup code to a shutdown code. For a hard shutdown, the major problems are large induced voltages in the ohmic-heating and equilibrium-field coils and high first-wall erosion. A literature search of plasma-wall interactions was carried out. Phenomena which occur at the plasma-wall interface can be quite complicated. For example, material evaporated from the wall can form a virtual limiter or shield protecting the wall from major damage. Thermal gradients which occur during the interaction can produce currents whose associated magnetic field also helps shield the wall.

4. Combination of Blip and Vertical Field (VF) Coil Mounted Outside the Toroidal Field (TF) Coils in Tokamaks With and Without Iron. Since a large amount of energy is needed if the plasma is initiated by inserting a "blip" resistor into the bias-current-carrying ohmic-heating coil, an effort was made to reduce the energy by using a set of unbiased blip coils. The blip coils are designed to generate zero field in the plasma region and supply the voltage pulse. Since most of the blip energy is supplied by magnetic coupling from the VF coil circuits, controlled power supplies are required to maintain the correct VF currents. It was concluded, therefore, that the blip coils and their driver circuits may best be combined with those for the VF circuits.

It is possible to distribute any given current among the individual turns forming the vertical field coil so the plasma region is virtually excluded from the poloidal field

generated by the current in the coil. Plasma initiation by inducing a pulsed voltage in the plasma region may thus be obtained by modulating the current in the equilibrium field coils. In the TNS case, it is expected that a flux swing of 40 Vs over the range -2 T...2 T may be obtained without varying the plasma major or minor radii.

The great advantage from a practical point of view of having the VF-and-blip coils mounted outside the TF coils is bought at the expense of a large increase in field energy, unless effective use is made of iron to reduce the reluctance of the poloidal-flux path. In addition to providing the VF-and-blip field, the VF coils are used as drivers for reversing the flux corresponding to -2 T at the start and >2 T at the end of the operating pulse. A constant-current superconducting bias coil is wound on the center post iron to provide the bias field of -2 T. Analysis and operation are complicated by the iron's presence at varying levels of saturation because the inductance matrix varies significantly over the operating range.

5. General TNS Studies. Problems associated with the ohmic-heating circuits of the TNS tokamak have been investigated over the last year. Some work was done to specify the power supply and OH-coil requirements of a TNS reference design generated by ORNL. The ohmic-heating coil of this reference design has a peak stored energy of about 300 MJ and a peak field of about 3 T for half-biased operation. Other possible designs for TNS would be smaller with correspondingly smaller OH coils operating at higher fields. The effect on power supply requirements of using time-dependent inductances caused by the change of plasma current distribution in flux conserving tokamaks was investigated. Generally the effects are small and tend to reduce the ohmic-heating energy requirements.

F. TPFS SWITCH DEVELOPMENT AND HVDC TEST FACILITY

1. Interrupter Facility Upgrade. The upgrade of the HVDC Interrupter Test Facility was completed. The upgrade was accomplished by essentially duplicating the original facility. In general, the same component design was used unless safety and reliability considerations suggested otherwise. Some of the design improvements incorporated were fiber-glass laminated capacitor racks, optical coupling for meter signals and high-speed trigger signals, pneumatic coupling for slower control signals, and a fiber-glass laminated balcony to hold the charging equipment. The original facility was also retrofitted where possible to include these improvements. The upgraded facility is shown in Fig. XV-2.

Safety and reliability received special attention during design and construction of the facilities. Safety to the operator is enhanced by automatic interlocks and grounding devices, automatic control operation, and physical separation and electrical isolation of control equipment from high-voltage equipment. Reliability is enhanced by reduction of electrical pickup through the use of single-point grounding and optical and pneumatic coupling of controls.

The dual facility was constructed to allow independent operation of the two facilities with a 30-kA, 60-kV capability or combined operation with a 60-kA, 60-kV capability. The facilities were successfully tested to these limits and can now be used to provide new test data for the switch development program.

Fig. XV-2.
Upgraded HVDC test facility.

Figure XV-3 shows a simplified circuit diagram of each of the interrupter facilities. Figure XV-4 shows the current and voltage wave forms and contact separation, S, of the test switch, typically a vacuum interrupter, VI. Also shown are the closing times of the various switches in the test facility: S1, S2, S3, and S4. A test sequence begins by charging storage capacitor bank C1 and counterpulse capacitor bank C2 to predetermined voltages of opposite polarity while switches S1 through S4 are open. The test current through storage coil L1 and test switch VI is initiated by closing switch S1. L1 and C1 form an LC circuit. When the peak current, I_{max}, is reached, switch S2 closes automatically to crowbar or shunt capacitor C1. This creates an exponentially decaying LR circuit involving L1 and the total loop resistance. The current decays slowly enough to allow the test switch VI to open while its current is still a large percentage of I_{max}. To achieve interruption the switch current must be driven through zero after the switch contacts have opened sufficiently to withstand the peak recovery voltage. This is done by closing switch S3 to connect the counterpulse bank across switch VI and saturable reactor L2. Closing S3 creates an LC circuit which includes C2 and the stray inductance around the counterpulse loop. The current in the interrupter is driven rapidly toward zero until L2 comes out of saturation to hold the current near zero. After interruption L1 and C2 form an oscillating LC circuit with the energy stored in L1 being transferred to C2, charging it to a peak voltage, V_{max}. This voltage is also the peak recovery voltage the switch must withstand. After the energy is transferred from C2 back into L1, switch S4 is closed to dissipate the energy in R1. This completes the test sequence. Some of the test parameters which can be varied are test and counterpulse current, recovery voltage, event timing, saturable reactance, and repetition rate.

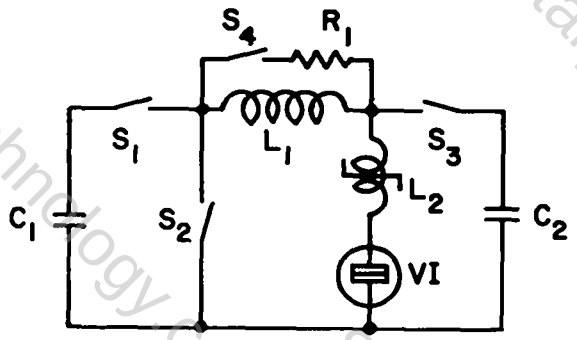

Fig. XV-3.
Simplified circuit diagram for the HVDC test facility.

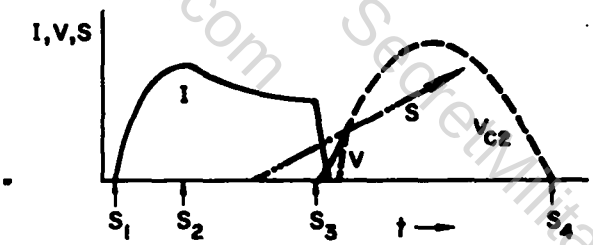

Fig. XV-4.
Typical current and voltage waveforms from an interrupter test.

One of the methods for paralleling the facilities is shown in Fig. XV-5. This method allows independent charging and triggering of the storage and counterpulse capacitor banks of both facilities. Only two connections are required. First, the ground plates are tied together at point 1 to achieve a common system ground. Second, the bases of the two saturable reactors are tied together at point 2. With this arrangement, both facilities feed current to the

switch independently with the total test current being the sum of the two individual test currents. Interruption is achieved when the switch current is driven to zero and held there by the combined action of the counterpulse banks and saturable reactors of both facilities.

2. Parallel System Operation. System A and its duplicate, system B, were operated together up to 60 kA. The operating mode was first employed in which the two systems were interconnected only at the interrupter under test as in Fig. XV-5. No problems of any sort were encountered. The systems were then connected at the tops of the saturable reactors, L_{2A} and L_{2B}, to parallel both facilities directly. This simulates more ideally the whole interrupting system which might be, for example, applied to an ohmic-heating system. In this second mode interactions were seen between the two counterpulse systems, which showed up as a fast "ringing" of energy between them. Modifications of the systems have been undertaken to reduce these interactions.

3. 2-MJ System. Circuit design has been started on the 2-MJ system, which is to be used to test interrupter systems above 100 kA. A decision was made to construct the system by assembling 5 to 7 smaller modules in parallel. The modules and the techniques used to parallel them would, in most respects, be the same as those already developed for the duplicate facilities. The capacitors and most other components for the 2-MJ system are already available. Some components, such as the storage coils, have been designed and are being purchased. The capacitor racks are being built. System layout and facility modifications are being studied.

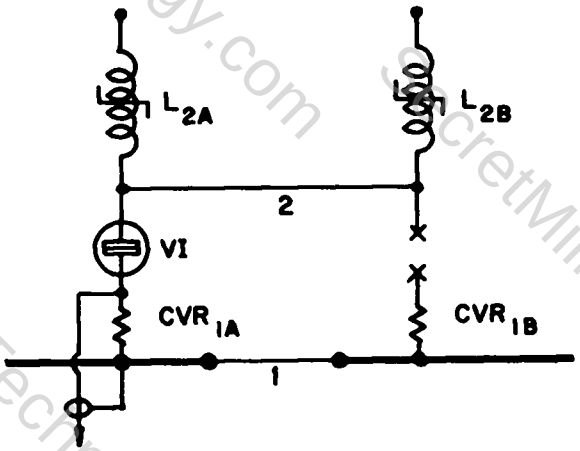

Fig. XV-5.
Circuit diagram for parallel operation of the HVDC test facility.

Existing coil modules used in the switch test facility were analyzed to determine the cause of cracking in the epoxy potting. This analysis was applied to the design of new coils for use with the 2-MJ capacitor bank. The new modules will be of similar construction to the existing double-spiral pancakes, but will incorporate a more complete magnetic force restraint system to allow operation at currents up to 60 kA, which is twice the rating of the original design.

4. Saturable Reactors. Tests were performed on silicon steel, ferrite, and Permalloy saturable reactors to determine the effect upon arc interruption of their flux rating, tape thickness, and air-gap size. Interruption was found to be independent of all of these variables within wide limits.

5. Axial Field Vacuum Interrupters Two special 17.8-cm-diam interrupters were purchased from Westinghouse for use with axial magnetic fields. One, PRI, had the field coils internal to the bottle; the other, PRII, needed external coils. PRI was tested to 37 kA at 38 kV without failure. This was the limit of the test facility. Higher current tests were postponed until the duplicate facility became operational.

PRII was tested at various fields to 29 kA. At low fields the maximum interruptible current was 14 kA. At the highest field used, about 0.05 T, the extrapolated maximum current would be well in excess of the system's limit.

Tests with other sizes of conventional interrupters in an axial field were also conducted. The performance of 10-cm-diam interrupters was not significantly improved. The 12.7-cm-diam interrupter performance improved about 50% in a field of 0.1 T. Conventional

17.8-cm-diam interrupters were not investigated pending availability of the duplicate facility.

6. Parallel Operation of Vacuum Interrupters. Two parallel-connected 17.8-cm-diam interrupters were tested for maximum interruptible current. A current-sharing transformer was sometimes used. Without the transformer a resistor as large as 1 mΩ placed in series with each interrupter was unable to force current sharing, leading to a failure to interrupt at a total current well below 30 kA. With the transformer, current sharing was usually very good and interruption at 30 kA, the system limit, was successful. Occasionally the flux rating of the transformer was inadequate, the current sharing was imperfect, and interruption was not successful. With the availability of the duplicate facility, a larger transformer will be used to test the interrupters to their maximum expected rating of about 45 kA.

7. Persistent Currents in Interrupters. Facility modifications were made to tie in the 20-kA homopolar generator to preheat the electrodes of the vacuum interrupters prior to opening. Investigations were made of contact heating, melting, welding, popping, and the effect of all of these on interruption. An actuator was modified to allow higher contact-closing forces, which reduces the contact resistance and most of the above undesirable effects. It was found (a) that under most circumstances, i.e., whenever the voltage across the closed interrupter was greater than 1/2 V, the contacting points on the electrodes melt; (b) if the electrodes are not immediately opened, such melting leads to welding; (c) if the electrodes are opened before the current is reduced, welding does not occur; (d) interruption is not affected by the melting until I^2t equals or exceeds 4×10^9 A^2s; (e) "popping," a chattering of the contacts caused by the magnetic repulsion of opposing electrodes, can cause welding problems but does not interfere with interruption; (f) very large contact-closing forces (136 kg to 227 kg)will be needed if currents of 50 to 100 kA are to be carried by one device; and (g) if welding occurs and the weld is broken mechanically, the roughness produced interferes with interruption until it can be smoothed away by a series of ~ 10 arcs.

8. Fast-Actuator Studies. There are important advantages to be gained if vacuum interrupters can be opened rapidly. Fast actuation provides the possibility of opening under no-current conditions thus resulting in minimal erosion rates of the contacts due to arcing. The conventional mechanical actuation systems routinely used achieve opening velocities of 1.6 mm/ms, which is relatively slow.

An actuator which uses repulsion coils was obtained and tested. At rated conditions opening velocities of 8 mm/ms were achieved. A second unit which utilizes a combination of repulsion coils and pneumatic systems is on order and will be tested early in 1978.

9. Gas Breakers for Tokamak Ohmic-Heating Duty. The current interrupting capacity of air blast and SF_6 breakers was reviewed for application in tokamak ohmic-heating circuits. Particular attention was paid to generator breakers for their large current interrupting capacity and suitability for ohmic-heating circuits.

10. Interactions With Other Laboratories and With Industry. Tests were performed on saturable reactors for Westinghouse Electric Corporation and for the Oak Ridge National Laboratory. These entities were involved with designing the ohmic-heating circuit of Ormak Upgrade and needed help with the design of the interrupter circuit.

Tests were performed on the largest commercially available interrupters of GE (Model PV07) and ITT-Jennings (Model RP-728A). Both interrupters failed to perform as well as expected. The GE sample developed a vacuum leak; the ITT interrupter could not interrupt large currents. New Interrupters have been procured for retests.

An extensive series of tests was performed with GE to re-evaluate the erosion of their special PV08 interrupter. These tests were performed with their actuator and with their supervision with respect to the method of mounting and actuating the interrupter. The results were the same as those of the earlier tests, i.e., erosion is much more rapid than for other similar interrupters.

A continuous dialog with Ebasco-Grumman has been held with regard to tests of vacuum interrupters for use on TFTR. Special components have been ordered for these tests, but they have not been started because of changes in the plans of Ebasco-Grumman.

G. CRITICAL-CURRENT STUDIES AND LOSS MEASUREMENTS

1. Dipole Magnet. The new 102-mm-bore, 6-T dipole magnet for the high-current test facility is almost complete. The winding has been finished, the magnet fully assembled, the transfer line and cooling tubes installed, the eddy current shield mounted, the shunts connected, and the magnet suspended from the dewar lid. The magnet assembly should be completed, tested, and operational early in 1978.

Critical-current measurements were made on samples of the conductor from the start of the winding, the break between the two halves of the dipole, and at the end of the winding. All samples met the specifications.

2. Critical-Current Measurements Below 1 kA. Short-sample critical-current measurements were made on a series of intermediate resistivity, multifilament NbTi wires as a part of an evaluation of the losses of the conductors. The critical-current densities at 3 T were 1.7, 2.0, and 2.2 x 10^5 A/cm^2, respectively, for wires of 0.25 mm, 0.36 mm, and 0.51 mm in diameter. By comparison, IGC mixed-matrix wire, for which this was to be a possible substitute, had a j_c of more than 2.4 x 10^5 A/cm^2 at 3 T.

Other miscellaneous wires were measured including some wire for the Q-10 SMES program.

3. Critical-Current Measurements Above 1 kA. Both samples of the cables for the HETS test coil were tested up to approximately 5 T. The extrapolation of the data to 6.4 T indicated that both cables met their specifications of 2800 A and 5500 A.

Additional measurements were made of SMES conductors by Q-10 personnel with assistance of CTR-9 personnel.

4. Loss Measurements. Hysteretic and pulsed energy loss measurements were made on a series of intermediate resistivity matrix wires manufactured by MCA. The wires had 156 NbTi filaments in a Cu 0.05 wt% Ni matrix. The matrix resistivity at 4.0 K was approximately one twentieth that of copper at 293 K. Theoretical analysis had indicated that the energy losses would be similar to equivalent mixed-matrix conductors, but experimentally, the dynamic losses were significantly higher.

In line with programmatic changes, preliminary work was begun to convert the loss apparatus operating parameters to a maximum field of 7 T with a bipolar sweep on the order of 14 T/s. A 7-T, 60-kJ coil was designed and the superconductor ordered. The method of swinging the coil has not yet been decided. Tests are under way to evaluate the possibility of using motor-generators. Initial investigations indicated that capacitors would be too expensive.

H. 300-kJ, 10-kA METS STORAGE COILS

1. Diagnostic Tests for the IGC Coil. In an effort to determine the source or sources of the failure of the Intermagnetics General Corp. (IGC) coil to perform to specifications, two series of tests were run, one on the 300-kJ coil and the second on a small test coil made from the 300-kJ coil cable.

On the 300-kJ coil the terminations were unsoldered, the 319 strands all separated and extensive testing done on individual wires and groups of wires. The most damaging fact which arose was that there were many interwire shorts within the cable. Because the shorts were internal in a multistrand, fully transposed cable and not turn to turn in a single strand winding; it was not obvious that the shorts were automatically the source of the problem. Some of the tests did show, however, that a resistively (rather than the normal inductively) induced voltage drop would be established across the short if there also existed high-resistance contacts at the termination and, in addition, if there were broken wires. The broken wires were verified; it was impossible, however, to determine termination contact resistances at the terminations of the individual strands. The variety of test results made it impossible to reach any totally unequivocal conclusions.

A small magnet was constructed from the excess 10-kA cabled conductor used in the original IGC 300-kJ coil. The purpose of the coil was to investigate, in particular, the effect that no potting might have had on the 300-kJ coil. The coil reached a maximum current of T 10 kA, about a factor of three higher than the 300-kJ coil. It was designed, however, to go to T 18 kA. Adding shorted, nonbroken, low terminal resistance wires to the cable did not degrade the coil performance. It was assumed that the coil did not reach design current because of wire motion since this coil was not potted. Unfortunately no definitive tests were run to establish this conclusively.

2. Energy Loss Measurements. The energy loss measurement data for the four 300-kJ coils have been analyzed and reported.[3] Reference 3 summarizes the results and describes the loss measurement apparatus. The losses were measured by both electrical and calorimetric methods to verify the results with two independent measuring methods. Comparison was also made with short sample measurements taken with the astatically wound pick-up coil method.

I. ONE-COMPONENT MODULE SUPERCONDUCTING PROTOTYPE METS SYSTEM

The fast-pulsed superconducting inductive energy storage program was initiated to provide a system capable of delivering 488 MJ to a theta-pinch experiment. An optimization study led to a modular design of superconducting coils, each to deliver 400 kJ of energy to create a 5.5-T field on the fusion plasma. To bring the program to a logical conclusion in view of the de-emphasis of theta-pinch research and to obtain a maximum amount of information for ongoing inductive energy storage systems, a complete one-module or one-component system is to be assembled and tested.

The one-component system to be assembled for the 400-kJ coil test will use a hybrid external switch to isolate the coil from the charging power supply, a cryogenic disconnect to withstand the 60 kV occurring during energy transfer, and a helium-vapor-cooled coaxial lead to conduct the current during the energy transfer. All three of these items are in a highly developed state and are being designed for final hardware fabrication.

1. METS Prototype Coil. A 400-kJ, 2.5-T, 25-kA superconducting coil is being designed and built by Westinghouse Electric Corporation. The coil is similar to the highly successful 300-kJ coil made by Westinghouse. The coil is to be tested with a 0.7-ms discharge time and a 60-kV voltage rise. Subsequently the coil will be tested in a slower 1- to 2-s bipolar field and energy transfer to simulate tokamak ohmic-heating performance. The conceptual engineering design on the coil is complete and detailed engineering has started. Mixed-matrix copper, copper-nickel NbTi superconductor has been ordered from IGC for the coil.

2. Cryogenic Disconnect. After evaluating several different materials it was decided that the 50-50 Pb-Sn alloy was the best suited for the contact surfaces. Plating or coating of the Pb-Sn alloy onto annealed OFHC copper seemed to offer the following advantages. Although not superconducting, the copper has a very low resistance at cryogenic temperatures and does not have the abrupt transition to the normal state as do the superconductors. The Pb-Sn alloy coating has a very low contact resistance, especially in the semigalling mode, and the resistance of the copper forces current to distribute more evenly in a multicontact switch.

After selecting the materials, the main effort was spent on the method of constructing a semigalling switch. The testing included ways of putting on a uniform coat of the Pb-Sn alloy, methods of controlling the galling action of the switch without seriously impairing the operating lifetime, methods of switch connection to the superconducting coil, and switch construction that would minimize any motion of the connecting leads.

A switch was constructed consisting of two cylindrical bushings connected by a 15.9-mm-diameter pin. All parts are made of copper, coated with Pb-Sn alloy. The two bushings are the contacts and remain in a fixed position; the pin is the movable element and forms the bridge between the two contacts by sliding through one bushing into the other. This switch carried a

current of 1.5 kA with a total resistance of less than 50 n after 1500 cycles of operation.

Tests on the above switch revealed the higher resistance portions of the switch and calculations were done to optimize the design to reduce the resistance in these places. The final design uses thinner fingers on the cups and a piece of multifilament superconductor soldered into a hole running through the length of each finger (12 fingers per cup with a 1.27-mm-diam superconducting wire in each finger). In the final design, the superconductors from each cup will pass through the mounting plate and attach closely to the superconducting cable from the coil.

A three-pin version of this switch was constructed and tested. It was able to carry a current of over 5000 A at a resistance of 15 nΩ. No degradation was observed after 500 cycles of operation. Work is under way to design and construct a similar switch with a current capability of 25 kA.

3. External Breaker. To allow the METS cryogenic disconnects to open under zero current conditions, the current in the series charging loop will be interrupted by a circuit breaker placed external to the dewar. The external breaker must carry the five-minute charging ramp to 26 kA, interrupt it, and withstand up to 60 kV. To meet these requirements the breaker will consist of a vacuum interrupter and bypass switch connected in parallel to form a hybrid switch.

A full-scale prototype of the bypass switch has been built and tested. Figure XV-6 shows the bypass switch and actuator in the open position. A 6-kA, 600-V switch by ITE Imperial was modified to withstand high voltages by using nonmetallic structural members and immersing the unit in oil. The switch was successfully hi-potted to 90 kV. Tests show that the bypass switch can handle the charging current requirements because of the increased heat transfer from the contacts due to the oil. The opening time from contact break to full open is about 30 ms. A 1.03-MPa pneumatic actuator is used to operate the switch.

The crucial transfer and interruption steps of the complete external breaker were tested in the interrupter test facility. Several different

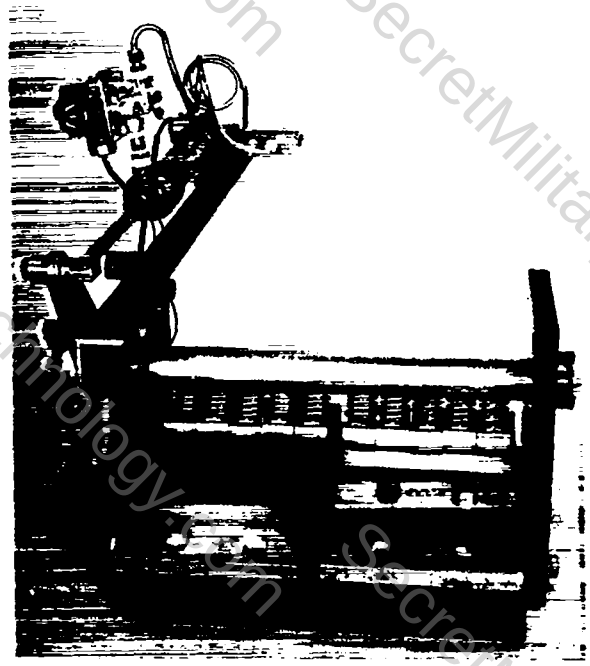

Fig. XV-6.
High-current bypass component of the hybrid switch.

modes of operation were investigated and extensive though preliminary data were collected. The switch worked about as expected. About 30 kA was carried by the bypass switch, transferred to the vacuum interrupter, and interrupted. Recovery voltages were as high as 51 kV.

Erosion of the copper contacts in the bypass switch was also investigated. The contact erosion, shown in Fig. XV-7, after 100 transfer operations at 26 kA indicates that 10^3 to 10^4 operations could probably be accomplished by the bypass switch before maintenance would be required. New electrodes with a silver-tungsten surface instead of copper have been ordered. These should provide 5 to 10 times better erosion resistance.

Testing has shown that the hybrid vacuum interrupter-bypass switch meets the requirements of the external breaker. Engineering drawings of the final bypass switch have been completed. Construction of the complete external breaker will begin soon.

Fig. XV-7.
Contact erosion on high current component of the hybrid switch.

4. 700-W, 4.5-K Refrigeration System.

Startup and successful operation of the Helix Corp. refrigeration system was accomplished during the year. Refrigeration rates of 880 W in the experimental dewar and 924 W in the 1000-gal dewar were achieved. As a liquefier, a rate of 250 ℓ/hr was measured in the 1000-gal storage dewar.

A GHe collection system was installed along the outside west wall of SM-253 to accommodate boiloff from the 3800-ℓ and 500-ℓ storage dewars and the LN_2 supply line was extended from SM-253 to SM-322 to facilitate automation of the helium recovery-purification system.

Micro Nova computer components were ordered for conversion of the refrigerator from manual to computer control.

5. Load Coils. A set of high-Q load coil modules wound of Litz wire was designed for use in testing the 400-kJ coil and general switch testing. The coils are fully epoxy potted. Specifications for their manufacture were composed. A contract for the construction was let to Elma Engineering Co. Discussions were held with the manufacturer and minor modifications made to ease construction and improve performance.

J. HOMOPOLAR MACHINE DEVELOPMENT PROGRAM

1. 10-MJ HETS Machine. The detailed design of the 10-MJ, 30-ms HETS homopolar machine was completed by Westinghouse and preliminary copies of the final report issued. A program was begun and pursued at Westinghouse to test brushes under conditions of speed and electrical loading similar to those found in the HETS machine.

Two magnetic characteristics were derived for optimizing the magnetic circuit of the machine. One is the linkage flux vs the cross-sectional area of the flux return and the other the total flux vs the coil current density. The remainder of the program was terminated due to lack of funding and a relevant application.

2. HETS Load Coil. As part of the design of the HETS 30-ms machine test facility, a high-Q 1.5-MA test coil was designed. The coil was to be capable of operation at 300 K and 80 K. Square, insulated, No. 7 aluminum conductors were to be formed into Roebel bars of which the coil was formed. Tooling and model bars were made to demonstrate the construction to potential manufacturers. General characteristics and linear dimensions for the coil are listed in Table XV-I.

The program was terminated due to loss of funding.

K. MISCELLANEOUS

1. Helium Conservation. A program was established to implement helium conservation at LASL. Laboratory overhead funds were made available to purchase capital equipment items such

TABLE XV-I
10-MJ LOAD COIL CHARACTERISTICS AND DIMENSIONS

Characteristic	0.060-s Swing	2.0-s Swing
Inductance, μH	5.81	10.5
Number of Turns	2	85
Resistance (No Bus), μΩ	0.7	
Time Constant (No Bus), s	8.28	8.28
Inefficiency (No Bus), %	0.7	24.2

as dewars and recovery compressors--$15k in 1977 and $50k in 1978. Recovery systems will be established at large liquid helium user sites within the Laboratory. The recovered helium will then be transported to CTR-9 where it will be purified and reliquefied using the Helix Corp., 1000-W, 4.5-K refrigerator. In addition to conserving an important natural resource, the program will result in cost savings to those users of liquid helium having recovery systems.

2. SCEPTRE. Several persons from other LASL Divisions indicated their interest to use the circuit analysis code SCEPTRE for problems that NET2 is unable to solve. SCEPTRE has been made available in public utility files on LASL's NOS systems and a users guide was written to complement the existing AFWL reports describing the code.

3. TPFS Workshop. A workshop on the problems of designing poloidal field coils for tokamaks was organized by, coordinated by, and held at LASL. Representatives of all major US tokamak research laboratories attended. Proceedings were prepared and submitted to DOE for distribution.

REFERENCES

1. H. Vogel, P. Thullen, and D. Weldon, et al., "TNS Doublet Tokamak Ohmic-Heating Power Supply Study," Los Alamos Scientific Laboratory report LA-7053-MS (November 1977).

2. H. Vogel, "Current control by a Homopolar Machine with Moving Brushes," Los Alamos Scientific Laboratory report LA-7090-MS (January 1978).

3. J. D. G. Lindsay and D. M. Weldon, "Loss Measurements in Superconducting Magnetic Energy Storage Coils," Los Alamos Scientific Laboratory report LA-6790-MS (May 1977).

XVI. SYSTEMS STUDIES

R.A. Krakowski, R.L. Miller, R.L. Hagenson, R.W. Moses, G.E. Gryczkowski,*
A.S. Tai,** G.E. Cort, R. Bartholomew, J.W. Barnes, J.O. Jacobson,
J.H. Pendergrass, K.E. Cox, D.J. Dudziak, P.D. Soran, D.W. Muir,
F.W. Clinard, Jr., J.M. Bunch, G.F. Hurley, and J.G. Hoffman

A. INTRODUCTION

The focus of all systems and design studies of magnetically confined fusion concepts has been on alternative or exploratory concepts. A major design effort on the Reversed-Field Pinch Reactor (RFPR) concept has been completed, and is based upon a moderately pulsed mode of operation. On the basis of this RFPR design, a second design study has commenced that investigates both the physics and technology associated with a longer, extended-burn operating mode. Studies of both the Fast-Liner Reactor (FLR) and Linear Magnetic Fusion (LMF) concepts have emphasized physics and energy-balance constraints for fusion power, although crucial technological issues for both the FLR and LMF concepts have been addressed. A study of toroidal bi-cusp confinement (Tormac) was begun and has focused on elucidating viable physics operating points with total power, energy balance, and first-wall loading being enforced as major constraints. Scoping studies of generalized hybrid (fusion/fission) and synfuel (thermochemical hydrogen) applications of fusion power have also commenced. The results of general studies of plasma systems analyses performed in support of all of the above-mentioned reactor studies are also reported. Finally, progress in neutronics studies and insulator research is summarized.

B. LINEAR THETA-PINCH REACTOR (LTPR) STUDIES

The heating and (radial) confinement principles for the Linear Theta-Pinch Reactor (LTPR) would be similar to those envisaged for the toroidal Reference Theta-Pinch Reactor[1,2] (RTPR) were it not for the rapid loss of plasma energy from the open ends of the former scheme. Hence, a pre-ionized DT gas is heated by a fast (~1-μs) implosion (~1 kV/cm azimuthal or "θ" electric field) to temperatures of ~1 keV; this preheated plasma is subsequently compressed adiabatically to ignition temperatures (~5 keV), and a burn cycle occurs along a plasma radius/temperature trajectory determined primarily by the dynamics of an energetic, high-beta plasma.

The loss of plasma particles and/or energy would make the achievement of this burn cycle on a reasonable time scale, while simultaneously meeting an energy-balance or Lawson-like criterion, technologically difficult for an open-ended linear device.[3] First, the end-loss problem can be ameliorated by use of extremely long plasma columns (>10 km). Second, the free-streaming ends could be replaced by solid or gaseous end-plugs, which would maintain the plasma pressure (i.e., contain the particles), but would conduct energy too rapidly, unless the plasma column were also very long. As shown later, this approach leads to the following condition on the confining (axial) field B(T) and plasma length ℓ(m) for ideal ignition (i.e., no loss of the 3.5-MeV alpha particles): $B^2\ell = 1.5(10)^6\ T^2$ m. This Lawson-like condition is based on classical axial electron conduction and predicts "acceptably" short (i.e., reasonable power levels and lengths) devices only for high fields and plasma densities; the instantaneous radiation heat flux at the first wall ultimately establishes an upper limit on the allowable plasma density,[4] not to mention the magnet design and energy transfer/storage (ETS) constraints which accompany high fields.

Although ongoing research may ultimately lead to solutions to these technology problems and permit use of the favorable $B^2\ell$ scaling, the approach adopted for the purposes of this study invokes the reentrant endplug (REP) scheme,[3] wherein the end-loss particles and energy emanating from a LTPR are directed by a small-radius-of-curvature conduit to a second, parallel device. The plasma column within the REP region may not necessarily be in "toroidal" equilibrium, it may contact and in part be supported by a structural

*Visiting Staff Member from the University of Michigan, Ann Arbor, Michigan.
**Visiting Staff Member from the Swiss Federal Institute of Technology, Lausanne, Switzerland.

wall and, therefore, will be subject to cross-field transport losses. On the other hand an intermittent toroidal equilibrium may be established in the REP region that is similar but not as effective as that envisaged for the RTPR;[2] the end loss would correspond to a periodic plasma dump to the end-region first wall. This issue has not yet been fully resolved. The REP is assumed to confine a majority of the 3.5-MeV alpha particles, which are vital to the successful operation of ignited devices like the LTPR. The issue of alpha-particle confinement within the context of ignition will be subsequently addressed.

The REP idea is sufficiently recent to preclude detailed study of either the end-region physics, a physics operating-point parameter search, or a detailed LTPR design based thereon. Many of the applicable RTPR design results[1,2] have been used for this study, and the design point should be viewed as interim. The major goal of this study is to develop a self-consistent and technologically credible design point which gives lengths of at most a few hundred meters, recirculating power fractions below 0.25, and plasma densities (compression fields) and confinement times that are technologically feasible.

The interim LTPR design configuration consists of two parallel, linear sections (ℓ = 150 m) joined at the ends by two semicircular reentrant sections of 5-m radius, giving a total reactor length of 331.4 m. The reactor is segmented into approximately 160 independent modules, nominally 2 m in length. As depicted in Fig. XVI-1, each module contains blanket, magnetic coil, and coolant system components. The modules are suspended in a vacuum/shielding trough such that pumping and gas fueling access to the plasma chamber is obtained through the gaps between adjacent modules. The modules used in the REP sections of the LTPR may differ somewhat from this design in order to compensate for the expected, increased heat removal requirements, although details of this aspect of the LTPR design have yet to be resolved. Each 2-m-long blanket module is composed of ~100 azimuthal segments, is 0.35 m thick, and is structurally and electrically independent of the magnet systems. The inboard

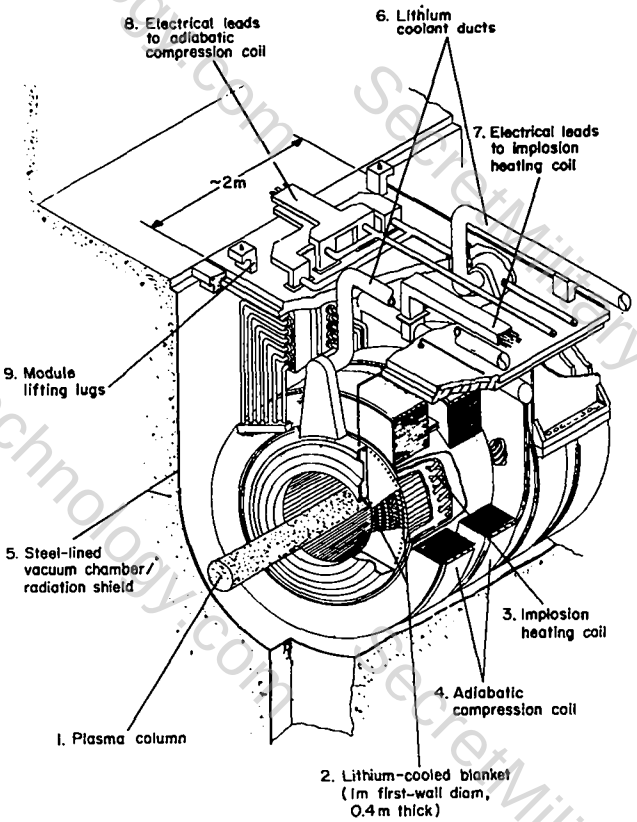

Fig. XVI-1.
Cutaway view of a 2-m long, 0.5-m-radius (first-wall) Linear Theta-Pinch Reactor (LTPR) module. This module is similar to that envisaged for the Toroidal Reference Theta-Pinch Reactor (RTPR).[1,2]

edges of these blanket segments provide the 0.5-m-radius first wall. Outboard of the blanket is the implosion heating coil, which is driven by a capacitive energy store. The room-temperature adiabatic compression coil, driven by homopolar motor generators, provides the subsequent, slower compression to ignition with a field of 8 T.

Table XVI-I through Table XVI-III summarize the essential plasma and engineering design features of the LTPR as presently envisaged. These plasma, energy-balance, and engineering design parameters have been generated by the three-particle (ions, electrons, alpha particles), time-dependent, one-dimensional (axial) pressure-balance code, 1DRBURN,[5] that dynamically computes the LTPR energy balance (Table XVI-III), all plasma parameters, as well as the first-wall thermal response. On the basis of the detailed computation model, the merits of exchanging axial heat-conduction losses for cross-field transport losses in the REP are quantified.

TABLE XVI-I
INTERIM LTPR DESIGN FEATURES

Shock Magnetic field, B_{SH}(T)	1.18
Maximum compression field, B_o(T)	8.0
Compression field rise time, τ_R(ms)	30.0
Compression field flat-top time, τ_{FT}(ms)	300.0
Fusion neutron energy worth, E_N(MeV/n)[a]	15.66
ETS efficiency (for τ_R = 30 ms), η_{ETS}	0.95
Thermal conversion efficiency, η_{TH}	0.40
Auxiliary power fraction, f_{AUX}[b]	0.02
First-wall radius, b(m)	0.50
Blanket thickness, Δb(m)	0.35
IH coil thickness, Δb_{IHC}(m)	0.04
AC coil thickness, Δb_{ACC}(m)[c]	0.08
Radius of reentrant sections, R(m)	5.0
Length of straight sections, ℓ(m)	150.0

(a) Based on neutronic calculations for the 0.35-m-thick blanket. This very thin blanket captures 86% of the fusion neutron energy, the remaining 14% or 11.84 MJ/m being removed from the implosion and adiabatic compression coils as low-grade ($\sim$ 300 K) heat; this compares to 7.36 MJ/m lost as low-grade heat as a result of joule losses. Although thickening the blanket to $\sim$0.40 m will lead to a recovery of nearly 100% of the fusion energy (i.e., the 11.84 MJ/m would add to the thermal output W_{TH} = 96.29 MJ/m), the increased coil radii would increase the ETS transfer and loss energy. An optimization of this trade-off is presently in progress.

(b) Fraction of total electrical power used for auxiliary plant needs (pumps, lighting, control, etc.).

(c) Total volume to outer radius of ACC = 9.29 m^3/m.

On the basis of the 1DRBURN design calculations, alpha-particle confinement has emerged as a crucial issue. Consequently, an analytic study of ignition in LMF systems has been conducted,[6] using a simplified alpha-particle thermalization model described in Sec. H.2. This analytic model integrates all reactivities across an appropriate axial temperature profile and defines an ignition condition (alpha-particle heating equals the sum of radiation and axial conduction losses) in the form of $B^2\ell$. Treating the alpha-particle trapping efficiency f_α analytically but consistently (Sec. XVI H.2), results in the $B^2\ell$ versus temperature ignition relationship depicted in Fig. XVI-2; alpha-particle thermalization treated according to classical slowing-down theories significantly limits the range of $B^2\ell$ where ignition is to be found. The influence of decreased thermal conduction relative to the classical value is also shown on Fig. XVI-2. It should be noted that in operating a LTPR, a trajectory of $B^2\ell$ versus temperature that reflects the dynamic startup and adiabatic compression must be followed to insure an ergonically acceptable burn, and the required (final) $B^2\ell$ values are generally above those given on Fig. XVI-2.[6]

C. REVERSED-FIELD PINCH REACTOR (RFPR) STUDIES

Dynamic plasma and energy-balance models were used to perform a parametric systems analysis of a wide range of RFPR burn cycles using the engineering Q-value Q_E as the object function.[7,8] Major system dimensions (first-wall radius, coil sizes and configurations, blanket location and thickness), initial plasma conditions (temperature, DT ratio, filling pressure), initial toroidal bias field, magnitude and wave form of the toroidal current, and the total burn time were varied over a wide parameter range. The magnitude of the first-wall temperature rise and associated thermal stresses, both of which were also computed as a function of time, and the total plasma beta were continually monitored and used as major constraints. The toroidal current I_z was increased sinusoidally with a rise time τ_R ($\sim$100 ms), which is consistent with a homopolar motor/generator supply for the poloidal coil system. I_z was held constant (crowbarred) for a time τ_B ($\sim$ 1 s) and then sinusoidally decreased with a fall time equal to τ_R. The value of τ_B and τ_R were selected to assure, conservatively, that the poloidal beta β_Θ at the quench time ($\sim 2\tau_R + \tau_B$) did not exceed a critical value ($\beta_{\Theta c}$ = 0.5) determined by detailed MHD stability computations. The quenched, expanded plasma and the trapped field were assumed to rest against the first wall and to cool over a period of a few seconds by classical cross-field conduction. The computed first-wall thermal history reflects all stages of this proposed RFPR burn cycle: startup, compression, burn, expansion, and quench. As for other fusion reactor models, notably tokamak systems,

TABLE XVI-II

THERMONUCLEAR BURN CONDITIONS FOR ℓ = 150-m, REP LINEAR THETA-PINCH REACTOR (LTPR) INTERIM DESIGN POINT

Initial Burn Conditions	
Initial DT filling pressure (297 K), P_A(mtorr)	10.0
Implosion-heating electric field, E_θ(kV/cm)	1.0
Implosion-heating voltage, V(kV)	222.1
Normalized plasma radius at shock, x_{SH}	0.70
Imploded electron temperature, T_{eSH}(keV)	0.8
Imploded ion temperature, T_{iSH}(keV)	1.33
Imploded ion density, n_{iSH}(m^{-3})	$1.45(10)^{21}$
Beta of imploded plasma, β_o[(a)]	0.9
Postimplosion plasma energy, W_{INTO}(MJ/m)	0.29
Implosion-heating energy, W_{SH}(MJ/m)	2.58
Implosion-heating efficiency, W_{INTO}/W_{SH}	0.11
Implosion magnetic field, B_{SH}(T)	1.18
Burn Conditions	
Adiabatic compression field rise and fall times, τ_R(ms)	30.0
Adiabatic compression field flat-top time, τ_{FT}(ms)	300.0
Adiabatic compression field, B_o(T)	8.0
Plasma radius at start of burn, a_i(m)	0.12
Plasma radius at end of burn, a_f(m)	0.27
Ion temperature at start of burn, $[kT_i]_i$(keV)	5.2
Ion temperature at end of burn, $[kT_i]_f$(keV)	26.1
Electron temperature at start of burn, $[kT_e]_i$(keV)	5.0
Electron temperature at end of burn, $[kT_e]_f$(keV)	24.4
Alpha-particle temperature at end of burn, $[kT_\alpha]_f$(keV)	205.0
Alpha-particle confinement efficiency, f_α[(b)]	0.9
Ion density at start of burn $[n_i]_i$(m^{-3})	$1.26(10)^{22}$
Ion density at end of burn $[n_i]_f$(m^{-3})	$2.75(10)^{21}$
Beta at start of burn, β_i[(c)]	0.81
Beta at end of burn, β_f	0.99
Fractional fuel burnup, f_B	0.06
Integrated Lawson parameter, $(n\tau)_L$(s/m^3)	$2.7(10)^{21}$

(a) On the basis of pressure balance and magnetic flux conservation the plasma beta is allowed to vary consistently throughout the LTPR burn. The dynamic burn code 1DRBURN reduces the fusion power density accordingly.

(b) Estimated by the ratio of linear section length to total circumferential length.

(c) Computed after adiabatic compression when ignition has been achieved.

the physical processes associated with both the turbulent startup and the quench phases are not well understood.

Achieving MHD stability during the initial startup phase seems unlikely, and turbulence similar to that exhibited by tokamaks may result. Pressure balance is assumed during startup, however, and the approximate field profiles are described by the Bessel function model. A homopolar generator[9] is applied at full voltage

TABLE XVI-III

INTERIM LTPR ENERGY BALANCE RESULTS

LTPR length, ℓ(m)	150.
Cycle time (for I_W = 2 MW/m^2), τ_c(s)	12.12
Implosion-heating energy, W_{SH}(MJ/m)	2.58
Postimplosion plasma energy, W_{INTO}(MJ/m)	0.29
Postquench plasma energy, W_{INTF}(MJ/m)	5.92
Bremsstrahlung energy, W_{BR}(MJ/m)	2.47
Reentrant section thermal loss, W_{EL}(MJ/m)(a)	1.86
Fusion neutron energy, W_N(MJ/m)(b)	84.59
Fusion alpha energy, W_α(MJ/m)	19.01
Direct conversion energy, W_{DC}(MJ/m)(c)	9.44
Direct conversion efficiency, η_{DC}(c)	0.50
ACC transport losses, W_T(MJ/m)	7.36
Blanket eddy current losses, W_{ED}(MJ/m)	0.49
Auxiliary energy needs, W_A(MJ/m)	0.77
ETS losses, W_{ETS}(MJ/m)	6.08
Maximum stored energy, W_B(MJ/m)	121.6
Total recoverable thermal energy, W_{TH}(MJ/m)	96.29
Total recirculating energy, W_c(MJ/m)	7.98
Total electrical output, W_{ET}(MJ/m)	38.52
Net electrical output, W_E(MJ/m)	30.54
Recirculating power fraction, ε	0.21
Engineering Q-value, Q_E	4.8
Thermal power density (MWt/m^3)(d)	0.85
Total thermal power (MWt)	2633.
Gross power output (MWe)	1053.
Net power output (MWe)	835.
Net plant efficiency $\eta_p = \eta_{TH}(1-\varepsilon)$	0.32

(a) Based on classical cross-field diffusion in the reentrant sections.

(b) Based on a thin 0.35-m blanket that is 86% efficient for capturing the fusion neutron energy.

(c) Derived from the expansion of the high-beta plasma against the confining magnetic field.

(d) Based on total volume enclosed by magnets.

(4-5 kV) to the poloidal field coil (PFC), and the toroidal current rises in ~ 0.1 s. The toroidal field coil (TFC) is simultaneously activated to generate the bias field B_{zo}. A tokamak startup code[10] models the initiation phase until the electron temperature has reached 0.1 keV. A minimum electric field of 5 V/m-mtorr, defined by the resistive voltage produced by the current in the plasma, is required for plasma initiation at initial filling pressures greater

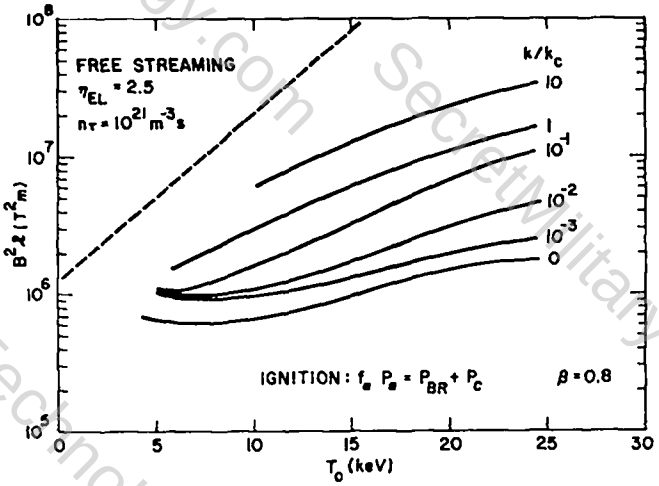

Fig. XVI-2.
Dependence on the center temperature of ignition conditions in the presence of classical axial (electron) thermal conduction to cold endplugs for a Linear Magnetic Fusion (LFM) device expressed as $B^2\ell$ with a consistent, classical treatment of the fraction f_α of alpha particles trapped in the plasma column of length ℓ(m).

than 0.5 mtorr and a plasma radius of 1 m. An electron runaway limit corresponds to a maximum of 20 V/m-mtorr and requires pressures above 0.1-0.2 mTorr. To minimize line-radiation power at low temperatures (0.01 keV), the pressure typically begins at 0.5-1 mtorr and is increased by gas injection to full density during the ~ 0.1-s toroidal current rise above 0.05 keV.

Above a plasma temperature of 0.1 keV a zero-dimension plasma model computes the RFPR burn dynamics. The toroidal current is held constant (crowbarred) at its maximum value for a burn time τ_B, and ohmic heating rapidly leads to plasma ignition. The vigorous burn associated with the ignited plasma (~ 250 MWt/m^3 of plasma) drives the poloidal beta β_θ above the $\beta_{\theta c_{11}} = 0.5$ limit established by MHD requirements.[11] The burn must either be "prematurely" quenched or the reaction rate reduced by other means (cold-gas injection, DT burnup) to maintain $\beta_{\theta c}$ throughout the burn cycle. Early quench is used for a 50-50% DT fuel mixture (by decreasing the plasma current), whereas 90%-10% DT fuel mixture controls β_θ by burnout. Generally, the use of a 10% tritium fraction achieves a near maximum Q_E at a minimum burn time. Future studies will model anomalous cross-field transport mechanisms as a means to control the poloidal beta.

The burn-cycle parametric studies varied the first-wall radius r_w, fixed the blanket thickness at 0.4 m, situated the room-temperature TFC immediately outside the blanket with a thickness of 0.15 (0.25)m, and outside the TFC was located the 0.6- (1.0-) m-thick room-temperature PFC system for the 50%-50% (90%-10%) DT fuel mixture cases. All joule losses accounted for a copper conductor filling fraction of 0.7 and parallel plate lead losses. An example of composite results for the 50%-50% DT "premature-quench" mode of operation is depicted in Fig. XVI-3 in the form of r_w vs the maximum toroidal current density for a given value of Q_E. Similar relationships have been generated for the 90%-10% DT "burn-out" mode of operation which produced Q_E values ~30% above those given on Fig. XVI-3. Selecting an experimentally achieved toroidal current density[11] of 20 MA/m^2 and limiting the first-wall temperature rise to 100-150 K, the interim design points for the 50%-50% and 90%-10% DT cases are summarized in Table XVI-IV. Burn times for the more conventional 50%-50% DT operating mode are 1 s as compared to the 6-s values found for the specific 90%-10% case given in Table XVI-IV.

The RFPR-I design uses a lithium-sodium-steam-heat transport system with a thermal cycle efficiency of 40% to produce 750 MWe at an overall plant efficiency of 30-33%. The design summarized herein is based primarily on the 50%-50% DT fuel mixture case, although both cases are similar. A plan view of the reactor system containing key RFPR subsystems is given in Fig. XVI-4. The heat-removal and thermal conversion systems are similar to those described in Ref. 12. Two 1250-MWt coolant loops transport the heat from the reactor to the single turbine/generator set. A lithium exit temperature of 820 K produces a sodium exit temperature of 810 K from the Li-Na heat exchangers. The remainder of the plant is similar to that envisaged for the Liquid-Metal

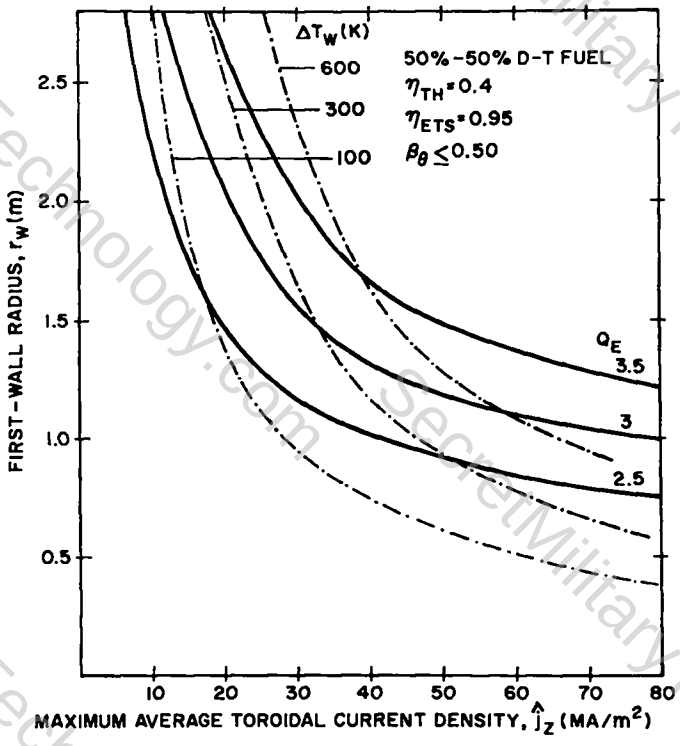

Fig. XVI-3.
Dependence of first-wall radius on the average (maximum) toroidal current density for a fixed engineering Q-value (inverse of recirculating power fraction) for the Reversed-Field Pinch Reactor (RFPR-I). The dashed curves represent lines of constant first-wall surface temperature rise.

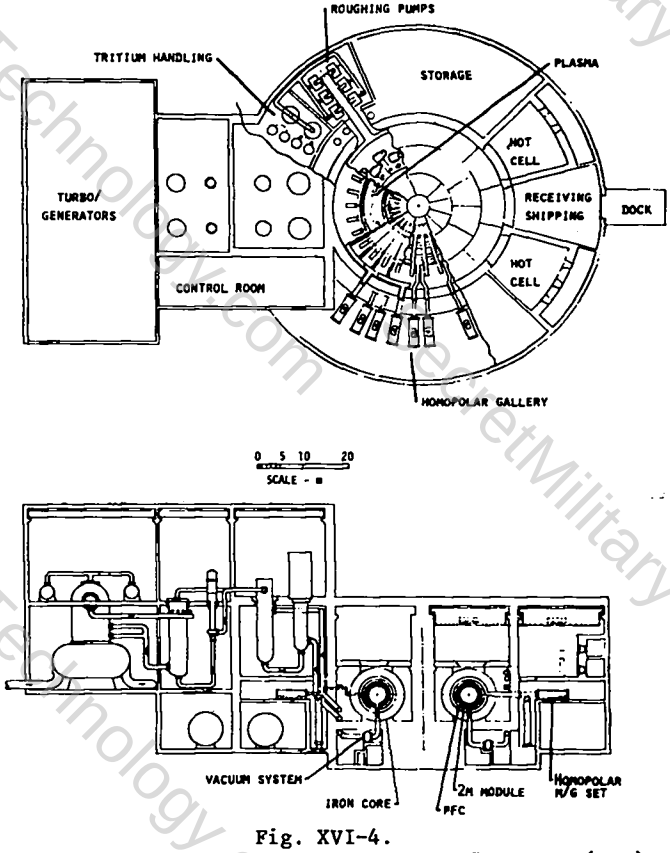

Fig. XVI-4.
Plan and elevation views of a 750 MWe (net) Reversed-Field Pinch Reactor (RFPR-I).

TABLE XVI-IV
SUMMARY OF TYPICAL RFPR PARAMETERS

Symbol	Definition	50%-50% DT	90%-10% DT
r_w	first-wall radius (m)	2.0	2.0
x_m	minimum plasma compression	0.4	0.4
I_z	peak toroidal plasma current (MA)	40.0	30.0
$\hat{j}_z$	average toroidal current density at minimum compression (MA/m^2)	20.0	15.0
P_A	ambient D-T filling pressure (mtorr)	2.0	1.35
n_i	ion density at ignition ($1/m^3$)	$8.52(10)^{20}$	$5.82(10)^{20}$
$n\tau$	time-integrated Lawson parameter (s/m^3)	$8.41(10)^{20}$	$2.64(10)^{21}$
f_T	initial tritium atom fraction	0.5	0.1
f_B	fractional burnup	0.109	0.184
T_{if}	ion temperature prior to quench (keV)	14.4	23.8
T_{ef}	electron temperature prior to quench (keV)	16.3	15.3
$(dT/dt)_Q$	post-burn plasma reactivity (keV/s)	18.5	-0.41
η_{TH}	thermal conversion efficiency	0.4	0.4
η_{ETS}	energy transfer/storage efficiency	0.95	0.95
W^o_{INT}	initial plasma energy (MJ/m)	0.086	0.058
W_{INT}	final plasma energy (MJ/m)	18.9	11.0
W_{BR}	bremsstrahlung energy (MJ/m)	5.38	19.9
W_{CY}	cyclotron energy into first wall (non-reflecting) (MJ/m)	1.72	16.9
W_N	fusion neutron energy (18 MeV/n) (MJ/m)	279.6	317.7
W_α	total alpha-particle energy (MJ/m)	54.7	62.1
W_{OHM}	plasma ohmic-heating energy (MJ/m)	5.11	5.85
W_{COND}	thermal conduction energy (MJ/m)	0.036	0.24
W_{DC}	direct-conversion energy (MJ/m)	34.7	21.3
W_{BZ}	energy requirements of toroidal field system (MJ/m)	13.3	7.3
$W_{B\theta}$	energy requirements of poloidal field system (MJ/m)	345.4	205.0
W_{BO}	total magnetic energy in ETS system (MJ/m)	358.7	212.3
W_{TR}	transport losses in coil and leads (MJ/m)	6.23	11.5
W_{ED}	eddy current losses in coil, leads, and blanket (MJ/m)	0.67	0.79
W^{IN}_B	field in plasma at end of burn (MJ/m)	37.1	19.6
W_{ETS}	ETS transfer losses $(1-\eta_{ETS})W_{BO}$ (MJ/m)	17.9	10.6
W_{TH}	total recoverable thermal energy (MJ/m)	342.7	385.5
W_{ET}	gross electric energy $\eta_{TH}W_{TH}$ (MJ/m)	137.1	154.2

TABLE XVI-IV cont'd.

Symbol	Definition	50%-50% DT	90%-10% DT
Q_E	engineering Q-value	4.06	5.39
W_C	total circulating energy (MJ/m)	33.8	28.6
ϵ	recirculating power fraction $1/Q_E$	0.25	0.19
W_E	net electric energy $(1-\epsilon)\ W_{ET}$ (MJ/m)	103.3	125.6
η_P	overall plant efficiency $\eta_{TH}(1-\epsilon)$	0.30	0.33
R	major radius (m)	10.0	10.0
τ_c	cycle time (s)	8.65	10.5
τ_B	burn time (s)	1.14	6.44
I_w	14-MeV neutron wall loading (MW/m^2)	2.00	1.87
P_{TH}	total thermal power (MWt)	2490.	2300.
P_{ET}	system gross electric power (MWe)	995.	921.
P_C	system circulating electric power (MWe)	245.	171.
P_E	net system electric power (MWe)	750.	750.
Δb	blanket thickness (m)	0.4	0.4
Δr_c	poloidal (toroidal) coil thickness (m)	0.60 (0.15)	1.00 (0.25)
P_{THB}	thermal power density in the the blanket (MWt/m^3)	7.18	6.63
P_{THT}	thermal power density averaged over total volume encompassed by the PFC (MWt/m^3)	2.71	1.66

Fast-Breeder Reactor. The plant operates at 755 K maximum steam temperature which is similar to the design temperatures of many fossil-fuel plants presently in operation.

As shown in Fig. XVI-4, the reactor is composed of thirty 2.1-m-long toroidal sections, resulting in a torus of 10-m major radius. An isometric view of a RFPR segment, given in Fig. XVI-5, shows the placement of major reactor components. The first wall also acts as the vacuum wall where the flanges at the ends of the 2.1-m-long modules are welded to form a vacuum seal. The lithium-cooled blanket and TFC are encircled by a structural ring which is used to lift the 2.1-m module. The blanket/first-wall assembly and vacuum ducting for each module is mechanically separate and supported by the iron-core structure. Outside the modules are located the 4-m-long poloidal field coils and the iron cores, which are divided into top and bottom semi-circular sections.

Referring to Fig. XVI-5, a vacuum pump and associated ducting is provided for each 2.1-m-long module with the vacuum tunnel located under the reactor floor. The inlet and outlet lithium coolant pipes encircle the torus at the reactor floor level, and separate connections are made to each module. The TFC is connected in parallel to a bus which also encircles the machine and is energized by two center-grounded homopolar machines. The PFC consists of wedge-shaped segments, where 1/15 of the conductors in each wedge are energized at each 4-m-long section, resulting in a single-turn transformer coil when the 15 sections are connected. Each of the PFC leads is then connected to two center-grounded homopolar machines.

The 20-30 homopolar generators used to energize the coils would be mounted on rails and

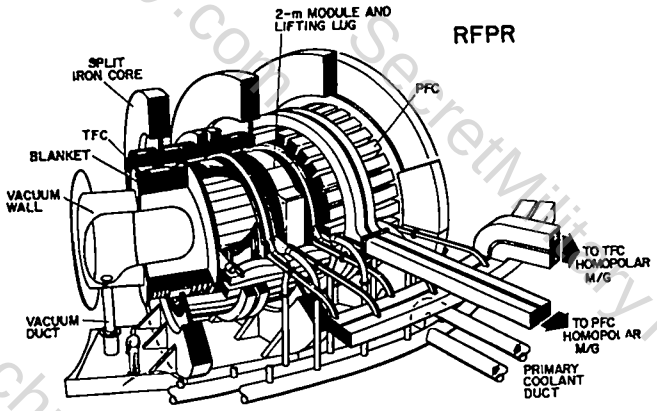

Fig. XVI-5.
Isometric view of 2-m-long Reverse-Field Pinch Reactor (RFPR-I) modules (six modules are shown) and associated poloidal field coil assemblies and iron-core pieces.

could easily be decoupled from the massive but permanent lead structure. A similar arrangement is envisaged for the banks of vacuum pumps with the additional difficulty of remote maintenance. The technology associated with the large number of remote manipulations of massive equipment will require considerable development. Other required reactor subsystems such as tritium handling/processing, He-gas coolant system for the coils, cryogenic facility for the superconducting homopolar energy stores, plant control system, and associated maintenance machinery will be addressed in future RFPR design studies. The balance of plant appears "standard" except for the Na/Li primary heat exchangers and Li pumps.

The 0.4-m-thick lithium-cooled (99% enriched ^{7}Li), Nb-1Zr blanket system[12] with 1- to 2-mm-thick niobium structural walls uses stagnant lead for neutron multiplication in the hard-spectrum regions, stagnant ^{6}Li (95% enriched) for tritium production, leading to an overall tritium breeding ratio of 1.10, and a combination of iron and boron carbide for attenuation of gamma rays and slow neutrons. The efficiency of the blanket in capturing neutron energy is to be near 100% resulting in a total thermal energy of 18 MeV/neutron. Division of the blanket into 30 azimuthal sections reduces the eddy-current losses.

The electrical circuit for both the TFC and the PFC is a basic LC or tank circuit wherein the homopolar machine acts as a capacitor. Closure of a switch (homopolar brushes) in the TFC circuit at time $-\tau_R/2$ connects the homopolar machine at full speed and voltage to the TFC. The current rises to a maximum, producing the initial toroidal bias field B_{zo}. The plasma is preionized, and the analagous switch on the PFC system is closed. The toroidal current I_z rises to a maximum value as the toroidal field continues to "ring" inductively, ultimately yielding the desired reversed toroidal field. At time τ_R a "crowbar" switch is closed, and the current I_z and reverse field are maintained at a near constant value during the burn period, τ_B. The homopolar machine remains at rest during this period. Following the burn the "crowbar" switch is opened, and the respective TFC and PFC currents are transferred back to the homopolar machine, which motors up to 100% speed and voltage (neglecting losses) at which time the brushes are lifted. The above cycle is repeated at the desired pulse rate. Losses incurred during the transfer are made up by bringing the homopolar generators up to full speed, using plant recirculating power.

Solid-state switching may be used for both TFC and PFC systems. The rating of commercially available solid-state devices is about 200 kA at 4-6 kV, and many such switches must be paralleled to give the desired current rating. The cost of this kind of switching element, however, is prohibitively high today. The present price estimates[13] are 10^4 $/MVA with total requirements on the order of $5(10)^4$ MVA. This problem may be alleviated by using hydraulic (oil) breakers[14] which can interrupt ~100 kA and may cost < $2000. This approach is favorable considering that ~300-400 switches are needed; the reliability of these switches must ultimately be resolved.

An iron core ideally couples the PFC current and plasma current, although requirements of 920(690)Wb for the 50%-50%(90%-10%) DT fuel mixture cases results in 230(170)m^2 of iron and represents a large economic penalty. Using an air-core system is most attractive when the PFC current is changed symmetrically from minus to plus during startup and returned to a minus value during the quench period. In this case the coil current cannot be extracted until after the quench (2-3 s) and should be left in the coil; using the

homopolar generator as a transfer capacitor to symmetrically swing the current from plus to minus would require an energy store equal to half that needed by the iron-core case. Operating in this mode greatly increases the ohmic losses in the coil when compared to an iron-core system, because of current flow during the reactor dwell time. These considerations have lead to future studies of iron-core and air-core systems using superconducting coils. In addition to altering significantly the RFPR burn cycle, ongoing design studies are based upon economic/cost oriented system optima. Generally, future RFPR conceptual studies will focus onto this long-pulse ($\sim$30 s) mode of operation.

D. FAST-LINER REACTOR (FLR) STUDIES

The fast-liner concept was subject to preliminary examination as a potential source of fusion power.[15] This approach to plasma heating and confinement is shown schematically in Fig. XVI-6. An axial current is driven through a thin ($\sim$3-mm) metal cylindrical shell to produce a large external magnetic field. For reactor applications the magnetic field would implode the liner at high speed ($\sim 10^4$ m/s) onto a warm (250-500 eV), dense ($\sim 10^{24}$ m^{-3}) plasma (r_{10} = 0.2 m, ℓ = 0.2 m). The compressed plasma would reach thermonuclear temperatures in $\sim$20 μs and release 2-4 GJ of D-T fusion energy during a $\sim$2-μs burn period. The plasma particle pressure would be supported directly by the liner surface and material

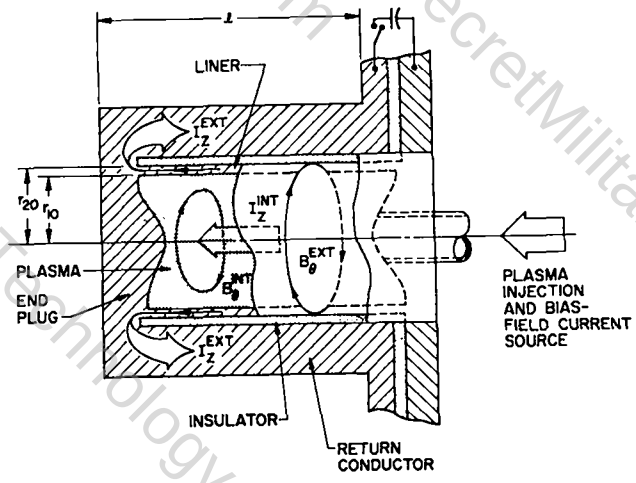

Fig. XVI-6.
Schematic diagram of essential elements of a Fast-Liner Reactor (FLR).

endplugs; thermal conduction to the liner and endplugs would be inhibited by an azimuthal field embedded in the plasma.

The FLR would provide a relatively small ($\sim$2.5-m-radius spherical containment vessel), high overall power density ($\sim$ 5-10 MWt/m^3) energy source. A recirculating power fraction of 0.20-0.30 is anticipated. Major engineering problems and/or uncertainties are i) plasma preparation and injection into the liner, ii) economical recycling and/or replacement of destroyed components, iii) blast confinement, iv) pulsed energy switching and transfer to the liner (reversible recovery of pulsed energy is not envisaged), and v) rapid liner and leads replacement. These problem areas are being assessed and quantified.

1. Plasma-Liner Simulation. The FLR thermonuclear burn code described in Section H.3 was used for this analysis. Thermal conduction and field diffusion are computed for the radial direction using an implicit Lagrangian method. A simple analytical model approximates axial thermal conduction to the liner endplugs. An azimuthal magnetic field embedded in the plasma substantially reduces thermal losses when the global beta at the wall is $\sim$ 0.5. Bremsstrahlung radiation losses are included, and an approximate liner compressibility model[16] is employed. Coupling to the driving circuit is not yet considered.

Figure XVI-7 illustrates the computation of scientific Q values (fusion energy relative to the initial liner energy) for a variety of plasma and liner parameters. The initial liner velocity, v_{10}, is treated as an independent variable, and the initial liner thickness becomes a variable proportional to v_{10}^{-2}; in this way the initial liner energy is held constant along each curve in Fig. XVI-7. The liner material is copper without resistivity.

The data in Fig XVI-7 represent initial liner/plasma conditions of W_{KRO} = 1.7 GJ/m, r_{10} = 0.2 m, $n_o = 1.25 \times 10^{24}$ m^{-3}, and B^{INT} = 13 T, where this choice of field corresponds to β_{10} = 0.5. These parameters were selected to produce a Q greater than 10 for a compressible liner model, including plasma losses, and v_{10} = 10^4 m/s. Two other plasma/liner models are

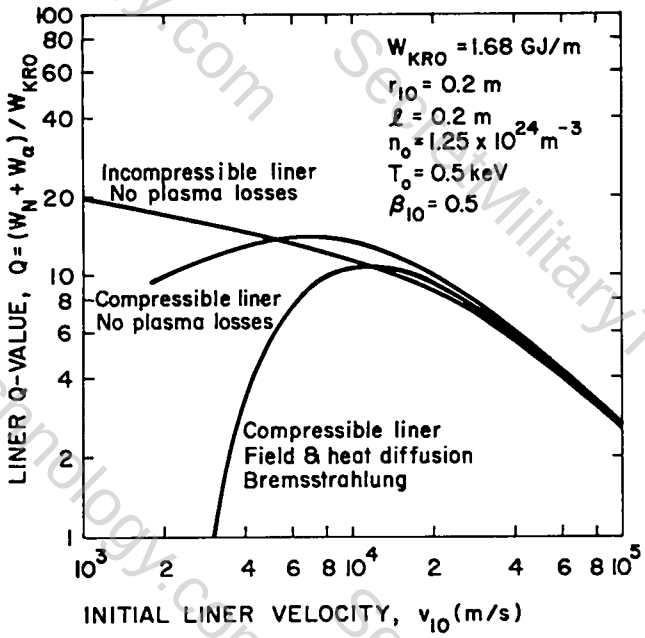

Fig. XVI-7.
Effects of various loss processes on FLR Q-value (neutron energy/liner kinetic energy) using single-fluid MHD model and analytic approximation for liner compression.

represented here: the lossless plasma with both compressible and incompressible liner.

To understand qualitatively the velocity dependence, the curve for a lossless plasma and incompressible liner in Fig. XVI-7 is first considered. For this case the kinetic energy of the liner can only be transferred to the plasma. Since W_{KRO} and the initial plasma conditions are independent of v_{10}, the plasma radius, temperature, and density are also independent of v_{10} at peak compression ($v_1 = 0$).* The maximum fusion power per meter of liner $P_F \simeq \pi/4\, r_{1f}^2 n_f^2 \langle\sigma v\rangle (E_N + E_\alpha)$, therefore, is independent of v_{10}. By defining a liner "dwell time" $\tau_d = r_{10}/v_{10}$, it is possible to approximate the energy per meter produced, $W_F \simeq P_F \tau_d$, and to estimate the gain, $Q \; W_F/W_{KRO} \propto 1/v_{10}$. The $1/v_{10}$ dependence of Q is clearly seen in Fig. XVI-7 for $v_{10} \gtrsim 10^4$ m/s. Although Q monotonically decreases as v_{10} increases in all cases, the $1/v_{10}$ proportionality is not followed for low v_{10} because of thick liner effects.

*The plasma radius at peak compression increases by 1% as v_{10} goes from 10^3 m/s to 10^5 m/s as a result of a change in the fractional DT burnup from 20% to 3%.

The compressible liner and lossless plasma model exhibits three interesting features. First, when the liner has a low velocity and is relatively thick, a large fraction of W_{KRO} is consumed in liner compression. Here, the reduced plasma energy is not compensated by the large dwell time (i.e., high burnup) and Q is reduced. Second, in the region of maximum Q approximately 30% of W_{KRO} is used to compress the liner, increasing the average liner density by a factor of 2.5. Although the final plasma energy and peak fusion power are reduced as compared to the incompressible case, the increased dwell time is sufficient to raise Q. Third, the compressible liner model approaches the incompressible case at high velocities.

Plasma losses are considered in the last example; these include thermal conduction to the wall in both the radial and axial directions, bremsstrahlung, and magnetic diffusion. At high velocities the dwell time is relatively short and only a small fraction of plasma energy is lost. Consequently little effect on Q results. As v_{10} is reduced τ_d increases and losses substantially reduce the plasma energy at peak compression. This accounts for the large reduction of Q by losses at low velocities.

Many physical effects must still be incorporated into the FLR plasma model, such as joule losses in the liner, alpha pressure, and turbulence. An interim reactor example is taken from Fig. XVI-7: W_{KRO} = 1.7 GJ/m, n_o = 1.24 x 10^{24} m^{-3}, T_o = 500 eV, B_{INT} = 13 T, r_{10} = 0.2 m, ℓ = 0.2 m, v_{10} = 1.2 x 10^4 m/s, and Δ_o = 2 mm, leading to Q = 11. For an energy transfer efficiency to the liner of 80%, a thermal-to-electrical energy conversion efficiency of 40%, and a neutron energy multiplication of 1.25 the liner Q-value of Q = 11 leads to a plant recirculating power fraction of 0.24.

2. Blast Containment. Approximately 20% of the fusion energy from the ~2-μs burn would be deposited in and near the liner by alpha particles, and this energy coupled with the initial kinetic energy of the liner would produce an explosion equivalent to several hundred kilograms of high explosive;[17] blast data are

being used with theoretical analyses to predict the containment requirements for the FLR.

In the simplest containment model the blast energy W is assumed to be thermalized in an ideal gas. The circumferential stress that would result in a spherical pressure vessel is computed using a thin-shell approximation

$$\sigma_\theta = W/4\pi R^2 \Delta R \quad , \qquad (1)$$

where R is the shell radius and ΔR its thickness. The corresponding strain is

$$\varepsilon = [(1-\nu)\sigma_\theta - \nu\sigma_r]/E \quad , \qquad (2)$$

where E is Young's modulus, ν is Poisson's ratio and σ_r is the radial stress. These expressions agree well with experimental data for vessels with R = 0.5 m that have elastically responded in vacuum to detonation equivalent to 1 kg of high explosive.[17] In the presence of air at atmospheric pressure, the blast-induced stresses were about four times the analytic predictions.

The computer program PAD[18] is being used to model shock spectra resulting from energy releases of the magnitude expected for the FLR. This code system is based upon a one-dimensional Lagrangian model that computes motion of the explosive gas and the response of the spherical container. Radiative heat transfer and thermal conduction, however, are not yet considered.

The preliminary FLR operating point[15] served as input to PAD for computations of the vacuum blast containment. The blast energy, W = 1.42 GJ, was initially deposited in a sphere of mass M with the density of solid copper situated at the vessel center; M represents destroyed liner and leads material. Based upon blast scaling with experimental data, the radius of the containment sphere equals 2.6 m, and the vessel wall thickness equals 0.15 m. The density and modulus for the containment vessel was that for 304 stainless steel, but the vessel was not allowed to yield. When the yield stress is exceeded in a computational result, ΔR can be appropriately scaled to reduce the stress-to-acceptable levels. Results of the PAD computations are shown in Fig. XVI-8, where the gas pressure at the inner wall and circumferential

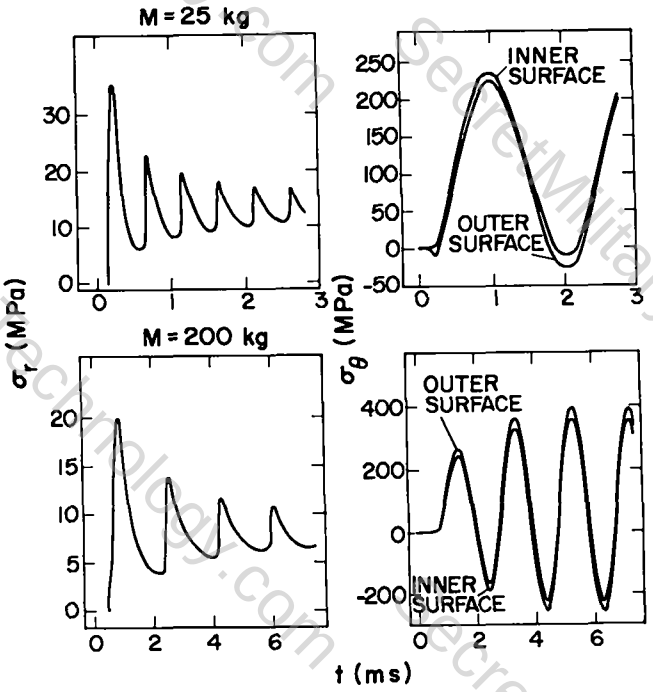

Fig. XVI-8.
One-dimensional Lagrangian hydrocode (PAD)[18] analysis of FLR blast containment in a 2.6-m-radius 0.15-m-thick evacuated sphere made of 304 stainless steel. Hydrostatic pressure is given as a function of time at the inner surface of the vessel, $\sigma_r(t)$, for explosive energy (1.42 GJ) deposition into liner and leads masses of 25 and 200 kg, respectively. Circumferential stress, $\sigma_\theta(t)$, is given at the inner and outer vessel surfaces.

stress at the inner and outer walls are plotted as functions of time. Figures XVI-8A and XVI-8B represent M = 25 and 200 kG, respectively. The vessel oscillates at a frequency of $f_v \simeq 475$ Hz, that is independent of ΔR under the thin-shell approximation. The reverberating gas oscillates at a frequency of $f_g \propto M^{1/2}$.

The maximum vessel strain is plotted as a function of explosive mass M in Fig. XVI-9. It is observed that the maximum stress is nearly constant for small values of M where $f_g >> f_v$. For this situation the gas pressure at the vessel wall oscillates about and is ultimately damped to the pressure of quiescent gas with energy W. Meanwhile, the vessel moves nearly as a harmonic oscillator from a condition of zero hoop stress to a maximum stress. The average hoop stress will support the pressure of a quiescent gas of energy W as given above. Since the shell oscillates harmonically from zero to a maximum, the peak stress is approximately twice the average

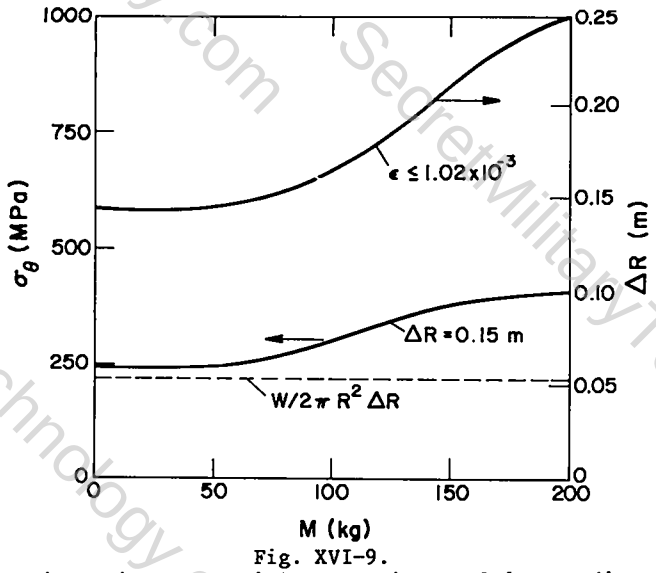

Fig. XVI-9.
Maximum circumferential stress in a 2.6-m-radius 0.15-m-thick sphere and minimum thickness required to limit strain to 1.02×10^{-3}. The explosive energy (1.42 GJ) is deposited in a mass M, representing a combined mass of destroyed leads and liner.

stress. This approximation fails when the explosive gas and shell come into resonance at $f_g \simeq f_v$, as observed in Fig. XVI-8B. In this case the maximum stress is 77% higher than the value given by the above-mentioned approximation.

Based on fatigue data,[19] as interpreted for liner blast containment,[17] a peak microstrain of 1016 is acceptable for a 10-year life $(2.5(10)^7$ shots) at 800 K. By taking $\nu = 0.29$, $\sigma_r = 20$ MPa and E = 160 GPa, the maximum allowable stress and minimum thickness as functions of M can be computed; this dependence is shown in Fig. XVI-9.

This work provides a preliminary estimate of the containment requirements for a FLR operating in an evacuated sphere. The computer program PAD has been modified to operate in the FLR regime, and analytic comparisons have checked the accuracy of PAD. It would be preferable to operate a FLR with a mitigating and tritium-breeding material in the blast chamber[15]; the newly modified version of PAD is now being used to improve on previous studies of mitigators.[17]

Two basic concepts are under consideration for blast mitigation in addition to containment in a vacuum. First is the possibility of immersing the liner assembly in a fluidized bed of lithium-bearing pellets or flakes.[17] It has been shown experimentally that some solids (vermiculite) can reduce the effect of a blast by a factor of 2 or more.[15] If a fluidized bed of Li_2O or $LiAlO_2$ could function similarly, the added benefits of tritium breeding and using the fluidizing gas for heat transfer would be accrued.

Another mitigating concept would fill the blast chamber with a mixture of gas (probably helium) and a lithium-bearing liquid such as $Pb_{0.9}Li_{0.1}$. This approach has been studied with simple shock models[17] that show great amplification of the blast effects. It is believed that an improved and proper model that perhaps includes a (mechanical) shock absorption mechanism at the wall could greatly reduce the containment requirements predicted thus far.

3. Current Leads. The FLR may require a driving current of ~200 MA at a voltage of 250 kV. Any structure within 1-2 m of the liner would be destroyed each shot. Hence, the leads and liner must be manufactured from material that can be easly recycled.[17]

A preliminary optimization study was made of coaxial current leads for use in the FLR. A generalized, coaxial lead configuration for use in the FLR which was subjected to a simultaneous configuration, cost and energy optimization. Costs were assigned to both metal and insulator lead components, and energy losses resulting from joule heating of the conductor, inductive energy storage in the leads, and mechanical energy transfer to the conductor by magnetic forces were included in this optimization program. It was found that 20-30% of the leads cost could be associated with the mechanical energy imparted to the conductor and that generally the coaxial lead structure yielded an optimized configuration that may be too expensive.

To reduce this cost, an alternative lead arrangement was devised as shown in Fig. XVI-10. In this leads configuration, currents flow alternately to and from the lines on adjacent conductors, and insulation is woven between conductors of opposite polarity. The impulse momentum imparted to this structure is typically 5% of that encountered for coaxial conductors. The kinetic energy lost to the interwoven leads structure is negligible. This and other leads concepts are being studied in an effort to reduce the overall

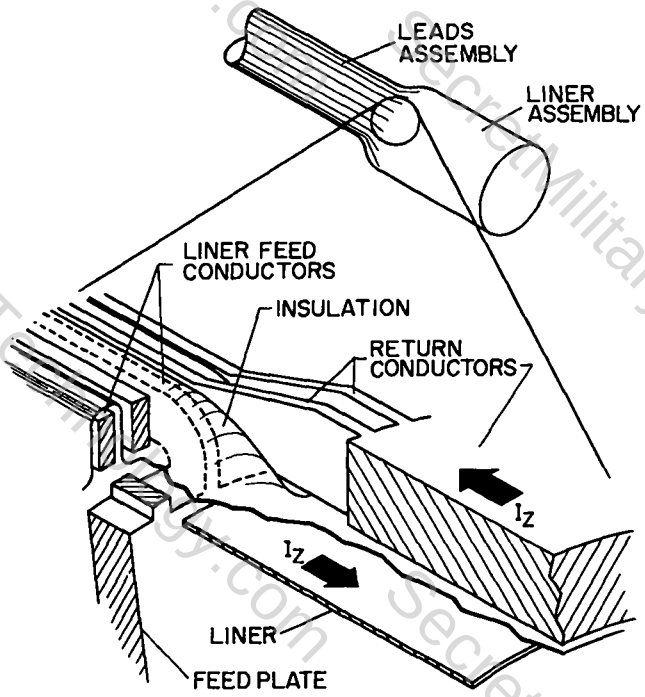

LEADS STRUCTURE FOR FLR

Fig. XVI-10.
Cross section of interleaved conductor lead structure. Current alternates to and from the liner in alternate conductors. Magnetic forces react on these conductors radially outward with only 5 to 10% of the momentum transferred to coaxial leads.

operating costs while maintaining an acceptable level of simplicity.

4. Liner Burn Code (LNRBRN). The computer program LNRBRN was developed to model FLR plasma and liner processes. Thermal conduction and field diffusion are computed numerically for the radial direction using an implicit Lagrangian method and resistivity coefficients from Braginskii.[20] A simple analytic model approximates axial thermal conduction to the endplugs of a liner. An azimuthal magnetic field embedded in the plasma substantially reduces thermal losses when the global beta approaches unity at the wall initially. Radiation losses by bremsstrahlung are also considered. At peak compression plasma pressures are high enough to increase the liner density by a factor of 2 or more. The impulse momentum approximation was used[16] to give an analytic model of liner compression and dynamics as related to the plasma. The liner electrical resistivity is not considered, but eventually will be incorporated.

The approximations described above provide a simple and rapid FLR modeling code. Comparison of LNRBRN to the detailed hydrodynamic code[21] CHAMISA shows good agreement. Within the limits of the physics model, the LNRBRN code provides a good description of the FLR, will continue to be used for reactor modeling, and will be subjected to continued evaluation against the CHAMISA code system as refinements are made.

E. OTHER NON-MAINLINE REACTOR STUDIES

1. Fusion Burner Studies. Hasegawa, et al.,[22] have presented a challenging idea for the operation of a steady-flow reactor that does not rely on magnetic field shaping or compression for its operation. An ignited reactor has been proposed to operate in a steady-state condition, much like a gas burner. The concept is very simple; cold fuel would be injected at the end of a linear solenoid. Somewhere along the machine the plasma is somehow ignited, and approximately one-half of the alpha particles generated by fusion would travel "upstream" along the magnetic field and heat the incoming, cooler plasma.

No flow limitations exist along any section of the plasma where the net heating is zero. This condition can be insured after the point where the plasma reaches ignition by increased radiation or reduced alpha-energy deposition. From the point of view of reactor feasibility, it is of interest to determine the length of the ignited region required to insure that the plasma may indeed be self-heated and sustained at ignition. The choke-flow conditions are determined by the laws of conservation of mass and momentum. Numerical solutions to the energy equation have been obtained and used to assess the reactor potential of a steady-state fusion burner. Figure XVI-11 depicts the fusion burner of length ℓ, mass flow M, specified inlet and exit conditions, and spatially dependent energy releases.

Figure XVI-12 gives the numerically determined relationship between the exit Mach number Ma_o and the steady-state mass flow rate M for the zero-gradient condition at the exit (y=0) end. As the exit Mach number is increased, the increased convective transport can be supplied only by increasing the source strength by means of

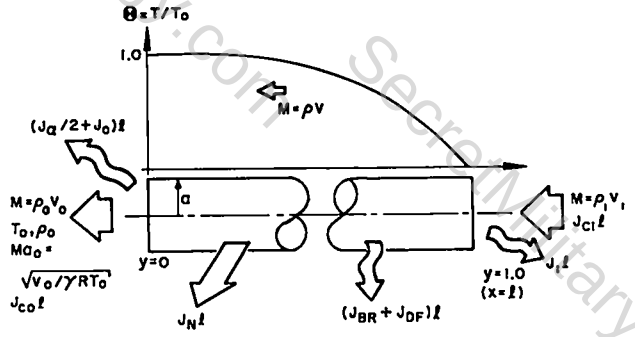

Fig. XVI-11.
Schematic diagram used to examine the steady-state solenoidal fusion burner. The normalized axial coordinate system is located at the (hot) exit end (y = 0) and the total alpha particle, bremsstrahlung, radial diffusion, conduction, and flow (convection) losses are expressed per unit cross-sectional area πa^2 as J_α, J_{BR}, J_{DF}, J_C, and J_0, respectively.

increased $M\ell$ values. For $Ma_o > 0.5$ the convective loss represents the major energy demand on the alpha-particle source, whereas for $Ma_o < 0.2$ conduction loss through the cold end dominates. For Mach numbers below ~0.04 the burnup of D-T fuel along the device length becomes so great that the zero-gradient condition at the hot end cannot

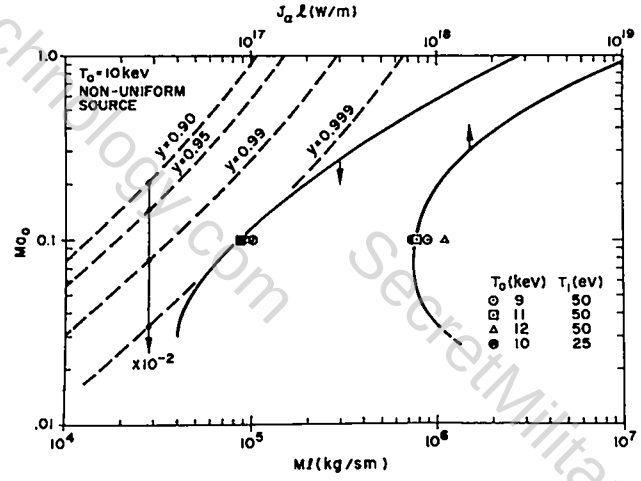

Fig. XVI-12.
Dependence exit mach number Ma_o on the product of fusion burner length ℓ(m) and mass flow rate M(kg/s m²) necessary to achieve a zero-gradient exit condition (no heat input). The associated fusion power, expressed as total alpha-particle power per unit cross-sectional area $J_\alpha(W/m^2)$ times the device length ℓ(m) is also shown. The curves denoted by "y=" indicate the $Ma_o - M\ell$ relationship for the condition when the electron-electron collision time equals the conduction time, which is a criterion where classical conduction is expected to break down at the designated axial position y (re: Fig. XVI-11).

be maintained, and a steady-state solution without external heat addition and/or refueling is not possible.

Figure XVI-12 also shows the dependence of the output power as measured by $J_\alpha\ell$(W/m). As expected, increasing Ma_o demands more fusion power to compensate for the increased convective loss from the hot end. As the exit Mach number drops below ~ 0.2, the major loss becomes conduction at the cold end, which is roughly independent of the flow condition. When burnup effects become important for very low Ma_o values, the fusion rate needed to maintain the zero-gradient condition at y = 0 must increase again, showing the minimum $J_\alpha\ell$ value. As Ma_o falls below ~0.04, no amount of fusion is possible to keep the net source positive, and a steady-state operation is not possible without external heat addition or DT refueling. The Ma_o value of 0.1 appears to represent a minimum power output at T_o = 10 KeV.

Although the steady-state "fusion burner" offers possibilities for a stable, very simple fusion reactor, classical thermal conduction along the axis of the device leads to large devices that develop enormous thermal powers. Unless a reduction in thermal conductivity relative to the classical value amounts to a few orders of magnitude, the self-sustained fusion burner will more than likely remain a large power producer.

2. Tormac Reactor Studies. The first phase[23] of a systems study of the toroidal bi-cusp Tormac[24] commenced in the last quarter of 1977. The simple reactor model and energy balance differs little from that used by Brown and Kunkel[25] for the purposes of the DOE/DMFE Evaluation of Alternative Fusion Concepts.[26] Emphasis is placed upon the sensitivity of the Tormac reactor performance to the cusp confinement, electron-to-ion temperature ratio and plasma beta. The algorithm used in this study is more general and the parameter variations are more extensive than those presented in Ref. 25. Also included were all major energy terms in the steady-state Tormac plasma energy balance, although some of these terms may be negligible in certain parameter ranges. More important, however, explicit and self-consistent expressions

are given for all aspects of the plasma energy balance, in order that differences in results can be more readily explained. Whenever possible, less sensitive parameters are chosen to agree with those used in Ref. 25. The questions of startup, steady-state operation, and radial profiles are the subject of ongoing study.

Figure XVI-13 depicts the steady-state Tormac reactor model. Although the steady-state, Maxwellian D-T plasma was described by one component (ions), the effect of differences in electron and ion temperatures on pressure balance and radiation losses was included by the parameter $\lambda = T_e/T_i$. The plasma was assumed to have no internal structure, but was described by an effective minor radius r_p(m) and major radius R(m). Ion and electron cusp losses P_ℓ(Wt) and the fraction $1-f_\alpha$ of the total alpha-particle power P_α(Wt) lost from the plasma (primarily through the cusps) were assumed to be deposited to the thermal cycle, as were the neutron (18.9 MeV/fusion) power P_N(Wt), the bremsstrahlung radiation P_{BR}(Wt) and the cyclotron radiation P_{CY}(Wt). The total thermal power,

$$P_{TH}(Wt) = P_\ell + (1-f_\alpha)P_\alpha + P_N + P_{BR} + P_{CY} \quad , \qquad (3)$$

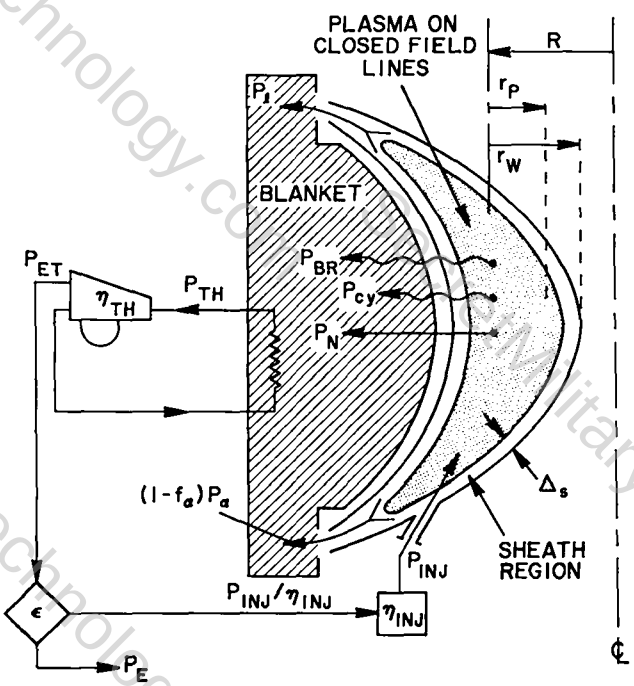

Fig. XVI-13.
Schematic diagram of idealized, steady-state Tormac reactor energy balance.

was assumed to be converted with efficiency η_{TH} to electrical power $P_{ET}(We) = \eta_{TH}P_{TH}$. Only the total electrical power P_{INJ}/η_{INJ} needed to drive an unspecified energy injector (e.g., neutral beams) at efficiency η_{INJ} was assumed to contribute the recirculating power needs; the power P_{INJ}(Wt) is simply that needed to maintain the Tormac plasma in a thermal steady state. That is,

$$P_{INJ}(Wt) = P_\ell + P_{BR} + P_{CY} - f_\alpha P_\alpha \quad , \qquad (4)$$

which is identical to the plasma energy balance used in Ref. 25. Hence, the fraction of the total electrical power generated by the Tormac reactor that must be recirculated to assure a thermal steady state is given by

$$\epsilon = (P_{INJ}/\eta_{INJ})/P_{ET} \quad . \qquad (5)$$

All results are expressed either in terms of an engineering Q-value, $Q_E = 1/\epsilon$, or the net electrical power $P_E = P_{ET}(1-\epsilon)$. Either Q_E or P_E(We) have been parametrically evaluated as a fuction of ion temperature T(keV), with the first-wall 14.1-MeV neutron current $I_W(MW/m^2)$ serving as a major constraint. Designating r_w(m) as an effective first-wall radius, r_p(m) as an effective plasma radius, and M equal to the blanket energy multiplication relative to the 14.1-MeV fusion neutron (M = 18.9/14.1 = 1.34 for the cases considered),

$$I_W(MW/m^2) = (P_N/M)/(2\pi)^2 r_w R \quad , \qquad (6)$$

and $x = r_p/r_w$. No attempt was made to distinguish between the inner vs outer neutron wall current, which for a small aspect ratio ($A = R/r_p$) cusp can differ appreciably from the averaged value, I_W, used here.

Reference 23 presents a complete parameter study of the Tormac reactor concept based upon this simple model. The sensitivity of the Tormac reactor performance (e.g., size and efficiency) to the sheath physics is noted, and future studies will explore more this aspect. Additionally, the question of startup, transport within the closed-field plasma, heating, and steady-state operation will be addressed.

F. HYBRID (FUSION-FISSION) ECONOMICS STUDIES

A majority of fusion-fission design studies generally have focused onto either detailed blanket studies or specific fusion-driven concepts. The economic performance of a given hybrid system, therefore, is based upon relatively detailed plasma, neutronic, and engineering models of a specific, rather narrow class of systems. In order to examine more generally the dependence of fusion-driver performance (as measured by the engineering Q-value, Q_E) on the characteristics of the hybrid blanket (as measured by the conversion ratio, [CV], and the in situ energy multiplication, M, and generalized economic parameters (energy cost c_p, fuel cost c_f, capital costs of hybrid and burner reactors C and C_p^*, fuel handling costs C_F and C_F^*, etc.) a simple but comprehensive expression has been derived that relates [CV] and M for a given economic constraint.[27] Figure XVI-14 depicts schematically the flow of fissile fuel and electrical energy upon which the simple economic model is based.

The return on investment over the time periods T and T* are Δ and Δ^*, respectively, for the hybrid and burner reactors. This cost/revenue derived relationship between [CV] and M was evaluated parametrically,[27] and the neutronic constraints imposed upon [CV] vs M for unenriched blankets have been taken into account.

Figure XVI-15 illustrates graphically the relation between [CV] and M for the range of

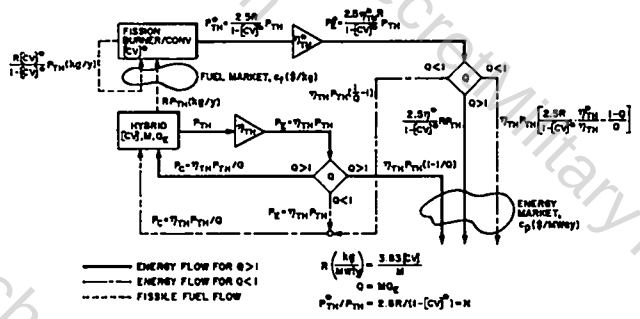

Fig. XVI-14.
Schematic representation of fusion-fission/burner-converter model used to evaluate cost-constrained flow of fissile fuel and energy. Quantities with (*) superscripts refer to burner-converter parameters, whereas quantities without superscript refer to the fusion-fission system.

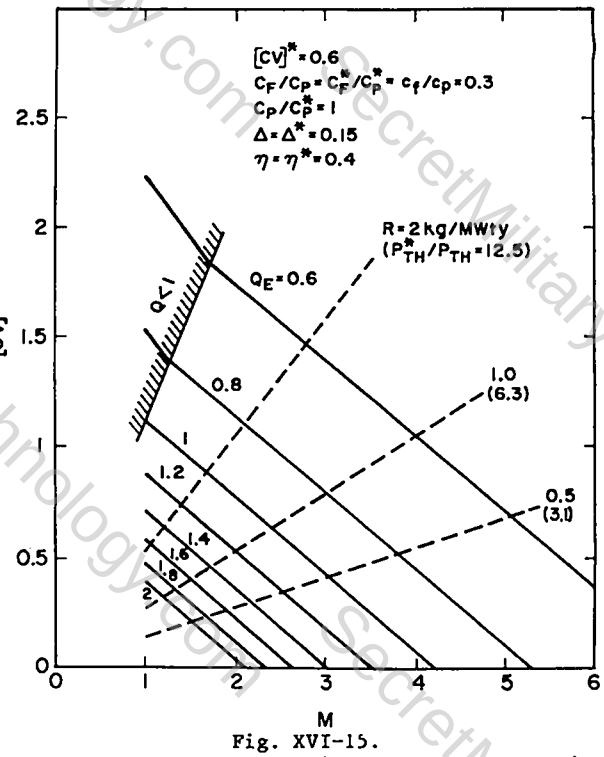

Fig. XVI-15.
Cost-constrained relationship between the fusion-fission conversion ratio [CV] and energy multiplication M for a range of fusion-driven engineering Q-values Q_E with the converter-burner conversion ratio $[CV]^* = 0.6$ and a fuel-to-power cost ratio $c_f/c_p = 0.3$.

parameters indicated. On the basis of this and similar[27] evaluations, the following conclusions have been made.

a) Fusion-fission systems which must be driven by external power sources (i.e., $Q = Q_E M < 1$) are economically possible only for very large values of [CV] and $\rho = c_f/c_p$. For a relatively wide range of fusion-fission blankets subjected to neutronic analysis[28] the required [CV] and M values have not been found, and the high ρ values required appear unrealistic. Hence, externally driven symbiotes ($Q < 1$, $M \simeq 1$) appear economically unacceptable for the assumed conditions.

b) The curves of constant Q_E shown on Fig. XVI-15, as expected, converge to the [CV] = 0, M = 1 point as Q_E increases, the rate of collapse to this pure-fusion operating point depending strongly on the magnitude of $\rho = c_f/c_p$ and $[CV]^*$. Generally, for $Q_E \gtrsim 3$ the pure-fusion system becomes attractive and preferable. Given that R(kg/MWt y) $\lesssim 1$ at best, symbiotes (i.e., M = 1) are feasible only for [CV] values that are

considerably below unity and for fusion-driver systems of reasonable efficiency ($Q_E > 2$). Unless the burner-converter system has a very low conversion ratio $[CV]^*$ and the fuel cost becomes an appreciable fraction of the total energy cost, and in view of conclusion a), pure symbiotes do not appear feasible for this combination of neutronic and economic reasons.

c) For the same values of [CV] and M, either increasing $[CV]^*$ or decreasing ρ forces the required fusion-fission system efficiency Q_E to higher and higher values. Low-efficiency fusion drivers are economic only if the fissile fuel cost becomes high and the burner-converters in themselves are poor generators of fissile fuel. In other words, for high values of $[CV]^*$ and low values of ρ, economic considerations force the fusion-fission system to generate more electrical power in order to remain competitive (a constraint imposed throughout this analysis).

d) Fissile fuel produced by the fusion-fission system would be attractive, according to the fissile fuel costs expected for the coming years, if the fuel-to-energy cost ratio is sufficiently low ($\lesssim 0.3$). The realization of this condition depends on technology advancement (high Q_E and M) and the difficult requirement on capital cost ($C_p/C_p^* \lesssim 1.3$).

e) Given that R(kg/MWt y) $\lesssim 1$ and that a kilogram of fissile fuel represents a potential thermal energy of 2.5 MWt y, the fusion-fission system will generate a quantity of in situ energy comparable to the energy content of the fissile fuel produced. For the more likely value[28] of R = 0.4 kg/MWt y, the in situ "real" energy generation equals the "virtual" energy production of the bred fissile fuel. Since $P_{TH}^*/P_{TH} = 2.5\ R/(1-[CV]^*)$, however, the power P_{TH}(MWt) accompanying the production of RP_{TH}(kg/y) of fissile fuel by the fusion-fission system is multiplied or amplified by a factor of $2.5\ R/(1-[CV]^*)$ when this fuel is consumed by a burner-converter system with an intrinsic conversion ratio $[CV]^*$. In effect the cost of the fusion-fission system is spread over the cost of $N = P_{TH}^*/P_{TH}$ burner-converter systems.

G. SYNTHETIC FUEL PRODUCTION BY FUSION POWER

A study of the feasibility of utilizing the unique features of D-T fusion power for the generation of hydrogen gas by means of a high-temperature ($\sim$ 1500 K) thermochemical cycle and a low-temperature ($\sim$ 300 K) electrolysis commenced in the last quarter of 1977. The general ground rules for this study include a) a generalized cylindrical blanket geometry will be used (i.e., the constraints imposed by a specific fusion driver will not be specified), b) the blanket must have a breeding ratio [BR] > 1, c) the plant capacity will be in the range 2-5 GWt, d) no net electricity will be generated, e) a pure dc hybrid (i.e., low-temperature electrolysis) thermochemical cycle will be used that has some basis in experimental fact. This synfuel study is divided into four tasks: a) overall energy balance and economics, b) neutronics analysis (tritium breeding, delineate low- and high-temperature regions, etc.), c) thermal/mechanical design of blanket, and d) (chemical) process design for the (ex-core) thermochemical cycle.

1. Energy Balance and Economics. A simplified but general fusion/thermochemical hydrogen model has been developed to examine the trade-offs between tritium breeding (assumed to occur in a low-temperature ($\sim$ 800-900 K) region of the blanket), electricity production, and production of high-temperature ($\sim$ 1500 K) process heat in an outer blanket region. Figure XVI-16 schematically depicts this model, which examines the economic trade-offs associated with overall system performance (i.e., fusion-driver efficiency $1-\varepsilon$, fraction f of fusion energy deposited in the outer high-temperature blanket versus tritium-breeding ratio [BR], thermochemical efficiency η^*, high- to low-temperature heat leaks ε_1, etc.) and the market prices associated with tritium, hydrogen, and electricity markets. In view of ground rule d) cited above, the parameter k in Fig. XVI-16 is set to zero (i.e., no electricity production). In conjunction with specified capital costs indicated on Fig. XVI-16, the energy "spectrum" (i.e., the mix between P_4(high-temperature), P_5(low-temperature), P_c^*(electrolysis) and P_3(recirculated)) of a given blanket design and the match of this

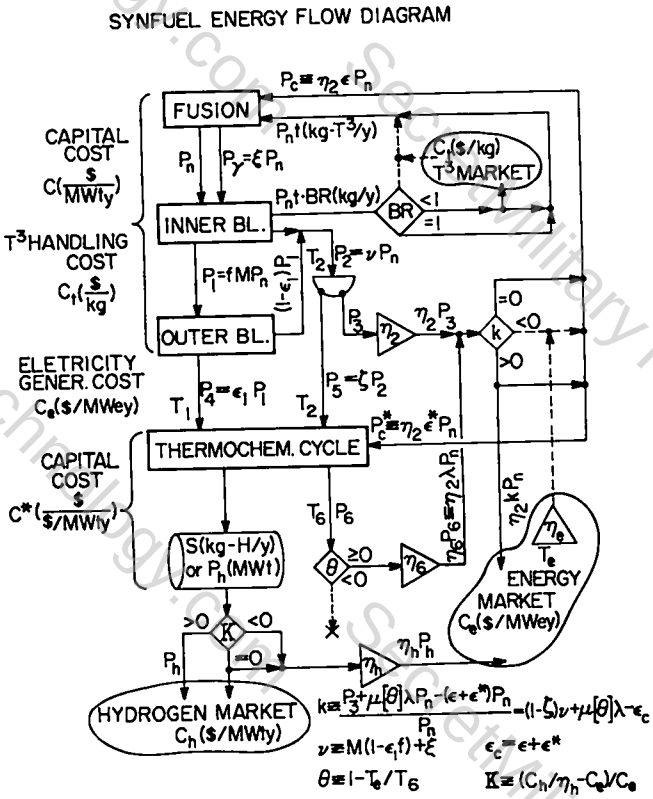

Fig. XVI-16.
Power flow diagram used to model the energy split for a fusion-driven thermochemical hydrogen plant. The inner blanket produces tritium and low-temperature (~ 800 K) process heat, whereas the outer blanket produces high-temperature (~ 1500 K) process heat. This system interacts economically with tritium, energy, and hydrogen markets as indicated.

"spectrum" to the load line of specific thermochemical cycles is examined.

2. Neutronics. The relationship between the fraction f of the total fusion energy passed through the low-temperature breeder region to the high-temperature process-heat blanket region and the tritium-breeding ratio represents a crucial parameter for the energy/economics balance task described above. Figure XVI-17 depicts a simple neutronics model used to examine numerically the relationship between f and [BR]. The effect of varying both the (neutron) multiplier thickness and composition on the energy E_N deposited in the outer blanket and [BR] was computed for a range of blanket compositions. Figure XVI-18 gives the dependence of f on [BR] for a more favorable Pb-multiplier case. The trend indicated on Fig. XVI-18 is similar for the other blanket systems studied; increased [BR] can be obtained only at

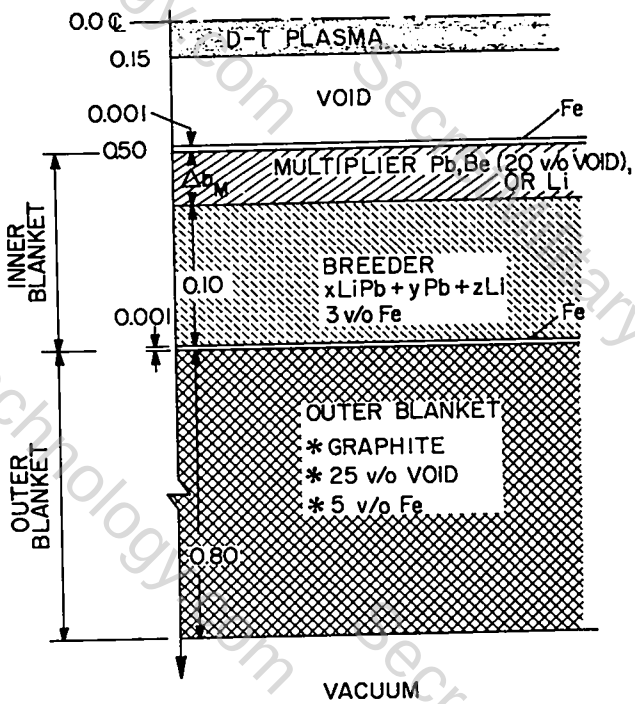

Fig. XVI-17.
Schematic diagram of synfuel fusion blanket used to study neutronics associated with high-temperature process heat generation and tritium breeding. Generally, only the "multiplier" region was varied both in composition and dimension.

the expense of less fusion energy deposited into the outer, high-temperature regions of the blanket. Relationships similar to that depicted on Fig. XVI-18 are used by the energy/economics balance task. The power density in the outer graphite region is used to perform thermal/mechanical design studies.

3. Thermochemical Blanket Concepts. As previously noted all thermochemical blanket models assume a simple one-dimensional (radial) cylindrical geometry with a low-temperature (~ 800-900 K) tritium-breeding inner region and a high-temperature (~ 1500 K) outer region (typically graphite). Either Li(metal), Li_2O, or $LiAlO_2$ was considered for the tritium breeder, and in some cases Pb was proposed for a neutron multiplier. Cooled structural first walls and thermal insulation represent essential elements for all blanket configurations, as illustrated schematically in Figs. XVI-19. Although direct neutron heating of key products in the thermochemical cycle was considered, all blankets depicted in Figs. XVI-19A-D ultimately generate a high-temperature (1400-1500 K) helium process heat stream. The

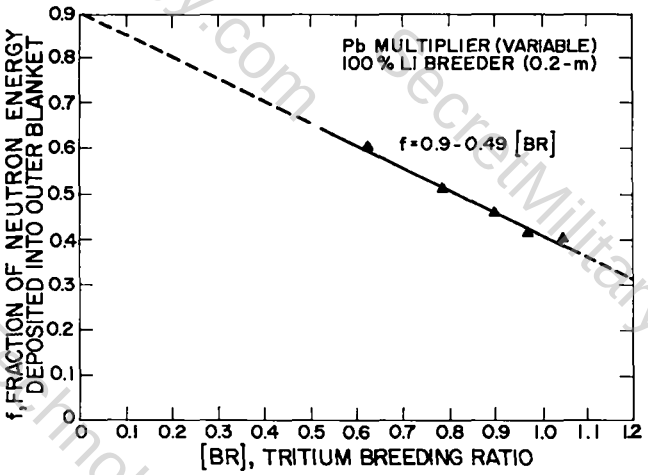

Fig. XVI-18.
Interrelationship between the fraction of the total fusion neutron energy deposited into the high-temperature (~1500 K) outer blanket region on the tritium breeding ratio [BR] for a Pb-Multiplier/100%-Li-breeder case.

fusion energy deposited in the cooled first-wall and inner tritiuim-breeding regions is used to generate electricity for in-plant use, although a portion of the lower temperature heat may be used to complete the thermochemical-cycle load line (energy requirement versus temperature); the possibility of a high-temperature topping cycle for electricity generation by the high-temperature process heat stream is also considered an option. Generally, vacuum tritium barriers are used between the process heat regions and the tritium regions, energy transport occurring between the two primarily by thermal radiation.

4. Thermochemical cycles. Specification of the blanket "energy spectrum" (e.g., the split between thermal energy versus temperature and the fraction thereof used for electrical energy production) cannot be made until a specific thermochemical cycle is adopted. Since detailed neutronic, thermal-hydraulic, mechanical, and materials engineering of the blanket cannot proceed until a thermochemical cycle is selected, an interim or preliminary cycle was chosen, even though the experimental basis for this cycle is not fully established. The following H_2SO_4/Bi_2O_3.x SO_3 cycle[29,30] is used:

$$SO_2 + 2H_2O = H_2SO_4 + H_2 \quad \text{(conventional 300 K electrolysis)} \qquad (7A)$$

$$H_2SO_4(aq) + 1/3\ Bi_2O_3 = 1/3\ Bi_2O_3.3SO_3 + H_2O(350\ K) \qquad (7B)$$

$$1/3\ Bi_2O_3.3SO_3 = 1/3\ Bi_2O_3 + SO_3 \quad (750\text{-}1200\ K) \qquad (7C)$$

$$SO_3 = SO_2 + 1/2\ O_2 \quad (1200\text{-}1500\ K) \qquad (7D)$$

Figure XVI-20 depicts a preliminary process flow diagram proposed for the $H_2SO_4/Bi_2O_3.3SO_3$ thermochemical cycle. Based on Pechonskii's experimental results,[31,32] as reported by Krikorian,[33] for the decomposition of zinc sulfate in air, the sulfate decomposition rate should be governed by heat transfer to the decomposing particles. The dominant mode of heat transfer at temperatures above 1000 K is thermal radiation. If bismuth sulfate ($Bi_2O_3.3SO_3$) particles were adequately dispersed, heat transfer might not be a limiting factor, and, assuming the decomposition to take place in times less than one minute, a decomposer might operate in a "falling bed" mode. The bismuth sulfate particles (100-200 μm in size and preheated to 700 K) would be dropped through a decomposer. The $Bi_2O_3.3SO_2$ particles emerge from the decomposer as bismuth oxide (Bi_2O_3).

The SO_3, SO_2, and O_2 product gases might then be passed through a catalyst bed to ensure that all the SO_3 is decomposed. Equilibrium conversions of the SO_3 to SO_2 and O_2 should be achieved at 1500 K to within 99.8% at moderate pressures. The bismuth oxide is physically separated from the product gases and is returned to a (chemical) reactor in which contact with fresh H_2SO_4 solution from the electrolyzer occurs to form bismuth sulfate. The gaseous products are separated, the SO_2 is recycled, and the O_2 is discarded after purification. A major unknown in the above process is the rate at which bismuth sulfate decomposes at elevated temperatures; experiments are planned at LASL to obtain these data, but the synfuel studies will treat the decomposition reaction rate as a major system parameter.

H. PLASMA SYSTEMS ANALYSIS

A number of computational and modeling activities associated with the magnetic confinement systems studies are not specifically associated with a given concept, but instead are more general and supportive of most design studies. This area

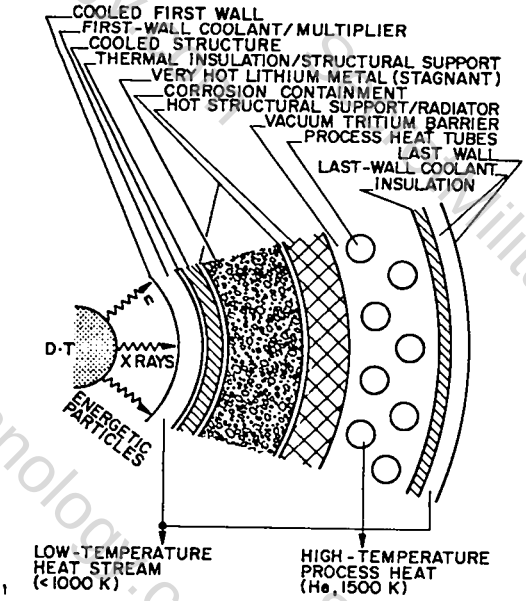

SIMPLE RADIATOR BLANKET

A

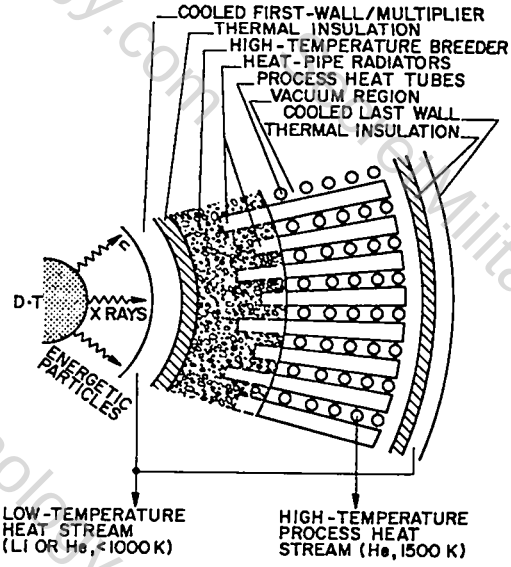

EXTENDED RADIATOR BLANKET

B

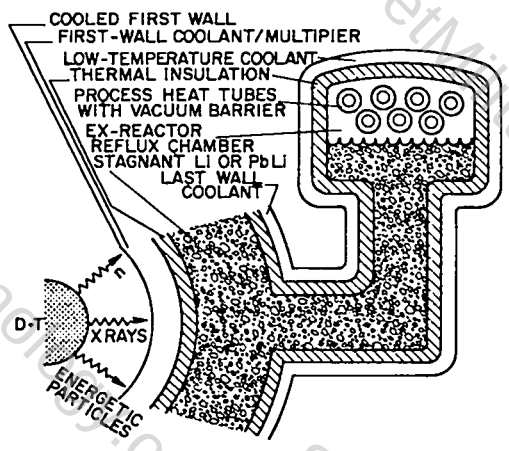

EX-REACTOR REFLUX BLANKET

C

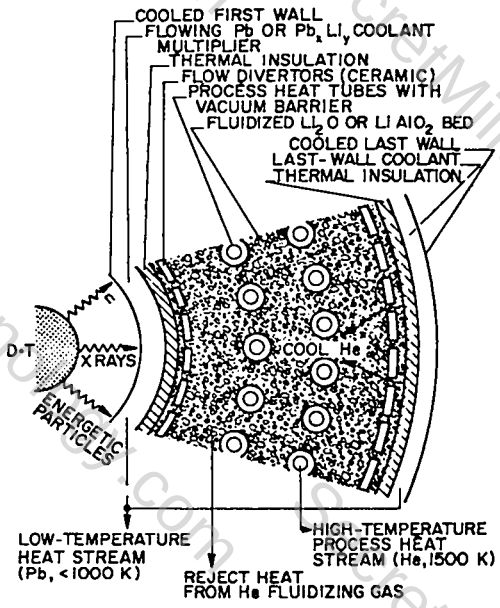

FLUIDIZED - BED BLANKET

D

Figs. XVI-19A-D

Schematic diagrams of a number of potential synfuel fusion blanket concepts:

A) Simple radiation blanket with bank of process heat tubes
B) Radiation blanket with radiator surface extended by heat pipes
C) Lithium reflux blanket, with radiation-heated process heat tubes located external to the blanket
D) Packet (fixed) or fluidized-bed blanket

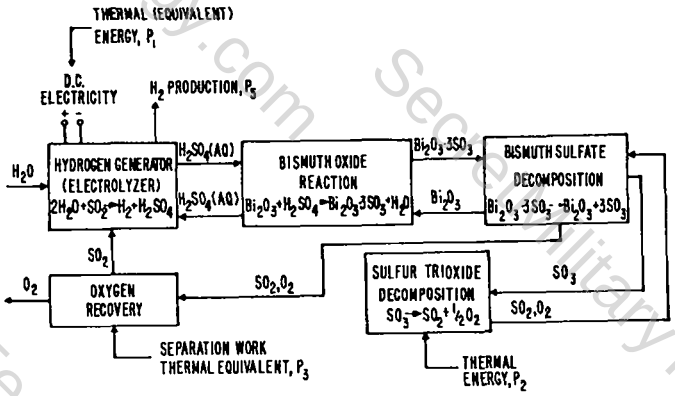

Fig. XVI-20.
Flow diagram for a hypothetical $Bi_2O_3.xSO_3$ thermochemical hydrogen cycle that is to be matched with a given synfuel fusion blanket design.

of activity is termed "Plasma Systems Analysis," and items which fall into this category are summarized.

1. D-T Fusion Reactivity Data. Averaging of the microscopic D-T fusion cross section over the Maxwellian ion velocity distribution expected in magnetically confined plasmas yields the well-known reactivity $\langle\sigma v\rangle$. Incorporation of the ion temperature dependence of $\langle\sigma v\rangle$ into fusion reactor computer codes is generally accomplished by either 1) numerical interpolation of $\langle\sigma v\rangle(T)$ using a finite table of discrete values, or 2) using an analytic representation to give a best least squares fit to the table of discrete $\langle\sigma v\rangle$ values.

As an example of the former approach, Table XVI-V provides the reactivity table used in the LASL fusion reactor design codes. This table is a modification, in the sense that temperatures below 1 keV are included,[34,35] of an ORNL table spanning the range 1-1000 keV, which has been provided to the US fusion research community on the National Magnetic Fusion Energy (MFE) computer network.[36] The ORNL table is representative of similar reactivity compilations,[37,38] and its general (US) availability makes it a standard. The ORNL table uses values of T incremented by 0.2 keV for 1<T<10, 2 keV for 10<T<100, and 20 keV for 100<T<1000. A linear interpolation scheme is employed in the ORNL subroutine package. Table XVI-V is less finely resolved, requiring fewer values for the same range, but uses a cubic spline interpolation scheme to give a smoother functional dependence.

For some applications, the analytic representation is preferred. Considered here are expressions of the form

$$\langle\sigma v\rangle = AT^{-2/3}\,[\,1 + CT^{4/3}\,]\quad \exp(BT^{-1/3}), \qquad (8)$$

for three fitting coefficients A, B, C. Several expressions which are two-parameter versions (C = 0) of Eq. (8) have been identified. Three such expressions came from the published literature, and a fourth was derived indpendently and is introduced here. Table XVI-VI presents the values of the coefficients and an indication of the temperature ranges for which the discrepancy $|\varepsilon|$ between the analytic expressions and the standard Table XVI-V values is less than a chosen maximum allowed, expressed as a nominal percentage (here 10% and 25%) of the standard value.

2. Alpha-Particle Thermalization Model. D-T fusion-product alpha particles, born at U_α = 3.52 MeV, will thermalize by Coulombic drag with the plasma electrons and to a lesser extent with the plasma ions, and thus should provide a plasma heating mechanism which may lead to ignition. To determine the rate of energy deposition, a Fokker-Planck model[39] is used. The alpha-particle range-energy relation for a plasma of thermonuclear interest (T = 10 keV) with several densities spanning 10^{21} -10^{23} m^{-3} is shown in Fig. XVI-21. The alpha-particle ranges exceed the length of any acceptable linear device, and to reduce the range to a few kilometers by increasing the plasma density requires large confining fields.

A possible solution to this problem involves magnetic mirrors to reflect alpha particles at the ends of the linear reactor to allow multiple passes. For a mirror ratio R_M the probability that an alpha particle will be reflected P_R is $\sqrt{1-1/R_M}$.[40] Hence, the effective path length of an alpha particle born at the center of a mirrored linear reactor of length ℓ, may be approximated by the infinite series representation, $\ell/2 + \ell P_R + \ell P_R^2 + \ldots$, which converges to $\lambda = (\ell/2)\,[\,1/(1-P_R) + P_R/(1-P_R)^2\,]$. An effective alpha-particle energy confinement efficiency can be defined, where λ_α is alpha-particle range; $R_\alpha \sim 1 - \exp(1-\lambda/\lambda_\alpha)$. R_α is calculated dynamically by the 1DRBURN code and is used to estimate

TABLE XVI-V

D-T FUSION REACTIVITY TABLE

Maxwellian Ion Temperature T_i (keV)	D-T Reactivity $\langle\sigma v\rangle$ (m^3/s)	Maxwellian Ion Temperature T_i (keV)	D-T Reactivity $\langle\sigma v\rangle$ (m^3/s)
0.05	7.00 (-41)[a]	40.0	7.93(-22)
0.1	3.00 (-36)	50.0	8.54
0.5	6.00 (-29)	60.0	8.76
0.8	2.00 (-27)	70.0	8.76
0.9	4.00	80.0	8.64
1.0	6.27	90.0	8.46
2.0	2.83 (-25)	100.0	8.24
3.0	1.81 (-24)	200.0	6.16
4.0	5.86	300.0	4.90
5.0	1.35 (-23)	400.0	4.13
6.0	2.53	500.0	3.63
7.0	4.14	600.0	3.28
8.0	6.17	700.0	3.02
9.0	8.57	800.0	2.83
10.0	1.13 (-22)	900.0	2.68
20.0	4.31	1000.0	2.55
30.0	6.65		

(a) To be read as $7.00(10)^{-41}$

TABLE XVI-VI

ANALYTIC D-T FUSION REACTIVITY EXPRESSIONS OF THE FORM:

$$\langle\sigma v\rangle = AT^{-2/3}\,[\,1 + CT^{4/3}\,]\,\exp\,(BT^{-1/3})$$

EXPRESSION	FITTING COEFFICIENTS			T(keV) RANGE	
	A	B	C	$\|\varepsilon\|<10\%$	$\|\varepsilon\|<25\%$
I	3.68(-18)	-19.94	0.0	2-3 and 28-37	2-6 and 20-43
II	5.00(-18)	-19.94	0.0	5-24	4-29
III	7.80(-18)	-20.70	0.0	5-16	3-21
IV	9.43(-18)	-21.11	0.0	1-15	1-20
V	9.46(-18)	-20.94	-4.55(-3)	5-38	3-44

the fraction of all alpha particles that are lost as a function of burn time, whether the alpha-particle thermalization model is analytic or based on a Fokker-Planck model.

3. Burn Code Development. An integral activity of magnetic confinement systems studies is the development and use of a variety of time-dependent thermonuclear burn codes. The major code systems that have been developed and used to model the dynamics of reactor-like plasmas are briefly described.

a. RFPR. This pressure-balance code uses analytic field profiles to model the dynamics of a three-species (electrons, ions, alpha particles) reversed-field pinch plasma. Bremsstrahlung and cyclotron radiations as well as radial diffusion and anomalous losses are included. Full engineering energy balance, first-wall heat transfer, and economics models are included in RFPR. The alpha thermalization is treated by a Fokker-Planck model.

b. DTBURN. This code system is an adaptation of an earlier approach[41] and is the theta-pinch counterpart of the RFPR code. End-loss energy/particle losses can be modeled by introduction of an ad hoc loss term to this zero-dimensional, pressure-balance code. Alpha-particle thermalization is modeled by a Fokker-Planck computation.

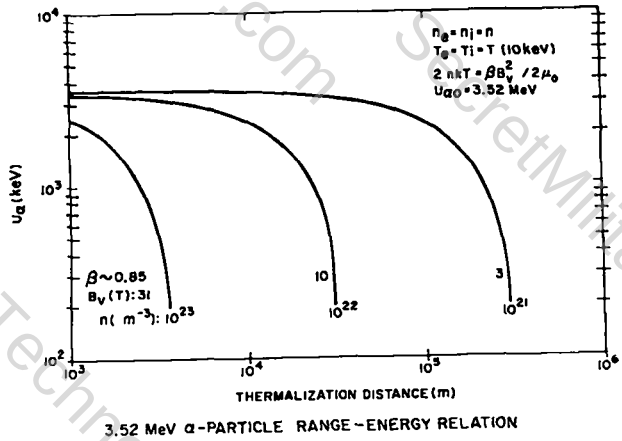

3.52 MeV α-PARTICLE RANGE-ENERGY RELATION

Fig. XVI-21.
Alpha-particle (3.5-MeV) range-energy relationship for a D-T background plasma. Pressure balance for a given beta value gives the required confining field B for the various densities.

c. 1DRBURN. This time-dependent, three-species code models the dynamics of a linear DT plasma in both the radial and axial dimensions. Since radial effects are generally averaged, 1DRBURN is used primarily as an axial burn code to compute the plasma energetics, first-wall response and overall energy balance of linear devices (primarily linear theta-pinch reactors) that are subject to various end-stoppering schemes (solid endplugs, reentrant endplugs, etc.). An analytic alpha-particle thermalization model is used, which has been previously calibrated by separate Fokker-Planck computations.

d. MHSBRN. This code system (actually two separate, but nearly identical systems) computes the burn dynamics of either a theta-pinch or a Z-pinch plasma in the radial direction using a full magnetohydrostatic (i.e., MHD with no inertial terms) procedure. MHSBRN is a single-particle time-dependent code with alpha-particle heating back fitted to simulate, on the basis of separate Fokker-Planck computations, the associated dynamics. This code is used to examine the effects of radial profiles and field diffusion on the results obtained from the previously described pressure-balance, zero-dimensional burn codes. The MHSBRN system is presently being modified to include ion-electon-alpha interactions as well as to join both theta- and Z-field profiles in order to model more accurately high-beta systems with helical fields (RFPR, screw pinches, Tormac, high-field Tokamak).

e. LNBURN. The coupled dynamics of a high-beta plasma and an imploding, compressible liner is modeled with the LNBURN system (Sec. XVI.D.) The Lagrangian MHS code treats only simple particles, has all major loss terms (radiation, axial and radial conduction, etc.), and uses an analytic model[16] to compute the liner compression. This fast-running code is continually calibrated against a complex MHD physics code, CHAMISA.[16]

f. NGBD. Both the transient and quasi-steady-state behavior of a neutral DT gas with the edge of a thermonuclear theta-pinch plasma is modeled by the neutral-gas-blanket code NGBD.[42,43] This MHS code system treats a wide spectrum of charged and neutral particles interacting with a three-particle (ions, electrons, alpha-particles) theta-pinch plasma. This code system will be modified to model neutral-gas blanket phenomena associated with the RFPR studies.

4. Neutral-Gas Blanket Theory. Research into the use of a neutral gas to cool a quenched RTPR plasma was concluded,[42] and produced a numercial code, NGBD, that models both the transient formation and quasi-steady operation of a neutral- gas blanket. The transient formation of a neutral-gas blanket at the plasma perimeter is examined to determine the conditions under which a neutral-gas layer can be stably formed. The main concern for formation is that the neutral gas together with the cold plasma adjacent to the wall can acquire sufficient density and thickness to shield the wall from energetic charge-exchange neutral species; during the formation wall damage is to be minimized. The penetration of monoenergetic, neutral-gas "slabs" into the plasma and the reaction rate of incoming diatomic and monoatomic gas with the plasma ions, electrons, and alphas are dynamically modeled. Hydrodynamic and radiation processes are simultaneously calculated, and first-wall (physical) sputtering and evaporation rates are computed on the basis of the computed particle and energy fluxes.

After the transient formation of the neutral-gas blanket a quasi-steady analysis determines whether or not the plasma energy can be extracted with minimal wall damage. Since heat flow through

the neutral gas and enhanced bremsstrahlung radiation are dominant cooling mechanisms during the quasi-steady-state stage, the rate of plasma energy loss should be determined primarily by the rate of neutral penetration into the plasma. This neutral penetration is determined by the two competing processes of neutral diffusion and neutral-plasma interaction. Control of the plasma energy loss rate by controlling the neutral diffusion rate, which in turn is determined by the diatomic neutral density in the neutral-gas reservoir, should be possible. Figure XVI-22 gives the monoatomic neutral particle spectral flux at the first wall 35 μs after injection for a diatomic neutral density of 10^{21} m^{-3}. The particle flux for energies less than 5×10^{-4} keV results from diatomic neutral charge-exchange with the low-temperature plasma adjacent to the wall. Between 10^{-2} and $5(10)^{-4}$ keV neutrals from the dissociation of diatomic ions primarily contribute to the spectrum. The diatomic neutral charge-exchange with the hot plasma in the core contributes to the spectrum above 10^{-2} keV.

Figure XVI-23 illustrates the sputtering yield and sputtering rate for Al_2O_3 as a function of time for the case given in Fig. XVI-22. The sputtering rate peaks at 25 μs, after which the neutral-gas blanket begins to moderate the outwardly directed monoatomic neutrals. Figure XVI-23 also gives the first-wall evaporation rate, which is small compared to physical sputtering, for a diatomic neutral density of 10^{21} m^{-3}. The first wall consists of a 0.3-mm layer of alumina, backed by a 1-mm layer of niobium and cooled by liquid lithium at 1100 K. The wall dose and integrated loss for both charge exchange and

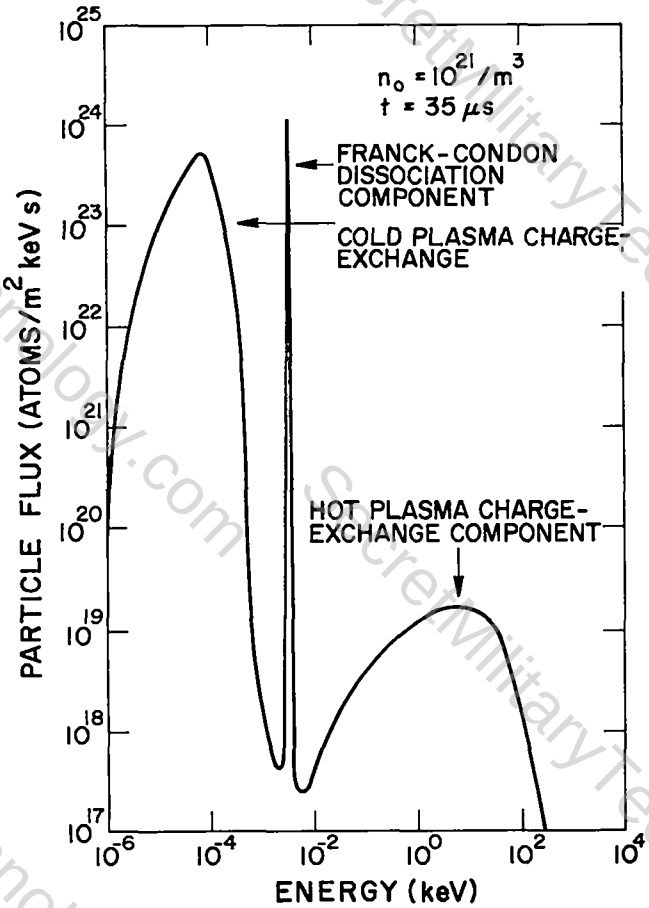

Fig. XVI-22.
A typical first-wall particle energy spectrum computed at 35 μs after the admittance of neutral gas at $n_o = 10^{21}$ m^{-3} adjacent to an energetic plasma.

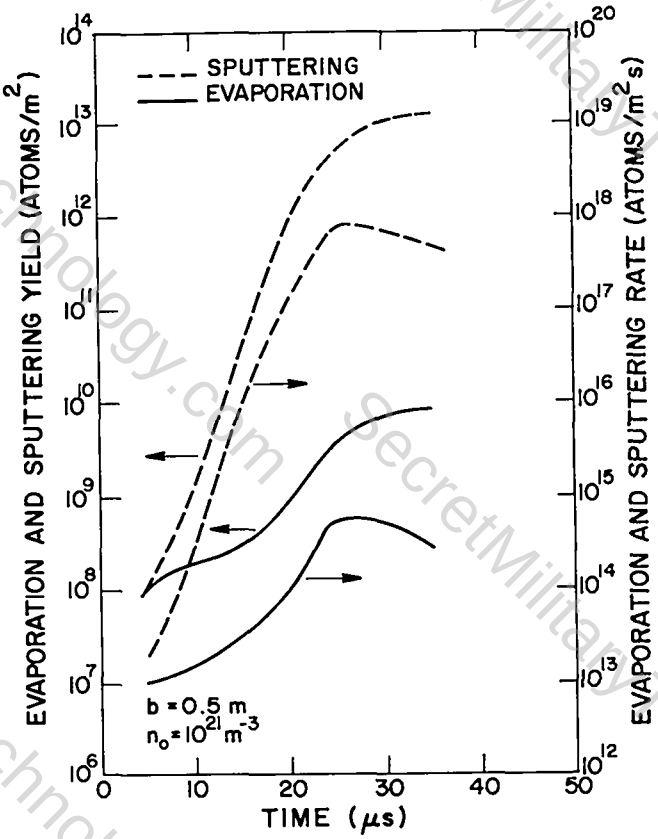

Fig. XVI-23.
Wall erosion rates and integrated yields computed as a function of time after the admittance of $n_o = 10^{21}$ m^{-3} of neutral gas adjacent to an energetic plasma.

evaporation are shown on Fig. XVI-24 as a function of neutral-gas density n_o. Wall erosion by sputtering increases rapidly for n_o less than 10^{22} m^{-3} as a result of increased neutral atom penetration into the hot plasma core. The bremsstrahlung energy dose dominates at high values of n_o, whereas sputtering dominates at low density. The composite evaporation curve indicates sputtering and evaporation are very small (for Al_2O_3, 10^{14} atoms/m^2 corresponds to $4.5(10)^{-15}$ m or $1.1(10)^{-2}$ μm/y at a 0.1-Hz pulse rate and an 80% duty factor). The major concern, instead, becomes one of thermal cyclic fatigue which generally will require that n_o be kept below $\sim 10^{21}$ m^{-3}.

5. Modeling of Plasma/First-Wall Interactions in High-Field LMF Reactors. A wide range of Linear Magnetic Fusion (LMF) concepts exhibit the significant advantages of plasma stability, simple geometry, a high level of physics understanding and high power density.[44] Classical scaling on the basis of either free-streaming particle loss or axial (parallel-field) thermal conduction predicts device lengths and total fusion powers that generally are excessive from the reactor viewpoint. It is possible, however, to reduce the size of machines while simultaneously maintaining a favorable overall energy balance, by exploiting the $B^2\ell$ scaling predicted by classical theories of end flow, where B is the confining field and ℓ is the total length of the plasma column.[44] In order to achieve ignition conditions with total alpha-particle confinement, $B^2\ell$ must exceed $(10)^6$ T^2 m at plasma temperatures of $\sim$ 7 keV when axial thermal conduction determines the energy containment time. Hence, if ℓ = 1000 m, then fields in excess of 30 T will be required. The resulting high plasma densities will cause a high bremsstrahlung radiation flux at the first wall, and a first-wall constraint is imposed. One approach to this problem is to relax the first-wall thermal-mechanical constraints, permitting evaporative ablation of impurity material into the plasma chamber. This work examines the interaction between a burning D-T plasma and an evaporating (liquid-lithium) first wall.

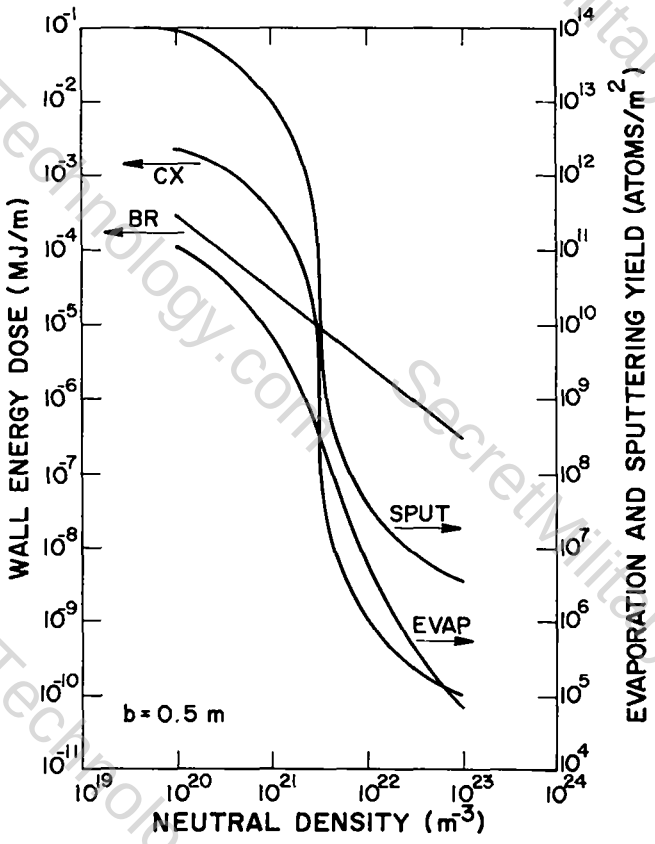

Fig. XVI-24.
Energy dose and integrated erosion yields at the first wall as a function of initial neutral gas density.

Although evaporation would provide the first-wall cooling during the short, intense burn, the evaporated lithium will also cool the ignited plasma, and the dynamic interaction between evaporating first-wall and the burning thermonuclear plasma, therefore, becomes a major question. The penetration of evaporated lithium into the high-beta, dense plasma will occur by the complex and coupled processes of diffusion, ionization, and charge-exchange; these processes occur on a time scale which may be comparable to the thermonuclear burn time. The question, therefore, becomes one of competing reaction and diffusion rates and the rapidity of the inevitable plasma quench relative to the burn time required to achieve a net energy balance. A simple surface evaporation model is coupled with a detailed, transient description of the (lithium) neutral-gas/plasma interaction to form the basis of a simple LMF reactor model with which to examine the viability of the evaporating first-wall scheme. The computational model and techniques are similar

to those used to describe neutral-gas blanket phenomena[42,43] (Sec.XVI H.4).

As illustrated in Fig. XVI-25, the reactor performance, as measured by the space-time integrated Lawson parameter, $n\tau$, increases to a maximum of $6(10)^{21}$ s/m^3 at about 45 T. After this point $n\tau$ gradually begins to decrease. The increase in $n\tau$ with B is considerably below that expected without lithium evaporation but nevertheless an appreciable gain in $n\tau$ is observed.

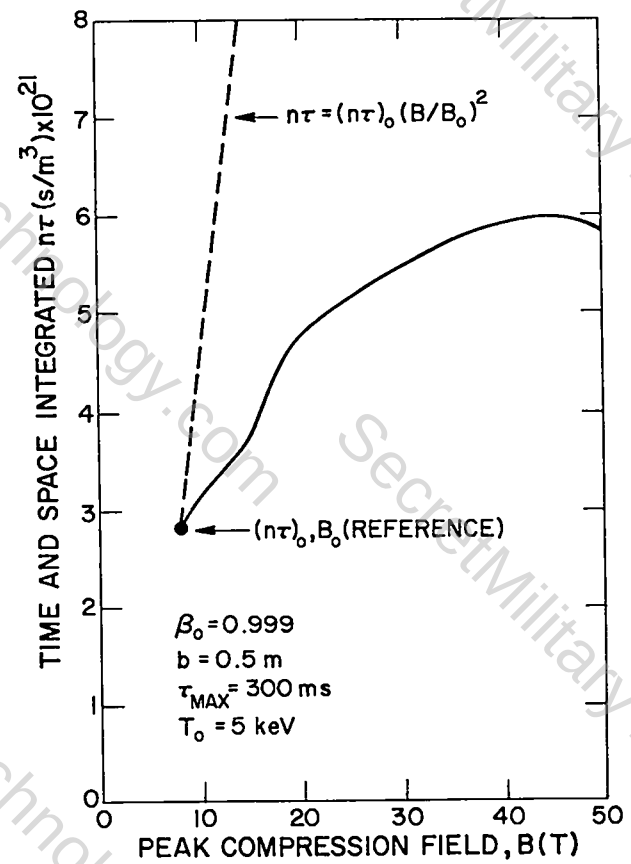

Fig. XVI-25.
Dependence of time- and space-integrated Lawson parameter as a function of peak compression field applied to dense Linear Magnetic Fusion (LMF) device with an evaporating liquid-lithium first wall.

I. FUSION REACTOR NUCLEONICS

Several tasks are included in the category of Fusion Reactor Nucleonics, including two-dimensional transport code development and applications, quantitative nuclear data assessment, computer code and data file standardization, deterministic streaming methods, and fusion reactor systems studies. These efforts support the national fusion energy development program. In addition, shielding and blanket analysis for the Intense Neutron Source Facility and consultation on other programs are provided. Blanket system nucleonics calculations for an ohmic-heated, small tokamak reactor concept (RIGGATRON) have continued in support of an INESCO Corporation conceptual study. Progress in each of these tasks is summarized below.

1. TRIDENT-CTR. TRIDENT-CTR[45] is a two-dimensional (rectangular and cylindrical geometry) triangular spatial mesh, neutron transport code, is designed specifically for the fusion community, and was written and partially tested during 1977. TRIDENT-CTR was developed from a previous code,[46] which was written for use in fission reactor design. The following modifications have been made to TRIDENT for use as a fusion reactor design tool.

a) The storage structure has been modified so that on a CDC 7600 computing system only the information required to solve one finite-element (triangular) band at a time is in small core memory. This modification increases the maximum allowable problem size from about 3000 triangles in TRIDENT to 10-15 000 triangles in TRIDENT-CTR.

b) The TRIDENT restriction that six triangles share each interior vertex has been relaxed; this modification has made the specification of spatial mesh less rigid and easier to establish.

c) An automatic mesh generator that performs triangulations of the spatial mesh is available in TRIDENT-CTR as an option. The option takes as input on a per-band basis the number of zones in the band, the number of triangles per zone, and the zone boundary coordinates. A zone is defined as a region of constant material specification, constant source, and constant starting flux estimate.

d) A group-dependent S_N order may be specified and used in TRIDENT-CTR. The S_N constants can be generated by the code (EQ_N sets[47]), read in, or a combination of both.

e) Options to allow interior boundary sources (right, left, top, and bottom) have been included in TRIDENT-CTR. This option allows the replacement of a distributed neutron source, isolated in a central vacuum region, and a deterministically

calculated boundary source at the first material surface (i.e., first wall).

The changes embodied in items a) and b) have increased the flexibility and scope of TRIDENT-CTR over TRIDENT with a minimal cost in increased computational time. The code has been tested on a large tokamak problem[48] (RIGGATRON). The solution of the RIGGATRON involved the calculations and storage of over 3 million flux moments and provided a realistic, large-scale test of TRIDENT-CTR.

2. RIGGATRON Blanket Nucleonics Study. One- and two-dimensional neutron/gamma-ray transport calculations have been performed for the INESCO RIGGATRON, a tokamak device using ohmic heating to induce deuterium-tritium fusion. Earlier efforts tested and evaluated various cross-section sets for consistency and accuracy and finally settled upon use of the (30 x 12) MATXS[49] coupled neutron/gamma-ray set for future analysis. In related work, sets of one-dimensional scoping calculations for possible plasma, coil, and blanket configurations were performed, and two-dimensional computations were initiated. Following correction of errors in the MATXS (30 x 12) library, predictions of the MATXS, CTR (collapsed) VITAMIN-C[50] (101 x 12) and NJOY[51] (30 x 12) libraries for various one-dimensional RIGGATRON configurations were compared. Results of that comparison are compiled in Table XVI-VII, which lists breeding ratios (T) and leakages (L) for various plasma, coil, and blanket thicknesses. Agreement between the three cross-section sets is ± 5%. In subsequent analysis, the MATXS (30 x 12) neutron/gamma-ray cross-section set will be used.

Additional one-dimensional calculations were performed on the RIGGATRON assuming a void between coil and blanket in order to increase the tritium breeding. The results of these computations are given in Table XVI-VIII for a plasma of radius 0.225 m, coil of thickness 0.10 m, void thickness

TABLE XVI-VII

CROSS-SECTION COMPARISONS[(a)]

r(plasma)	Δr(Cu)	Δr(Li)	T_6(Li^6)	T_7(Li^7)	T	L	T + L		
22.5	10	100	0.640	0.138	0.778	0.182	0.960	CTR 101 x 21	7% H_2O Coil[2]
			0.637	0.132	0.769	0.182	0.951	MATXS 30 x 12	
			0.638	0.135	0.773	0.182	0.955	NJOY 30 x 12	
22.5	10	0	-	-	-	0.932	-	CTR 101 x 21	
			-	-	-	0.914	-	MATXS 30 x 12	
			-	-	-	0.884	-	NJOY 30 x 12	
22.5	10	100	0.760	0.128	0.888	0.257	1.145	CTR 101 x 21	no H_2O Coil
			0.757	0.123	0.880	0.249	1.129	MATXS 30 x 12	
			0.801	0.126	0.927	0.252	1.179	NJOY 30 x 12	
22.5	10	0	-	-	-	1.119	-	CTR 101 x 21	
			-	-	-	1.096	-	MATXS 30 x 12	
			-	-	-	1.081	-	NJOY 30 x 12	

(a) all dimensions in centimeters

T_6 = ^{6}Li tritium breeding ratio
T_7 = ^{7}Li tritium breeding ratio
$T = T_6 + T_7$
L = leakage per fusion neutron

TABLE XVI-VIII
COMPARATIVE BREEDING AND LEAKAGE FOR RIGGATRON WITH H_2O (7%) AND FULLY DENSE COILS WITH/WITHOUT VOID BETWEEN COIL AND BLANKET(a)

r(plasma)	Δr(coil)	Δr(void)	Δr(blanket)	T_6	T_7	T	L	T + L	
22.5	10	0	100	0.643	0.135	0.778	0.182	0.960	
		300	100	0.739	0.139	0.878	0.159	1.037	7% H_2O
		0	0	--	--	--	0.884	--	coil
22.5	10	0	100	0.757	0.123	0.880	0.248	1.129	
		300	100	0.874	0.129	1.003	0.205	1.20	no H_2O
		0	0	--	--	--	1.096	--	coil

(a) all dimensions in centimeters
T_6 = ^{6}Li tritium breeding ratio
T_7 = ^{7}Li tritium breeding ratio
T = $T_6 + T_7$
L = leakage per fusion neutron

of 2.0 m, and blanket thickness of 1.0 m. An S_8 quadrature set and P_3 cross-section expansion were employed. It is seen that the addition of the void between coil and blanket produces approximately 7%-9% increases in breeding ratios for the two cases considered.

For a more realistic one-dimensional model a graphite reflector (0.25 m) was placed outside the blanket, similar to the two-dimensional mockup of the RIGGATRON shown in Fig. XVI-26. Neutron and gamma-ray heating was also computed using the MATXS kerma factors with 7% D_2O coolant in the copper coils. The results of these calculations for coil thicknesses of 0.07 m and 0.10 m appear in Table XVI-IX. The Q values for neutrons and gammas in the copper, lithium, and graphite are given in MeV.

As an additional check on the cross sections as well as the discrete-ordinates calculational model, a continuous energy Monte Carlo calculation (MCNP code) was performed. This Monte Carlo calculation duplicated the one-dimensional discrete-ordinates calculation for a 0.225-m-radius plasma, 0.07-m-thick copper coil, and a 1-m-thick natural Li blanket. All calculations of tritium breeding and neutron leakage were performed to a relative standard deviation of 1%. Table XVI-X shows results of comparisons among various cross-section sets, where the MATXS library was processed from ENDF-IV. These calculations show direct comparison of the MATXS library with a calculation using its progenitor ENDF-IV point-wise library. The comparison includes errors associated with the discrete-ordinates approximation and the statistical error in the Monte Carlo results. In all cases agreement is to within 4% for both tritium breeding and leakage. The higher breeding value from the Monte Carlo calculation is inferred to be caused by the resonance self-shielding effect, and further study of this effect is being undertaken.

3. Committee on Computer Code Coordination (CCCC). During the past year neutron and photon multigroup cross sections in the proposed CCCC format called MATXS were produced. A code (TRANSX) for processing the MATXS libraries was also provided. With this code, neutron, photon, or coupled cross-section sets can be easily generated

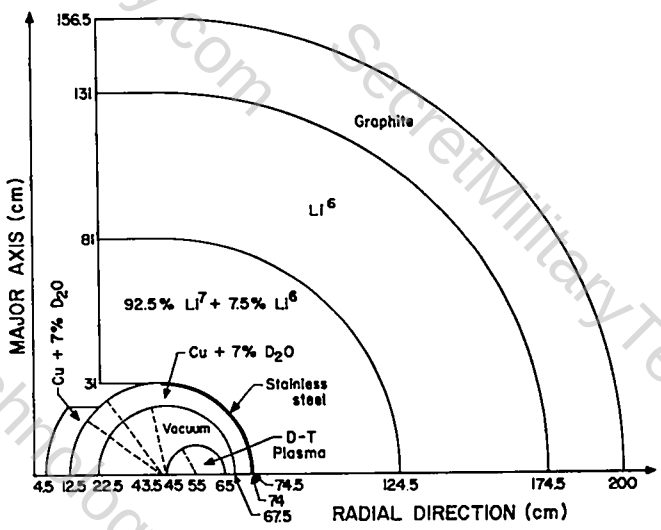

Fig. XVI-26.
Two-dimensional RIGGATRON blanket model used for neutronics computations.

TABLE XVI-IX

COMPARATIVE BREEDING AND HEATING FOR RIGGATRON WITH 7% D_2O COILS
(200-cm VOID AND 25-cm GRAPHITE REFLECTOR)[a]

r(plasma)	Δr(coil)	Δr(void)	Δr(blanket)	Δr(graphite)	T_6	T_7	T	L	T + L	Q^n_{Cu}	Q_{Cu}	Q^n_{Li}	Q_{Li}	Q^n_C	Q_C
22.5	7	200	100	25	1.081	0.229	1.31	0.004	1.314	1.09	6.11	7.69	1.05	0.03	0.16
22.5	10	200	100	25	0.969	0.139	1.108	0.003	1.111	1.34	8.55	6.22	0.75	0.02	0.13

(a) all dimensions in centimeters
T_6 = ^{6}Li tritium breeding ratio
T_7 = ^{7}Li tritium breeding ratio
$T = T_6 + T_7$
L = leakage per fusion neutron
Q in units of MeV

TABLE XVI-X

COMPARISON OF MONTE CARLO RESULTS WITH DISCRETE-ORDINATES CALCULATIONS FOR .07-m COIL, 7 vol% D_2O and 1-m BLANKET (^{n}Li)

Calculational Method	Cross-Section Set	Leakage	%Difference from Monte Carlo	T	% Difference from Monte Carlo
Monte Carlo, MCNP	ENDF-IV Pointwise	0.267	-	1.097 4	-
S_8 P_3, ONETRAN	LASL/TD 30-Group	0.277	3.74	1.054 5	-3.91
S_8 P_3, ONETRAN	MATXS 30-Group	0.275	3.00	1.056 5	-3.73

to user specifications. Individual reaction cross sections, such as tritium production and gas production (if present in the ENDF source library), are readily available through the TRANSX-MATXS link. These reaction cross sections can be included in the cross-section tables that are used in various transport codes, or they can be extracted from TRANSX as individual response vectors.

Considerable testing of the TRANSX-MATXS system has occurred. MATXS cross-section sets, such as those used in the RIGGATRON studies,[52] have been generated and are being used for CTR-related analyses.

4. Adoption of LASL Codes to the Magnetic Fusion Energy Computer Network. Progress in linking LASL/LTSS with the Lawrence Livermore Laboratory (LLL) MFE network has been significant. An introductory manual to LTSS at LLL, which is aimed at the beginning user, has been released in final form. The document is intended for users who have had some contact with FORTRAN, but who do not understand complex computer systems. A tape conversion process for moving files back and forth from LASL/LTSS to LLL/LTSS has been formalized, and a document explaining how to do that has been circulated within LASL. Using the tape procedure, the MCNP Monte Carlo code has been standardized to be identical both on LLL/LTSS and LASL/LTSS, allowing updates to be made more easily.

The standardization of graphics routines, which allows switching from one machine to another with a minimum of difficulty, has also been made. Toward this end the TRIDENT-CTR code on LASL/LTSS has been modified to use system-independent, machine-independent, device-independent, subroutines that can easily be modified for the particular system or machine in question. This change should make the graphics transportable with a minimum of effort. At LASL these routines were written using the Common Graphics System (CGS)

routines with respect to the SENSIT code; a similar scheme was used on LLL/LTSS using the TV80LIB graphics package.

5. Use of Monte Carlo Computations In the Study of Deep Penetration Problems. A Monte Carlo method was developed to generate correlation information on the forward and adjoint flux, providing a means to calculate contributon density via forward Monte Carlo. A simple transformation between surface integrals of the contributon current and the volume integral of the current provides a new approach to detector response calculations. This approach proves useful in deep-penetration problems. Calculations made for such problems in the analog Monte Carlo mode indicated up to 90% time saving for the contribution method as compared to the regular analog method. The two methods are now being tested with various biasing schemes. Biasing considerations for the contributon Monte Carlo are very different than those used in regular Monte Carlo. Preliminary results indicate that advantages similar to those for the analog case may be obtained for the biased case, especially for highly scattering media.

6. Sensitivity Profiles for Secondary Energy and Angular Distributions. In many deep-penetration transport calculations the integral-design or response parameter of interest is determined mainly by secondary particles which are produced by interactions of the primary radiation with the material. If the primary radiation consists of neutrons in the MeV range, then the secondary neutrons from inelastic scattering events or (n,2n) reactions, and the gamma rays from (n,γ) reactions are of primary concern in most fusion reactor blanket/shield calculations. These secondaries can be considered additional radiation sources within the blanket or shield. In most reactor shielding calculations the biological dose rate at a given point of interest is dominated by the contribution from secondary gamma rays, and in fusion reactor nucleonics calculations important design parameters (tritium breeding, radiation damage, and induced radioactivity) depend strongly on (n,2n) and (n,3n) reactions in the blanket and shield. The methods of standard cross-section sensitivity analysis can be used to calculate the sensitivities to the production cross sections of such secondaries. A sensitivity to either the energy or angular distribution of these secondary particles, however, could not be given.

An extension of the classical sensitivity theory, which allows one to calculate sensitivity profiles for secondary energy and angular distributions, has been developed and is being incorporated in the LASL sensitivity and uncertainty analysis code system (LASS).[53]

7. Quantitative Data Assessment. The adequacy of existing neutron and gamma-ray cross sections needed to perform the nuclear design calculations for TNS have been assessed. This assessment was performed quantitatively using established sensitivity and uncertainty analysis techniques as demonstrated in previous conceptual designs of TFTR and EPR. The ERRLIB cross-section error data base developed for the TFTR and EPR studies was expanded and used extensively to assess the data accuracy requirements for TNS applications. The sources of error estimates for ERRLIB include: (1) local assessments, (2) nuclear systematics, and (3) the rapidly developing ENDF/B formatted "error files." Considerable effort has been devoted to a collaborative effort with ORNL to improve and generalize the ENDF/B error formats. Parallel developments have also occurred in the error processing capabilities of the LASL-developed NJOY cross-section processing code. Multigroup error estimates for ^{6}Li and ^{10}B from the ENDF/B-V library were processed into the ERRLIB format for test purposes. The first TNS design considered was provided by General Atomic Company and is being updated continually through close cooperation with the design team.

An attempt was made to scope the uncertainties in secondary energy by performing a statistical analysis of the 14-MeV neutron inelastic-scattering spectra for all important structural metals. Large differences (typically 50%) are found between materials that should have similar spectra. These large discrepancies indicate that for some design calculations uncertainties in spectra will be as important as uncertainties in the cross sections themselves.

8. Gas-Production Cross Sections. In support of the LASL materials program for the development of radiation-damage-resistant insulators for fusion applications, the neutron cross sections for 27 hydrogen- and helium-production reactions have been evaluated and spectrum-averaged. These data are needed to analyze planned fission reactor irradiation experiments and are summarized in Table XVI-XI. A fast-neutron energy spectrum typical of the Oak Ridge Reactor (ORR) was used to perform the spectrum-averaging.

9. Cross-Section Evaluation and Calculation. An evaluation of selected neutron-induced cross sections for ^{9}Be has been completed and incorporated into the ENDF/B-V evaluation from LLL. Particular emphasis was placed on accurately representing the neutron emission spectra from (n,2n) reactions, as measured recently at LASL.[54] In addition, the total cross section was updated above 500 keV to include new measurements from the NBS[55] and LASL[56].

The ENDF/B formats are presently not suited for accurate representation of energy-angle correlations in neutron-emission spectra from ^{9}Be reactions. For this reason a special format was used to incorporate the ^{9}Be(n,2n) data. Cross sections and angular distributions for a

TABLE XVI-XI
GAS-PRODUCTION CROSS SECTIONS FOR C, N, O, Mg, Al and Si

Reaction	Thermal Cross Section (b)	Spectrum Averaged Cross Section (b)[a]	Method
^{12}C(n,α)		1.27(-3)[b]	ENDF/B
^{13}C(n,α)		8.59(-3)	Estimated
^{14}N(n,p)	1.81 ± 0.5	3.58(-2)	ENDF/B
^{14}N(n,α)		9.65(-2)	ENDF/B
^{16}O(n,α)		1.10(-2)	ENDF/B
^{17}O(n,α)	.235 ± .01	1.05(-1)	Calculated
^{17}O(n,nα)		1.59(-3)	Calculated
^{Nat}Mg(n,p)		1.35(-3)	ENDF/B
^{Nat}Mg(n,α)		3.48(-3)	ENDF/B
^{24}Mg(n,p)		1.47(-3)	Experimental
^{25}Mg(n,p)		1.39(-3)	Estimated
^{25}Mg(n,α)		2.83(-2)	Estimated from ENDF/B
^{27}Al(n,p)		4.94(-3)	ENDF/B
^{Nat}Si(n,p)		8.07(-3)	ENDF/B
^{Nat}Si(n,α)		3.46(-3)	ENDF/B
^{28}Si(n,p)		6.68 ± .08(-3)	Experimental Spectrum
^{28}Si(nα)		4.70(-3)	Experimental
^{29}Si(n,p)		2.9 ± .1(-3)	Experimental Spectrum
^{29}Si(n,)		6.24(-3)	Estimated

(a) Cross sections estimated to be less than 10^{-3} barn are deleted.
(b) To be read as 1.27×10^{-3}.

series of (n,n') level excitation energy bins that suitably represent the LASL[54] experimental data at 5.9, 10.1, and 14.2 MeV were derived. Because the evaluated excitation data actually represent (n,2n) reactions, a multiplicity factor of 2 is specified in the evaluation. The level excitation functions were smoothly interpolated and extrapolated to other incident neutron energies, so that the energy from threshold to 20 MeV is covered.

Because of the special data format used, it was necessary to modify the NJOY code to permit multigroup processing. This modification is complete, and the new evaluation has been processed into the LASL 30-neutron by 12-gamma group structure.

Under funding from the Division of Physical Research (DPR) of DOE, development of the nuclear theory code GNASH[57] was continued, and a variety of cross-section calculations were performed that are of fusion reactor interest. Neutron-induced charged-particle emission spectra were calculated for 15-MeV neutrons on stainless steel 316,[58] and reaction cross sections, including (n,γ), (n,n'), (n,p), (n,α), (n,pn), (n,2n), (n,np), (n,nα), and (n,αn) reactions, were calculated up to 20 MeV for all five isotopes of titanium and for several zirconium isotopes. These results will be incorporated in ENDF/B-V evaluations. Reviews of calculations and capabilities of the GNASH code and general data needs were presented[59-61] between 10 and 40 MeV.

Also under DPR funding, development of the EDA R-matrix code progressed, and analyses of several mass systems that included reactions of fusion reactor interest were continued. These studies include analyses of the important $D(d,n)^3He$, $D(d,p)T$, $T(d,n)^4He$, $^3He(d,p)^4He$, and $^6Li(n,\alpha)T$ reactions.

J. INSULATOR AND CERAMICS RESEARCH

Activities during 1977 included studies of structural effects (swelling, thermal diffusivity, microhardness, and fracture toughness) and electrical effects (multiple-pulse dielectric breakdown strength) in unirradiated and irradiated ceramics. Transmission electron microscopy studies have been conducted to evaluate the nature of radiation damage in order to assist in interpretation of radiation-induced changes in physical properties. In response to a request from OFE/DOE, an irradiation test plan was developed to study concurrent displacement-damage and gas-generation effects in a model ceramic. To support the OFE Fusion Materials planning effort reports were prepared assessing insulator and ceramic problems and describing a program plan for their solution.

1. Structural Effects. Nine candidate refractory ceramics (six oxides and three nitrides) were irradiated to doses of 1-2 $\times 10^{22}$ n/cm^2 ($E_n > 0.1$ MeV) at 925 and 1100 K in EBR-II. Swelling measurements have been made on these materials, with results which may be summarized as follows:

- $MgAl_2O_4$, $Y_3Al_5O_{12}$, Si_2ON_2, and SiAlON exhibited low swelling (less than 0.5 vol%)
- Si_3N_4, Y_2O_3, Y_2O_3-1%ZrO_2 showed moderate swelling (0.5 to 1.5 vol%)
- Only Al_2O_3 and BeO swelled more than 1.5 vol% (in the 3-10% range).

With the exception of the last two materials, the tested ceramics behaved well compared to the swelling criterion at high damage levels under the conditions utilized.

Thermal diffusivity tests have been completed on samples irradiated earlier in EBR-II to a dose of 2.8×10^{21} n/cm^2 ($E_n > 0.1$ MeV) at 1015 K. Earlier work showed significant degradation (8 to 68%) at room temperature for eleven ceramics after this moderate-dose irradiation. The measurements have been concluded by determining the change in thermal diffusivity for polycrystalline Y_2O_3 and Y_2O_3-1%ZrO_2. These materials showed a reduction in this property of 25% and 33%, respectively.

Temperature dependence of the degradation in thermal diffusivity was measured for single-crystal Al_2O_3, which showed a 45% reduction at 300 K, and compared with the temperature dependence for unirradiated Al_2O_3. Thermal diffusivity for both materials decreased with increasing temperature, consistent with phonon scattering theory, and the irradiation decrement

also decreased, in agreement with temperature-dependence of scattering from defect sites (Fig. XVI-27). The observed reduction in degradation to 15% at 723 K indicates that problems associated with an irradiation-induced decrease in thermal diffusivity should be lessened at higher operating temperatures.

Thermal diffusivity of unirradiated plasma-sprayed Al_2O_3 was also investigated in a cooperative project with the LASL Materials Technolgy group. This material has been proposed for applications where neutron flux is low but thermal throughput is significant. It was found that "as-sprayed" Al_2O_3 has a thermal diffusivity equal to approximately one-tenth that of conventional alumina, because of the presence of transition phases and porosity. Isochronal and isothermal anneals up to 1925 K showed that

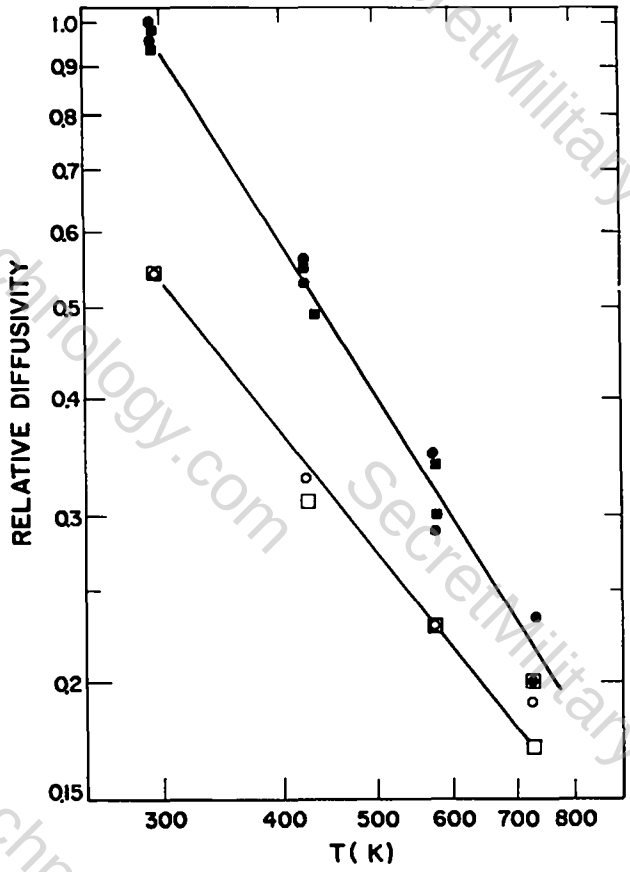

Fig. XVI-27.
Relative thermal diffusivity as a function of temperature for unirradiated and irradiated TYCO and LINDE sapphire:
filled circles--unirradiated LINDE, C-plane
filled squares--unirradiated TYCO, R-plane
open circles--irradiated LINDE, C-plane
open squares—irradiated TYCO, R-plane

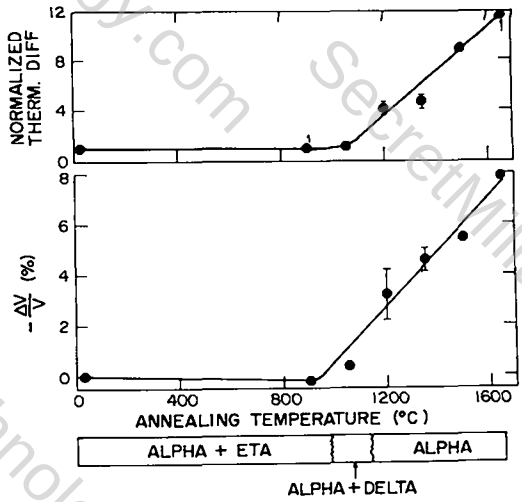

Fig. XVI-28.
Thermal diffusivity, volume shrinkage, and occurrence of phases plotted as a function of isochronal annealing temperature (1 h). All points are the average of two samples except where 1 is indicated. Scatter fell within circles except where error bars are shown.

restoration of the alpha phase and closure of the pores result in large improvements in thermal diffusivity (Figs. XVI-28 and XVI-29), but that microcracking accompanying the phase transformations retards this recovery until very high temperatures are reached. Changes in density during annealing would probably result in failure of the ceramic/metal bond in fusion reactor applications. The use of such a materials system in high thermal flux applications will require

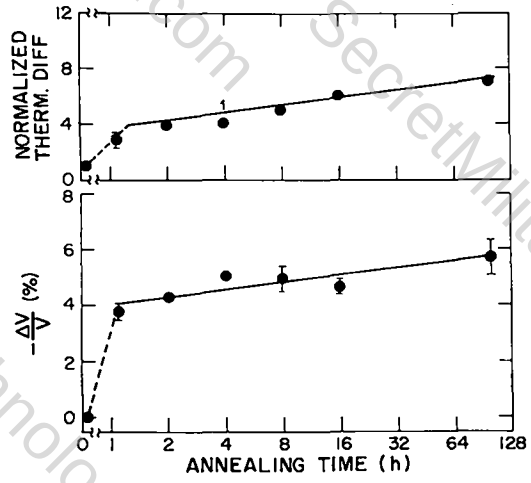

Fig. XVI-29.
Thermal diffusivity and volume shrinkage plotted versus annealing time at 1625 K. Symbols have the same significance as in previous figure.

development of special techniques, such as spraying onto a heated substrate to optimize the as-sprayed ceramic structure.

Microhardness and indentation fracture testing of ceramics irradiated to moderate doses in EBR-II has begun. In this work room-temperature microhardness is obtained from dimensions of the indent, and fracture toughness is determined by applying fracture mechanics techniques to interpretation of crack patterns around the indentation. Preliminary results for YAG ($Y_3Al_5O_{12}$), spinel ($MgAl_2O_4$), and sapphire (Al_2O_3) are presented in Figs. XVI-30 and XVI-31. Figure XVI-30 shows room-temperature hardness for the three ceramics in unirradiated and irradiated form. This parameter is an indicator of the resistance to plastic flow. Figure XVI-31 presents values of fracture toughness, which is directly related to brittle fracture strength and which allows strength comparisons if the flaw size distribution is known. These data show that both hardness and fracture toughness of sapphire increased upon irradiation, while the properties remained nearly unchanged in YAG and spinel. The slopes of the hardness curves increased in a negative sense following irradiation; large indents gave lower hardness readings for each material, with the effect being more marked after irradiation. This behavior may indicate that yield stress is affected more by radiation damage

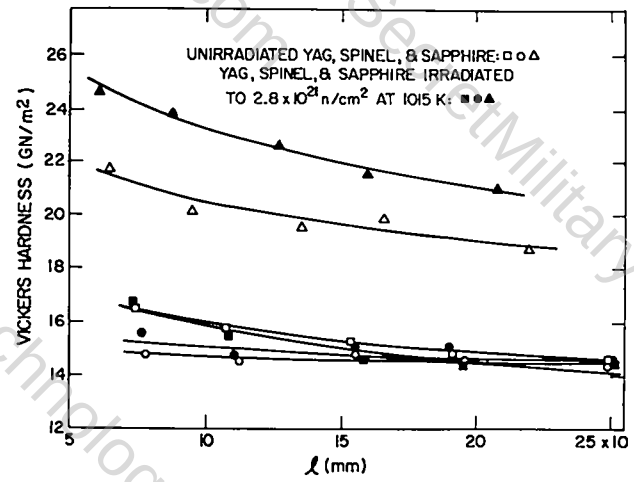

Fig. XVI-30.
Microhardness as a function of diagonal dimension of indentation for three single-crystal ceramics in the unirradiated and irradiated condition.

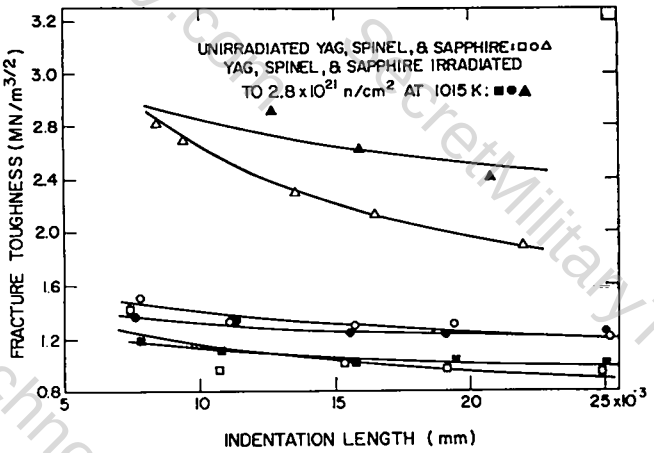

Fig. XVI-31.
Fracture toughness as a function of diagonal dimension of indentation for three single-crystal ceramics in the unirradiated and irradiated condition.

than is flow stress, a phenomenon observed in metals.[62]

Table XVI-XII compares changes in thermal diffusivity, hardness, and fracture toughness at 200-g load, and volume changes for spinel, YAG, and sapphire. These changes are interrelated and can be associated with the defect structure observed in transmission electron microscopy (TEM). TEM studies have shown that irradiated sapphire contains a fine dispersion of small pores with possibly a background dislocation network which is presumed at least partly to result from intersecting loops caused by radiation damage. Calculations based on the thermal conductivity change have shown that large concentrations of point defects must also be present. YAG crystals investigated by TEM also show evidence of radiation damage in the form of damage clusters. The exact nature of these clusters is not known, but they may consist of small loops or point defect aggregates. It could also be speculated that local atomic rearrangements (e.g., cations on the wrong sites) or metamictized regions make up the damage clusters. The large decrease in thermal conductivity (Table XVI-XII) further suggests a significant concentration of point defects.

The small changes in properties of spinel are mutually consistent. No evidence of substantial concentrations of defects from either TEM or thermal conductivity measurements could be found.

TABLE XVI-XII

PROPERTY CHANGES FOR SINGLE-CRYSTAL SPINEL, YAG, AND SAPPHIRE AFTER IRRADIATION TO 2.8×10^{21} n/cm^2 at 1015 K

Material	Thermal Diffusivity Change/Starting Value (%/cm^2 s^{-1})	Hardness Change/Starting Value %/GN m^{-2} (at 200 g)	Fracture Toughness Change/Starting Value %/MN m$^{3/2}$ (at 200 g)	Volume Change (%)
$MgAl_2O_4$ (111)	- 8/0.056	+ 2/14.6	- 4/1.3	+ 0.1
$Y_3Al_5O_{12}$ (111)	- 62/0.028	+ 2/15.3	+ 6/1.0	0
Al_2O_3 (0001)	- 45/0.11	+ 13.9	+ 17/2.3	+ 2.5

Interpretation of the behavior of YAG is not as straightforward. Hardness and fracture toughness changes were small, and only a slight change in indentation size dependence of these parameters was noted. The lack of substantial hardness change argues against damage which could affect dislocation motion. Studies of the effect of vacancies on yielding in copper[63] have shown that the unagglomerated vacancies did not affect yielding while vacancy clusters did cause hardening. The present results are consistent with the presence of point defects in the substructure (accounting for the thermal conductivity decrease) but not consistent with the presence of agglomerated vacancy clusters or small loops. The small change of fracture toughness would follow the similar absence of change in hardness.

The behavior of sapphire was very different from either YAG or spinel, since for Al_2O_3 all properties changed and considerable visible and inferred damage is available to account for the property changes. The large increase in hardness may be accounted for by the background dislocation tangles alone (or possibly by the combined effect of tangles and pore array). The latter may act to impede dislocation movement by pinning the dislocation line once it has reached a pore. Problems with this model exist, since if the pores are considered to act as obstacles, not only the yield stress but also the rate of strain hardening should be increased; this expectation may be inconsistent with the increase in the indentation size dependence of microhardness with irradiation.

Changes in fracture toughness may also occur in more than one way. Decreasing plasticity would be expected to decrease fracture toughness by reducing the plastic work term. Changing the elastic modulus would change the fracture toughness in the same sense. Modulus decreases, however, are generally associated with irradiation;[64] hence, neither of these effects could account for the observed increase. The most likely cause for increased fracture toughness is the pore lattice, which could effectively increase fracture toughness by blunting and/or lengthening the crack.

2. Electrical Effects. Studies are under way to determine whether repeated application of sub-breakdown voltage pulses to a ceramic insulator will lead to a decrease in dielectric strength (an "electrical fatigue" effect). Measurements to date have been made at room temperature along the c-axis of single-crystal Al_2O_3, using pulses of a few - microseconds duration. Tests on twelve unirradiated samples showed a gradual decrease in dielectric strength from a one-pulse value of $\sim$1.8 MV/cm to $\sim$1.4 MV/cm at 10^4 pulses (Fig. XVI-32). Three samples, however, exhibited no fatigue effect up to $\sim 10^5$ pulses. Statistical calculations based on dislocation density, as revealed by etch-pit techniques, indicate that the likelihood of a sample not showing electrical fatigue correlates roughly with the likelihood of dislocations being absent from the breakdown area of a dimpled sample.

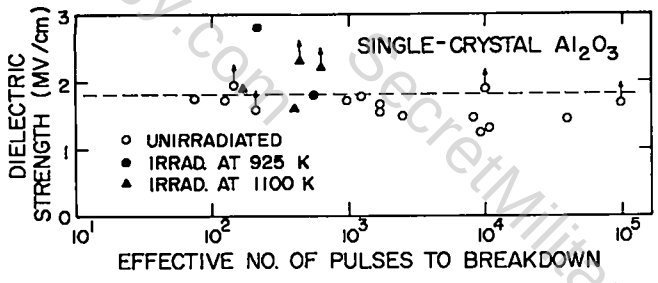

Fig. XVI-32.
Dielectric strength of sapphire at room temperature as a function of effective number of voltage pulses to breakdown. Arrowed data points represent samples which did not break down at the indicated electric field.

Breakdown measurements have also been made on Al_2O_3 after EBR-II irradiation to 1-2 x 10^{22} n/cm^2, a dose which resulted in 3 to 6 vol% swelling. Two samples irradiated at 925 K showed pulsed dielectric strengths of 1.8 and 2.8 MV/cm; two irradiated at 1100 K broke down at 1.6 and 1.9 MV/cm, while two samples could not be broken down at fields of 2.2 and 2.3 MV/cm (Fig. XVI-32). The number of pulses for these tests varied between 10^2 and 10^3. Results to date show considerable scatter but indicate a significant electrical fatigue effect at room temperature for this ceramic; however, no obvious degradation could be attributed to radiation damage under the test conditions utilized.

3. Nature of Radiation Damage in Ceramics. Emphasis has been placed on TEM examination of ceramics irradiated to 2.8 x 10^{21} n/cm^2 ($E_n > 0.1$ MeV) at 1015 K. These studies have been carried out in conjunction with Prof. L. W. Hobbs, consultant. Results obtained may be added to those from earlier studies at similar doses but different temperatures give an overall picture of the aggregated defects formed in ceramics irradiated at elevated temperature. In Table XVI-XIII the defects and the observed macroscopic swelling are described. TEM results obtained to date may be summarized as follows:

- voids are formed in Al_2O_3 at several elevated temperatures and in ZrO_2-6% Y_2O_3 over a narrow temperature range.
- $MgAl_2O_4$ shows no resolvable defect aggregates.
- aggregated damage in all other ceramics takes the form of dislocation loops or defect clusters.

Unlike metals, ceramics may contain a high concentration of point defects after irradiation at

TABLE XVI-XIII

DEFECT STRUCTURES AND SWELLING VALUES FOR IRRADIATED CERAMICS

Ceramic	Irradiation Temp., K	Resolved Defect Structure	Swelling Vol%
Al_2O_3 (single cry. and polycry.)	650	clusters	1.3
	875	voids	1.4
	1015	voids	1.9
	1025	voids	1.4
ZrO_2-6% Y_2O_3 (polycry.)	650	loops	0.2
	875	voids	1.8
	1025	clusters	0.0
Y_2O_3 (polycry.)	650	clusters	0.3
	875	clusters & loops	0.0
	1025	loops	-0.3
Y_2O_3-10% ZrO_2 (polycry.)	875	clusters	0.0
	1025	clusters	0.0
$MgAl_2O_4$ (single cry.)	1015	none attributable to irradiation	0.1
$Y_3Al_5O_{12}$ (singly cry.)	1015	clusters	0.0
Si_3N_4 (polycry.)	1015	clusters	0.3
SiAlON (polycry.)	1015	clusters	0.5
Si_2ON_2 (polycry.)	1015	clusters[(a)]	0.1

(a) At limit of detectability

elevated temperatures. This behavior can lead to lattice dilation and significant swelling and may account for the 1.3 vol% change in Al_2O_3 after irradiation at 650 K.

4. Fission Reactor Irradiation Testing. All neutron irradiation tests conducted to date by this project have made use of the EBR-II reactor. Samples thus irradiated suffer displacement damage, but the absence of high-energy neutrons such as those produced in a D-T reaction, prevents the concurrent transmutation-induced formation of H and He gases. Since these gases can affect the nature of radiation damage, their presence is required in order to simulate more closely fusion reactor damage effects.

Certain isotopes of elements common to ceramics will undergo (n,p) and (n,α) reactions with thermal neutrons to produce the gases of interest. An irradiation program plan has been developed to use the mixed-spectrum Oak Ridge Reactor (ORR) to induce concurrently displacement damage and gas formation in a model ceramic, SiAlON. This material is known to have high strength in the unirradiated condition, and LASL measurements on ARL SiAlON have shown a good dielectric strength (~330 kV/cm at room temperature and ~240 kV/cm at 875 K for pulsed voltages). EBR-II irradiation at 1015 K to 3×10^{21} n/cm^2 results in a modest 22% reduction in thermal diffusivity. Swelling after EBR-II exposure is low (an average of 0.5 vol% under the above conditions, 0.7 vol% when irradiated to 2×10^{22} n/cm^2 at 925 K, and 0.2 vol% when irradiated to the same dose at 1100 K).

A significant advantage of this ceramic for ORR studies is that four different damage states can be achieved, depending on isotopic content. Calculations show the following:

SiAlON with a nitrogen content of 99.5 isotopic percent ^{15}N (the maximum attainable) in a year will sustain a damage dose of 6 dpa with low concurrent gas formation.

With a ^{14}N content of 6 isotopic percent, 394 ppm of H will be generated, primarily from the $^{14}N(n_{th},p)^{14}C$ reaction, thus achieving the dpa/H ratio expected at the first wall of a fusion reactor.

With a ^{17}O content of 50 isotopic percent (the maximum attainable), roughly two-thirds of the desired He level (also 394 appm) will be attained, primarily from the $^{17}O(n_{th},\alpha)^{14}C$ reaction.

The last two conditions can be achieved simultaneously.

Thus such a study will allow H and He generation with the two gases of interest being added separately or together.

5. Other Activities. As a contribution to the effort by the Materials and Radiation Effects Branch of OFE to create an overall plan for fusion reactor materials development, an assessment was made of insulator and ceramic problems and a program plan was proposed. The resulting reports contain input from ceramic workers at LASL, BNWL, GA, LLL, and ORNL, and represent a consensus from the field and the fusion materials community. The plan is intended to serve as a guide and basis for future activities.

REFERENCES

1. R.A. Krakowski, F.L. Ribe, T.A. Coultas, and A.J. Hatch, "An Engineering Design Study of a Reference Theta-Pinch Reactor (RTPR)," Los Alamos Scientific Laboratory report LA-5336/ANL-8019 (March 1974).

2. R.A. Krakowski, R.L. Miller, and R.L. Hagenson, "Operating Point Considerations for the Reference Theta-Pinch Reactor (RTPR)," Proc. Technol. of Controlled Nuclear Fusion 1, 359 (September 21-23, 1976).

3. J.P. Freidberg et al., "Review of the Linear Theta Pinch (LTP) Concept," Los Alamos Scientific Laboratory unpublished data (1977).

4. G. Sawyer (ed.), Proc. of Workshop on End-Stoppering of Linear Magnetic Fusion Systems, Santa Fe, NM, October 12-14, 1977.

5. R.L. Miller and R.A. Krakowski, "A Linear Magnetic Fusion (LMF) Reactor Design Code: 1DRBURN," Los Alamos Scientific Laboratory, to be published (1978).

6. R.L. Miller and R.A. Krakowski, "Alpha-Particle Trapping and Thermal Conduction Constraints for the Ignition of Linear Magnetic Fusion Reactors," submitted to Nucl. Fusion (1978).

7. R.L. Hagenson, "A Toroidal Fusion Reactor Design Based on the Reversed-Field Pinch," dissertation, Iowa State University (1978).

8. R.L. Hagenson, R.A. Krakowski, and K.I. Thomassen, "A Toroidal Fusion Reactor Based on the Reversed-Field Pinch (RFP)," IAEA Conf. and Workshop on Fusion Reactor Design, Madison, Wisconsin (1977).

9. K.I. Thomassen et al. "Conceptual Engineering Design of a One-GJ Fast Discharging Homopolar Machine for the Reference Theta-Pinch Fusion Reactor," EPRI-ER-246, Project 469. Electric Power Institute (1976).

10. K.I. Thomassen et al., "Ohmic Heating Systems Study for a Tokamak EPR," Los Alamos Scientific Laboratory Unpublished data (1977).

11. D.A. Baker, J.N. DiMarco, and A. Haberstich, personal communication, Los Alamos Scientific Laboratory, (1977).

12. G.E. Cort and R.A. Krakowski, "Heat Transfer in the Lithium-Cooled Blanket of the Reference Theta-Pinch Reactor," to be presented at Sixth International Heat Transfer Conference, Toronto, Canada (1978).

13. F.M. Heck, E.I. King, Jr., and R.E. Stillwagon, "Experimental Power Reactor Ohmic Heating Energy Storage Study," Westinghouse Electric Corporation Fusion Power Systems Department report WEPS-TME-038 (1976).

14. H.F. Vogel, personal communication, Los Alamos Scientific Laboratory (1977).

15. R.A. Krakowski, R.W. Moses, R.L. Miller and R.A. Gerwin, "Fusion Power From Fast Imploding Liners," Workshop on Fusion Reactor Technology, Madison, WI October 1977 (to be published in Nucl. Fusion), Los Alamos Scientific Laboratory report (October 1977).

16. R. Gerwin and R. Malone, "Theory of Plasma Heating by Fast Liner Implosion," submitted to Nucl. Fusion (1977).

17. R.A. Krakowski and R.W. Moses, "Energy-Balance and Blast Containment Consideration for FLR "Los Alamos Scientific Laboratory unpublished data (1976).

18. W. Fickett, "PAD, a One-Dimensional Lagrangian Hydrocode," Los Alamos Scientific Laboratory report LA-5910-MS (April 1975).

19. L.F. Coffin, "Fatigue at High Temperature-Prediction and Interpretation," Proc. Instn. Mech. Engrs. (London) 188, 109 (1974).

20. S.I. Braginskii, "Transport Phenomena in a Completely Ionized Two-Temperature Plasma," Soviet Physics JETP 6 (33), 358-369 (February 1958).

21. A.R. Sherwood et al., "Fast Liner Proposal," Los Alamos Scientific Laboratory report LA-6707-P (August 1977).

22. A. Hasegawa, T.Hatori, K. Itah, T. Ikuta, Y. Kodama, and K. Nozaki, "Concept of a Fusion Burner," Nucl. Fusion 16, 5 (1976).

23. R.A. Krakowski, R.L. Miller, and R.L. Hagenson, "Preliminary Energy Balance Considerations for the Toroidal Magnetic (Bi-) Cusp: Tormac," Los Alamos Scientific Laboratory report to be published (1978).

24. A.H. Boozer and M.A. Levine, "Particle Trapping in Magnetic Line Cusps," Phys. Rev. Lett. 31, 21, 1287 (1973).

25. I.G. Brown and W.B. Kunkel, "Tormac Reactor Scaling," personal communication, Lawrence Berkeley Laboratory (May 12, 1977).

26. J.F. Decker, "An Evaluation of Exploratory Fusion Concepts," to be published, 1978 (also, "A Status Report on the Current DMFE Review of Alternative Magnetic Confinement Systems," Trans. Am. Nucl. Soc. 27, 41 (1977)).

27. R.A. Krakowski and A.S. Tai, "A Simple Economics Parametric Analysis of Fissile-Fuel Production by Fusion-Fission Reactors," Proc. 2nd DMFE Fusion-Fission Energy Systems Review Meeting," Washington, DC, November 2-3, 1977.

28. Shang-Fon, G.W. Woodruff, and N.J. McCormick, "A High-Gain Fusion-Fission Reactor for Producing Uranium-233," Nucl. Technol. 29, 392 (1976).

29. K.E. Cox and M.G. Bowman, "The LASL Program on Thermochemical Processes for Hydrogen Production: Status on October 31, 1977," Los Alamos Scientific Laboratory unpublished data (1977).

30. M.G. Bowman, "Thermochemcial Production of Hydrogen from Water," International Symp. on Energy Sources and Development," Barcelona, Spain (October 9-21, 1977).

31. V.V. Pechovskii, "Thermochemical Decomposition of Zinc Sulfate," J. Inorg. Chem. USSR (Engl. Trans.) 11, 1467 (1957).

32. V.V. Pechovskii, "Decomposition of Zinc and Cobalt Sulfates in a Current of Air and Sulfur Dioxide," J. Appl. Chem., USSR (Engl. Trans.) 31, 1130 (1958).

33. O.H. Krikorian and H.H. Otsuki, "Revised Flowsheet and Process Design for the ZnSe Thermochemical Cycle," Proc. of the DOE Chemical Energy Storage and Hydrogen Energy Systems Contracts Review Meeting, Hunt Valley, Md. (November 1977).

34. J.L. Tuck, "Thermonuclear Reaction Rates," Los Alamos Scientific Laboratory report LAMS-1640 (1954).

35. F.L. Ribe, T.A. Oliphant, Jr., and W.E. Quinn, "Feasibility Study of a Pulsed Thermonuclear Reactor," Los Alamos Scientific Laboratory report LA-3294-MS (1965).

36. Fusion Forefront 10, 3, 7 (August, 1977).

37. W.C. Wolkenhauer, Ed., "The Pacific Northwest Laboratory Annual Report on Controlled Thermonuclear Research Technology," BNWL-1685 (November 1972).

38. G.H. Miley, H. Towner, and N. Ivich, "Fusion Cross Sections and Reactivities," University of Illinois report COO-2218-17 (1974).

39. D.V. Sivukhin, Reviews of Plasma Physics, M.A. Leontovich Ed., Consultants Bureau, New York 4, 93 (1966).

40. S. Glasstone and R.H. Lovberg, Controlled Thermonuclear Reactors, (Van Nostrand Reinhold Co., NY, 1961), p. 345.

41. T.A. Oliphant, "Fuel Burn-Up and Direct Conversion Energy in a D-T Plasma," Proc. BNES Conf. on Nuclear Fusion Reactors, UKAEA Culham Laboratory (September 17-19, 1969), p. 309.

42. G.E. Gryczkowski, "The Application of Neutral-Gas Blankets to Theta-Pinch Reactors," Thesis, University of Michigan, to be published (1978).

43. T.A. Oliphant, G.E. Gryczkowski, and T. Kammash, "Transient Charge-Exchange Effects in a Neutral Gas Blanket," Nucl.Fusion 16, 2, 263 (1976).

44. R.A. Krakowski, "A Survey of Linear Magnetic Fusion Reactor Concepts," 3rd ANS Topical Meeting on Controlled Thermonuclear Fusion, May 8-11, 1978, Santa Fe, NM (to be published).

45. T.J. Seed, "TRIDENT-CTR Code Manual,"Los Alamos Scientific Laboratory, to be published (1978).

46. T.J. Seed, W.F. Miller, Jr., and F.W. Brinkley, Jr., "TRIDENT: A Two-Dimensional Multigroup, Triangular Mesh Discrete Ordinates, Explicit Neutron Transport Code," Los Alamos Scientific Laboratory report LA-6735-MS (March 1977).

47. B.G. Carlson, "Tables of Symmetric Equal Weight Quadrature EQ_n Over the Unit Sphere," Los Alamos Scientific Laboratory report LA-4734 (July 1971).

48. W.F. Miller, Jr., D.J. Dudziak, R.D. O'Dell, and M.F. Gomez, "Transport and Reactor Theory, October 1 - December 31, 1977," Los Alamos Scientific Laboratory report LA-7131-PR (February 1978).

49. C.I. Baxman and P.G. Young, "Applied Nuclear Data Research and Development, January 1 - March 31, 1977," Los Alamos Scientific Laboratory report LA-6893-PR (July 1977)

50. R.W. Roussin, Oak Ridge National Laboratory, personal communication (September 1977).

51. C.I. Baxman, G.M. Hale, and P.G. Young, "Applied Nuclear Data Research and Development, January 1 - March 31, 1976," Los Alamos Scientific Laboratory report LA-6472-PR (August 1976).

52. B.R. Wienke, Donald J. Dudziak, and G.E. Bosler, "RIGGATRON Nucleonics: One-Dimensional Analysis," Los Alamos Scientific Laboratory report LA-7183-MS (1978).

53. Donald J. Dudziak, S.A.W. Gerstl, and D.W. Muir, "Application of the Sensitivity and Uncertainty Analysis System LASS to Fusion Reactor Nucleonics," Proc. Specialists Meeting on Differential and Integral Data Requirements for Shielding Calculations, Vienna, Austria, 12-16 Oct. 1976.

54. D.M. Drake, G.F. Auchampaugh, E.D. Arthur, C.E. Ragan, and P.G. Young, "Double Differential Beryllium Neutron Cross Sections at Incident Neutron Energies of 5.9, 10.1, and 14.2 MeV," Los Alamos Scientific Laboratory report LA-6257 (1976).

55. R.A. Schrach, R.B. Schwartz, and H.T. Heaton, II, "Total Cross Sections of Silicon and Beryllium," Bull. Am. Phys. Soc. 16, 495 (1971).

56. G.F. Auchampaugh, S. Plattard, R. Extermann, and C.E. Ragan, III, "MeV Neutron Total Cross Sections of Be, B, and C," Proc. of the International Conference on the Interactions of Neutrons with Nuclei, Lowell, Mass., p. 1389 (1976).

57. P.G. Young and E.D. Arthur, "GNASH: A Preequilibrium, Statistical Nuclear Model Code for Calculation of Cross Sections and Emission Spectra," Los Alamos Scientific Laboratory report LA-6947 (1977).

58. E.D. Arthur and P.G. Young, "Calculations of 15 MeV Neutron-Induced Charged Particle Spectra on Stainless Steel Type 316," Trans. Am. Nucl. Soc. 26, 503 (1977).

59. E.D. Arthur and P.G. Young, "Cross Sections in the Energy Range 10 to 40 MeV Calculated with the GNASH Code," Symp. on Neutron Cross Sections from 10 to 40 MeV, Brookhaven National Laboratory-NCS-50681, p. 467 (1977).

60. Leona Stewart and Edward D. Arthur, "Neutron Evaluation at High Energies - Problems and Prospects," Symp. on Neutron Cross Sections from 10 to 40 MeV, Brookhaven National Laboratory-NCS-50681, p. 435 (1977).

61. P.G. Young, "Data Evaluation and Nuclear Model Codes, "Workshop Chairman's report at Symp. on Neutron Cross Sections from 10 to 40 MeV," Brookhaven National Laboratory-NCS-50681, p. 41 (1977).

62. D. McLean, Mechanical Properties of Metals, (John Wiley and Sons, NY 1962),p. 367.

63. J. Galligan and J. Washburn, "Effect of Vacancy Clusters on Yielding and Strain Hardening of Copper," Phil. Mag. 8, 1455-66 (1963).

64. D.H. Bowen and F.J.P. Clarke, Chemical and Mechanical Behavior of Inorganic Materials, A.W. Searcy, D.V. Ragone, and U. Colombo, Eds., (Wiley-Interscience, NY,1970) pp. 585-613.

XVII. ENGINEERING

G. P. Boicourt, R. T. Buck, G. I. Chandler, R. S. Dike, C. F. Hammer, K. W. Hanks
L. D. Hansborough, R. W. Kewish, Jr., K. J. Kutac, J. G. Melton, and W. C. Nunnally.

A. ZT-40 SYSTEM DESIGN

The design, simulation, and development of the ZT-40 system and components continued during 1977. The basic system consists of 12 identical circuits, one of which is shown in Fig. XVII-1. All of the circuits are connected in parallel at the circular mixer structure that surrounds the plasma torus. The toroidal plasma experiment has 12 poloidal current feed slots and 12 sets of toroidal field coils. Each of the poloidal current feed slots and each of the 12 sets of toroidal field coils will initially be connected in parallel at the mixer output. However, the system is designed to permit many series-parallel combinations of the poloidal current feed slots or the toroidal field coils, all of which are to be driven from the mixer output.

The load flexibility permits the current risetimes to be varied over a very large range, and thus permits a large range of conditions in the experiment. The capacitor bank parameters for the ZT-40 system are listed in Table XVII-I.

The continuing design of the ZT-40 system in 1977 included the design of the transient "snubber" circuits, the mixer system circuit and hardware, and the power crowbar circuits, all of which are illustrated in Fig. XVII-1.

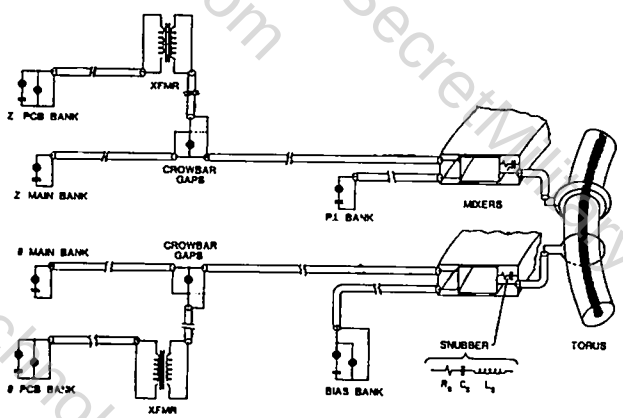

Fig. XVII-1.
ZT-40 circuit-one feedslot.

TABLE XVII-I
ZT-40 EXPERIMENT
CAPACITOR BANK PARAMETERS

Poloidal Bias Bank	
Energy	1.5 MJ
Voltage	10 kV
No. capacitors	180-170 μF
No. start switches	36 Size D
No. crowbar switches	36 Size D
Poloidal Main Bank	
Energy	0.67 MJ
Voltage	50 kV
No. capacitors	288-185 μF
No. start switches	288-Fig. XVII-11
No. crowbar switches	144-Fig. XVII-12
Poloidal Power Crowbar Bank	
Energy	1.0 MJ
Voltage	10 kV
No. transformers	12-20:2
No. capacitors	120-170 μF
No. start ignitrons	24-Size D
No. crowbar ignitrons	24-Size D
Toroidal Preionization Bank 1	
Energy	275 J
Voltage	5 kV
No. capacitors	12-1.85 μF
No. start ignitrons	12-Size A
Toroidal Preionization Bank 2	
Energy	227 kJ
Voltage (two stage Marx)	30 kV
No. capacitors	144-14 μF @ 20 kV
No. Marx ignitrons	48-Size D
Toroidal Main Bank	
Energy	0.67 MJ
Voltage	50 kV
No. capacitors	288-1.85 μF
No. start switches	288-Fig. XVII-11
No. crowbar switches	144-Fig. XVII-12
Toroidal Power Crowbar Bank	
Energy	3.1 MJ
Voltage	10 kV
No. transformers	12-14:2
No. capacitors	480-170 μF
No. start ignitrons	36-Size D
No. crowbar ignitrons	36-Size D

The snubber circuit was designed to limit the switching transients due to impedance mismatch at the coaxial cable terminations. The basic snubber electrical circuit is shown in Fig. XVII-1. The cables are terminated in their composite characteristic impedance by the snubber resistance,

R_s. A series capacitor, C_s, is used to prevent large energy drain after the first few hundred nanoseconds. The inductance, L_s, shown in Fig. XVII-1 is inherent in the system and is minimized by paralleling many RLC circuits. The value of C_s is determined by simulation and by experimental tests on a prototype system. The simulation of the system using NET-2 indicated that the optimum location for the snubber circuit was at the mixer output. The transients from the cable between the mixer output and the load are not suppressed, but there is insufficient room at the load for additional RLC units.

The mixer system for ZT-40 was designed to "mix" or to average the individual load currents and voltages when a portion of the capacitor bank malfunctions. The mixer prevents excessive voltages at any feed slot and minimizes current differences in the parallel loads. The mixer system was designed using a scale model mixer structure and SCR-switched capacitors to simulate the capacitor banks. The final design was a compromise between reliable collector plate fabrication techniques and mixing performance. The model tests indicate that only a 5% maximum difference in load currents will occur for a localized malfunction of 1/12 of the capacitor bank. A cross section of the mixer is shown in Fig. XVII-1. Essentially, the mixer system consists of two, parallel flat-plate transmission lines that encircle the load torus. The load current traverses the mixer structure radially when the capacitor banks operate normally. In the event of a capacitor bank malfunction, the current can travel circumferentially to equalize the individual load currents and voltages.

The power crowbar (PCB) system for ZT-40 was designed to sustain the initial load currents of 10^7A within ±7% for 250 μs, as shown in Fig. XVII-2. In general, the I_ϕ and the I_θ systems are very similar, and thus a basic PCB circuit for both systems is shown in Fig. XVII-3. The 50-kV capacitor bank establishes the desired initial current in the load and is shorted out with the crowbar switch. A low-leakage inductance transformer in series with the load supplies a voltage to cancel the circulating current voltage drop and sustain the current. The low leakage transformer was chosen to supply the sustaining voltage of about 1000-1500 V because economical 10-kV, high-density capacitors could be used via a step-down transformer. Electrolytic capacitors were too costly and bulky because of their voltage and current limitations. The transformer must have low total leakage inductance as seen from the secondary terminals in order to maximize the energy delivered to the low-inductance load.

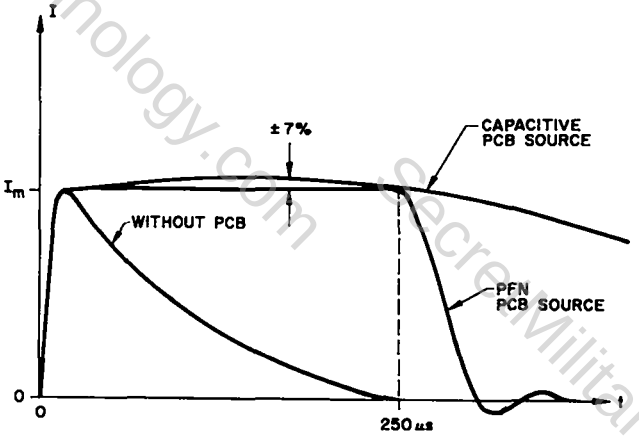

Fig. XVII-2.
General ZT-40 current waveforms.

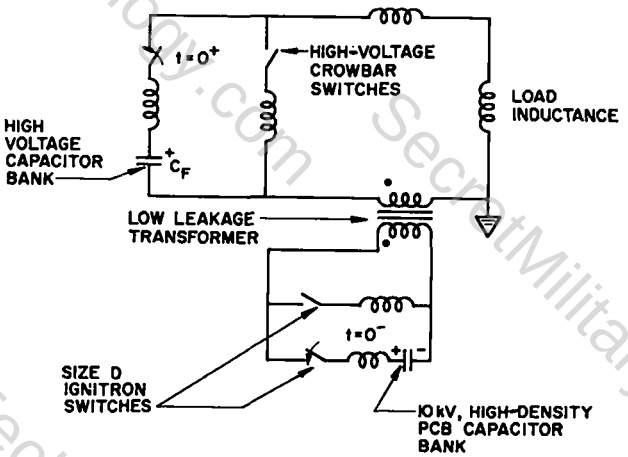

Fig. XVII-3.
Basic ZT-40 power crowbar circuit.

The low-leakage transformer and the crowbar switch are the main components to be developed for the ZT-40 PCB system. Computer circuit-plasma simulation was used to determine the required parameters for these components. The parameters for the PCB system and the required parameters for the PCB transformers and the PCB crowbar switches are listed in Table XVII-II.

B. ZT-40 CIRCUIT-PLASMA SIMULATION

Computer simulation of the entire ZT-40 circuit, including plasma dynamics, was a major activity in 1977. The plasma-circuit interaction has a great influence on the overall system. The simulation provided circuit component requirements as well as information about the possible operating modes and physics-related results. Basically, four operating modes were simulated: the Matched Mode (MM), the Padua Mode (PM), Slow Mode I (SMI), and Slow Mode II (SMII). These modes are compared in Table XVII-III with respect to their basic time constants and maximum currents.

The circuits for the Matched Mode, the Padua Mode, and Slow Mode II are shown in Fig. XVII-4 and representative Matched Mode waveforms are shown in Fig. XVII-5. The Matched Mode utilizes the separate bias bank of Fig. XVII-1 to provide a slow-rising initial toroidal field.

TABLE XVII-II
ZT-40 POWER CROWBAR SYSTEM
AND COMPONENT REQUIREMENTS

Component Requirements	I_ϕ	I_θ
Capacitor Bank		
Energy	3 MJ	1 MJ
Voltage	10 kV	10 kV
Power Crowbar Bank Switches		
No. required		
Start-size D	3 x 12	2 x 12
CB-size D	3 x 12	2 x 12
High Voltage Crowbar Switches		
Peak current	200 kA	200 kA
Average current	50 kA	50 kA
Inductances	30 nH	50 nH
Coulomb capacity	50 C	50 C
No. required	144	144
Low-Leakage Transformer		
No. required	12	12
Leakage inductance	4 nH	4 nH
Secondary current	750 kA	500 kA
Pulse duration	1 ms	1 ms
Primary voltage	10 kV	10 kV
Turns ratio	14:2	20:2
Core flux	0.187 Vs	0.125 Vs

The Padua Mode circuits are shown in Fig. XVII-4 and representative waveforms are shown in Fig. XVII-6. The Padua Mode can use the main I_θ bank to provide an additional fast-rising bias field. The main bias bank is not used in the representative waveforms of Fig. XVII-6.

The Slow Mode I method of operation is also termed the Self-Reversal Mode. The 50-kV capacitor banks are not used in either circuit. The I_θ circuit PCB system is also shorted and the bias bank is now used for reversing the field. The I_θ circuit utilizes the preionization (PI) circuit to initiate the plasma and the I_θ PCB system to drive the plasma current. The Slow Mode I circuits are shown in Fig. XVII-7, and a typical waveform is shown in Fig. XVII-8.

Slow Mode II is similar to the Matched Mode and is also termed the Aided Self-Reversal Mode. The basic circuit that is used for Slow Mode II operation is shown in Fig. XVII-4. Representative waveforms for Slow Mode II are shown in Fig. XVII-9. The I_ϕ and the I_θ loads, respectively, are arranged in several possible series-parallel combinations to produce very large load inductances for SMI and SMII operation.

The plasma was modeled using a snow-plow formulation for the majority of the simulations to date. A more appropriate, diffuse boundary plasma formulation is being programmed and will be used in future simulations.

The power crowbar transformer utilizes an iron core to increase the transfer efficiency. The transformer operation using the flux model shown in Fig. XVII-10 was simulated to determine the required core flux and the circuit effect of core saturation.

In all the circuit-plasma ZT-40 simulation studies, the Poynting flux of the plasma system was studied. The computer simulation program used the Poynting flux to determine possible and optimum bank switching times and to correlate future ZT-40 operation with other experiments.

TABLE XVII-III

ZT-40 MODE CHARACTERISTICS FOR NOMINAL TRAPPED FIELD OF 0.6 TESLA

	Matched Mode	Padua Mode	Slow Mode I	Slow Mode II
Bias				
B_Z (operating point)	0.6 T	0.0 T	0.6 T	0.6 T
τ_{RISE}	77. μs	77. μs	435. μs	840. μs
$I_{\theta\ Bank}$ (max)	3.44 MA	---	0.353 MA	0.344 MA
Toroidal				
B_Z (max)	0.5 T	0.6 T→0.5 T	0.0 T	-0.5 T
τ_{RISE}	---	3.4 μs	---	---
$\tau_{REVERSAL}$	2.3 μs	4.0 μs	---	20.3 μs
$I_{\theta Bank}$ (max)	26. MA	7.0 MA	---	3. MA
τ_{FLAT}	~300. μs	~300. μs	---	~1500. μs
Poloidal				
B_θ (max)	0.6 T	0.6 T	0.54 T	0.6 T
τ_{RISE}	1.9 μs	2.6 μs	1160. μs	18.3 μs
$I_{Z\ Bank}$ (max)	12.5 MA	8.2 MA	0.59 MA	3.7 MA
τ_{FLAT}	~200. μs	~200. μs	>3000. μs	~4000. μs
Computing Runs	65	37	56	47

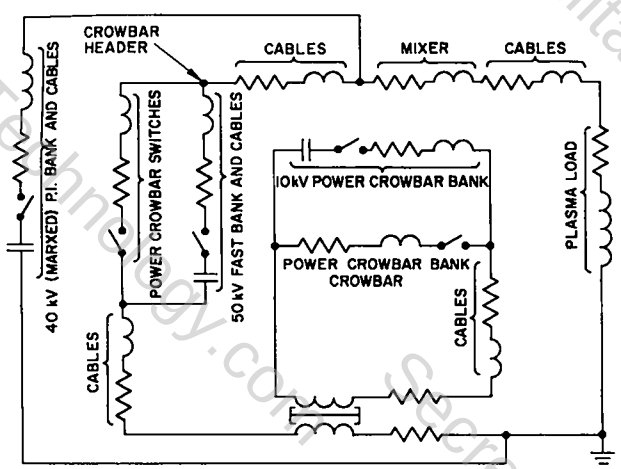

Fig. XVII-4.
Matched Mode, Padua Mode, and Slow Mode II circuits.

C. COMPONENT DEVELOPMENT

The component development program for ZT-40 was another major activity during 1977. The following paragraphs indicate the wide area encompassed by this development program.

1. ZT-40 Field Distortion Start-Gap. The start switch of Fig. XVII-11 was chosen for the ZT-40 application because a wide voltage operating

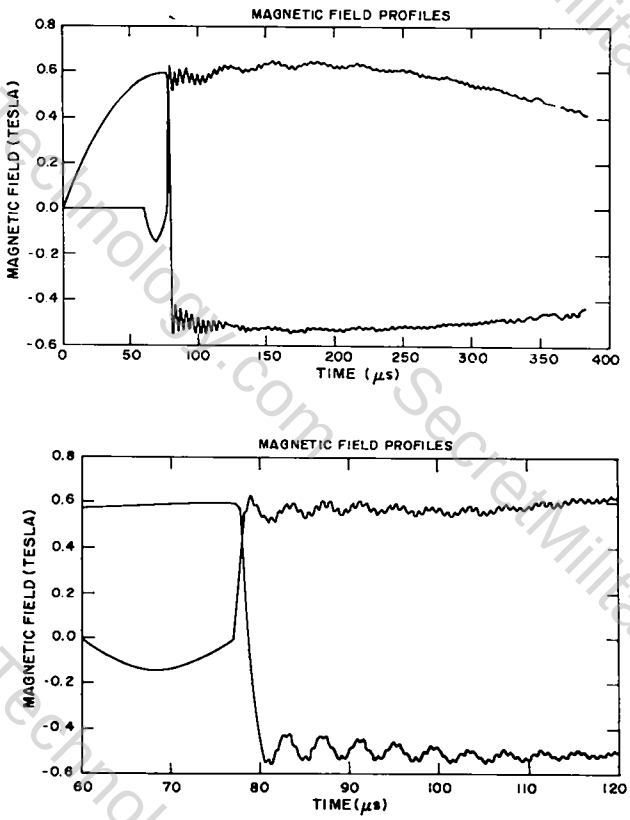

Fig. XVII-5.
Representative Matched Mode waveforms.

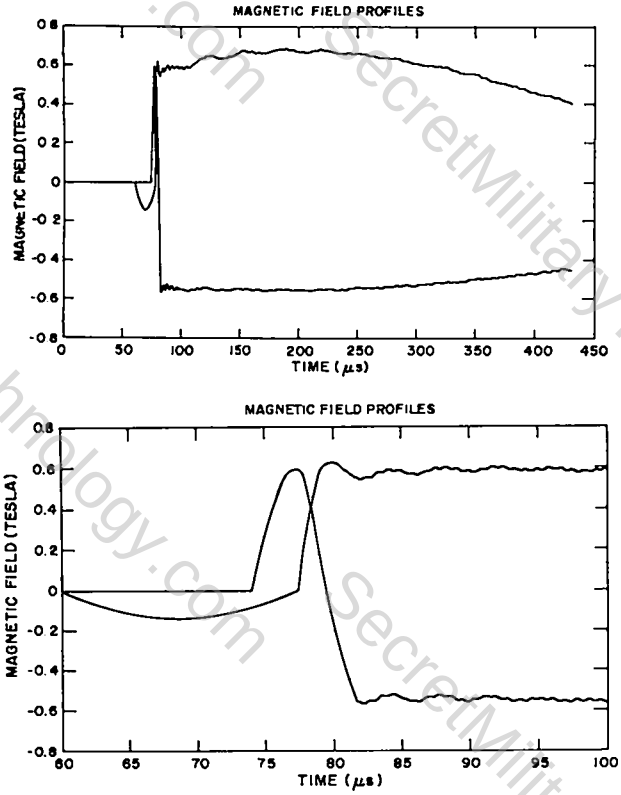

Fig. XVII-6.
Representative Padua Mode waveforms.

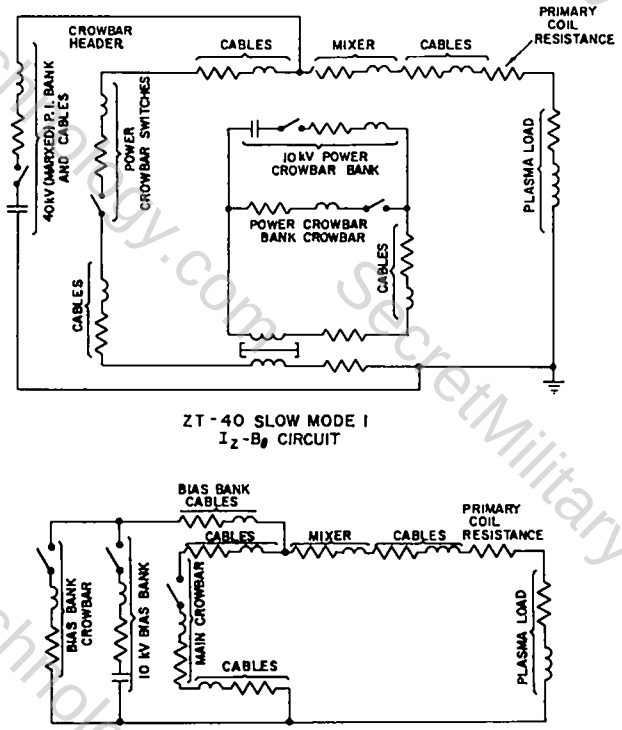

Fig. XVII-7.
Slow Mode I circuits.

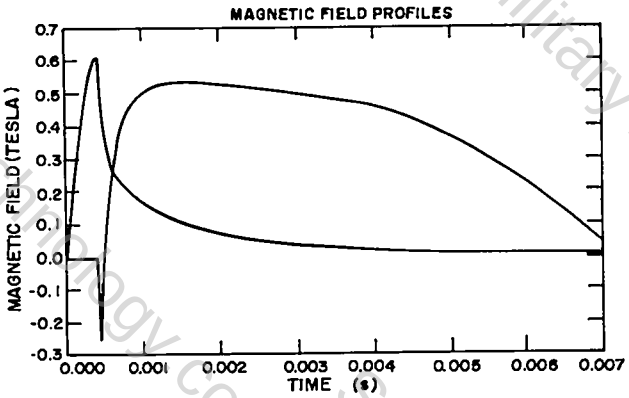

Fig. XVII-8.
Representative Slow Mode I waveforms.

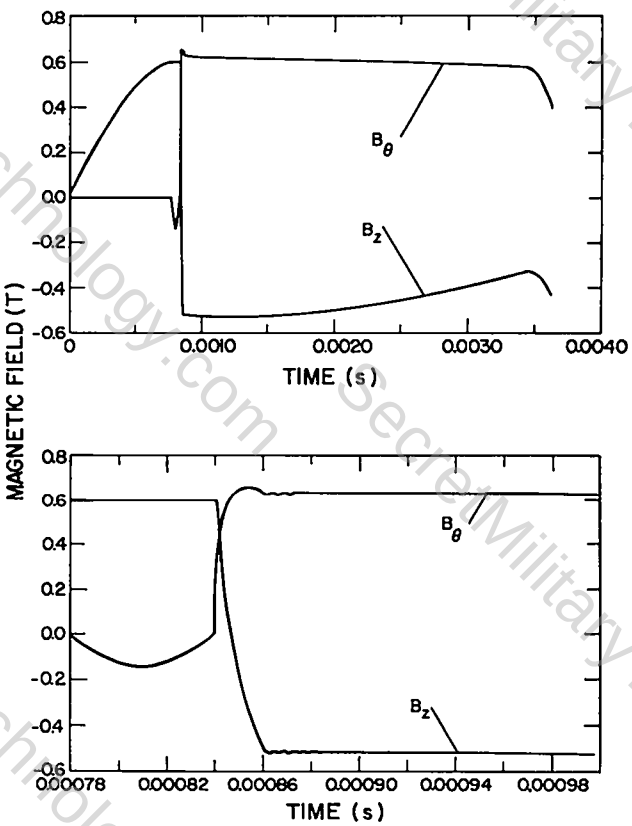

Fig. XVII-9.
Representative Slow Mode II waveforms.

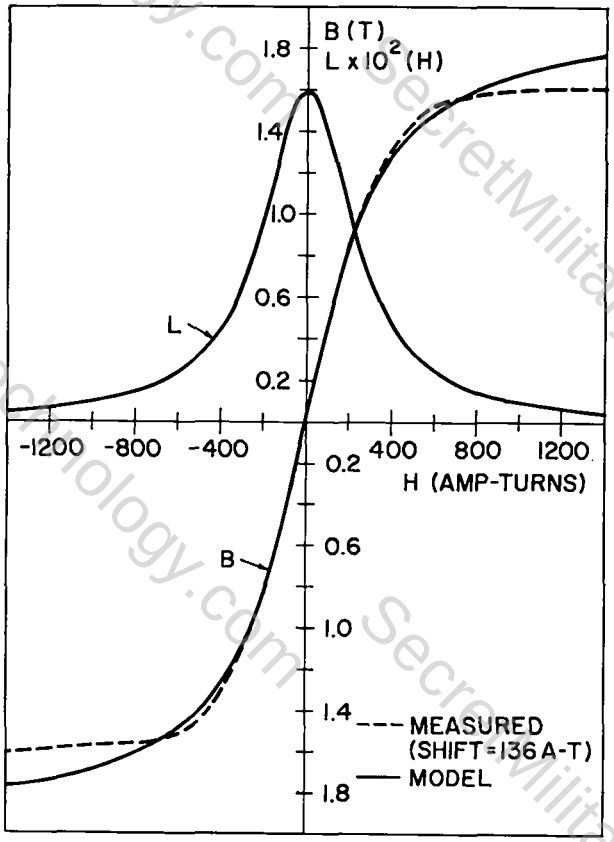

Fig. XVII-10.
Transformer simulation flux model.

range of 10-50 kV was desired. The field distortion switch was tested and evaluated thoroughly with the following results: (a) the main electrodes with press-formed moly caps operate about 5000 shots at a current of 100 kA before destruction; (b) the nylon insulators are viable until 10 000 shots when they begin to track; (c) spun moly electrode caps can extend the electrode life to 20 000 shots; (d) the optimum spacing for a voltage range 10-50 kV and reasonable air pressures is 0.635 cm; (e) the best switching performance occurs with negative capacitor charge and a negative trigger pulse; (f) the 3 kV/ns, 100-kV trigger pulse planned for ZT-40 start switch produces an average delay of 50 ns and an average jitter of 5 ns for nominal operating conditions; (g) the prefire rate is between 0.1 and 0.4%; (h) a brass modification of the electrode geometry has since reduced the prefire rate to less than 0.1% up to 25 000 shots.

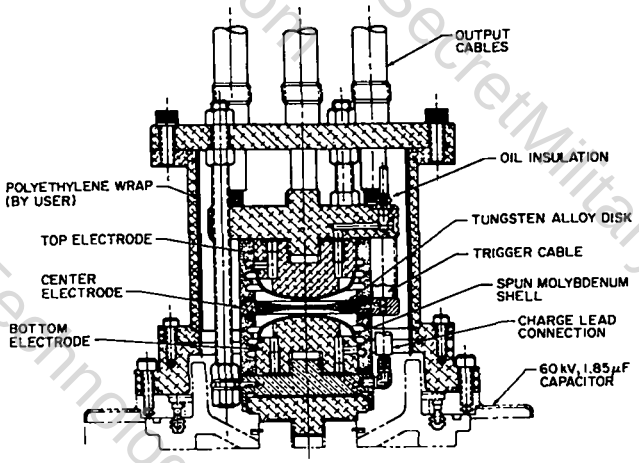

Fig. XVII-11.
ZT-40 field distortion start switch.

2. ZT-40 Passive CB Switch. Life test and modification studies of the ferrite-loaded ZT-40 passive crowbar spark gap shown in Fig. XVII-12 were completed in June 1977. The passive crowbar switch was tested at voltages of 60 kV with a peak current over 200 kA, an average maximum current of 140 kA, and a C load of 17 C. After the initial test, the average maximum current was reduced to 60 kA and the voltage reduced to 50 kV for life test. The results of the development test are as follows. (a) The electrode spacing that permits operation from 10 to 50 kV at reasonable air pressures and minimizes erosion and spark plug damage is 1.25 cm. (b) The average operational lifetime of the passive crowbar gap is approximately 4000 shots at 50 kV, 60 kA, 7.2 C, with the 1.25-cm spacing and a trigger circuit modification.

3. ZT-40 Power Crowbar Transformer. The initial tests of the first prototype power crowbar transformer were completed in 1977. A schematic indicating the transformer winding geometry is shown in Fig. XVII-13. The initial results indicate that a transformer with a total leakage inductance of about 1 nH, measured in the secondary with the primary shorted, is possible with a single-turn secondary. In addition, the initial primary to secondary insulation scheme seems to function satisfactorily. The winding interconnect scheme and the primary winding

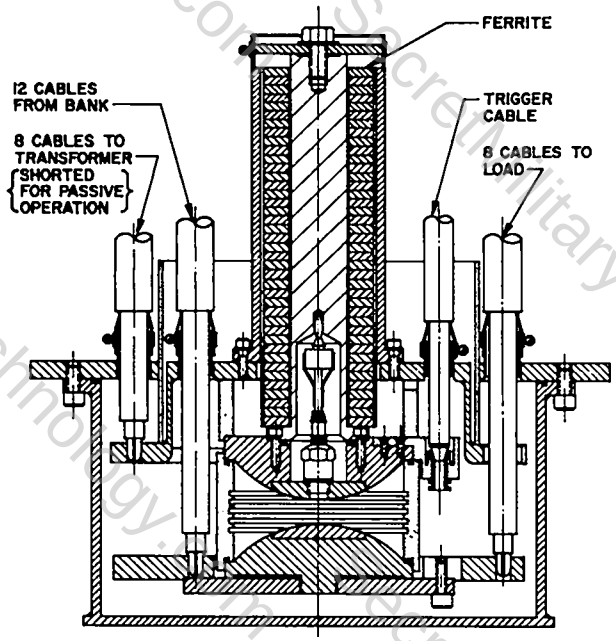

Fig. XVII-12.
ZT-40 passive crowbar switch.

insulation technique need to be modified to prevent tolerance build-up problems and voltage tracking. Further transformer design was restricted by limited personnel availability in 1977.

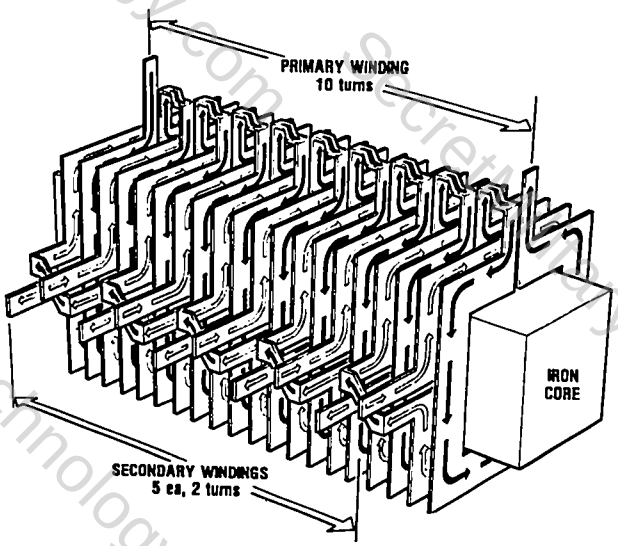

Fig. XVII-13.
ZT-40 power crowbar transformer winding geometry.

4. ZT-40 Power Crowbar Spark Gap. The first prototype of a high-voltage, high-Coulomb spark gap for ZT-40 power crowbar duty was procured in 1977. The test arrangement for the switch was fabricated and the gap installed. Initial tests will begin in 1978. The power crowbar spark gap is shown in Fig. XVII-14.

5. ZT-40 Trigger Initiation System. The trigger initiation system for ZT-40 is diagrammed in Fig. XVII-15. The digital time-delay system in the screen room controls the timing of various events in the ZT-40 circuit. The pulser system translates the timing pulse from the screen room to the experimental area using an injection laser and fiber-optic cable for isolation and EMI suppression. The air-powered, light-pulse receiver-amplifier generates a 5-kV pulse that in turn triggers a 200-kV pulse generator, which initiates the various high-voltage systems of ZT-40. The fiber-optic cable and the air-powered receiver permit the pulser system to be completely decoupled from ground, thus affording complete isolation.

The 200-kV pulse generator is a small, eight-stage, Marx circuit, termed a micromarx. The Marx stage switches are coupled by the ultraviolet light from the first-stage triggered switch. The Marx circuit incorporates barium titanate capacitors for a total stored energy at

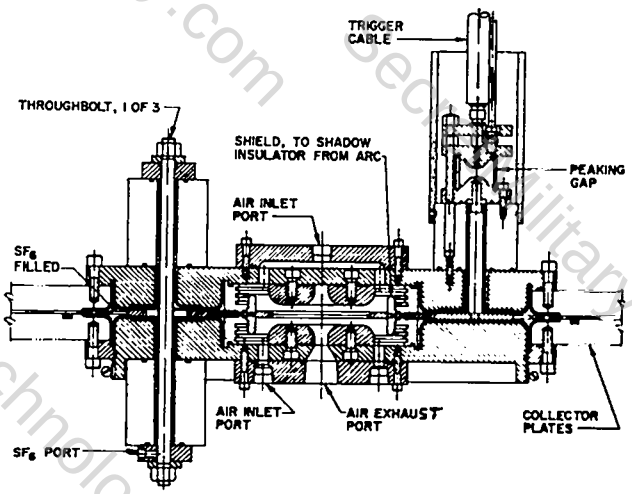

Fig. XVII-14.
ZT-40 power crowbar switch.

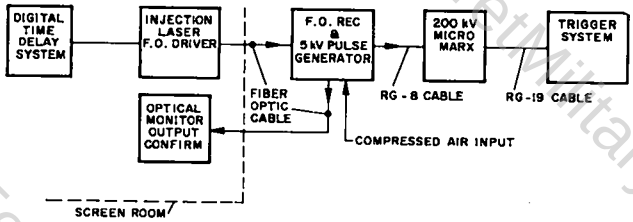

Fig. XVII-15.
ZT-40 trigger initiation system.

30-kV charge of 9 joules. The micromarx output rises to approximately 200 kV in 20 ns with a jitter of ±10 ns. The risetime can be reduced to 10 ns with an internal series pulse sharpening spark gap. The Marx electrical circuit is shown in Fig. XVII-16, and the generator is shown in Fig. XVII-17. The fiber-optic coupled pulser system and the micromarx generator were operated for 15 000 shots during the crowbar switch test.

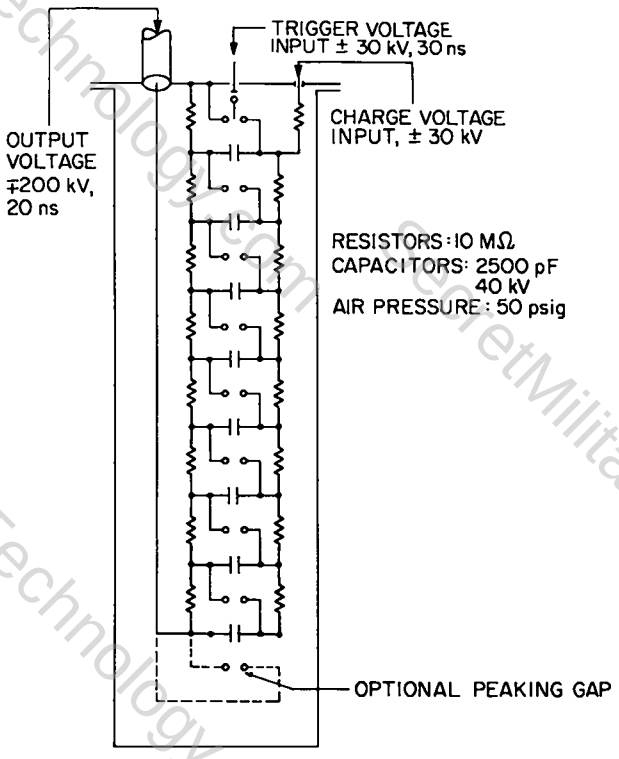

Fig. XVII-16.
ZT-40 micromarx electrical circuit.

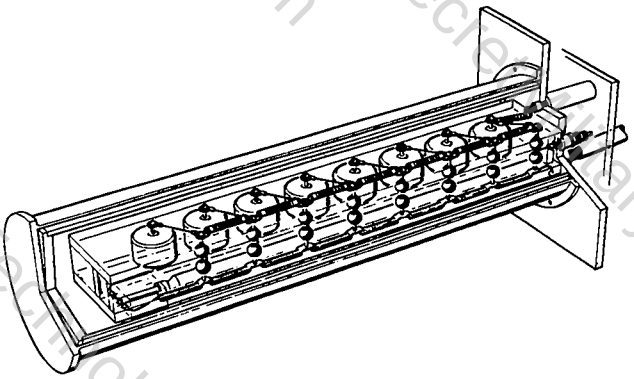

Fig. XVII-17.
ZT-40 micromarx 200-kV pulse generator.

D. ZT-40 ENGINEERING PROTOTYPE

A major effort in hardware evaluation was initiated in 1977. A prototype was constructed consisting of 1/24 of the ZT-40 circuit. This system was installed, a control system was fabricated, and checkout began in December 1977. The prototype will be used to test the following subsystems or components: (1) mixer assembly insulation and cable stripback, (2) snubber circuit hardware and components, (3) trigger system performance, (4) master trigger spark gap operation, (5) fiber-optic spark gap monitor system, and (6) power crowbar system.

E. ZT-40 MACHINE CONTROL AND DATA ACQUISITION FACILITIES

The ZT-40 experiment will be controlled and data will be accumulated with a Prime 400 computer via standard CAMAC interface equipment. The arrangement of the computer control system is a major concern requiring very careful specification and placement of the screen room, the signal conduits, the screen-room penetrations, the control and monitoring interface hardware, and the system components. The ZT-40 experiment has been very thoroughly planned as a system to minimize ground loops and to reduce the noise level to a value determined by the signal-to-noise ratio required in the screen room.

The screen room is a double-wall room manufactured by Erik A. Lindgren. Each wall consists of a layer of 24-gauge galvanized steel and a layer of 24-gauge silicon steel. The location of all diagnostic conduits, charge leads, control leads, and ground planes has been carefully determined to minimize ground loops and associated noise. Ground loops were also minimized in the screen room by decoupling individual control rack power with shielded isolation transformers. In addition, the electrical input power is filtered and the air-conditioning system is isolated and conducted through the screen room walls via wave-guide-below-cutoff structures.

The control function of the computer located in the screen room is accomplished via an 18-channel "byte parallel, serial highway" fiber-optic link. This type of fiber-optic control scheme was chosen because it will permit system shutdown in a 200-ms cycle time and still be cost effective. The fiber-optic highway is required to operate at 5 megabaud over a 40-m path. The system developed at LASL operates at 22 megabaud with a signal-to-noise ratio of about 70 for a bit error rate of 10^{-32} over the required distance. The fiber-optic system can also be used as an analog link with a 3-dB bandwidth of 8 MHz.

A fiber-optic spark gap monitor system was also developed to determine the firing time of the system's 288 crowbar spark gaps. The system looks at the spark gap light via a fiber-optic cable. The electronic system records a current pulse corresponding to the spark gap light time in a given window with a duration of 25-100 ns. The data are stored and read out at a later time by the computer system. A block diagram of the ZT-40 system is shown in Fig. XVII-18.

F. PULSE-POWER TECHNOLOGY AND COMPONENT DEVELOPMENT

The pulse-power engineering development group at LASL was involved in the following four major areas in 1977: ZT-40 system and component development, high-density Z-pinch system and component development, capacitor and ignitron switch life testing, and advanced pulse-power technology development.

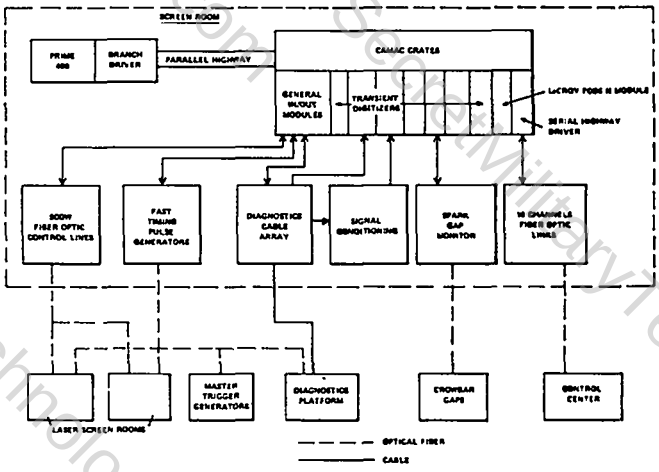

Fig. XVII-18.
ZT-40 control and data acquisition system block diagram.

1. ZT-40 System and Component Development.

The pulse-power engineering development for the ZT-40 system is detailed in the ZT-40 engineering section of this report. The development effort included the following areas:

ZT-40 System Development
- a. Basic System Circuit
- b. Power Crowbar Circuit Design
- c. Snubber Circuit Design
- d. Mixer System

ZT-40 Circuit-Plasma Simulation
- a. Matched Mode study
- b. Padua Mode study
- c. Slow Mode I study
- d. Slow Mode II study
- e. Plasma Model
- f. Poynting Flux studies
- g. Transformer Core Model

ZT-40 Component Development
- a. Field distortion start switch
- b. Passive crowbar switch
- c. Power crowbar transformer
- d. Power crowbar switch
- e. Trigger initiation system
  - (1) digital time delay
  - (2) fiber-optic air-powered pulser
  - (3) 200-kV micromarx pulse generator
- f. Prototype facility

2. High-Density Z-Pinch System and Component Development. The High-Density Z-Pinch (HDZP) experiment at LASL was designed to produce a time-varying current waveform greater than that shown in Fig. XVII-19 at any time in a small, high-pressure gas load. The experimental load is a small-diameter (100-μm) current filament between two electrodes spaced 10 cm-apart with a 20-cm-diameter coaxial return conductor. The current filament is to be initiated with a 20-J, 20-ns Q-switched Nd:glass laser through one electrode. One version of the load geometry is shown in Fig. XVII-20. The load inductance is on the order of 100 nH and the initial I from Fig. XVII-19 is on the order of 5×10^{12} A/s. Thus the load voltage at t=0 must be on the order of 500 kV. When the pulse-power source inductance is considered, the power supply voltage must be on the order of 1 MV and the resulting maximum current is on the order of 1 MA.

A study was undertaken in July 1977 to determine the system most suited for the desired HDZP power supply. A low-inductance Marx system, a Marx-charged water-capacitor system, and a low-inductance Marx-charged water transmission line system were investigated and evaluated. All of the systems were simulated using NET-2 to determine realistic operating parameters and

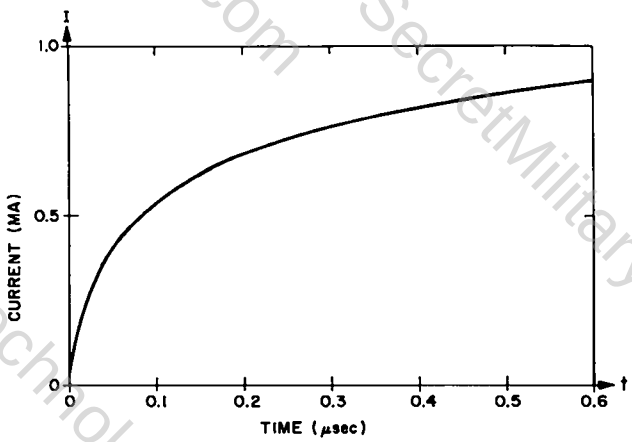

Fig. XVII-19.
HDZP minimum current waveform.

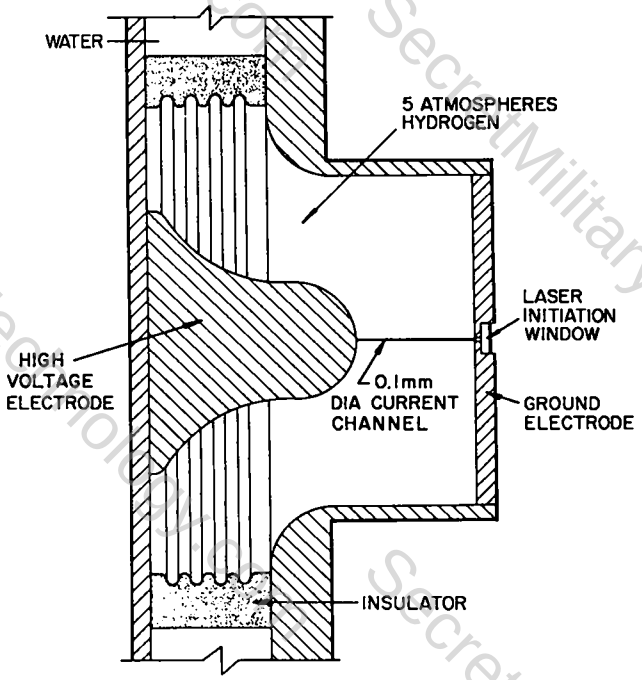

Fig. XVII-20.
HDZP load geometry.

performance. The low-inductance Marx system requires a 1-MV

Marx output voltage for a 100-nH source inductance. In order to achieve the required inductance, many Marx circuits must be paralleled and triggered with very low jitter into an initially open circuit. The other two schemes use water-insulated intermediate energy-storage systems, require less Marx voltage and triggering simultaneity, and permit more Marx inductance. The system using the water-insulated transmission line produced the best waveform with respect to Fig. XVII-19; but because of space considerations, the Marx-charged water-capacitor circuit shown in Fig. XVII-21 was chosen for HDZP. The water capacitor system produces a voltage risetime across the gas load that is approximately four times slower than the water load system using the same Marx bank.

The six-stage, 600-kV Marx system was designed using commercial components. The HDZP Marx system consists of 12 parallel Marx circuit modules that are to be triggered with ±20 ns jitter. The Marx module circuit diagram is shown in Fig. XVII-22 and a side view of the module is

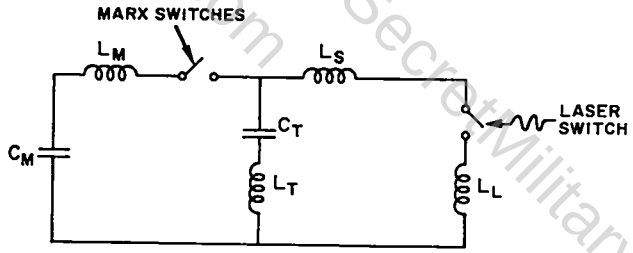

Fig. XVII-21.
Basic HDZP circuit.

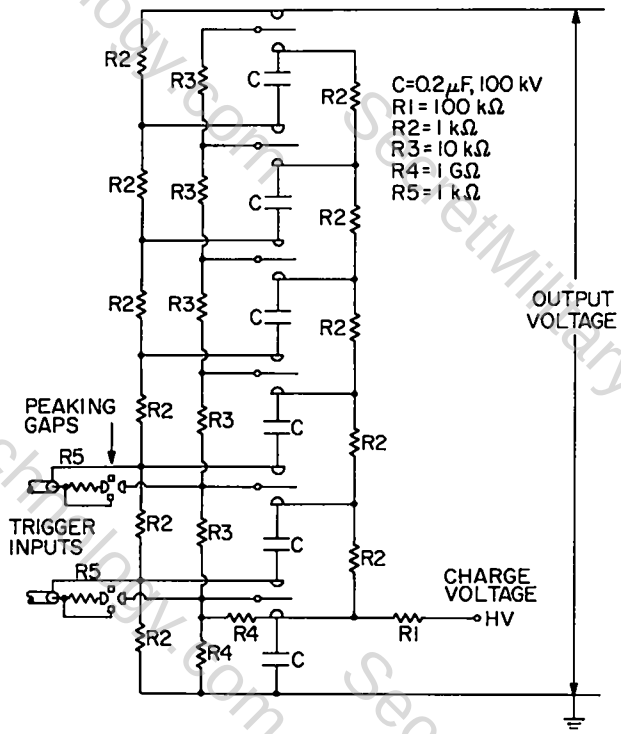

Fig. XVII-22.
HDZP Marx module circuit diagram.

shown in Fig. XVII-23. Two, 0.1-μF, 20-nH, 100-kV, 50%-reversal capacitors are used for each module stage. At 1 MA total output current, each capacitor is required to yield 42 kA. A capacitor reversal of 50% was required to prevent excessive capacitor damage due to fault modes. Physics International T670 100-kV, 100-kA, 60-nH spark gap switches are used between capacitor stages. Both components, the spark gap switch and the capacitors, will be operated near their maximum ratings. Future systems of similar nature will require the

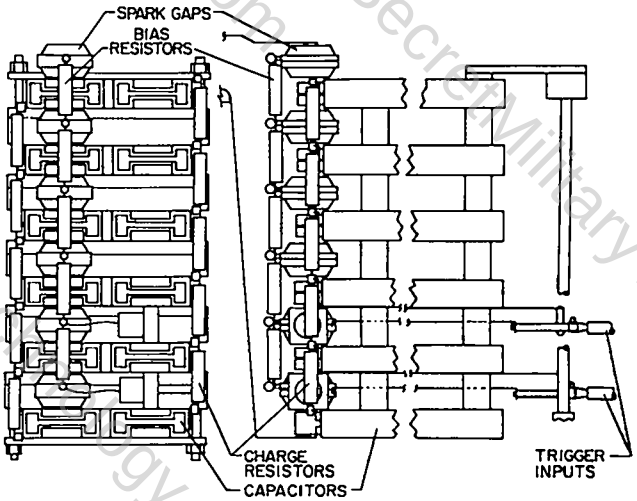

Fig. XVII-23.
Marx module configuration.

development of better components. The parameters of the HDZP Marx system are listed in Table XVII-IV.

The intermediate, water-insulated energy storage line was designed, as illustrated in Fig. XVII-24, using flat aluminum plates because the capacitance can be varied easily. The large diameter of comparable coaxial water capacitor was incompatible with the extremely small size of the gas load. The energy can be stored close to the load when a flat-plate capacitor is used and thus reduce the source inductance. The maximum value of the water capacitance was made equal to the

Marx capacitance in order to achieve efficient Marx energy transfer. The capacitor inductance is approximately 40 nH, which is only a factor of 2 better than the Marx system alone, but different operating modes can be obtained by

TABLE XVII-IV.
HDZP MARX PARAMETERS

Parameter	
Energy	72 kJ
Voltage	600 kV
Current	1 MA
Inductance	75 nH

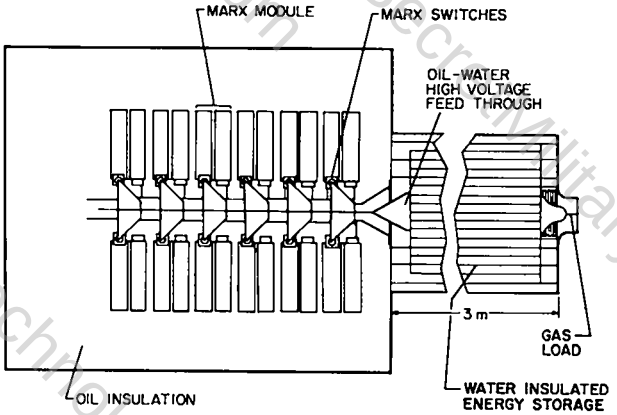

Fig. XVII-24.
HDZP system diagram.

varying capacitance and load current initiation times in order to use the capacitor as a peaking circuit and vary the initial current slope over a wide range.

The Marx trigger system must insure erection of all Marx modules within ±20 ns. The water capacitor appears as a very low impedance to the parallel Marx modules and facilitates triggering. Several methods for triggering the Marx system were evaluated with the NET-2 circuit analysis code. The trigger system shown in Fig. XVII-25 was then selected, designed and fabricated, and tested in 1977. The triggering scheme is a modification of those suggested by Fitch.[1] Basically, a fast-erecting trigger Marx is used to initiate shorted cable trigger generators at each stage voltage level. The 12-parallel, 36-W cables, are charged to 100 kV, and when shorted by the Marx stage switch, provide a 200-kV open-circuit voltage pulse for triggering the main Marx switches. The peaking gaps on Fig. XVII-25 isolate the spark gap trigger electrode potential from the cable potential until the fast-rising trigger pulse breaks down the gap. The peaking gap also serves to decrease the trigger pulse risetime seen by the Marx switch trigger electrode. Only two stages of the trigger Marx will be used because prototype tests of one Marx module indicate very little delay and jitter in Marx erection time after the second Marx switch is

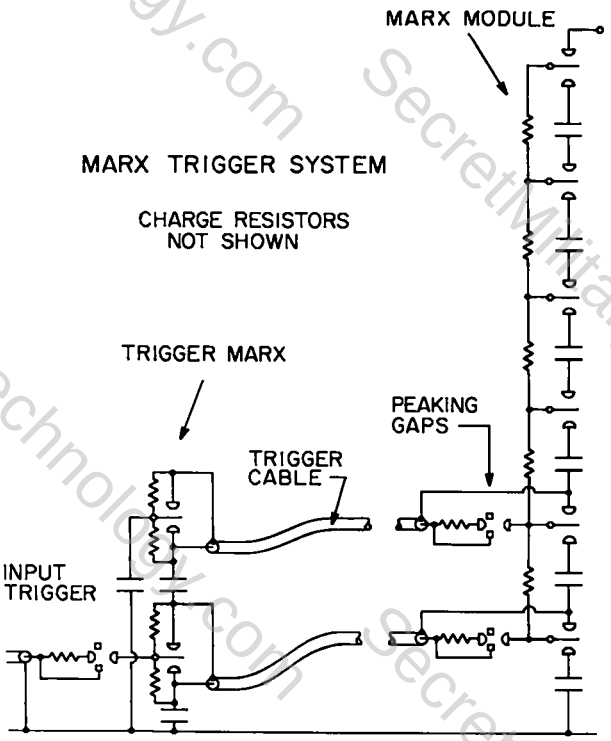

Fig. XVII-25.
HDZP Marx trigger system.

triggered. The first trigger Marx switch is triggered by an external 200-kV micromarx; then, switching transient of the first gap is used to trigger the second trigger Marx gap with a delay of 15 ns. The second trigger Marx stage switch cannot overvolt because transient overvoltages are severely damped by the composite coaxial cable impedance (3 W) across the switch. Thus, the two-stage trigger Marx erects sequentially and very reliably. The 12 coaxial cables from trigger Marx Switch 2 can be shortened with respect to those attached to trigger Marx Switch 1 such that the trigger pulses arrive at the first two main Marx stages simultaneously. Initially, the trigger cables will be the same length producing a 15-ns delay between Stage 1 and Stage 2 switches. The trigger Marx system also provides isolation from ground for the shorted cable pulse generators through the trigger Marx stage capacitors.

Evaluation of the high-voltage components and geometries using computer solutions of Laplace's equation was a major activity during the last quarter of 1977. The voltage stress of many parts of the HDZP system were evaluated, and mechanical

designs modified to reduce dielectric stress to acceptable levels.

A prototype HDZP system consisting of one Marx module and a 60-ns, 6-W water line was constructed during the last quarter of 1977. A control and power supply system was designed and fabricated, and initial operation has begun.

The prototype HDZP system will permit full voltage simulation of the final HDZP system at 1/12 the peak current. High-pressure hydrogen gas breakdown studies and laser channel formation studies will be carried out on the prototype system. From an engineering viewpoint, the Marx module operation can be monitored, evaluated, and modified to produce a reliable unit for the larger system.

3. Capacitor and Ignitron Switch Life Testing. The test program for capacitors, high-voltage coaxial cable, and ignitrons at LASL is unique nationally. The test program involves life testing of components and examination and evaluation of the malfunctioning units to determine the reason for failure. In many instances, the failure mode can be eliminated by changing the design or the manufacturing process. New units are then again life tested to determine the next failure mode. The test program requires a constant effort over many months and even years. Many capacitors that have been developed and tested at LASL are the basic components of many pulse-power systems nationwide, including those used for laser fusion, E-beam fusion, laser isotope separation, and weapons simulation.

During calendar year 1977, the LASL test program continued the evaluation of 10-kV high-density capacitors, 60-kV high-density capacitors, size D ignitrons, and a 160-kV low-inductance capacitor.

The 10-kV test bay is used to life test size D ignitrons and 10-kV high-density capacitors simultaneously. The 10-kV, 170-μF, 20%-reversal capacitors were developed because the lowest cost per joule (0.03 cents/joule) in a capacitor occurs at 10 kV. The test bay operated for 180 000 shots in 1077 during which two of the ten test capacitors failed. During the same test period, five of the size D ignitrons used to switch and crowbar the capacitors failed. In addition, the test load coil, which has accumulated 40 0000 shots at a stored energy of 85 kJ, failed and was repaired and reinstalled, causing a two-month delay in testing. The test program also evaluated methods of making reliable, high-current connections to the ignitrons and headers.

The 60-kV, 2.8-μF, 20%-reversal high-density test bay was operated a total of only 14 000 shots due to a personnel shortage. One capacitor reached end-of-life at 49 000 total shots. Most of the test shots were used to test a spark gap trigger circuit modification.

The 160-kV low-inductance capacitor was designed for high-voltage implosion heating systems. The standard 60-kV, 1.85-μF capacitor has a series inductance of approximately 24 nH, of which approximately 20 nH is the header. Two capacitor windings for this capacitor were fabricated by Maxwell using a polypropylene paper system and a standard paper system. During 1977 the capacitor was assembled and the inductance measured at approximately 12 nH. The capacitor will be impregnated by Maxwell Laboratories and a life test will be initiated in 1978.

The parameter and test data for the above components are listed in Table XVII-V.

C. ADVANCED PULSE-POWER TECHNOLOGY

The pulse-power group at LASL seeks to evaluate technology applicable to magnetic fusion experiments. During 1977, several concepts were investigated for future applications.

LASL-CTR has pioneered the 60-kV, Scyllac-type capacitor bank technology. The trigger systems for a 60-kV capacitor bank are a major portion of the overall system and are responsible for most of the system malfunctions. New concepts for both the start trigger system and the crowbar trigger system were investigated.

Triggering spark gap switches with a laser pulse is a well-developed technology pioneered by the Air Force Weapons Laboratory.[2] However, the number of optic components and the beam transport system required to switch many gaps simultaneously become excessive and expensive. The continuing development of fiber-optic cables for communication has presented another method of transporting high-power laser pulses to trigger many parallel

TABLE XVII-V

COMPONENT TEST DATA

Component/Parameter	
10 kV HD Capacitor	
Voltage	10 kV
Current	5 kA
Reversal	5%
Capacitance	170 μF
Average life	120 000[1]
Maximum life	50 0000[1]
Inductance	40 nH
Size D Ignitron	
Voltage	10 kV
Peak current	100 kA
Coulombs	1000 C
Average life	30 000[1]
Maximum life	180 000[1]
60-kV HD Capacitor	
Voltage	60 kV
Current	60 kA
Reversal	20%
Capacitance	2.85 μF
Average life	32 000[1]
Maximum life	49 000[1]
Inductance	30 nH
160 kV LI Capacitor	not life tested
Voltage	160 kV
Reversal	85%
Capacitance	0.3 μF
Inductance	12 nH

[a]Tests still in progress.

or many series (Marx) spark gaps. A laser fiber optic for a spark gap trigger (LFOTS) system is diagrammed in Fig. XVII-26. In order to trigger a spark gap operating close to self-breakdown, only 0.1 to 1 mJ of energy is required at the spark gap.[2] The power density when focused on the spark gap target electrode is the major parameter to be maximized, and thus, the power density in the fiber-optic cable is the limiting factor in determining the amount of energy transferred using the fiber cable. The laser pulse is focused on the target electrode with a lens after leaving the fiber cable. The empirical power density threshold for low jitter and delay switching is 0.33 GW/cm^2.[3] The power density in the fiber is limited by stimulated Raman and Brillouin scattering to a maximum of about 0.8 GW/cm^2 in short cables.[4,5] Previous fiber-optic cable studies and laser triggered spark-gap work thus indicate that a laser fiber-optic trigger system is very feasible. This concept will be tested early in 1978.

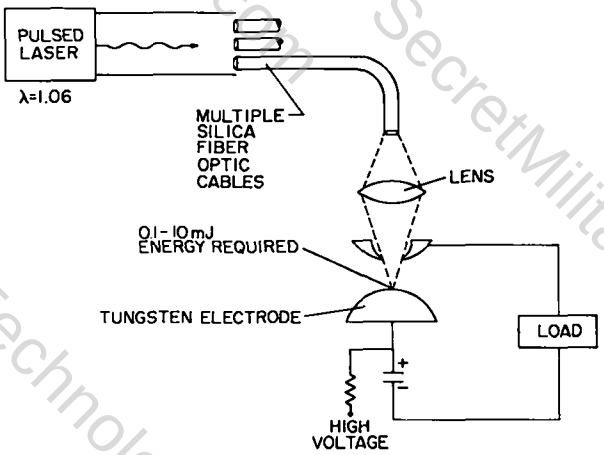

Fig. XVII-26.
Laser fiber-optic spark gap trigger system.

The 60-kV capacitor-bank crowbar gaps are required to short out the capacitors at peak current or switch at zero voltage. The present system requires a very complex trigger system that supplies about 300-500 joules to each gap. The trigger system components have a limited lifetime and thus limit the crowbar system lifetime.

The technology of solid-state diodes has advanced in recent years into the range of currents required of the 60-kV capacitor crowbar switch. For example, a 7.5-cm silicon diode wafer has a one-half cycle (60-Hz) surge current of 30 kA with a reverse holdoff voltage of 2000 V. The 60-kV crowbar switch operates with a duty cycle of 1 pulse per 5 minutes in a transformer oil medium.

A new package arrangement for low-duty cycle operation and cooling in oil will be investigated in 1978. The current industrial package is made for air operation and repetitive duty, and thus is too bulky and expensive for 60-kV crowbar duty,. The 60-kV crowbar diode must withstand a 60-kV reverse voltage for several microseconds and then conduct a peak current of 60 kA for several hundred microseconds. The reverse voltage parameter requires stacking many diode wafers. This concept was initiated in 1977, and a preliminary conceptual design of a 60-kV crowbar diode will be completed in 1978 if manpower permits.

The technolgical challenge of sustaining or power crowbarring fast-rising magnetic fields for many hundred microseconds into the millisecond range has been a major activity in 1977. A basic power crowbar circuit is diagrammed in Fig. XVII-27. The development of a high-Coulomb, high-voltage, low-inductance crowbar switch shown in Fig. XVII-27 has been of major concern. A low-inductance spark gap is being developed as the power crowbar switch for ZT-40. However, spark gaps are probably limited to about 100°C at 100 kA, or 1-ms conduction time. In order to sustain fields into the many millisecond range, a mechanical switch must be closed in parallel with the fast-switching power crowbar switch. It is desirable to use simple mechanical switches (i.e., hydraulic or pneumatic), which close in about 3-5 ms, because fast-closing mechanical switches (<3 ms) are complex, require large amounts of power, and must be timed accurately.

In order to use simple mechanical switches, a crowbar switch with a conduction time of approximately 5 ms at 100 kA must be developed to bridge the Coulomb region between spark gap switches and simple mechanical switches. Spark gaps operate at high voltages with low inductance and large I at t=0 but have a Coulomb limit due to electrode erosion. On the other hand, ignitrons have large Coulomb capacity due to the renewable mercury electrodes but have rather high inductance, operate at only moderate voltages, and I is restricted at t=0. Thus a program to combine the desirable characteristics of a spark gap and an ignitron into a mercury-wetted spark gap was initiated in 1977. Initially, a research contract to a university was proposed to determine the switching and voltage hold-off phenomena of a composite switch. However, budget limitations delayed the program and finally required that the investigations be done in house. These investigations will start in 1978. A conceptual design of a mercury-wetted spark gap is shown in Fig. XVII-28.

During 1977, the radially fed implosion heating coil (RFIHC), or Marshall coil, was received from CMB-6. The RFIHC was manufactured using techniques applicable to a ceramic substrate for a fusion-type reactor. The RFIHC was to be used for implosion heating in a future Scyllac-type experiment, but because of the

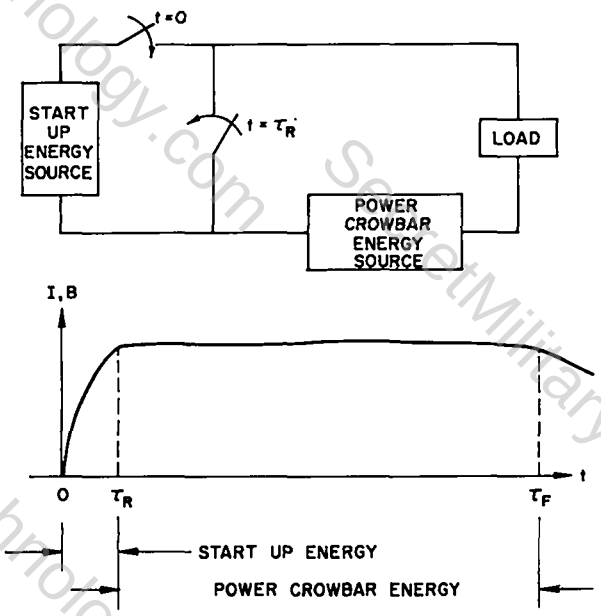

Fig. XVII-27.
Basic power crowbar circuit.

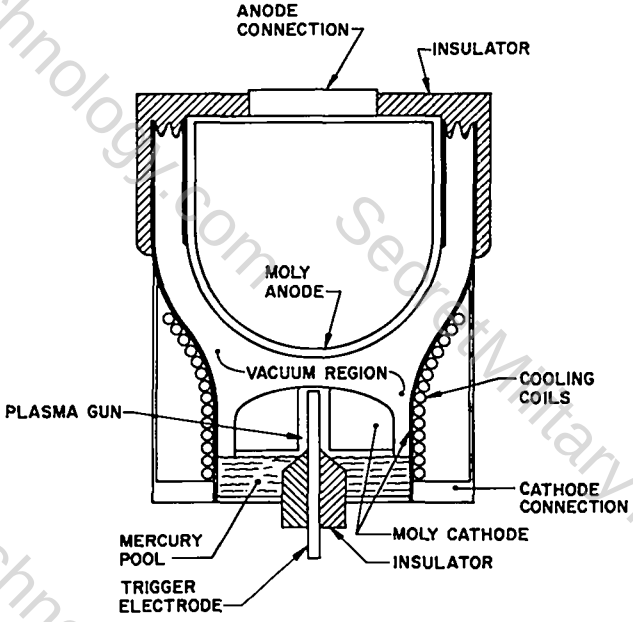

Fig. XVII-28.
Conceptual mercury-wetted switch.

Scyllac program termination, it will not be used. Measurements of the coil parameters and operation were conducted using small signals to verify inductance calculations and to wrap up the RFIHC development program. The RFIHC is shown in Fig. XVII-29.

The trigger systems used in fusion power supplies routinely use series, peaking spark gaps to isolate various circuit voltages and to reduce trigger pulse voltage risetimes. The peaking gaps are irradiated with an initial arc to reduce jitter. However, the initial arc has been created with a small center pin trigatron configuration as shown in Fig. XVII-30(a). The trigger pin assembly distorts the electric field between the main electrodes, reducing the main gap self-breakdown voltage and also wearing out prematurely. A new "inside-out" trigatron configuration shown in Fig. XVII-30(b) was designed to overcome the problems with the standard trigatron. The new peaking gap, shown in Fig. XVII-31, reduces a 200-kV pulse rise time of 30 ns to 7 ns with less than 2-ns jitter into a 50-W load. The irradiating electrode is now more massive to reduce wear, and the desired interelectrode capacitances required to provide the correct breakdown characteristics are inherent in the design.

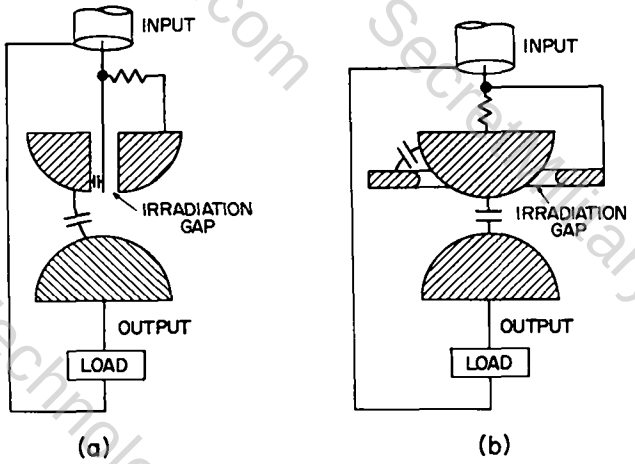

Fig. XVII-30.
Peaking gap systems.

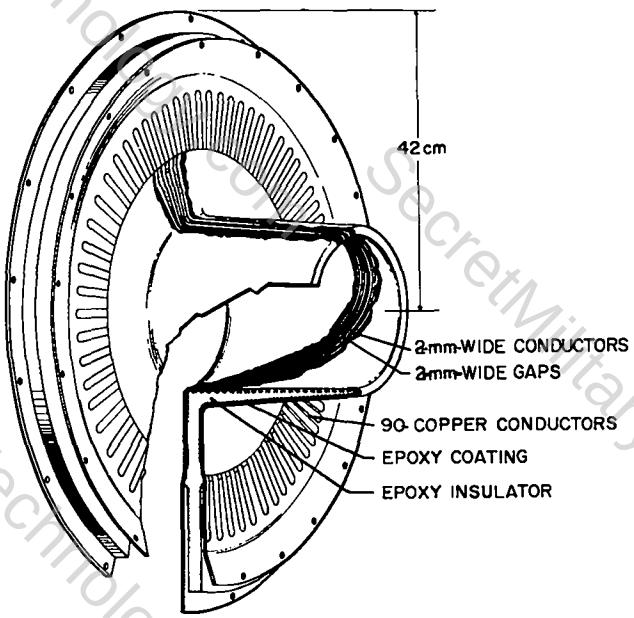

Fig. XVII-29.
Radially fed implosion heating coil.

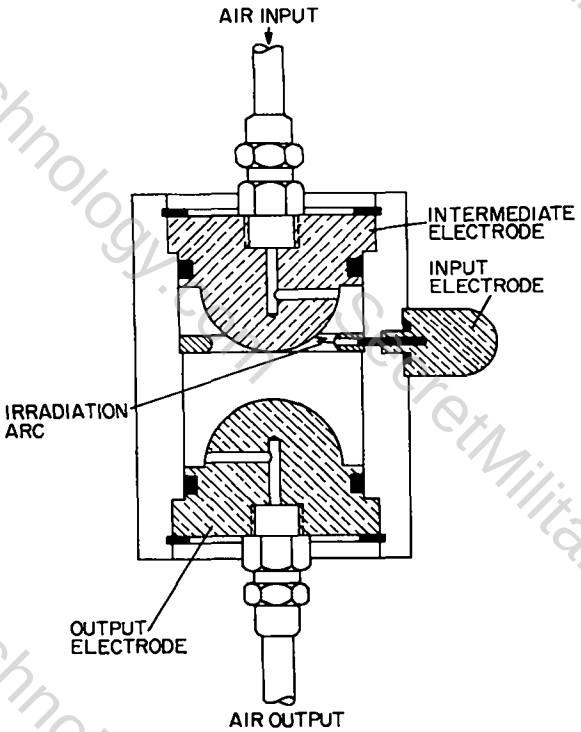

Fig. XVII-31.
Inside-out trigatron peaking gap.

Another area of interest in all fusion experiments is monitoring spark gap operation and switching times. A small development program was initiated in 1977 to use the spark gap arc light as a monitor signal and transport this signal via fiber-optic bundles to the screen room for analysis. The basic development was a window in the spark gap to observe the light.

REFERENCES

1. R. A. Fitch, "Marx and Marx-Like High-Voltage Generators," Maxwell Labs, Inc., IEEE Trans. on Nuclear Science NS18 4, (1971).

2. A. H. Guenther and J. R. Bettis, "Everything You Ever Wanted To Know About Laser Triggered Switching," Air Force Weapons Laboratory, Kirtland Air Force Base, NM.

3. J. R. Bettis and A. H. Guenther, "Subnanosecond-Jitter Laser-Triggered Switching at Moderate Repetition Rates," IEEE J. Quant. Elec., QE-6, 8, (1970).

4. R. G. Smith, "Optical Power Handling Capacity of Low Optical Fibers as Determined by Stimulated Raman and Brillouin Scattering," Appl. Opt. 11, 2489-2494 (1972).

5. S. M. Jansen and M. K. Barnoski, "Stimulated Raman Scattering in Multimode Fibers," Proc. Topical Meeting on Optical Fiber Transmission II, Feb. 22-24, 1977 Williamsburg, VA, Paper TuD7.

XVIII. TRITIUM SYSTEM TEST ASSEMBLY

James L. Anderson

A. INTRODUCTION

The Tritium System Test Assembly (TSTA), project was initiated at LASL in February 1977. This project is funded by the Office of Fusion Energy as a Major Device Fabrication (MDF) project. A detailed proposal,[1] including cost and schedule projections was generated during the February-May 1977 period. In June 1977 the results of this study were presented at a MDF review at DOE Headquarters. The project was recommended for approval by the DOE appointed review panel at that time. The Office of Fusion Energy acting on this recommendation approved the TSTA project in early July 1977. The TSTA project was approved with a baseline Total Estimated Cost (TEC) of $13.2 M. Of this, $4.8 M is for LASL operations, $6.9 M for hardware and equipment procurement and installation and $1.5 M is contingency funding. The baseline schedule projection calls for TSTA to be on-line and operating by FY-1981.

B. TSTA FUNCTION

The Tritium Systems Test Assembly (TSTA), Fig. XVIII-1, is dedicated to the development, demonstration, and interfacing of technologies related to the deuterium-tritium fuel cycle for fusion reactor systems. The first such system to be built will be a tokamak TNS (The Next Step) deuterium-tritium burning machine. This TNS will be followed by a TNS-upgrade or an Experimental Power Reactor (EPR). Either of these later devices will build and expand on the tritium handling system used in TNS. The principal program objectives for TSTA can be stated as:

1. demonstrate the fuel cycle for fusion power reactors;
2. develop and test environmental and personnel protective systems;
3. develop, test, and qualify equipment for tritium service in the fusion program;
4. provide a final facility that can be used for demonstration and as an example that could be directly copied by industry;
5. demonstrate long-term reliability of components;
6. demonstrate long-term safe handling of tritium with no major releases or incidents; and
7. investigate and evaluate the response of the fuel cycle and environmental packages to normal, off-normal, and emergency situations.

The objectives of the TSTA Project are to design, fabricate, construct, and bring into operation the Tritium Systems Test Assembly at LASL within approved envelopes of technical schedule and cost baselines.

The TSTA will consist of a large gas loop, Fig. XVIII-2, which can simulate the proposed fuel cycle for a fusion facility. The loop, as shown, does not include any specific fuel injection system, but will be sufficiently versatile so that such systems can be added as the design requirements are better defined. The gas loop will be designed to handle up to 360 moles of DT per day. This flow will provide cycle operating experience on a scale that is equal to or greater than the full-scale fuel cycles currently being addressed for TNS and EPR systems. To accomplish this at TSTA will require an on-site tritium inventory of approximately 150 g.

The assembly to do this will consist of a number of integrated subsystems as follows:

- Vacuum pumping
- Transfer pumping
- Fuel cleanup (ash and impurity removal)
- Hydrogen isotope separation
- Fuel mixing and injection (including impurity simulation)
- Interfaces with external systems (neutral beam, coolant breeding blanket systems)
- Fuel storage

Essential functions associated with the overall assembly include:

- Tritium waste treatment
- Emergency room cleanup and effluent controls

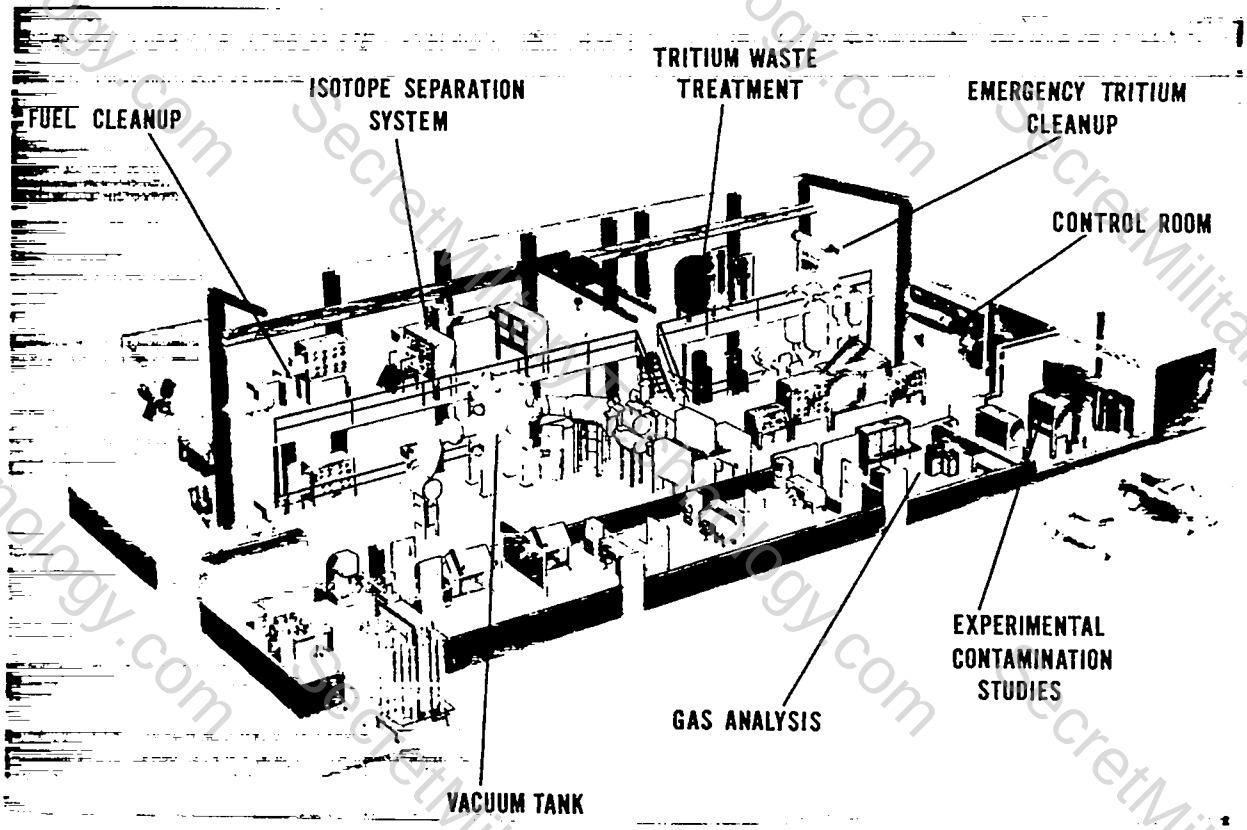

Fig. XVIII-1

Artist's concept of TSTA.

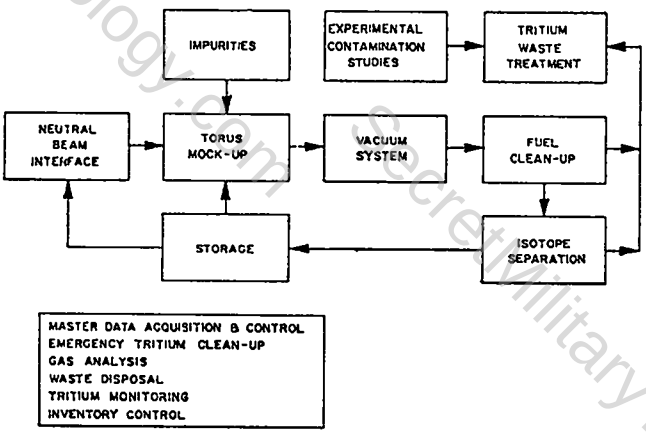

Fig. XVIII-2

Main process loop and auxiliary systems.

- Waste disposal
- Radiation monitoring
- Personnel safety
- System maintenance
- Instrumentation
- Computer control and simulation
- Analytical system (i.e., gas analysis), and quality assurance procedures.

C. PROJECT INTERFACE WITH THE U.S. FUSION PROGRAM

The development of TSTA at this time will permit design and evaluation of the required fuel cycle well in advance of the final design of a TNS tritium system. This timely accumulation of data will insure that the design and development of the tritium system will not be a pacing item in the design of TNS. The development of the tritium technology required at TSTA for the fuel cycle environmental packages will not require any large scientific or technical breakthroughs. There currently exists within DOE, and specifically within the Los Alamos Scientific Laboratory, a considerable amount of experience and expertise in tritium technology. This experience and expertise will be used at TSTA to insure that the design of the

facility will reflect the most current information and philosophy pertaining to tritium technology.

While the design of any specific subsystem may not require a significant technology advancement, the integration of all of these subsystems into one package is a significant advance. There currently exists nowhere within the DOE complex a facility which integrates all of these subsystems into a continuously operating computer controlled system. The flow rate and the total quantity of tritium to be handled in a fusion reactor on a routine basis necessitate the establishment of TSTA as a demonstration facility. Table XVIII-I gives a comparison of the projected tritium inventories and release goals for five fusion facilities. This comparison serves to emphasize the need for the timely development of TSTA. The Tokamak Fusion Test Reactor, TFTR, is currently in the early stages of construction at Princeton, NJ. All of the other projected facilities in the table will follow TSTA and will utilize the information obtained at TSTA.

A very significant goal at TSTA will be to demonstrate that these large quantities of tritium can be handled safely on a routine basis. The establishment of environmental and safety packages for tritium systems within the Office of Fusion Energy (ETM) program, will be a significant milestone. The TSTA will serve as a base-line facility that will provide a large data base that can be used to establish future guidelines and requirements for fusion facilities.

TABLE XVIII-I

TRITIUM INVENTORIES IN FUSION FACILITIES

Facility	T_2 Inventory (kg)	T_2 Release Fuel Feed (kg/day)	Goal (Ci/day)
TFTR	0.005	0.001	1
TSTA	0.2	0.5-1.5	1
TNS	0.25	0.25-0.5	1-10
EPR	4-6	1-2	5
[a]DEMO	6-12	2-6	5-10

[a]DEMO = 1000-MWe net output

REFERENCE

1. J. L. Anderson and R. H. Sherman, "Tritium Systems Test Assembly Design for Major Device Fabrication Review," Los Alamos Scientific Laboratory Report LA-6855-P (June 1977).

W. T. Armstrong	"Stimulated Brillouin Backscatter Detection from a Theta-Pinch Plasma"	submitted to J. Appl. Phys.
E. D. Arthur P. G. Young	"Calculation of 15-MeV Neutron-Induced Charged-Particle Spectrum on Stainless Steel Type 316"	Trans. Am. Nucl. Soc. 26, 503 (1977)
D. C. Barnes J. U. Brackbill	"Computation of Magnetohydrodynamic Flow in a Magnetically Confined Plasma"	Nucl. Sci. Eng. 64, 18 (1977)
D. C. Barnes	"A Vacuum Field Solver for an Arbitrary Three-Dimensional Mesh"	J. Comput. Phys.
D. C. Barnes	"An Approximate Model for Toroidal Force Balance in the High-Beta Stellarator"	submitted to Phys. Fluids
R. R. Bartsch E. L. Cantrell R. F. Gribble K. A. Klare K. J. Kutac G. Miller W. E. Quinn	"Feedback Stabilization of a ℓ=0,1,2 High-Beta Stellarator"	submitted to Nucl. Fusion
R. D. Bengtson S. A. Eckstrand A. G. Sgro C. W. Nielson	"Plasma Rotation During Implosion in a Theta-Pinch"	Phys. Rev. Lett. 39, 884, (1977)
C. J. Buchenauer A. R. Jacobson	"Quadrature Interferometer for Plasma Density Measurements"	Rev. Sci. Instrum. 48, 769 (1977)
J. M. Bunch	"Mollwo-Ivey Relation Between Peak Color-Center Absorption Energy and Average Ion Spacing in Several Oxides of Group II and III Metals"	Phys. Rev. B 16, 724, (1977)
J. M. Bunch J. G. Hoffman A. H. Zeltman	"On the Nature of Features Seen by TEM in Fast Neutron Irradiated Al_2O_3"	to be published in J. Nucl. Mater.
E. L. Cantrell G. Miller W. E. Quinn W. Riesenfeld	"Observation of Propagating m=1 Waves in Scyllac"	Nucl. Fusion Letters 17, 1191 (1977)
T. E. Cayton	"The Laboratory Spring Mass Oscillator: An Example of Parametric Instability"	Am. J. Phys. 45, 723 (1977)
T. E. Cayton	"Energy Anisotrophy Instabilities in the Vlasov-Fluid Description of High-Beta Plasmas"	submitted to Phys. Fluids
F. W. Clinard D. L. Rohr W. A. Ranken	"Neutron Irradiation Damage in Stabilized ZrO_2"	J. Am. Ceramic Soc. 60, 287 (1977)
R. J. Commisso C. A. Ekdahl K. B. Freese K. F. McKenna W. E. Quinn	"Solid-End-Plug Experiment on a Theta Pinch"	Phys. Rev. Lett 39, 137 (1977)
R. J. Commisso H. R. Green	"Experimental Study of the Post-Implosion Phase of a Theta Pinch"	Phys. Fluids 20, 44 (1977)
R. Y. Dagazian R. B. Paris	"Stationary Convective-Like Modes in a Plasma Slab with Magnetic Shear"	Phys. Fluids 20, 917 (1977)
R. Y. Dagazian	"Internal Ring End Stopper for Open Ended Devices"	submitted to Nucl. Fusion

R. Y. Dagazian	"Nonlinear Effects on Free Boundary Modes in Slab Geometry"	submitted to Phys. Fluids
D. M. Drake G. F. Auchampaugh E. D. Arthur C. E. Ragan P. G. Young	"Double Differential Beryllium Neutron Cross Sections at Incident Neutron Energies of 5.9, 10.1, and 14.2 MeV"	Phys. Rev. C 16, 1792 (1977)
A. Dubi Y. S. Horowitz	"Simultaneous Two Sample Activation Measurement Immune to Detector Inter-calibration"	Int. J. Appl. Radiat. and Isotopes 28, 291 (1977)
A. Dubi Y. S. Horowitz	"A Semi-Analytic Solution to the Transport Equation in Spherical Geometry"	to be published in Nucl. Sci. Eng.
A. Dubi S.A.W. Gerstl D. J. Dudziak	"Monte Carlo Aspects of Contributions"	to be published in Nucl. Sci. Eng.
A. Dubi Y. S. Horowitz H. Rief	"Calculation of the Total Flux at a Point by the Monte Carlo Track Rotation Estimator"	submitted to Nucl. Sci. Eng.
A. Dubi Y. S. Horowitz	"A Note on the Interpretation of Conditional Monte-Carlo as a Form of Importance Sampling	submitted to SIAM
J. P. Freidberg R. A. Gerwin	"Lower Hybrid Drift Instability at Low Drift Velocities"	Phys. Fluids 20, 1311 (1977)
J. P. Freidberg R. A. Gerwin	"Stability of a Closed-Line Scyllac, Revisited"	Nucl. Fusion 17, 443 (1977)
J. P. Freidberg D. W. Hewett	"Finite-Gyroradius Stabilization of Diffuse High-Beta Stellarators"	submitted to Phys. Fluids
J. P. Freidberg L. D. Pearlstein	"Rotational Instabilities in a Theta Pinch"	submitted to Phys. Fluids
S. P. Gary W. C. Feldman	"Solar Wind Heat Flux Regulation by the Whistler Instability"	J. Geophys. Res. 82, 1087 (1977)
S. P. Gary	"Electrostatic Heat Flux Instabilities in the Solar Wind"	submitted to J. Geophys. Res.
S. P. Gary A. G. Sgro A. W. DeSilva	"Axial Density Profiles and Nonclassical Thermal Conduction in Linear Theta Pinches"	submitted to Phys. Fluids
S. P. Gary J. J. Sanderson	"Density Gradient Drift Instabilities: Oblique Propagation at Zero Beta"	submitted to Phys. Fluids
S. P. Gary	"The Electromagnetic Ion Beam Instability and Energy Loss of Fast Alpha Particles"	submitted to Nucl. Fusion
S.A. W. Gerstl D. J. Dudziak D. W. Muir	"Experience with Quantitative Data Assessment, and Results for Fusion Reactors"	Trans. Am. Nucl. Soc. 26, 482 (1977)
S.A.W. Gerstl	"Comments on the Concept of Spatial Channel Theory Applied to Reactor Shielding Analysis"	Nucl. Sci. Eng. 64, 798 (1977)
R. Gribble G. Miller	"Plasma Position Detector Using a Segmented Photo-diode"	Rev. Sci. Instrum. 48, 778 (1977)
R. L. Hagenson R. A. Krakowski K. I. Thomassen	"The Reversed-Field Pinch Reactor"	Trans. Amer. Nucl. Soc. 27, 47 (1977)
I. Henins M. S. Kelly	"Optically Isolated High Voltage Trigger System"	Rev. Sci. Instrum. 48, 168 (1977)

D. W. Hewett C. W. Nielson	"A Multi-Dimensional Quasi-Neutral Hybrid Simulation Code"	submitted to J. Comput. Phys.
J. G. Hoffman	"Some Observations of the Interaction of Alumina with a Deuterium Plasma	to be published in J. Nucl. Mater.
J. G. Hoffman	"Refractory Oxides for Fusion Reactor First Walls - the Effects of the Reducing Environment"	to be published in Rev. Int. des Hautes Temperatures et des Refractaires
F. Hohl S. P. Gary	"Electron Kinematics in a Plasma Focus"	Phys. Fluids 20, 683 (1977)
Y. S. Horowitz B. Ben Shahar S. Mordechai A. Dubi H. Pinto	Thermoluminescence in LiF Induced by Monoenergetic, Parallel Beam, 13.8 MeV and 18.0 MeV Diffracted Neutrons: The Intrinsic TL Response per Absorbed Neutron"	Radiat. Res. 69, 402 (1977)
A. R. Jacobson	"A Heterodyne Quadrature Interferometer for Simultaneous Measurements of Plasma Density Along Several Chords"	submitted to Rev. Sci. Instrum.
T. R. Jarboe	"Measurement of Faraday Rotation in the Implosion Heating Experiment"	J. Appl. Phys. 48, 557 (1977)
D. S. Lemons S. P. Gary	"Electromagnetic Effects on the Modified Two-Stream Instability"	J. Geophys. Res. 82, 2337 (1977)
D. S. Lemons S. P. Gary	"Current Driven Instabilities in a High Beta, Quasi-Perpendicular Shock"	submitted to J. Geophys. Res.
H. R. Lewis L. Turner	"Formation of the Linearized Vlasov-Fluid Model for a Sharp-Boundary Screw Pinch"	submitted to Phys. Fluids
H. R. Lewis K. R. Symon	"Linearized Analysis of Inhomogeneous Plasma Equilibria: General Theory"	submitted to Phys. Fluids
R. C. Malone R. L. Morse	"Material End Plugging of Straight Theta Pinches"	Phys. Rev. Lett. 39, 134 (1977)
K. F. McKenna T. M. York	"End Loss from a Collision Dominated Theta Pinch Plasma"	Phys. Fluids 20, 1556 (1977)
G. Miller	"Long Wavelength m=1 Magnetohydrodynamics of a Theta Pinch"	Phys. Fluids 20, 928 (1977)
R. L. Miller R. A. Krakowski	"Thermal Conduction and Alpha-Particle Constraints for the Ignition of a D-T Linear Magnetic Fusion (LMF) Reactor"	submitted to Phys. Fluids
D. Montgomery L. Turner G. Vahala	"Three-Dimensional Magnetohydrodynamic Turbulence in Cylindrical Geometry"	submitted to Phys. Fluids
D. W. Muir	"Data Covariance Estimation Methods for Sensitivity-Based Data Assessment"	Trans. Am. Nucl. Soc. 26, 484 (1977)
D. W. Muir W. A. Reupke	"Data Adjustment in the Fusion Regime: Experience and Future Directions"	Trans. Am. Nucl. Soc. 27, 884 (1977)
M. G. Olsson E. T. Osypowski L. Turner	"Resolution of an Ambiguity in Alternative Soft-Pion Approaches to $\pi N \rightarrow \pi\pi N$ Near Threshold"	Phys. Rev. Lett. 38, 296 (1977)
L. D. Pearlstein J. P. Freidberg	"Finite Larmor Radius Equations in an Arbitrary Near Theta Pinch Geometry"	submitted to Phys. Fluids

J. D. Rogers D. J. Blevins J.D.G. Lindsay G. A. Miranda C. E. Swannack D. M. Weldon J. J. Wollan C. J. Mole E. Mullan P. W. Eckels H. E. Haller M. A. Janocko S. A. Karpathy D. C. Litz P. Rerchner Z. N. Sanjana M. S. Walker	"0.54-MJ Superconducting Magnetic Energy Transfer and Storage"	to be published in Adv. in Cryogenic Eng. 24
J. L. Schwarzmeier H. R. Lewis B. A. Shrauner K. R. Symon	"Stability of BGK Equilibria"	submitted to Phys. Fluids
A. G. Sgro	"Calculations of the Effects of Incomplete Preionization in High Voltage Theta Pinches"	submitted to Phys. Fluids
E. L. Simmons D. J. Dudziak S.A.W. Gerstl	"Nuclear Design Sensivity Analysis for a Fusion Reactor"	Nucl. Technol. 34, 317 (1977)
L. Turner	"Vlasov-Fluid Theory of Short-Wavelength Instabilities of a Sharp-Boundary Screw-Pinch"	Phys. Fluids 20, 662 (1977)
L. Turner	"Finite-Larmor-Radius Stabilization in a Sharp-Boundary Vlasov-Fluid Screw-Pinch"	Phys. Fluids 20, 654 (1977)
L. R. Veeser E. D. Arthur P. G. Young	"Cross Sections for (n,2n) and (n,3n) Reactions Above 14 MeV"	Phys. Rev. C 16, 1792 (1977)
D. Winske P. C. Liewer	"Particle Simulation Studies of the Lower Hybrid Drift Instability"	submitted to Phys. Fluids
P. G. Young E. D. Arthur	"^{59}CO + n Calculations up to Neutron Energies of 40 MeV"	Trans. Am. Nucl. Soc. 26, 503 (1977)

P. E. Armstrong R. A. Krakowsi	"Thermal Shock Experiment (TSEX)"	LA-6861-MS
D. A. Baker J. N. Di Marco P. R. Forman J. A. Phillips	"Preliminary Engineering Calculations for a Toroidal Reverse-Field Pinch Reactor"	LA-6815-MS
L. C. Burkhardt	"Toroidal Z-Pinch Demonstration"	LASL-77-3 Mini Review
D. J. Dudziak	"Imploding-Liner Reactor Nucleonic Studies"	LA-6948-MS
A. R. Jacobson	"A Novel Interferometer for the Measurement of Plasma Density"	LA-6727-MS
A. R. Jacobson	"A Design for Coordinated Measurements of Faraday Rotation and Line-of-Sight Electron Density Using Heterodyne Techniques"	LA-6875-MS
J.D.G. Lindsay D. M. Weldon	"Loss Measurements in Superconducting Magnetic Energy Storage Coils"	LA-6790-MS
J. D. Rogers H. F. Vogel D. M. Weldon R. W. Warren	"Proposed Tokamak Poloidal Field System Development Program"	LA-6811-P
T. J. Seed W. F. Miller, Jr. F. W. Brinkley, Jr.	TRIDENT: A Two-Dimensional Multigroup, Triangular Mesh Discrete Ordinates, Explicit Neutron Transport Code"	LA-6735-M
A. R. Sherwood B. L. Freeman R. A. Gerwin T. R. Jarboe R. A. Krakowski R. C. Malone J. Marshall R. L. Miller B. Suydam	"Fast Liner Proposal"	LA-6707-P
R. E. Siemon	"A Summary of Scyllac Results"	LA-7125-MS
E. L. Simmons S.A.W. Gerstl D. J. Dudziak	"Cross-Section Sensitivity Analyses for a Tokamak Experimental Power Reactor"	LA-6942-MS
P.C.T. Van der Laan	"Effects of Flux Conservation on the Field Configuration in Scyllac"	LA-6767-MS
H. Vogel T. Thullen D. Weldon	"TNS Doublet Tokamak Ohmic-Heating Power Supply Study"	LA-7053-MS
H. Vogel	"Current Control by a Homopolar Machine with Moving Brushes"	LA-7090-MS
R. W. Warren	"Experiments with Vacuum Interrupters Used for Large DC-Current Interruption"	LA-6909-MS
R. L. Whitman F. C. Jahoda R. P. Kruger	"Automated Computer Analysis of Plasma Streak Traces from Scyllac"	LA-6961-MS

SEVENTH SYMPOSIUM ON ENGINEERING PROBLEMS OF FUSION RESEARCH

KNOXVILLE, TENNESSEE

OCTOBER 1977

G. P. Boicourt	"Circuit and Plasma Simulation for the Design of ZT-40"
L. C. Burkhardt R. S. Dike	"Spark Gap Overpressures in the 0.2 Megampere Range"
R. Conrad J. W. Lillberg R. W. Wilkins	"Scylla IV-P Computer Based Control and Data Acquisition System"
K. W. Hanks T. R. Cole	"A Toroidal Helical Quartz Forming Machine"
L. D. Hansborough T. R. Cole R. J. Commisso K. D. Williamson	"Material End-Plugging for the Scylla IV-P Linear Theta Pinch"
L. D. Hansborough J. M. Dickinson J. G. Melton W. C. Nunnally	"Design and Fabrication of a Radially Fed Implosion Heating Coil"
E. M. Honig	"Dual 30-kA, HVDC Interrupter Test Facility"
K. J. Kutac R. W. Kewish G. Miller R. F. Gribble	"Final Analysis of the Engineering Data on the Scyllac Feedback Stabilization Experiment"
M. D. Machalek	"Recent Work on Normal and Superconducting Inductive Energy Storage Switching at the Efremov Institute, Leningrad, USSR"
J. G. Melton R. S. Dike K. W. Hanks W. C. Nunnally	"Development of Switching Components for ZT-40"
W. C. Nunnally G. P. Boicourt	"Design of the ZT-40 Power Crowbar System"
W. C. Nunnally A. T. Brousseau	"Air Driven Fiber Optic Coupled Pulsed System for ZT-40"
W. C. Nunnally	"Power Crowbar Component Requirements for High-Beta Fusion Reactors"
H. F. Vogel	"Gas Breakers for Tokamak Ohmic-Heating Duty"
R. W. Warren	"Vacuum Interrupters Used for the Interruption of High D.C. Currents"

IEEE 1977 INTERNATIONAL CONFERENCE ON PLASMA SCIENCE

TROY, NEW YORK

MAY 1977

C. A. Ekdahl R. J. Commisso K. B. Freese R. Kristal K. F. McKenna R. E. Siemon W. E. Quinn	"Reduction of Plasma End Loss With Solid End Plugs in the Scylla IV-P Linear Theta Pinch"

R. K. Linford D. A. Platts E. G. Sherwood	"Field-Reversal Theta Pinch Experiments"
K. F. McKenna R. J. Commisso C. A. Ekdahl K. B. Freese R. Kristal R. E. Siemon W. E. Quinn	"Plasma Parameters and End-Loss Measurements in the Scylla IV-P Linear Theta Pinch"
H. F. Vogel P. Thullen K. D. Williamson, Jr.	"1.5-MA, 10-MJ Load Coil for a Pulsed Homopolar Machine"
R. W. Warren	"Interruption of High DC Currents"

EIGHTH EUROPEAN CONFERENCE ON CONTROLLED FUSION AND PLASMA PHYSICS

PRAGUE, CZECHOSLOVAKIA

SEPTEMBER 1977

R. R. Bartsch E. L. Cantrell R. F. Gribble K. B. Freese L. E. Handy R. Kristal G. Miller W. E. Quinn	"Feedback Stabilization Experiments Using ℓ=2 Equilibrium Windings in Scyllac"
D. A. D'Ippolito J. P. Freidberg J. P. Goedbloed J. Rem	"High-Beta Tokamaks Surrounded by Force-Free Fields"
H. Höthker J. Downing	"Experimental Study of Magnetic Field Diffusion in a High-β-Plasma of a 7-m θ-Pinch at Low Densities"
H. R. Lewis L. Turner M. Menzel	"Finite-Gyroradius Effects in Screw Pinches"
K. F. McKenna R. J. Commisso C. A. Ekdahl K. B. Freese R. Kristal W. E. Quinn R. E. Siemon	"Experiments on End-Loss Phenomena and Material End Plugs in a 5-m Linear Theta Pinch"
K. R. Symon J. L. Schwarzmeier H. R. Lewis	"Stability of BGK Equilibria"

FIFTH INTERNATIONAL CONFERENCE ON REACTOR SHIELDING

KNOXVILLE, TENNESSEE

APRIL 1977

M. E. Battat D. J. Dudziak	"Shield Analyses for Intense 2.2-pJ (14-MeV) Neutron Sources"
M. E. Battat	"Shielding Standards - A Case History"

A. Dubi Y. S. Horowitz	"Applications of the Monte Carlo Track Rotations Estimator"
S.A.W. Gerstl	"Sensitivity Profiles for Secondary Energy and Angular Distributions:
J. L. McDonald E. D. Cashwell C. J. Everett	"Calculation of Toroidal Fusion Reactor Blankets by Monte Carlo"

SYMPOSIUM ON NEUTRON CROSS SECTIONS - 10-40 MeV

UPTON, NEW YORK

MAY 1977

E. D. Arthur P. G. Young	"Cross Sections in the Energy Range from 10 to 40 MeV Calculated with the GNASH Code"
D. J. Dudziak D. W. Muir	"Review of MFE Neutron Cross-Sections Needs - Neutronics Viewpoint"
L. Stewart E. D. Arthur	"Neutron Evaluation at High Energies - Problems and Prospects - Review"

OTHER CONFERENCES

D. C. Barnes J. V. Brackbill W. Schneider	"Analytic and Numerical Studies of Diffuse, Three-Dimensional Equilibria in Scyllac," Third International (Kiev) Conference on Plasma Theory, Trieste, Italy, April 1977.
R. L. Hagenson R. A. Krakowski K. I. Thomassen	"A Toroidal Fusion Reactor Based on the Reversed-Field Pinch (RFP)," IAEA Conference and Workshop on Fusion Reactor Design, Madison, Wisconsin, October, 1977.
R. A. Krakowski R. W. Moses R. L. Miller R. A. Gerwin	"Fusion Power from Fast Imploding Liners," IAEA Conference and Workshop on Fusion Reactor Design, Madison, Wisconsin, October 1977.
R. A. Krakowski A. S. Tai	"A Simple Parametric Analysis of Fissile Euel Production by Fusion-Fission Reactors," Second DMFE Fusion-Fission Energy Systems Review Meeting, Washington, D.C., November 1977.
R. L. Miller R. A. Krakowski	"Magnetic Fusion Alternate Concepts Heating Requirements," DOE/DMFE Plasma Heating Development Requirements Workshop, Gaithersburg, Maryland, December 1977.
J. D. Rogers D. J. Blevins J.D.G. Lindsay G. A. Miranda C. E. Swannack D. M. Weldon J. J. Wollan C. J. Mole E. Mullan D. W. Deis P. W. Eckels H. E. Haller M. A. Janocko S. A. Karpathy D. C. Litz P. Rerchner Z. N. Sanjana M. S. Walker	"Pulsed Superconducting Inductive Energy Storage Coils," Sixth International Conference on Magnet Technology, Bratislava, Czechoslovakia, 1977.

H. F. Vogel
M. D. Driga
"Magnetics and Superconducting Coil Design of a 10-mJ, Fast-Discharging Homopolar Machine," Sixth International Conference on Magnet Technology, Bratislava, Czechoslovakia, 1977.

G. J. Shevchuk
P. Thullen
"Vibrations of Electromagnetic Shields in Superconducting Alternators," World Electrotechnical Congress, Moscow, Russia, June 1977.

☆ U.S. Government Printing Office: 1979 — 677-013/13

Printed in the United States of America. Available from
National Technical Information Service
US Department of Commerce
5285 Port Royal Road
Springfield, VA 22161

Microfiche $3.00

001-025	4.00	126-150	7.25	251-275	10.75	376-400	13.00	501-525	15.25
026-050	4.50	151-175	8.00	276-300	11.00	401-425	13.25	526-550	15.50
051-075	5.25	176-200	9.00	301-325	11.75	426-450	14.00	551-575	16.25
076-100	6.00	201-225	9.25	326-350	12.00	451-475	14.50	576-600	16.50
101-125	6.50	226-250	9.50	351-375	12.50	476-500	15.00	601-up	

Note: Add $2.50 for each additional 100-page increment from 601 pages up.